Groundwater temperatures, their spatiotemporal distribution and drivers of groundwater temperature evolution in the Netherlands

Visser, P.W.

DOI
10.4233/uuid:f27cba52-fc9c-49bf-99a4-8db7a945fefc

Publication date
2024

Document Version
Final published version

Citation (APA)
Visser, P. W. (2024). *Groundwater temperatures, their spatiotemporal distribution and drivers of groundwater temperature evolution in the Netherlands*. [Dissertation (TU Delft), Delft University of Technology]. https://doi.org/10.4233/uuid:f27cba52-fc9c-49bf-99a4-8db7a945fefc

Groundwater temperatures, their spatiotemporal distribution and drivers of groundwater temperature evolution in the Netherlands

Philip Visser

Groundwater temperatures, their spatiotemporal distribution and drivers of groundwater temperature evolution in the Netherlands

Dissertation
for the purpose of obtaining the degree of doctor
at Delft University of Technology
by the authority of the Rector Magnificus Prof.dr.ir. T.H.J.J. van der Hagen;

Chair of the Board for Doctorates
to be defended publicly on
Monday 30 September 2024 at
15:00 o'clock
by
Philippus Wilhelm VISSER
Master of Science in Agricultural Sciences, Wageningen University, the Netherlands
born in Zoetermeer, the Netherlands

This dissertation has been approved by the promotor.

Composition of the doctoral committee:

Rector Magnificus,	Delft University of Technology, chairperson
Prof.dr. P.J. Stuijfzand	Delft University of Technology, promotor
Dr. H. Kooi	Deltares, copromotor

Independent members:

Prof.dr. P.J. Vardon	Delft University of Technology
Prof.dr. P. Blum	Karlsruhe Institute of Technology
Dr.ir. J.M. Bloemendal	Delft University of Technology
Dr. V.F. Bense	Wageningen University & Research
Prof.dr.ir. Uijlenhoet	Delft University of Technology, reserve member

Dr. H. Kooi, Deltares, has, as supervisor, contributed significantly to the preparation of this dissertation.

This work was performed within the cooperation framework of Wetsus, European centre of excellence for sustainable water technology (www.wetsus.eu). Wetsus is co-funded by the Dutch Ministry of Economic Affairs and Ministry of Infrastructure and Environment, the Province of Fryslân and the Northern Netherlands Provinces.

This work was carried out at KWR Watercycle Research Institute, Arcadis Nederland B.V., VU University Amsterdam and Delft University of Technology.

Cover: Monitoring well B33D0168 near the highest point of the Veluwe, featuring in Chapter 2.
Photograph by the author.

To Fatiha, Beagy and Happy

Table of contents

List of abbreviations and symbols

Symbol or Abbreviation	Description	Unit
Re_*	roughness Reynolds number	dimensionless
EC_o	specific electrical conductance of soil sample	S.m^{-1}
EC_w	specific electrical conductance of water	S.m^{-1}
EV_{act}	actual evaporation	mm.h^{-1}
$GR_{Clean\ Rock}$	response of the gamma ray log clean rock	API units
$GR_{Log\ Signal}$	natural gamma ray radiation	API units
GR_{Shale}	response of the gamma ray log shale body	API units
I_{GR}	gamma ray index	dimensionless
K_e	Kersten number	dimensionless
N_t	total cloud cover	fraction
Q_v	excess of surface charge per unit pore volume	eq.L^{-1} or Coulomb.m^{-3}
R_{app}	apparent thermal retardation factor	dimensionless
R_{eff}	effective thermal retardation factor	dimensionless
R_o	resistivity of fluid-filled porous rock	Ω.m
R_w	resistivity of water	Ω.m
S_r	normalized soil water content (effective saturation)	dimensionless
T_a	air temperature	ºC
T_R	radiometric surface temperature	ºC
V_{sh}	shale volume fraction	dimensionless
c_b	bulk volumetric heat capacity of the aquifer	J.m^{-3}.K^{-1}
c_s	volumetric heat capacities of aquifer solids	J.m^{-3}.K^{-1}
c_w	volumetric heat capacities of water	J.m^{-3}.K^{-1}
k_{dry}	dry thermal conductivity	W.m^{-1}.K^{-1}
k_o	thermal conductivity of minerals other than quartz	W.m^{-1}.K^{-1}
k_q	thermal conductivity of quartz	W.m^{-1}.K^{-1}
k_s	thermal conductivity soil solids	W.m^{-1}.K^{-1}
k_{sat}	saturated thermal conductivity	W.m^{-1}.K^{-1}
k_w	thermal conductivity water	W.m^{-1}.K^{-1}
r_h	resistance to heat transfer from the surface	m^{-1}
u_*	the friction velocity	m.s^{-1}
$z_{0\mathrm{h}}$	roughness lengths for heat	m
$z_{0\mathrm{m}}$	roughness lengths for momentum	m
α_m and β_m	Makowski-Mochlinski factors depending on the clay content	dimensionless
α_j	soil texture dependent parameter in Johansen equation	dimensionless
ρ_a	air density	kg.m^{-3}
ρ_b	bulk density	kg.m^{-3}
ρ_d	dry density	kg.m^{-3}
ρ_s	density solids	kg.m^{-3}
ρ_w	water density	kg.m^{-3}
ATES	Aquifer thermal energy storage	
bgl	Below ground level	
EVP	Evapotranspiration	m.s^{-1}
GST	Ground surface temperature	ºC
GWT	Groundwater temperature	ºC

LAI	Leaf area index	
LN100/ LN200	long normal resistivity 100/200 cm electrode spacing	Ω.m
q_x	horizontal component of specific discharge	m.s^{-1}
q_z	Darcy flux in vertical direction	m.s^{-1}
r_{am}	aerodynamic resistance for momentum	s.m^{-1}
r_b	bulk aerodynamic excess resistance	s.m^{-1}
Rl	long-wave radiation	W.m^{-2}
r_r	radiometric excess resistance	s.m^{-1}
Rs	short-wave radiation	W.m^{-2}
SARB	Surface-atmosphere radiation balance	
SAT	Surface air temperature	ºC
SP	self-potential	mV
SUHI	Subsurface urban heat island	
T	Temperature	ºC
T20-35	Temperature at 20-35 m below ground level	ºC
T_{-20m}	Temperature at 20 m below ground level	ºC
TD	Temperature-depth	
T_w	Surface water temperature	ºC
UHI	Urban heat island	
UTES	Underground thermal energy storage	
B	equivalent conductance of clay exchange cations	S.m^{-1}
CEC	cation exchange capacity	eq.L^{-1} or Coulomb.m^{-3}
F	formation resistivity factor	dimensionless
G	ground heat flux density	W.m^{-2}
H	sensible heat flux density	W.m^{-2}
K	Von Kármán constant	dimensionless
L	heat of vaporization	J.m^{-2}.h^{-1}
Q	quartz content	Fraction
C	clay content	% dry weight
k	thermal conductivity	W.m^{-1}.K^{-1}
m	Archie cementation exponent	dimensionless
S	silt content	% dry weight
w	moisture content	% of dry weight
α	thermal diffusivity	m^{2}.s^{-1}
ε	emissivity of the Earth’s surface	W.m^{-2}
σ	Stefan-Boltzman constant	J.K^{-1}
υ	kinematic molecular viscosity	m.s^{-1}
φ	porosity	Fraction

Summary

Groundwater is a valuable natural resource, providing irrigation water and water for industrial processes and supplying about half of the world's population with drinking water.
Groundwater temperature (GWT) is important for the physical and chemical state of groundwater. Insight in the GWT field has many practical applications. Groundwater temperature is being used as a tracer in research into the lateral and vertical flow of groundwater and hydraulic properties of the subsurface. Temperature-depth (TD) profiles have been used in paleo-climate reconstruction. Subsurface and groundwater temperature is also an important design parameter for underground infrastructure, such as power transmission networks.

GWT is determined by quasi-equilibrium between heat flow from the Earth's interior (geothermal heat flow) and the long-term ground surface temperature (GST). GST is subject to various short- and long-term fluctuations and changes. These disturbances propagate downward as thermal waves, while being attenuated with depth. Diurnal fluctuations dominate GWT at very shallow depths (<0.5 m), while seasonal fluctuations at the surface propagate to a depth of approx. 15 m.

Human-induced climate change resulted in an observed surface air temperature (SAT) rise since approx. 1900. SAT in the Netherlands shows an accelerated increase since the late 1970's. Climate change results in increasing GST and rising temperatures of infiltrating rain and surface water, resulting in higher GWT. Other drivers affecting GWT include changes in land use (agriculture, urbanization, deforestation) and the hydrological system by pumping or managed aquifer recharge. Furthermore, the subsurface temperature is affected by anthropogenic heat sources, such as underground constructions and infrastructure. Aquifers are increasingly being used worldwide for storage and recovery of (seasonal) thermal energy, such as underground thermal energy storage (UTES), or aquifer thermal energy storage (ATES). These may cause local, large temperature anomalies.

Insight into subsurface and groundwater temperatures, their spatial distribution and change in time is important for groundwater management and optimum use of the subsurface e.g. for UTES. The aim of this thesis is to improve the understanding of groundwater temperatures, their spatiotemporal distribution and drivers of groundwater temperature evolution in the Netherlands. The most important drivers of groundwater temperature change are climate change, land use change (in particular urbanization), and underground thermal energy storage. Based on this, the following main research questions have been formulated:

1. How are groundwater temperatures distributed in the Netherlands, and how are the mapped patterns explained?
2. What are the regional temporal trends in groundwater temperature. How are these trends related to changes in land use, climate and groundwater management or exploitation?
3. What is the impact of urbanization on subsurface and groundwater temperatures?
4. What is the impact of aquifer thermal energy storage (ATES) on local groundwater temperatures? Is this impact related to hydraulic and thermal heterogeneity of the subsurface?

Chapter 2

Regional patterns and trends in groundwater temperature with drivers of change are studied in this chapter to provide answers to research questions 1 and 2. Temperature-depth (TD) profiles, field measurements of groundwater sample temperatures and temperature data of abstracted water at public supply well fields (PSWFs) are used to map, discern and explain groundwater temperature patterns and trends.

Between 1976 and 1982, hundreds of TD profiles were measured by previous researchers. Between 2010 and 2018, dozens of TD profiles were measured by the author. Some of the same wells of the 1976-1982 campaign were used, making comparison between the different time periods possible. Field temperatures of groundwater samples collected between 1908 and 2012 were derived from the national groundwater information database. Sample temperatures were filtered by depth (20-35 m bgl) and time series of at least 4 samples per piezometer. Unlikely low (<5ºC) and high (>17ºC) temperatures were discarded. This resulted in a set of 2893 temperature readings from 383 observation wells, collected between 1991 and 2011 at depths of 20-35 m (T20-35). Temperature time series of abstracted groundwater at PSWFs were obtained from the KIDAP database (Mendizabal & Stuyfzand, 2009). for phreatic, semi-confined and riverbank filtrate (RBF) water sources.

T20-35 values were averaged for each selected monitoring well. The averaged T20-35 values were mapped and interpolated. This resulted in mapped regional patterns of higher and lower GWT at 20-35 m depth. Lowest GWT are found in the topographically high areas, and higher GWT in the highly urbanized west of the country. Monitoring wells deeper than 20 m with time series of groundwater sample temperatures are scarce in urban areas. Highest temperatures associated with urban heat islands and subsurface urban heat islands (SUHI) were, therefore, not detected in the mapped T20-35. The study of the suburban heat island of Amsterdam (Chapter 3) shows that anomalous high temperatures occur at 20 m depth in city centers. Uncommonly high T20-35 is found in the southeast of the country. It was tested by a numerical 1D model whether shallow or deep occurrences of rock with different thermal properties play a role in this. Shallow occurrence of low-conductivity (low solidity) rock in the thermally anomalous area could explain a small contribution to the higher T20-35. Vertical flow of groundwater along fault planes remains a likely cause of local thermal anomalies but provides no satisfactory explanation for the high T20-35 values in larger stretches of the southeast of the study area.

Time-dependent GWT trends were determined for each of the 383 monitoring wells, using the Mann-Kendall test. Trends were classified in (probably) increasing and decreasing and stable trends. For 237 locations, a statistically significant trend was discerned. By far, most (77%) of the locations show a (probably) increasing GWT trend. A smaller percentage (22%) of the locations indicate a stable GWT, while at 3 locations a (probably) decreasing trend was found.

The topographical distribution of GWT and trends shows a clear regional pattern. Low, but increasing temperatures dominate in the topographically higher parts of the country, stable, but higher GWT temperatures in the lower areas. This is explained by recharge in the higher regions conveying low but increasing GSTs to greater depths. In the low-lying west of the country, recharge is less dominant and in deep polders seepage occurs. Relatively high percentages of built-up areas in the west cause a high GST, but hamper groundwater recharge. In those areas, increasing GST only propagates downward by conduction, which is a slower process than the combination of conduction and advection in the high parts of the country.

The relation and spatial distribution of GWT, GWT increase, and GST trends were further investigated by applying a surface-atmosphere radiation balance (SARB) model. With this model, hourly data from 1965 to 2020 of 5 meteorological stations in different parts of the country were used to estimate the GST. A paved (asphalt) surface, grass covered surface and forest floor were simulated. These calculations demonstrate how the GST of comparable surfaces varies between different parts of the country and to which extent the GST deviates from SAT (GST-SAT offset).

Historical field data of the GST-SAT offsets and drainage water temperatures of lysimeters with different types of vegetation were collected. Inverse modeling of TD profiles provided GST-SAT offsets for various types of land cover and different periods. High frequency (6-hourly) ground surface (up to 5 cm below ground surface) temperature measurements at 4 meteorological stations in the Netherlands provided detailed temperature information for grass covered surfaces from 1981 onwards. These field data allowed comparison with the SARB derived GSTs. The observed grass surface GST of nearby stations shows that the SARB model provides a reasonable estimate of the GST and GST trend. The modeled forest GST-SAT offset is, similar to that of a mature pine forest in the lysimeter studies, smaller than zero. This shows that, on the average, the forest floor is cooler than SAT. Bare soil (sand) lysimeter GST-SAT offsets are high, but lower than asphalt offsets, due to the higher albedo of sand.

SARB model-based GST-SAT offsets were applied to different types of land cover on a 1km^2 grid covering the Netherlands. SAT data from the 5 meteorological stations used were assigned to the grid as well. This resulted in an estimated GST map and a GST-SAT offset map. These maps show similar patterns as the interpolated T20-35 map, with low GST values in the northeast and east of the country and higher GST values in the urbanized areas in the west. The extent of the high T20-35 area in the west is significantly larger than mapped by previous researchers in the 1970's and '80's. The observed average T20-35 values show a statistically significant relation with the calculated GSTs. The anomalously high T20-35 values in the southeast, that could not satisfactorily be explained by the geological structure, do coincide with areas with a high simulated GST. The southeast of the country receives the lowest annual amount of precipitation, minimizing the effect of infiltrating winter precipitation.

Including rainfall and groundwater recharge in the SARB model resulted in a less accurate (too low) GST estimate. This indicates that rainfall and groundwater recharge are not directly affecting GST. However, as precipitation conveys the surface temperature downward through groundwater recharge, it plays an important role in the GWT evolution. In the Netherlands, equal amounts of precipitation fall in summer and winter. During the summer season, there is no net-surplus of precipitation over evapotranspiration. During winter, evapotranspiration is less, and recharge rates are higher. Therefore, lower winter surface and precipitation temperatures are disseminated to the subsurface through infiltration. In topographically high areas, where low T20-35 and GST prevail, annual precipitation is high. This strengthens these "heat sinks". Annual precipitation is also high in the urban areas in the west. As less infiltration takes place in these areas, the “cooling” precipitation effect on GWT is less.

Studies of the temperature field of the subsurface often assume a constant GST-SAT offset over time and space (unless obvious land use change occurred). SARB model results show that this offset does not only depend on the land cover, but also on the meteorological/climatological characteristics of the site. These characteristics differ even on a small scale as the Netherlands. The GST-SAT offsets are variable in time. SAT and global (incoming) radiation largely determine GST. Dependence on these two factors makes a GST-SAT relation less unambiguous. Evapotranspiration used is based on the Makkink method, and, therefore, it is related to SAT and global radiation as well. Estimates of the actual evapotranspiration in the SARB model of grass and forest assume a perfectly watered vegetation. This is rarely the case. Actual evapotranspiration is, therefore, over-estimated in the SARB model, resulting in a systematically too low calculated GST.

The phreatic PSWF temperatures show, despite their greater depth of groundwater abstraction, generally a good correlation with observed and interpolated T20-35 values. PSWFs tapping deeper (semi-)confined aquifers show relatively high water temperatures. The highest temperatures are associated with the deepest well fields in the Roer Valley Graben. Despite river water temperatures being higher than T20-35, RBF abstracted by PSWFs in the gaining reaches of the major rivers show temperatures that are equal or even sometimes lower than T20-35. Apparently, there most of the abstracted water is autochthonous groundwater flowing towards the river. In lower, infiltrating reaches of the major rivers, the RBF temperature is higher than the interpolated T20-35 and lower than the river water temperature, due to mixing of infiltrating river water and autochthonous groundwater. Detailed temperature observations of river water, groundwater and extracted RBF could possibly be used as a tool to determine autochthonous groundwater and river water mixing ratios.

Chapter 3

Chapter 3 describes the development of the subsurface urban heat island (SUHI) of the city of Amsterdam, as an example of a typical mid-sized, mid-latitude city. This chapter provides answers to research question 3. The city of Amsterdam is especially well suited to describe the evolution of its SUHI, as it has been growing since the Middle Ages in a well-documented and somewhat concentric pattern, resulting in the city center being the oldest part of the city, and the farther away from the center, the younger the building stages are.

Surface air temperature (SAT) data were collected from nearby Schiphol meteorological station and from semi-professional amateur stations at various locations in the city. Historical data (1785-1961) of a meteorological station in the city center were retrieved. A reconstruction of the annual temperature data for The Netherlands, dating back to the eighth century, was used for historical SAT data before 1785. GWT data at 20 m below ground level (T_{-20m}) were collected in 63 monitoring wells in and around the city. Few monitoring wells deeper than 20 m are available. In 6 deeper (45-115 m) wells TD profiles were measured. The TD profiles show a concave shape, characteristic of increasing ground surface temperatures. For one location, comparison with an older temperature log shows that temperatures have increased to a depth of approx. 62 m in the period 1979–2012.

The Schiphol SAT tracks the SAT at De Bilt, central Netherlands, very closely. The Schiphol SAT, therefore, shows little influence of the urban heat island (UHI) of Amsterdam. The long-term average SAT in the city center is 1.1°C higher than at Schiphol and De Bilt. This is confirmed by the amateur station measurements. This UHI effect is quite constant since the late 18th century.

The measured minimum and maximum T_{-20m} are respectively 10.8 and 15.1 °C. The mean is 12.5 °C with a 1.1 °C standard deviation, resulting in a 95% reliability interval of approx. 10.3–14.7 °C. T_{-20m} values below 11.0 °C are found near the city limits. These temperatures are only marginally higher than the long-term average SAT for Schiphol and, therefore, considered to be the (rural) background temperature. T_{-20m} values between 11 and 13 °C are found scattered over all built-up areas of the city. All T_{-20m} >13 °C are concentrated in and near the city center, in the parts of the city that were built before 1900 CE, whilst also highest T_{-20m} values are associated with the higher built-up densities.

A 2D cross-sectional numerical model, parallel to the regional groundwater flow and stretching from the city center to the city margins and reaching to 200 m below ground level, was used to describe the development of the temperature distribution from 1350 to 2012. To be able to distinguish between the GST of various types of pavements that is used through the centuries in the city, a separate SARB model was used. The heat loss from buildings has changed over time with introduction of space heating and central heating. The building density, pavement types and heat loss from buildings were incorporated into the 2D model as a time-dependent thermal top boundary condition.

The calculated temperature distributions clearly reflect the staged urban expansion in the shifting of the front of higher temperatures from the city center to city margins. The effect of groundwater flow is obvious from a slight tilting of the thermal fronts. The calculated TD profiles show, as expected, the concave deviation of the curves from the straight deeper end of the curves at larger depth for the older urban expansion stages. The calculated TD profiles fit in the measured ranges, supporting the suitability of the approach; however, it is recommended to repeat the TD logging and T_{-20m} measurements in the future to be able to validate the model. Validation of the model would allow the use of the model to predict the future thermal state of the SUHI. Site specific developments and conditions cannot be incorporated in the 2D model, using rather large intervals to schematize the urban development. Although no direct comparison is possible, the calculated TD profiles appear to have systematically slightly higher temperatures than the observed TD profiles. A possible over-estimation of the GST may play a role in this. One measured TD profile showed anomalous high temperatures in the deeper part of the observed curve. This must be caused by lateral advection from a deep-seated heat source, possibly a subway station, although other sources, like an underground thermal energy storage (UTES) system, cannot be excluded.

The distribution of the T_{-20m} values, as a measure of the SUHI intensity, is rather well explained by the model. This leads to the observation that the maximum T_{-20m} on a regional (model) scale, which can be explained from the urban expansion history and land cover, is 13.5 °C. The TD observations, however, are only representative of a small subsurface volume around the observation well. These differences in scale explain, at least in part, deviations between the maximum modeled and observed T_{-20m} values. T_{-20m} observations between 13.5 and 14.0 °C may suggest that the lower value is a slight underestimation of the actual maximum. Values above 14 °C can be linked to localized anthropogenic heat sources and have no great extent. The actual maximum SUHI intensity at 20 m depth is, therefore, between 2.5 and 3.0 °C for Amsterdam.

The study demonstrates that, through modeling of centuries-long (from fourteenth to twenty-first century) urban development and climate change, along with the history of both the surface urban heat-island temperatures and ground surface temperatures, it is possible to simulate the development and present state of the Amsterdam SUHI. The results provide insight into the drivers of long-term SUHI development, which makes it possible to distinguish subterranean heat sources of more recent times that are localized drivers (such as geothermal energy systems, sewers, boiler basements, subway stations or district heating) from larger-scale drivers (mainly heat loss from buildings and raised ground surface temperatures due to pavements). Because these findings have consequences for the assessment of the UTES/ATES potential of the SUHIs, it is proposed to distinguish between (1) a regional, long-term SUHI that has developed over centuries due to the larger-scale drivers, and (2) local anomalies caused by anthropogenic heat sources less than one century old.

Chapter 4

In Chapter 4, results are presented of a comprehensive thermal impact study on an aquifer thermal energy storage (ATES) system in Bilthoven, the Netherlands. The study involved monitoring of the thermal impact and modeling of the three-dimensional temperature evolution of the storage aquifer and over- and underlying units. Special attention was paid to non-uniformity of the background temperature, which varies laterally and vertically in the aquifer and levels of detail regarding initial conditions and heterogeneity of hydraulic and thermal properties. This chapter provides answers to research question 4.

The number of ATES systems in the Netherlands has grown exponentially since their introduction in 1987. Comprehensive understanding of the thermal impact of the ATES systems on the utilized aquifers is a fundamental element for risk (being the product of the probability and impact) assessment. The present study focuses on these thermal impacts. The thermal impact is a change in the temperature conditions of the aquifer or the groundwater regime. The spatial extent over which this impact occurs is named thermal affected zone (TAZ) by some authors or temperature affected areas (TAA). However, an accurate and unique definition of this zone does not appear to exist at present. In many assessments for ATES systems, which are rarely published in mainstream literature, the thermal impact is defined as the temperature changes greater than an arbitrary threshold (e.g. 0.5 °C) above and below the natural background temperature. The impact is commonly evaluated through pre-operational predictive modeling where background temperature is usually assumed constant throughout the aquifer and the thermal impact is evaluated as uniform over the storage aquifer thickness. The fact that once operational, a high percentage of ATES systems do not perform as expected in terms of thermal efficiency and thermal balance strongly suggests that the pre-deployment models developed for licensing purposes provide rather poor tools for predicting actual thermal impacts. Few studies are available where the actual temperature development and the influence of the subsurface characteristics were evaluated for a relatively long period after system deployment.

The present study adds to the currently limited set of observation-based case studies of the temperature development in storage aquifers through a detailed investigation of the thermal impact of an ATES system at RIVM in Bilthoven, the Netherlands. The study involved monitoring of the thermal impact in observation wells and modeling of the three-dimensional (3D) temperature evolution of the storage aquifer and over- and underlying units. In contrast to other studies, focus here is on the thermal impact of the ATES system (extent of the thermally impacted zone, maximum and minimum temperatures reached, and temporal variability) rather than on ATES system efficiency. The objective of the study is to evaluate the significance of two factors that influence the impact: (1) complexity associated with the non-uniformity of the “natural” background temperature (both horizontally and vertically), and (2) storage aquifer heterogeneity. The impact under actual operating conditions is also compared to the predicted impact for the design-operating conditions.

The ATES system at RIVM consists of four wells: two wells that are used to inject and abstract cold water (“cold” wells) and two wells that are used to inject and abstract warm water (“warm” wells). The wells are placed along a 230 m long transect. Screens are placed between 47 and 106 m below ground level (m bgl). The ATES system has been in operation since January 2008. Detailed information on volumes of water pumped per well and temperatures of abstracted and injected water were collected for the 2008-2011 period. Monitoring of the ATES system was done with existing nearby piezometers and piezometers placed in the boreholes of the ATES wells. Two additional piezometers were placed as “sentry wells”, approximately on the boundary of the zone that could be influenced by the re-injected water.

The background temperature field was studied using TD logs for monitoring wells at some distance from the ATES system. The background temperature field is complex and nonuniform (both horizontally and vertically). This temperature field forms (a) the reference situation for thermal impact assessment and (b) initial and boundary conditions for the thermal modeling. The background temperature field of the ATES site was constrained using monitoring wells where repeat TD logs collected in the present study (2010–2012) showed stable temperature conditions at depths corresponding to the storage aquifer.

Information on the actual thermal impact of the system was obtained by frequent TD logging in the ATES well piezometers and nearby monitoring wells for several years. Between 2010 and 2012, a total of 120 TD logs were obtained with a measurement interval of 1 m.

The thermal impact was modeled using the TD data, ATES operational data, and a broad set of hydrogeological data. Two site models were developed with different levels of detail regarding representation of the background temperature field and the hydraulic and thermal properties (heterogeneity). A larger scale regional groundwater flow model was used to determine appropriate boundary conditions and initial hydraulic parameters for the site models. Groundwater flow, solute transport and heat transport calculations were performed with the model code SEAWAT (version 4), a coupled version of MODFLOW and MT3DMS designed to simulate 3D variable-density variable-viscosity saturated groundwater flow. Temperature dependency of the fluid density and viscosity were included in the calculations. Fine-scale heterogeneity of the thermal properties was derived from geophysical logs. The method of this derivation is elaborated in Chapter 5.

The results show that a fine-scale heterogeneity model construed the lateral and vertical temperature distribution more realistically than a simplified model which represented the aquifer system with only a limited number of homogeneous layers. Fine-scale heterogeneity was shown to be important to accurately model the ATES-impacted vertical temperature distribution and the maximum and minimum temperatures in the storage aquifer, and the spatial extent of the thermal plumes. The fine-scale heterogeneity model resulted in larger thermally impacted areas and larger temperature anomalies than the simplified model. The models show that scattered and scarce monitoring data of ATES-induced temperatures can be interpreted in a useful way by groundwater and heat transport modeling, resulting in a realistic assessment of the thermal impact.

Chapter 5

Heterogeneity of the thermal properties of the geological strata plays an important role in the development of the subsurface temperature field. This is not only the case for ATES systems, but also under more natural conditions.

In-situ measurement techniques for determining fine-scale vertical thermal properties heterogeneity of aquifers and aquicludes are lacking. Thermal response tests using a closed loop system provide a “bulk” thermal conductivity and capacity. In the past, thousands publicly available, geophysical borehole logs, mainly gamma ray, long-normal (LN) electrical resistivity and self-potential (SP) logs, were collected. For these reasons, it is investigated in this chapter whether “standard” geophysical borehole logging techniques can be usefully applied to assess thermal properties.

Thermal properties were estimated through empirical relationships between physical properties of the subsurface and the thermal conductivity, capacity and retardation. Geophysical logs were used to derive the physical properties of the aquifers and aquitards or aquicludes, and groundwater.

Five boreholes with a maximum depth of 145 m below ground level were analyzed. Borehole lithological and geophysical logs and grainsize data collected at sites in the vicinity and penetrating the same geological formations, amended the data. The geophysical logs were collected in the 1970’s and 1980’s at 0.02 m intervals along the borehole depths.

First, the vertical distribution of the clay percentage was analyzed, using gamma ray logs. Grainsize data revealed a correlation between clay percentage and the fraction silt. The latter is of importance for one of the empirical methods used to estimate thermal conductivity.

Second, the porosity was estimated. Porosity logs e.g., neutron-neutron logs or neutron-gamma logs were not available. In the present case, use has been made of the electrical resistivity logs (LN100 and LN200) to derive the porosity. Porosity was estimated using the Archie’s formation resistivity factor and the ‘Humble equation’ providing a correlation between formation resistivity, porewater resistivity and porosity. Porewater resistivity was shown by numerous samples from the site and its vicinity to be depth- and time-dependent. A depth-resistivity correlation, representative for the period of borehole logging, was derived. Another complicating factor is the electrical conductivity of the clay fraction. In the presence of a significant amount of clay, the Archie method loses accuracy. The conductance of the strata was corrected for the clay content. The method used assumes the presence of an electrical double layer (EDL) and surface electrical conduction at the clay-water interface as explained with the Stern theory. At the low salinity of the porewater of the site, the clay conductivity behaves non-linear with the porewater conductivity. This necessitated to iteratively estimate the electrical conduction of the clay fraction, resulting in a lower clay-conduction factor than based on the cation exchange capacity of the clay minerals.

Calculated clay percentages vary between 0 and 43.2% (weight) with median clay percentages along the entire borehole lengths between 2.1 and 6.9. The porosity of the sand and gravel strata in all boreholes varies between 12.2 and 58.3% (the highest value occurs in a layer that, based on the estimated clay%, just classifies as sand, but its porosity is more representative of clay), with median porosities between 26.4 and 35.4%. With the detailed estimates of clay, silt and porosity, the thermal properties were calculated.

The results show a not normally distributed wide range of thermal conductivities between 0.4 and 3.6 W.m^{-1}.K^{-1}, with median values between 2.3 and 2.9 W.m^{-1}.K^{-1}. The bulk aquifer volumetric heat capacity varies between 2.6 and 4.0 MJ.m^{-3}.K^{-1}, with median values between 2.8 and 2.9 MJ.m^{-3}.K^{-1}. These values match literature values. Vertical (in individual boreholes) and horizontal (between boreholes) distribution of these properties is highly variable. These parameters vary by 100% or more in apparent uniform strata. Average (literature) values should, therefore, be considered with caution. Despite complicating factors, such as the variable groundwater electrical conductivity and the clay fraction electrical conductivity, the use of geophysical logs to derive thermal properties is effective and provides insight into the heterogeneity of thermal properties in apparent uniform strata. It is recommended that these “standard” geophysical logs are collected in every deep borehole to be drilled, either for ATES systems or for other purposes, to allow wider analysis of the distribution of thermal properties. This analysis of the heterogeneity of thermal properties and application in numerical models leads to better model results, as is shown in Chapter 4.

Samenvatting

Grondwater is een waardevolle natuurlijke hulpbron die irrigatiewater en water voor industriële processen levert en ongeveer de helft van de wereldbevolking van drinkwater voorziet.

Grondwatertemperatuur (GWT) is belangrijk voor de fysische en chemische toestand van grondwater. Inzicht in GWT heeft veel praktische toepassingen. Warmte wordt gebruikt als tracer in onderzoek naar de laterale en verticale stroming van grondwater en hydraulische eigenschappen van de ondergrond. Temperatuur-diepte (TD) profielen zijn gebruikt in paleo-klimaat reconstructies. De temperatuur van de ondergrond en het grondwater is ook een belangrijke ontwerpparameter voor ondergrondse infrastructuur, zoals elektriciteitsnetwerken.

GWT wordt bepaald door quasi-evenwicht tussen de warmtestroom vanuit het binnenste van de aarde (geothermische warmtestroom) en de lange-termijn temperatuur aan het grondoppervlak (GST). De GST is onderhevig aan verschillende korte- en lange-termijnfluctuaties en veranderingen. Deze verstoringen planten zich naar beneden voort als thermische golven, terwijl ze met de diepte in amplitude afnemen. Dagelijkse fluctuaties domineren GWT op zeer geringe diepte (<0,5 m), terwijl seizoens-fluctuaties aan het oppervlak zich voortplanten tot een diepte van ongeveer 15 m.

Door de mens veroorzaakte klimaatverandering heeft geleid tot een waargenomen stijging van de luchttemperatuur bij het aardoppervlak (SAT) sinds ongeveer 1900. SAT in Nederland vertoont een versnelde stijging sinds het eind van de jaren 1970. Klimaatverandering resulteert in toenemende GSTen stijgende temperaturen van infiltrerend regen- en oppervlaktewater, wat resulteert in een hogere GWT. Andere factoren die GWT beïnvloeden zijn veranderingen in landgebruik (landbouw, verstedelijking) en het hydrologische systeem door het oppompen van grondwater of kunstmatige aanvulling van grondwater. Bovendien wordt de temperatuur van de ondergrond beïnvloed door antropogene warmtebronnen, zoals ondergrondse constructies en infrastructuur. Watervoerende lagen worden wereldwijd steeds meer gebruikt voor opslag en terugwinning van (seizoensgebonden) thermische energie, zoals ondergrondse thermische energieopslag (UTES) of aquifer thermische energieopslag (ATES). Deze kunnen lokaal grote temperatuuranomalieën veroorzaken.

Inzicht in de ondergrond- en grondwatertemperaturen, hun ruimtelijke verdeling en verandering in de tijd is belangrijk voor grondwaterbeheer en optimaal gebruik van de ondergrond, bijvoorbeeld voor UTES. Het doel van dit proefschrift is het verbeteren van het begrip van grondwatertemperaturen, hun tijdruimtelijke verdeling en drijvende krachten achter de ontwikkelingvan grondwatertemperaturen in Nederland. De belangrijkste drijvende krachten achter de verandering van de grondwatertemperatuur zijn klimaatverandering, veranderingen in landgebruik (met name verstedelijking) en ondergrondse opslag van thermische energie. Op basis hiervan zijn de volgende onderzoeksvragen geformuleerd:

1. Hoe zijn de grondwatertemperaturen in Nederland verdeeld en hoe worden de in kaart gebrachte patronen verklaard?
2. Wat zijn de regionale tijdsafhankelijke trends in grondwatertemperatuur? Hoe zijn deze trends gerelateerd aan veranderingen in landgebruik, klimaat en grondwaterbeheer of -exploitatie?
3. Wat is de invloed van verstedelijking op de temperatuur van de ondergrond en het grondwater?
4. Wat is de invloed van de opslag van thermische energie in watervoerende pakketten (ATES) op de lokale grondwatertemperaturen? Is deze invloed gerelateerd aan de hydraulische en thermische heterogeniteit van de ondergrond?

Hoofdstuk 2

Regionale patronen en trends in grondwatertemperatuur en de drijvende krachten achter verandering worden in dit hoofdstuk bestudeerd om antwoord te geven op onderzoeksvragen 1 en 2. Temperatuur-diepte (TD) profielen, veldmetingen van grondwatermonstertemperaturen en temperatuurgegevens van onttrokken water bij drinkwaterwinningen (PSWF's) worden gebruikt om grondwatertemperatuurpatronen en -trends in kaart te brengen, te onderscheiden en te verklaren.

Tussen 1976 en 1982 zijn honderden TD-profielen doorgemeten door eerdere onderzoekers.Tussen 2010 en 2018 zijn tientallen TD-profielen door de auteur doorgemeten. Enkele van dezelfde putten van de 1976-1982 meetcampagne zijn opnieuw doorgemeten, waardoor vergelijking tussen de verschillende tijdsperiodenmogelijk was. Veldtemperaturen van grondwatermonsters verzameld tussen 1908 en 2012 zijn afgeleid uit de nationale grondwaterinformatiedatabase. Deze zijn gefilterd op diepte (20-35 m beneden maaiveld) en tijdreeksen van ten minste 4 monsters per peilbuis. Onwaarschijnlijk lage (<5°C) en hoge (>17°C) temperaturen zijn verwijderd. Dit resulteerde in een set van 2893 temperatuurmetingen in 383 waarnemingsputten, verzameld tussen 1991 en 2011 op 20-35 m diepte (T20-35). Tijdreeksen van temperaturen van onttrokken grondwater door PSWF's zijn verkregen uit de KIDAP-database (Mendizabal & Stuyfzand, 2009) voor winningen in freatische en semi-gespannen watervoerende pakketten en oeverwaterwinningen (RBF).

De T20-35-waarden zijn gemiddeld voor elke peilbuis. De gemiddelde T20-35 waarden zijn in kaart gebracht en geïnterpoleerd. Dit resulteerde in regionale patronen van hogere en lagere GWT op 20-35 m diepte. De laagste GWT wordt gevonden in de topografisch hooggelegen gebieden en de hoogste GWT in het sterk verstedelijkte westen van het land.

Monitoringputten dieper dan 20 m met tijdreeksen van grondwatermonstertemperaturen zijn schaars instedelijke gebieden. De hoogste temperaturen die geassocieerd worden met stedelijke hitte-eilanden (UHI) en ondergrondse stedelijke hitte-eilanden (SUHI) zijn daarom niet gedetecteerd in de T20-35. De studie van het SUHI van Amsterdam (Hoofdstuk 3) toont aan dat afwijkend hoge temperaturen voorkomen op 20 m diepte in stadscentra. Ongewoon hoge T20-35 wordt gevonden in het zuidoosten van het land. Met een numeriek 1D-model is getest of ondiep of diep voorkomen van gesteente met verschillende thermische eigenschappen hierbij een rol speelt. Ondiep voorkomen van gesteente met een laag geleidingsvermogen (lage dichtheid) in het thermisch afwijkende gebied zou een kleine bijdrage aan de hogere T20-35 kunnen verklaren. Verticale stromingvan grondwater langs breukvlakken is een waarschijnlijke oorzaak van lokale thermische anomalieën, maar biedt geen bevredigende verklaring voor de hoge T20-35 waarden in grotere delen van het zuidoosten van het studiegebied.

Tijdsafhankelijke GWT-trends zijn bepaald voor elk van de 383 peilbuizen, met behulp van de Mann-Kendall test. Trends zijn ingedeeld in (waarschijnlijk) stijgende en dalende en stabiele trends. Voor 237 locaties is een statistisch significante trend vastgesteld. Verreweg de meeste locaties (77%) laten een (waarschijnlijk) stijgende GWT-trend zien. Een kleiner percentage (22%) van de locaties geeft een stabiele GWT aan, terwijl op 3 locaties een (waarschijnlijk) dalende trend is gevonden.

De topografische verdeling van GWT en trends laat een duidelijk regionaal patroon zien. Lage, maar stijgende temperaturen domineren in de topografisch hoger gelegen delen van het land. Stabiele, maar hogere GWT-temperaturen domineren in de lagergelegen gebieden. Dit wordt verklaard door de grondwateraanvulling in de hogere gebieden die de lage, maar stijgende GST naar grotere dieptes transporteert. In het laaggelegen westen van het land is de grondwateraanvulling minder dominant en in diepe polders treedt kwel op. Relatief hoge percentages bebouwd gebied in het westen veroorzaken een hoge GST, maar belemmeren de grondwateraanvulling. In deze gebieden plant de toenemende GST zich naar beneden voort alleen door geleiding, wat een langzamer proces is dan de combinatie van geleiding en advectie in de hoge delen van het land.

De relatie en ruimtelijke verdeling van GWT, GWT toename en GST-trends zijn verder onderzocht door toepassing van een bodem-atmosfeer stralingsbalans (SARB) model. Met dit model zijn uur-gegevens van 1965 tot 2020 van 5 meteorologische stations in verschillende delen van het land gebruikt om de GST te schatten. Een verhard (asfalt) oppervlak, een met gras bedekt oppervlak en een bosbodem zijn gesimuleerd. Deze berekeningen laten zien hoe de GST van vergelijkbare oppervlakken varieert tussen verschillende delen van het land en in welke mate de GST afwijkt van SAT (GST-SAT offset).

Historische veldgegevens van de GST-SAT offsets en drainagewatertemperaturen van lysimeters met verschillende vegetatietypen zijn verzameld. Inverse modellering van TD-profielen leverde GST-SAT offsets op voor verschillende soorten bodembedekking en verschillende perioden. Hoogfrequente (6-uurs) metingen van de temperatuur aan het grondoppervlak (tot 5 cm onder het grondoppervlak) op 4 meteorologische stations in Nederland leverden gedetailleerde temperatuurinformatie voor met gras bedekte oppervlakken vanaf 1981. Deze veldgegevens maakten een vergelijking met de door SARB afgeleide GSTs mogelijk. De waargenomen GST van het grasoppervlak van nabijgelegen stations laat zien dat het SARB-model een redelijke schatting geeft van de GST en GST-trend. De gemodelleerde bos GST-SAT offset is, vergelijkbaar met die van een volwassen dennenbos in de lysimeterstudie, kleiner dan nul. Dit laat zien dat de bosbodem gemiddeld koeler is dan SAT. Kale bodem (zand) lysimeter GST-SAT offsets zijn hoog, maar lager dan asfalt offsets, vanwege de hogere albedo van zand.

GST-SAT-offsets op basis van het SARB-model zijn toegepast op verschillende soorten bodembedekking op een grid van 1 km^2 voor heel Nederland. SAT-gegevens van de 5 gebruikte meteorologische stations zijn ook toegewezen aan het raster. Dit resulteerde in een geschatte GST-kaart en een GST-SAT-offsetkaart. Deze kaarten laten vergelijkbare patronen zien met de geïnterpoleerde T20-35, bestaande uit lage GST-waarden in het noordoosten en oosten van het land en hogere GST-waarden in de verstedelijkte gebieden in het westen. De omvang van het hoge T20-35 gebied in het westen is aanzienlijk groter dan in kaart gebracht door eerdere onderzoekers in de jaren 1970 en 1980. De waargenomen gemiddelde T20-35 waarden vertonen een statistisch significante relatie met de berekende GSTs. De afwijkend hoge T20-35 waarden in het zuidoosten, die niet afdoende verklaard konden worden door de geologische structuur, vallen samen met gebieden met een hoge gesimuleerde GST. Het zuidoosten van het land ontvangt de laagste jaarlijkse hoeveelheid neerslag, waardoor het effect van infiltrerende winterneerslag minimaal is.

Het opnemen van regenval en grondwateraanvulling in het SARB-model resulteerde in een minder nauwkeurige (te lage) GST schatting. Dit geeft aan dat neerslag en grondwateraanvulling niet direct van invloed zijn op de GST. Echter, omdat neerslag de oppervlaktetemperatuur naar beneden transporteert via grondwateraanvulling, speelt het een belangrijke rol in de GWT ontwikkeling. In Nederland valt 's zomers en 's winters evenveel neerslag. Tijdens het zomerseizoen is er geen netto-overschot van neerslag ten opzichte van evapotranspiratie. In de winter is de evapotranspiratie lager en de grondwateraanvulling hoger. Hierdoor worden de lagere wintertemperaturen van het grondoppervlak en de neerslag naar de ondergrond verspreid door infiltratie. In topografisch hooggelegen gebieden, waar lage T20-35 en GST heersen, is de jaarlijkse neerslag hoog. Dit versterkt deze "heat sink". De jaarlijkse neerslag is ook hoog in de stedelijke gebieden in het westen. Omdat in deze gebieden minder infiltratie plaatsvindt, is het "verkoelende" neerslageffect op GWT minder.

Studies naar het temperatuurveld van de ondergrond gaan vaak uit van een constante GST- SAT offset in tijd en ruimte (tenzij er een duidelijke verandering in landgebruik heeft plaatsgevonden). De SARB-modelresultaten laten zien dat deze offset niet alleen afhangt van de bodembedekking, maar ook van de meteorologische/klimatologische eigenschappen van de locatie. Deze eigenschappen verschillen zelfs op een kleine schaal als Nederland. De GST-SAT-offsets zijn variabel in de tijd. SAT en de globale (inkomende) straling bepalen grotendeels de GST. De afhankelijkheid van deze twee factoren maakt een GST-SAT relatie minder eenduidig. De gebruikte evapotranspiratie is gebaseerd op de Makkink-methode en is daarom ook gerelateerd aan SAT en de globale straling. Schattingen van de werkelijke evapotranspiratie in het SARB-model van gras en bos gaan uit van een perfecte vochtbeschikbaarheid voor de vegetatie. Dit is zelden het geval. De werkelijke evapotranspiratie wordt daarom overschat in het SARB-model, wat resulteert in een systematisch te lage berekende GST.

De temperaturen van de freatische PSWFs vertonen, ondanks de grotere diepte waarop zij grondwater onttrekken, over het algemeen een goede correlatie met de waargenomen en geïnterpoleerde T20-35 waarden. PSWFs die diepere (semi-)gespannen watervoerende lagen aanboren, vertonen relatief hoge watertemperaturen. De hoogste temperaturen komen voor bij de diepste putvelden in de Roerdalslenk (RVG). Hoewel de rivierwatertemperaturen hoger zijn dan de T20-35, vertonen oevergrondwaterwinningen in de drainerende delen van de grote rivieren temperaturen die gelijk zijn aan of soms zelfs lager dan T20-35. Blijkbaar is het meeste onttrokken water daar autochtoon grondwater dat naar de rivier stroomt. In de lager gelegen, infiltrerende delen van de grote rivieren is de oevergrondwater-temperatuur hoger dan de geïnterpoleerde T20-35 en lager dan de rivierwatertemperatuur, als gevolg van menging van infiltrerend rivierwater en autochtoon grondwater. Gedetailleerde temperatuurwaarnemingen van rivierwater, grondwater en onttrokken RBF kunnen onder ideale omstandigheden worden gebruikt als hulpmiddel om mengverhoudingen tussen autochtoon grondwater en rivierwater te bepalen.

Hoofdstuk 3

Hoofdstuk 3 beschrijft de ontwikkeling van het ondergrondse stedelijke hitte-eiland (SUHI) van de stad Amsterdam, als voorbeeld van een typische middelgrote stad op een gematigde breedtegraad. Onderzoeksvraag 3 wordt in dit hoofdstuk beantwoord. De stad Amsterdam is bijzonder geschikt om de ontwikkeling van haar SUHI te beschrijven, omdat de stad sinds de middeleeuwen is gegroeid in een goed gedocumenteerd en enigszins concentrisch patroon, met als resultaat dat het stadscentrum het oudste deel van de stad is en hoe verder van het centrum, hoe jonger de bouwfasen zijn.

Gegevens over de luchttemperatuur (SAT) zijn verzameld van het nabijgelegen weerstation Schiphol en van semiprofessionele amateurstations op verschillende locaties in de stad. Historische gegevens (1785-1961) van een meteorologisch station in het centrum van de stad zijn opgevraagd. Een reconstructie van de jaarlijkse temperatuurgegevens voor Nederland, die teruggaan tot de achtste eeuw, is gebruikt voor historische SAT-gegevens van voor 1785. GWT-gegevens op 20 m onder het maaiveld (T_{-20m}) zijn verzameld in 63 peilbuizen in en rond de stad. Er zijn maar weinig peilbuizen dieper dan 20 m beschikbaar. In 6 diepere (45-115 m) putten zijn TD-profielen gemeten. De TD-profielen vertonen een concave vorm, kenmerkend voor stijgende temperaturen aan het aardoppervlak. Voor één locatie laat vergelijking met een ouder TD-profiel zien dat de temperatuur in de periode 1979-2012 tot ongeveer 62 m diepte is gestegen.

Schiphol SAT volgt SAT in De Bilt, in centraal Nederland, zeer nauwkeurig. Schiphol-SAT vertoont daarom weinig invloed van het stedelijk hitte-eiland (UHI) van Amsterdam. De langjarig gemiddelde SAT in het centrum van de stad is 1,1°C hoger dan op Schiphol en De Bilt. Dit wordt bevestigd door de metingen van de amateurstations. Dit UHI-effect is vrij constant sinds het einde van de 18^{e} eeuw.

De gemeten minimum en maximum T_{-20m} zijn respectievelijk 10,8 en 15,1°C. Het gemiddelde is 12,5°C met een standaardafwijking van 1,1°C, wat resulteert in een 95%

betrouwbaarheidsinterval van ongeveer 10,3-14,7°C. T_{-20m} waarden onder 11,0°C worden dicht bij de stadsgrenzen gevonden. Deze temperaturen zijn slechts marginaal hoger dan het langjarig gemiddelde SAT voor Schiphol en worden daarom beschouwd als de (niet-stedelijke) achtergrondtemperatuur. T_{-20m} waarden tussen 11 en 13°C worden verspreid over alle bebouwde gebieden van de stad gevonden. Alle T_{-20m} >13°C zijn geconcentreerd in en nabij het stadscentrum, in de delen van de stad die voor 1900 CE zijn gebouwd, terwijl ook de hoogste T_{-20m} waarden geassocieerd zijn met de hogere bebouwingsdichtheden.

Een 2D numeriek model, parallel aan de regionale grondwaterstroming en zich uitstrekkend van het stadscentrum tot de stadsranden en tot 200 m onder het maaiveld, is gebruikt om de ontwikkeling van de temperatuurverdeling van 1350 tot 2012 te beschrijven. Om onderscheid te kunnen maken tussen de GST van verschillende soorten bestrating die door de eeuwen heen in de stad zijn gebruikt, is een apart SARB-model gebruikt. Het warmteverlies van gebouwen is in de loop der tijd veranderd door de introductie van ruimteverwarming en centrale verwarming. De bebouwingsdichtheid, typen bestrating en het warmteverlies van gebouwen zijn opgenomen in het 2D-model als een tijdsafhankelijke thermische bovenrandvoorwaarde.

De berekende temperatuurverdelingen weerspiegelen duidelijk de gefaseerde stadsuitbreiding door de verschuiving van het front van hogere temperaturen van het stadscentrum naar de stadsranden. Het effect van de grondwaterstroming is duidelijk zichtbaar in een lichte kanteling van de warmtefronten. De berekende TD-profielen laten, zoals verwacht, voor de oudere staduitbreidingsfasen een concave afwijking van de curven zien van het rechte diepere uiteinde van de curven op grotere diepte. De berekende TD-profielen passen in het gemeten bereik, wat de geschiktheid van de benadering ondersteunt; het wordt echter aanbevolen om de TD-profielen en T_{-20m} metingen in de toekomst te herhalen om het model te kunnen valideren. Validatie van het model zou het mogelijk maken het model te gebruiken om de toekomstige thermische toestand van de SUHI te voorspellen. Locatie specifieke ontwikkelingen en omstandigheden kunnen niet worden opgenomen in het 2D-model, dat vrij grote intervallen gebruikt om de stedelijke ontwikkeling te schematiseren. Hoewel er geen directe vergelijking mogelijk is, lijken de berekende TD-profielen systematisch iets hogere temperaturen te hebben dan de waargenomen TD-profielen. Een mogelijke overschatting van de GST kan hierbij een rol spelen. Eén gemeten TD-profiel vertoonde afwijkend hoge temperaturen in het diepere deel van de waargenomen curve. Dit moet veroorzaakt worden door laterale advectie van een diepgelegen warmtebron, mogelijk een metrostation, hoewel andere bronnen, zoals een ondergronds warmteopslagsysteem (UTES), niet uitgesloten kunnen worden.

De verdeling van de T_{-20m} waarden, als maat voor de intensiteit van het SUHI, wordt vrij goed verklaard door het model. Dit leidt tot de vaststelling dat de maximale T_{-20m} op regionale (model)schaal, die kan worden verklaard met de stedelijke uitbreidingsgeschiedenis en de bodembedekking, 13,5°C is. De TD-waarnemingen zijn echter alleen representatief voor een klein ondergronds volume rond de peilbuis. Deze schaalverschillen verklaren, tenminste gedeeltelijk, de afwijkingen tussen de maximale gemodelleerde en waargenomen T_{-20m} waarden. T_{-20m} waarnemingen tussen 13,5 en 14,0°C suggereren dat de lagere waarde een lichte onderschatting is van het werkelijke maximum. Waarden boven 14 °C kunnen worden gekoppeld aan lokale antropogene warmtebronnen en hebben geen grote omvang. De werkelijke maximale SUHI-intensiteit op 20 m diepte ligt daarom voor Amsterdam tussen 2,5 en 3,0°C.

Het onderzoek toont aan dat door modellering van eeuwenlange (van veertiende tot eenentwintigste eeuw) stedelijke ontwikkeling en klimaatverandering, samen met de geschiedenis van zowel de luchttemperaturen van het stedelijke warmte-eiland als de temperaturen aan het aardoppervlak, het mogelijk is om de ontwikkeling en huidige staat van het Amsterdamse SUHI te simuleren. De resultaten geven inzicht in de drijvende krachten achter de ontwikkeling van het SUHI op de lange termijn, waardoor het mogelijk wordt om onderscheid te maken tussen ondergrondse warmtebronnen uit recentere tijden die lokale drijvende krachten zijn (zoals geothermische energiesystemen, rioleringen, verwarmingskelders, metrostations of stadsverwarming) en grootschaliger drijvende krachten (voornamelijk warmteverlies door gebouwen en verhoogde oppervlaktetemperaturen door bestrating). Omdat deze bevindingen gevolgen hebben voor de beoordeling van het potentieel van de SUHIs voor warmte- en koudeopslag (WKO, ATES) en verticale bodemwarmtewisselaars, wordt voorgesteld om onderscheid te maken tussen (1) een regionale, langdurige SUHI die zich eeuwenlang heeft ontwikkeld als gevolg van grootschaliger oorzaken, en (2) lokale anomalieën veroorzaakt door antropogene warmtebronnen die minder dan een eeuw oud zijn.

Hoofdstuk 4

In hoofdstuk 4 worden de resultaten gepresenteerd van een uitgebreid onderzoek naar de thermische impact van een WKO-systeem (ATES) in Bilthoven, Nederland. Het onderzoek omvatte monitoring van de thermische impact en modellering van het driedimensionale temperatuurverloop van het opslagpakket en de boven- en onderliggende eenheden. Er is speciale aandacht besteed aan de niet-uniformiteit van de achtergrondtemperatuur, die lateraal en verticaal varieert in de watervoerende laag, en aan de mate van detail met betrekking tot de initiële omstandigheden en de heterogeniteit van de hydraulische en thermische eigenschappen. Dit hoofdstuk geeft antwoord op onderzoeksvraag 4.

Het aantal ATES-systemen in Nederland is sinds introductie in 1987 exponentieel gegroeid. Een goed begrip van de thermische impact van ATES-systemen op de gebruikte aquifers is een fundamenteel element voor risicobeoordeling (het product van de waarschijnlijkheid en de impact). Deze studie richt zich op deze thermische effecten. De thermische impact is een verandering in de temperatuur van de watervoerende laag of het grondwater. De ruimtelijke omvang van deze impact wordt door sommige auteurs thermisch beïnvloede zone (TAZ) of temperatuur beïnvloed gebied (TAA) genoemd. Een nauwkeurige en unieke definitie van deze zone lijkt momenteel echter niet te bestaan. In veel beoordelingen voor ATES-systemen, die zelden in de reguliere literatuur worden gepubliceerd, wordt de thermische impact gedefinieerd als de temperatuurveranderingen groter dan een arbitraire drempelwaarde (bijv. 0,5°C) boven en onder de natuurlijke achtergrondtemperatuur. De impact wordt meestal geëvalueerd door middel van voorspellende modellering vóór ingebruikname van het systeem, waarbij de achtergrondtemperatuur meestal constant wordt verondersteld in het gehele watervoerende pakket en de thermische impact wordt geëvalueerd als uniform over de dikte van het opslagpakket. Het feit dat een hoog percentage van ATES-systemen, eenmaal operationeel, niet presteert zoals verwacht in termen van thermische efficiëntie en thermische balans, wijst er sterk op dat de modellen die vóór ingebruikname zijn ontwikkeld voor vergunningsdoeleinden, nogal slechte hulpmiddelen zijn voor het voorspellen van de werkelijke thermische effecten. Er zijn maar weinig studies beschikbaar waarin de werkelijke temperatuurontwikkeling en de invloed van de eigenschappen van de ondergrond zijn geëvalueerd voor een relatief lange periode na ingebruikname van het systeem.

Deze studie draagt bij aan de momenteel beperkte reeks op observatie gebaseerde casestudies van de temperatuurontwikkeling in opslagpakketten, door gedetailleerd onderzoek naar de thermische impact van een ATES-systeem bij het RIVM in Bilthoven, Nederland. Het onderzoek omvatte het monitoren van de thermische impact in peilbuizen en het modelleren van de driedimensionale (3D) temperatuurontwikkeling van het opslagpakket en de bovenliggende en onderliggende eenheden. In tegenstelling tot andere studies ligt de nadruk hier op de thermische impact van het ATES-systeem (omvang van de thermisch beïnvloede zone, bereikte maximum- en minimumtemperaturen en variabiliteit in de tijd) in plaats van op de efficiëntie van het ATES-systeem. Doel van deze studie is om het belang te evalueren van twee factoren die de impact beïnvloeden: (1) complexiteit die samenhangt met de niet-uniformiteit van de "natuurlijke" achtergrondtemperatuur (zowel horizontaal als verticaal), en (2) heterogeniteit van het opslagpakket. De invloed onder werkelijke bedrijfsomstandigheden wordt ook vergeleken met de voorspelde invloed voor de ontwerpbedrijfsomstandigheden.

Het ATES-systeem bij het RIVM bestaat uit vier bronnen: twee bronnen die worden gebruikt voor het injecteren en onttrekken van koud water ("koude" bronnen) en twee bronnen die worden gebruikt voor het injecteren en onttrekken van warm water ("warme" bronnen). De bronnen zijn geplaatst langs een 230 m lange lijn. De bronfilters zijn geplaatst tussen 47 en 106 m onder het maaiveld (m -mv). Het ATES-systeem is sinds januari 2008 in gebruik. Voor de periode 2008-2011 is gedetailleerde informatie verzameld over de hoeveelheden water die per bron zijn opgepompt en de temperaturen van het onttrokken en geïnjecteerde water. Het ATES-systeem is gemonitord met bestaande peilbuizen in de buurt en peilbuizen die in de boorgaten van de ATES-bronnen zijn geplaatst. Er zijn Twee extra peilbuizen geplaatst als "schildwachtputten", ongeveer op de grens van de zone die beïnvloed zou kunnen worden door het geïnjecteerde water.

Het achtergrondtemperatuurveld is bestudeerd met behulp van TD-logs voor de peilbuizen op enige afstand van het ATES-systeem. Het achtergrondtemperatuurveld is complex en niet uniform (zowel horizontaal als verticaal). Dit temperatuurveld vormt (a) de referentiesituatie voor de beoordeling van de thermische impact en (b) de begin- en randvoorwaarden voor de thermische modellering. Het achtergrondtemperatuurveld van de ATES-locatie is bepaald met behulp van peilbuizen waar herhaalde TD-metingen, verzameld in het kader van deze studie (2010-2012), stabiele temperatuurcondities lieten zien op dieptes die overeenkomen met het opslagpakket.

Informatie over de werkelijke thermische impact van het systeem is verkregen door gedurende meerdere jaren regelmatig TD-metingen uit te voeren in de peilbuizen van de ATES-bronnen en nabijgelegen peilbuizen. Tussen 2010 en 2012 zijn in totaal 120 TD profielen verkregen met een meetinterval van 1 m.

De thermische impact is gemodelleerd aan de hand van de TD-gegevens, operationele gegevens van ATES systeem en een uitgebreide reeks hydrogeologische gegevens. Er zijn twee locatie-specifieke modellen ontwikkeld met verschillende detailniveaus wat betreft de weergave van het achtergrondtemperatuurveld en de hydraulische en thermische eigenschappen (heterogeniteit). Een grootschaliger regionaal grondwaterstromingsmodel is gebruikt om de juiste randvoorwaarden en initiële hydraulische parameters voor de locatie-specifieke modellen te bepalen. Berekeningen van grondwaterstroming, transport van opgeloste stoffen en warmtetransport zijn uitgevoerd met de modelcode SEAWAT (versie 4). Dit is een gekoppelde versie van MODFLOW en MT3DMS, ontworpen om verzadigde grondwaterstroming met variabele dichtheid en viscositeit in 3D te simuleren. Temperatuur afhankelijkheid van de vloeistofdichtheid en viscositeit is meegenomen in de berekeningen. Fijnschalige heterogeniteit van de thermische eigenschappen is afgeleid uit geofysische boorgatmetingen. De methode voor deze afleiding wordt uitgewerkt in hoofdstuk 5.

De resultaten laten zien dat een fijnschalig heterogeniteitsmodel de laterale en verticale temperatuurverdeling realistischer weergeeft dan een vereenvoudigd model dat het watervoerende systeem modelleerde met slechts een beperkt aantal homogene lagen. Het bleek dat heterogeniteit op kleine schaal belangrijk was voor het nauwkeurig modelleren van de door ATES beïnvloede verticale temperatuurverdeling en de maximum- en minimumtemperaturen in het opslagpakket en de ruimtelijke omvang van de thermische pluimen. Het fijnschalige heterogeniteitsmodel resulteerde in grotere thermisch beïnvloede gebieden en grotere temperatuuranomalieën dan het vereenvoudigde model. De modellen laten zien dat verspreide en schaarse monitoringgegevens van door ATES veroorzaakte temperaturen op een bruikbare manier kunnen worden geïnterpreteerd door grondwater- en warmtetransportmodellering, wat resulteert in een realistische beoordeling van de thermische impact.

Hoofdstuk 5

Heterogeniteit van de thermische eigenschappen van de geologische lagen speelt een belangrijke rol in de ontwikkeling van het ondergrondse temperatuurveld. Dit is niet alleen het geval voor ATES-systemen, maar ook onder meer natuurlijke omstandigheden.

In-situ meettechnieken voor het bepalen van verticale heterogeniteit van thermische eigenschappen van watervoerende lagen en waterremmende lagen ontbreken. Thermische responstests met gesloten bodemwarmtewisselaars leveren een "bulk" thermische geleidbaarheid en capaciteit op. In het verleden zijn duizenden, algemeen beschikbare, geofysische boorgatmetingen verricht, voornamelijk gammastraling, ‘long-normal’ (LN) elektrische weerstand en ‘self-potential’ (SP)-logs. Om deze redenen wordt in dit hoofdstuk onderzocht of "standaard" geofysische boorgatmetingen nuttig kunnen worden toegepast om thermische eigenschappen te bepalen.

Thermische eigenschappen zijn geschat via empirische relaties tussen fysische eigenschappen van de ondergrond en de thermische geleidbaarheid, capaciteit en retardatie. Geofysische boorgatmetingen zijn gebruikt om de fysische eigenschappen van de watervoerende lagen en het grondwater af te leiden.

Vijf boorgaten met een maximale diepte van 145 m onder het maaiveld zijn geanalyseerd. De gegevens zijn aangevuld met lithologische en geofysische boorgatmetingen en korrelgrootte-gegevens die zijn verkregen op nabije locaties en in dezelfde geologische formaties. De geofysische boorgatmetingen zijn in de jaren 1970 en 1980 verricht met intervallen van 0,02 m langs het boorgat.

Eerst is de verticale verdeling van het lutumpercentage geanalyseerd met behulp van natuurlijke gammastraling metingen. Gegevens over de korrelgrootte zijn gebruikt om de slibfractie vast te stellen. Dit laatste is van belang voor één van de empirische methoden die wordt gebruikt om de thermische geleidbaarheid te schatten.

Vervolgens is de porositeit geschat. Porositeitsmetingen, bijvoorbeeld neutronen-neutronenlogs of neutronen-gamma-logs, waren niet beschikbaar. In dit geval is gebruik gemaakt van de elektrische weerstandsmetingen (LN100 en LN200) om de porositeit af te leiden. De porositeit is geschat met behulp van Archie's formatieweerstandsfactor en de 'Humble-vergelijking' die een correlatie geeft tussen formatieweerstand, poriewaterweerstand en porositeit. Uit talrijke monsters van de locatie en de omgeving bleek dat de elektrische weerstand van het poriewater diepte- en tijdafhankelijk was. Er is een diepte-weerstandscorrelatie afgeleid die representatief was voor de periode waarin de boorgatmetingen zijn uitgevoerd. Een andere complicerende factor is de elektrische geleidbaarheid van de kleifractie. Bij de aanwezigheid van een significante hoeveelheid klei verliest de Archie-methode aan nauwkeurigheid. De elektrische geleidbaarheid van de bodemlagen is gecorrigeerd voor het kleigehalte. De gebruikte methode gaat uit van de aanwezigheid van een elektrische dubbele laag (EDL) en elektrische oppervlaktegeleiding op het klei-water grensvlak zoals in de Stern theorie. Bij het lage zoutgehalte van het poriewater van de locatie gedraagt de kleigeleiding zich niet- lineair met de poriewatergeleiding. Hierdoor moest de elektrische geleiding van de kleifractie iteratief worden geschat, wat resulteerde in een lagere kleigeleidingsfactor dan gebaseerd op de kationen-uitwisselingscapaciteit van de kleimineralen.

Berekende kleipercentages variëren tussen 0 en 43,2% (gewicht) met mediane kleipercentages over de gehele boorgatlengte tussen 2,1 en 6,9%. De porositeit van de zand- en grindlagen in alle boorgaten varieert tussen 12,2 en 58,3% (de laag met de hoogste waarde heeft een berekend lutumpercentage dat het net als zand classificeert, maar de porositeit is meer representatief voor klei), met een mediaan van de porositeit tussen 26,4 en 35,4%. Met de gedetailleerde schattingen van klei, slib en porositeit zijn de thermische eigenschappen berekend.

De resultaten laten een niet-normale verdeling zien van een brede variatie aan warmtegeleidingsvermogens tussen 0,4 en 3,6 W.m^{-1}.K^{-1}, met mediaanwaarden tussen 2,3 en 2,9 W.m^{-1}.K^{-1}. De bulk volumetrische warmtecapaciteit varieert tussen 2,6 en 4,0 MJ.m^{-3}.K^{-1}, met mediaanwaarden tussen 2,8 en 2,9 MJ.m^{-3}.K^{-1}. Deze waarden komen overeen met literatuurwaarden. De verticale (in individuele boorgaten) en horizontale (tussen boorgaten) verdeling van deze eigenschappen is zeer variabel. Deze parameters variëren met 100% of meer in ogenschijnlijk uniforme lagen. Gemiddelde (literatuur)waarden moeten daarom met voorzichtigheid worden gehanteerd. Ondanks complicerende factoren, zoals de variabele elektrische geleidbaarheid van het grondwater en de elektrische geleidbaarheid van de kleifractie, is het gebruik van geofysische logs om thermische eigenschappen af te leiden effectief en geeft het inzicht in de heterogeniteit van thermische eigenschappen in ogenschijnlijk uniforme lagen. Het wordt aanbevolen om deze "standaard" geofysische boorgatmetingen uit te voeren in alle toekomstige diepe boorgaten, hetzij voor ATES-systemen of voor andere doeleinden, om een bredere analyse van de verdeling van thermische eigenschappen mogelijk te maken. Dat een dergelijke analyse van de heterogeniteit en gebruik hiervan in numerieke modellen leidt tot beter modelresultaten is aangetoond in Hoofdstuk 4.

Chapter 1

Introduction

Groundwater is an important source of domestic water, irrigation water, and water for industrial processes. It supplies half of the world's population with drinking water (UNESCO, 2022). In the 27 member states of the European Union, the average share of groundwater in drinking water supply is 65% (European Environment Agency, 2022). In the Netherlands in 2019, groundwater abstraction supplied 62% (810 Mm^3) of all drinking water (VEWIN, 2022). The remaining 38% was drawn from fresh river and lake water. Apart from the use of groundwater for drinking water, agricultural and industrial purposes, the subsurface and aquifers are worldwide increasingly being used for storage and recovery of (seasonal) thermal energy.

Groundwater temperature (GWT) is important for the physical and chemical state of groundwater (Stumm & Morgan, 1981; Brons et al.,1991; Bonte et al., 2011, 2011a; Jesußek et al., 2013; Jyväsjärvi et al., 2015; Miller et al., 2019; Riedel, 2019). For instance, GWT impacts density (Kell, 1975; Jones & Harris, 1992), viscosity (Huber et al., 2009), heat capacity (Mallamace et al., 2020), thermal expansion coefficient (Irvine & Duignan, 1985), diffusion rate (Longsworth, 1954; Gillen et al., 1972; Mehrer, 2007) and evaporation of water (Jakubczyk at al., 2007), and on the solubility of gases and solids, reaction kinetics, volatilization of pollutants, ionization of water and dissolved compounds (Stumm & Morgan, 1981; Appelo & Postma, 2005). Increasing GWT may introduce groundwater quality changes e.g. by enhancing redox reactions in which bacteria often play a crucial role (Prommer & Stuyfzand, 2005; Bates et al., 2008; Dao, et al., 2024).

Groundwater flowrate is related to its dynamic viscosity (Darcy's Law). At 5ºC, water has a dynamic viscosity of approx. $1.5E^{-3}$ $kg.m^{-1}.s^{-1}$, and approx. $1.0E^{-3}$ $kg.m^{-1}.s^{-1}$ at 20ºC. As a result, at constant intrinsic permeability and hydraulic head, the flow rate of the warmer water is 50% higher. Temperature-dependent diagenetic processes such as dissolution, recrystallization, cementation, affect the aquifer permeability (Machel, 1999) and groundwater flow rate.

GWT temperature affects groundwater density and may result in density-driven flow. Hydrothermal convection of groundwater occurs where the geothermal heat flow is high near heat sources, such as magmatic intrusions. Obvious examples being geysers in volcanic regions. These do not occur in the Netherlands. Nevertheless, hydrothermal convection may affect the thermal state of the Roer Valley Graben (for location, see Section 1.4) at depths of 1000-1500m (e.g. Luijendijk et al., 2010). Convection possibly affects the subsurface temperature also at greater depths (>4000 m) (Struijk et al., 2019). Deep (>1000 m) free convection is unlikely to influence GWT at depths <500m, as convection cells are easily split-up even by thin clay layers (Luijendijk et al., 2010). Density driven groundwater flow, as a result of GWT differences, is not likely to occur at natural GWT in shallow

(<500 m deep) aquifers, although it may occur in monitoring wells as will be explained in section 1.3. Ambient natural GWT differences are too small to induce free convection. Forced convection in aquifer thermal energy storage (ATES) systems, due to injection of warm and cold water, may occur (Buscheck et al., 1983). Buoyancy in high temperature (>60ºC) ATES systems is known to potentially limit recovery rates (Marif, 2019; Sheldon et al., 2021).

Isobaric specific heat of water is lower at higher temperatures. In combination with a lower density at higher temperature, the volumetric heat capacity of water decreases almost 1% when GWT increases from 5 to 20ºC. Specific heat capacity of sand drops sharply at temperatures to approx. 30ºC (Shafigh et al., 2020). Therefore, at higher temperatures, less thermal energy is required for GWT increase. Thermal conductivity of liquid water increases with temperature. Temperature dependency of the thermal conductivity of aquifer and aquiclude material at naturally occurring temperatures is less well researched. Kersten (1949) found that thermal conductivities for various soils at 21ºC was, on the average, about 4% greater than at 4ºC. Tarnawski et al. (2000) developed a temperature dependent Kersten relation for soil thermal conductivity, which holds for temperatures between 30 and 90ºC. It shows conductivity increase with temperature in this range. As a result of temperature dependent heat capacity and thermal conductivity, thermal diffusivity, as a measure of how quickly an imposed change in temperature is transmitted through the aquifer by conduction, rises with increasing temperature.

The major aquifers of the Netherlands consist of sand and gravel, mainly made up of quartz and feldspar, with a minor percentage of calcium carbonate and heavy minerals (Griffioen et al., 2016; De Mulder et al., 2003) or a low to moderate mica content (TNO, 2012). Aquitards in the Netherlands are composed of clay, loam, silt and peat. Both in Pleistocene sediments of the Rhine basin and marine clays in the Netherlands illite dominates, followed by vermiculite and smectite (Griffioen et al., 2016; Van der Veer, 2006). Quartz and feldspar dissolution is temperature dependent at ambient aquifer temperatures (Crundwell, 2017; Rimstidt, 1997; Williams et al., 2010; Welch & Ullman, 2000). Ions are mobilized by temperature dependent processes such as pyrite oxidation (Prommer & Stuyfzand, 2005), surface complexation and cation-exchange (Bonte et al., 2014), (Hartog et al., 2013). Degradation of organic matter, both dissolved and not dissolved (as soil organic carbon) is temperature dependent (Brons et al., 1991).

Bacterial growth is stimulated by higher temperatures, till an optimum is reached, after which growth rates decline. Ambient groundwater temperatures (below 20ºC) are optimum for growth of psychrophile and psychrotroph bacteria (Morita & Moyer, 2001). The inactivation of public health-related, pathogenic microorganisms in groundwater increases with higher temperatures (John & Rose, 2005; Pinon & Vialette, 2018; Olive et al., 2020). Higher temperatures can increase the mobility of non-aqueous phase contaminants, enhancing spreading of these substances. On the other hand, higher temperatures may enhance natural attenuation of contaminants (Zuurbier et al., 2013; Randhawa et al., 2016).

Another ecology related aspect of GWT was described by Kaandorp et al. (2019). Groundwater seepage to ecologically valuable lowland streams buffers the temperature effect of climate warming, potentially making groundwater dominated streams more climate robust.

1.1 Groundwater temperature

The main factor determining GWT consists of quasi-equilibrium between heat flow from the Earth's interior (geothermal heat flow) and the long-term surface temperature (Bense & Beltrami, 2007). Geothermal heat originates from the cooling of the Earth's core and radiogenic heat production in the Earth's lithosphere (Yukutake, 2000). Heat flow in the Netherlands, derived from deep bottom hole temperatures, varies between 51.4-128.2 mW.m^{-2} (Fuchs et al., 2023). Bonté et al. (2012) modeled heat flow at the base of the sediments to range between 42 and 80 mW.m^{-2}. Anomalies in heat flow in the Netherlands may be caused by radiogenic heat production of magmatic intrusions, or by the high thermal conductivity of the Zechstein Group evaporites (Bonté et al., 2012). For example, it was suggested that magmatic intrusion could explain anomalous high temperatures in borehole LTG-01 at depths >4000 m (Bonté et al., 2012), although other authors suggest the influence of deep hydrothermal convection as explanation (Struijk et al., 2019). Kooi (2016), on the other hand, demonstrated that groundwater-driven convective cooling exceeds groundwater-driven warming of the Earth's crust. Net temperature reductions of groundwater basins are caused by groundwater flow systems. This cooling extends into the underlying crust and lithosphere.

The Zechstein Group consists mainly of thick successions of evaporites (De Mulder et al., 2003). In the north and east of the Netherlands, diapirs and salt domes have formed as a result of salt flow up to depths <400 m. Anomalous high temperatures are known to exist around a salt diapirs (Bonté et al, 2012). Bonté et al. (2012), Zhang& Alves (2024) and Van den Berg (2023) attributed these anomalies to high thermal conductivity of rock salt ("chimney effect"). Thick anhydrite deposits are present in the Zechstein Group. Local heat production due to exothermic dissolution of anhydrite (Corti & Fernandez-Prini, 1982), could be hypothesized.

Ground surface temperature (GST) is subject to various short- and long-term fluctuations and changes. Carslaw & Jaeger (1959) showed that such disturbances propagate downward as thermal waves, while being attenuated with depth. Attenuation during propagation is frequency dependent, resulting in longer period waves attenuating less with depth than shorter period waves (Pollack & Huang, 2000). At very shallow depths (<0.5 m), diurnal temperature fluctuations of the surface dominate the GWT. GWT is affected by seasonal fluctuations at the surface to a depth of approx. 15 m (Bense & Kooi, 2004). Diurnal and annual fluctuations of temperature, calculated for an aquifer with a thermal diffusivity of 8.4E^{-7} m^2.s^{-1} and an equation for the sinusoidal temperature variation of the soil at various depths in time (Hillel, 1982), are illustrated in Figure 1.1. Diurnal fluctuations of temperature >0.1^{o}C are calculated to reach depths <0.8 m. Annual fluctuations of this magnitude are calculated to reach depths <17 m. Thermal waves with period lengths of decades and centuries may propagate tens to hundreds of meters depth (Pollack & Huang, 2000). Apart from GST disturbances, vertical groundwater flow can disturb the temperature-depth profile to great depths (Taniguchi et al., 1999).

Climate change is one of several drivers that affect groundwater temperature. Increasing surface air temperature (SAT) leads to rising ground surface temperature (GST) (Harris & Chapman, 1998; Kooi, 2008; Bense et al., 2017) and a rising temperature of recharging rain or surface water, resulting in higher GWT (Stuyfzand et al., 2007). Other drivers include changes in land use (agriculture, urbanization) and the hydrological system by pumping or managed aquifer recharge, and temperature changes of infiltrating surface waters by e.g. the discharge of (treated) sewage effluent or cooling water (Earman & Dettinger, 2011; Dao et al., 2024). Furthermore, the subsurface temperature is affected by anthropogenic heat sources, such as underground constructions, infrastructure (Epting et al., 2020), shallow geothermal energy exploitation, so called underground thermal energy storage (UTES), or aquifer thermal energy storage (ATES) (Visser et al., 2015), district heating networks, sewers, etc. These may cause local, large temperature anomalies.

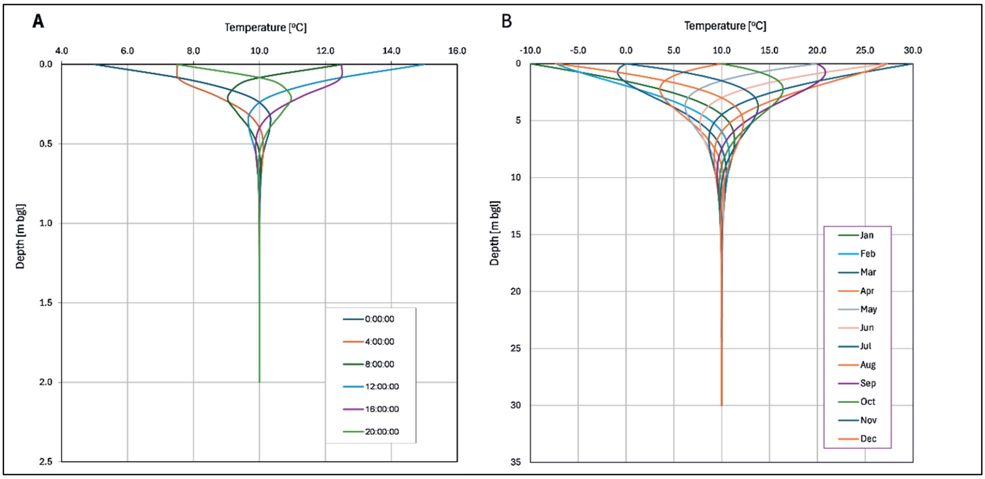

Figure 1.1: Calculated diurnal (A) and annual (B) fluctuations of the temperature with depth.

1.2 Applications

GWT is utilized to gain insight in hydrogeological processes and parameters, using heat as a tracer or studying the temperature-depth distribution. Some paleo-climate reconstruction is based on GWT observations and GWT plays a role in engineering applications.

1.2.1 Groundwater temperature as a tracer

In the Netherlands, pre-treated fresh river water is being infiltrated in coastal dunes to supplement the freshwater lenses from which groundwater for drinking water production is drawn. Temperature-depth (TD) profiling has been used to track the spreading of infiltrating water. For example, Stuurman (1984), Stuyfzand (1988), Des Tombe et al. (2018, 2019). Temperature also forms an important parameter in measurements of flow resistance e.g. in the monitoring of clogging of recharge basins or injection wells (Olsthoorn 1982).

TD profiling beneath streams has been used to quantify surface water - groundwater interactions (Anderson, 2005). Heat as a tracer for estimating lateral groundwater inflow to rivers could be an alternative to chemical tracers (Chen et al., 2023).

Geothermal patterns have been used by Bense (2004) and Bense & Kooi (2004) as mapping tool for shallow groundwater flow around a major fault zone in the Netherlands. The origins of saline water ingress at the Noordbergum public water supply well fields were studied using TD profiling and temperature measurements of produced water (Greinaert & Sprong, 1983).

1.2.2 Quantifying groundwater recharge and flux rates

Groundwater flow disturbs subsurface temperature distribution by advection. A steady-state solution to estimate vertical groundwater fluxes from GWT perturbations was provided by Bredehoeft & Papadopulos (1965). An overview and evaluation of alternative approaches is given by Bense et al. (2017) and Kurylyk et al. (2019). Since the 1960’s, these methods have been widely applied to quantify groundwater recharge and vertical flux rates. For example, Kurylyk et al. (2017) and Bense et al. (2020) used TD profiles to reveal temporal variability in deep groundwater flow conditions.

1.2.3 Paleo-climate reconstruction

In the 1920’s and 1930’s, it was already recognized that past climate changes perturb the subsurface temperature field. Since then, attempts have been made to infer past climates from TD profiles. E.g. Ingersoll (1932) concluded (albeit not correctly), from temperature measurements in drill holes in deep copper mines of northern Michigan, that possibly more than 30,000 years have passed since the last glacial epoch. Climate history reconstruction by formal inversion of TD profiles in deep boreholes in Canada was done by Cermak (1971) and Shen & Beck (1992). Pollack & Smerdon (2004) employed a large global set of TD profile derived GST changes to estimate a GST increase of 1^{o}C during the interval 1500– 2000.

Temperature-dependent deviation in ratios of stable isotopes of water recharging into aquifers (amongst others, δ18O, δ2H) is also applied in paleo-climate reconstruction. Environmental isotopes solubility in groundwater is a useful method to reconstruct the recharge temperature. Together with groundwater dating it is a very powerful tool for paleo-climatic reconstruction (Túri et al., 2020).

1.2.4 (Underground) infrastructure

One of the first researchers into the thermal properties of soils (Kersten) did his much-quoted research in 1945-1948 as a part of a program of research on problems of (road) construction in regions of permafrost. It was recognized that observations in the field and the correct solution of design problems of structures depend upon a knowledge of the thermal properties of the soils (Kersten, 1949).

The energy transition involves shifting from fossil-based systems of energy production to renewable energy sources like wind and solar. This requires extension and intensification of high- and mid-voltage electricity transmission line networks. Where possible, high-voltage lines are placed in the subsurface in the Netherlands, e.g., by horizontal directional drilling, down to depths of tens of meters. Underground transmission lines produce heat but have a maximum allowable temperature. Engineering underground cable traverses requires insight in the thermal properties of the subsurface and subsurface temperatures. This has resulted in the collection of large amounts of field and laboratory data of subsurface thermal properties, the majority of which remains unpublished. However, various modeling approaches of the temperature development around these traverses have been published by, e.g. Kroener et al. (2014); Quan et al. (2019), Ocłon et al. (2020).

The energy transition in the Netherlands also involves the construction of underground piped networks for the transport of industrial excess heat to district heating networks. E.g. the transport pipeline conveying temperatures up to 100°C from the Rotterdam harbor to the cities of Vlaardingen and The Hague, the effects of which on soil temperature and moisture has been investigated by Deltares (2021).

1.2.5 Groundwater as industrial cooling water

In industrial processes, groundwater is used as a cooling agent. Efficiency of this type of groundwater use depends on GWT. After usage, the groundwater is reinjected into the aquifer, or discharged into surface waters or sewers. Reinjection affects the aquifer temperature.

1.3 GWT measurement techniques

GWT is usually measured by lowering a temperature sensor in a monitoring well. Stonestrom & Blasch (2003) reviewed a variety of sensors available for logging GWT, including thermistor, thermocouple, resistance type, and integrated circuit devices. Open borehole logging (OBL) or logging in piezometers installed in the borehole assumes that the temperature of the water column represents the temperature of the surrounding aquifer. This assumption is only true when equilibrium exists, and the water column is stable.

In section 1.1, it is shown that at depths below the seasonal zone (>20 m), temperature fluctuations are small (frequency > half a year). The maximum variation of average annual air temperatures in the Netherlands is approx. 2°C. Assuming a similar fluctuation with a 1-year frequency also occurs in aquifers below the seasonal zone (very conservative, as this would mean no damping with depth), it can be demonstrated by a simple 2D model that the water column temperature in an open borehole or piezometer (PVC or HDPE), follows these small changes in aquifer temperature closely. Model results indicate a maximum temperature difference between the center of a water-filled 0.05 m diameter piezometer and surrounding aquifer of <<0.01°C.

Temperature gradients in the water column may introduce convective flow inside the borehole or monitoring well. Sammel (1968) showed that for a 2” diameter well and pure water at 10°C, the critical gradient for the onset of convection is approx. $0.1^{\circ}C.m^{-1}$. At 15°C, the critical gradient is approx. $0.08^{\circ}C.m^{-1}$. More recent studies, e.g. Berthold & Resagk (2012) confirmed a critical gradient of $0.1^{\circ}C.m^{-1}$ for a 5 cm diameter water column in laboratory experiments. Most monitoring wells in the Netherlands have a diameter of 1.8-5 cm, reducing the risk of free convection inside the well. Furthermore, gradients of $0.1^{\circ}C.m^{-1}$ or more generally occur only in the upper 10-15 m of the subsurface, the zone where diurnal and seasonal fluctuations of subsurface temperature and GWT prevail. Bonte et al. (2017) showed that convection is responsible for oxygen intrusion in monitoring wells down to a depth of around 12 m. An example of a high frequency temperature measurements by the author at various depths in a 51 mm diameter monitoring well is shown in Figure 1.2.

The measurements were performed between 14:00 and 15:00 on December 28, 2011. The GWT fluctuates due to free convection at 1.35 and 3.35 m below the water table. At 5.35 m below the water level, the temperature fluctuation reduced to 0.02°C during the 18 minute interval. During the experiment, the air temperature rose from 5.8 to 6.2°C. The drop in shallow water temperature at 1.35 m below water table can, therefore, be only explained by free convection.

Some studies, e.g. Koubikana Pambou et al. (2019) and Smith et al. (2023), used a wired temperature and pressure datalogger to monitor GWT in thermal response tests. Numerous monitoring wells in the Netherlands have been equipped with pressure loggers, many of which also register GWT. However, most of these loggers are placed at a relatively shallow depth (<20 m) and are susceptible to diurnal and seasonal fluctuations of the subsurface temperature.

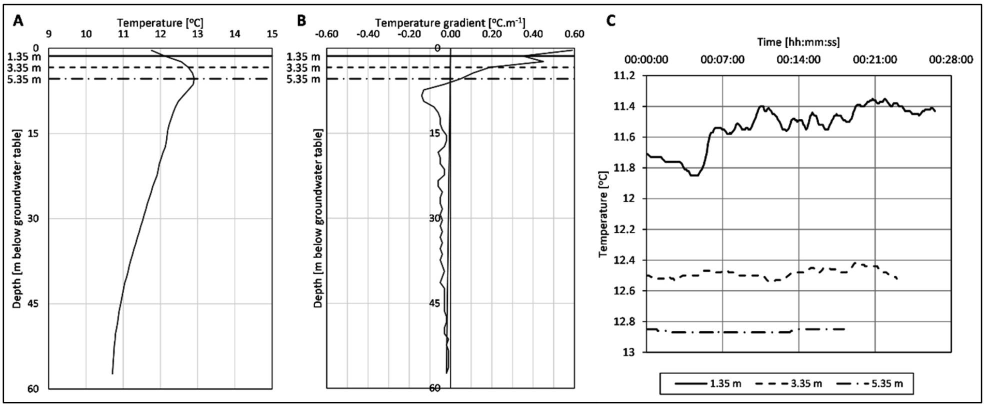

Figure 1.2: Temperature-depth profile (A), temperature gradient (B) and temperature vs. time at 1.35, 3.35, 5.35 m below water level (C) in monitoring well B51G0695, December 28, 2011. NOTE: the temperature scale in (C) is in reverse order.

Distributed temperature sensing (DTS) is a relatively new method to measure subsurface temperature and GWT. An optical fiber is placed in a borehole or monitoring well. Raman back-scatter characteristics of a laser pulse introduced into the optical fiber are used to infer the distribution of temperature along the fiber (Bense et al., 2016). This technique allows high frequency and high accuracy temperature logging. As DTS optical fibers need to be installed more or less permanently in a borehole or well, this technique is less suitable for incidental GWT logging at multiple sites and wells. Examples of DTS logging include monitoring artificial dune water infiltration (Des Tombe et al., 2019), where the optical fibers have been placed into the subsurface by a direct push technique (Van der Made et al., 2014), or monitoring of an ATES system by Sommer (2015).

Temperature influences the electrical resistivity of the subsurface. This feature is utilized in mapping the subsurface temperature distribution through electrical resistivity tomography (ERT). Hermans et al. (2015) used cross-hole ERT to trace infiltration of warm water. The degradation of permafrost in the Austrian Alps was monitored by Kellerer-Pirklbauer & Eulenstein (2024) by repeated ERT. This technique is attractive but requires large temperature differences to be able to discern electrical resistivity variations.

In gas and oil exploration, the temperature at a borehole's maximum depth is recorded as bottomhole temperature (BHT). After 24 hours of static conditions upon reaching the maximum depth, the bottomhole static temperature (BHST) is assumed to be equal to the formation temperature

(Kutasov & Eppelbaum, 2005). BHT and BHST from various depths are used to derive the geothermal gradient. This gradient can be used to estimate the temperature of formations at any other depth (Matiz-León, 2023), (Erkan & Balkan-Pazvantoğlu, 2023). Gies et al. (2021) derived a geothermal gradient of 0.0215 ^{o}C.m^{-1} for the Netherlands from a shallow (<600 m) database of TD profiles, but BHT data down to 6000 m depth indicate a geothermal gradient of 0.0314 ^{o}C.m^{-1}.

Remote sensing (RS) of land surface temperatures has been applied to identify groundwater flow, such as seepage zones (Londoño-Londoño et al., 2023). However, direct measurement of GWT by RS remains beyond present possibilities. Benz et al. (2015) used remotely sensed land surface temperature and interpolated GWT measurements to compare the spatial properties of subsurface urban heat islands.

1.4 The study area

1.4.1 Topography

The Netherlands is a low-lying country in northwestern Europe, bounded by the North Sea in the west and north (Figure 1.3). Topographically low areas dominate the western and northern parts of the country (the coastal plain) and the valleys of the major rivers. Elevation ranges from 50 m above mean sea level (m amsl) in coastal dunes to 6 m below mean sea level in reclaimed lakes. The terrain in the south, east and northeast is higher, up to approx. 50 m amsl. The glaciotectonic ridges (Gooi, Utrechtse Heuvelrug, Veluwe, Sallandse Heuvelrug) reach an elevation of over 100 m amsl. The very southeast of the country has elevations over 100 m amsl, up to 325 m amsl.

1.4.2 Geology and hydrogeology

The Netherlands and the adjoining southern region of the North Sea have a complicated tectonic and sedimentary history, being part of a large subsiding area. This area was either a shallow sea or a coastal lowland (Zagwijn, 1989). The oldest rocks, of Carboniferous age (Table 1.1) are exposed at the very southeastern border of the country. Younger Paleozoic rocks are not exposed but comprise (among others) Permian sedimentary rock and a thick succession of rock salt and anhydrite in the deeper subsurface (Doornenbal & Stevenson, 2010). Mesozoic rocks are exposed in a quarry at the eastern border of the country (Triassic Muschelkalk limestones) and thick Cretaceous successions of chalk that are locally exposed in the southeast (see Figure 1.4) (Wong, et al., 2007).

Since the Paleogene (early Tertiary), the European Cenozoic Rift System (ECRS) has been forming (Ziegler, 1992). The Netherlands is located at the northwesternmost extension of the ECRS, formed by the southeast-northwest running Lower Rhine Graben (LRG) (Zagwijn, 1989). The LRG in the Netherlands extends from the southeast into the North Sea basin (see major faults Figure 1.4) and is locally named Roer Valley Graben (RVB). The south of the Netherlands is topographically higher, being linked to the geology of the Ardennes and the London-Brabant Massif (Van Balen, et al., 2005; Willems, et al., 2020).

Table 1.1: Chronostratigraphy and stratigraphic units of formations and groups mentioned in the text or cross sections. After TNO-NITG (2023).

Chronostratigraphy			Stratigraphic units					
			Marine	Fluviatile			Glacial	Other
				Eastern rivers	Rhine	Meuse		
Quaternary (Present-2.6 Ma)	Holocene (0-11.7 ka)		Naaldwijk		Echteld	Beegden		Nieuwkoop (peat)
	Pleistocene (11.7 ka-2.6 Ma)	Late Pleistocene (Eemian and Weichselian)	Eem		Kreftenheye			Boxtel (aeolian)
		Middle Pleistocene (Chibanian) (Elsterian and Saalian)		Appelscha	Urk, Sterksel		Drenthe Peelo	
		Calabrian		Peize	Waalre			
		Gelasian	Maassluis					
Neogene (2.6-23 Ma)	Pliocene		Oosterhout		Kiezeloöliet			
	Miocene		Breda		Inden			
Paleogene (23-66 Ma)	Oligocene		Rupel					
	Eocene		Dongen					
	Paleocene		Landen					
('Late') **Cretaceous** (66-100.5 Ma)	Danian		Houthem					
	Maastrichtian		Maastricht, Gulpen					
	Campanian		Vaals					
	Santonian		Aken					
Triassic (201-255 Ma)	Anisian		Muschelkalk					
Permian (252-299 Ma)	Lopingian		Zechstein Group					
	Guadalup							Rotliegend Group
	Cisuralian							
Carboniferous (299-359 Ma)	Pensylvanian		Limburg Group					
	Mississippian (~Dinantian)		Carboniferous. Limestone Group					

The Cenozoic of the Netherlands is further characterized by a shallowing sea, resulting in marine Paleocene deposits to shallow marine and coastal Eocene and Oligocene deposits (Figure 1.5). These deposits mainly comprise (fine) sands and thick sequences of clay (Wong, et al., 2004). During the Quaternary, changes in sea level due to the buildup of inland ice and repeated climatic changes, led to increased sediment discharge (Witmans, et al., 2004). Pleistocene deposits are characterized by thick sandy to gravelly deposits by braided rivers flowing from northeast, originating in the Baltic region (Eridanos river system), and from the southeast (early Rhine and Meuse systems) (Westerhoff, 2009). The rivers formed fluviatile to deltaic, estuarine and shallow lagoonal deposits. These coarse deposits now form the most prominent aquifers of the country. The sandy deposits are intercalated with clay and locally peat layers, forming aquitards (TNO-NITG, 2023).

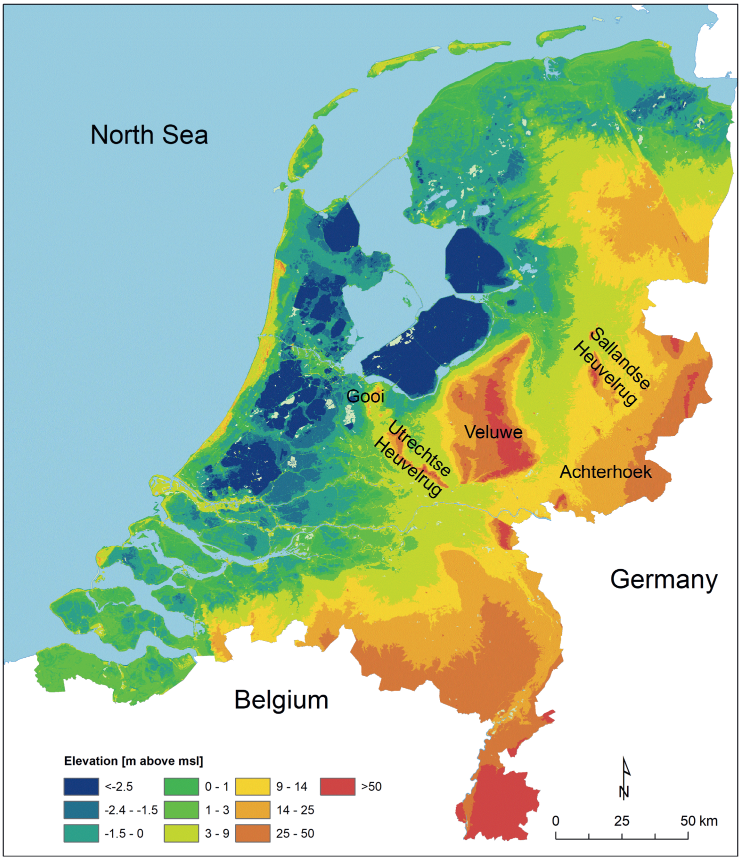

Figure 1.3: Elevation map of Netherlands in m above mean sea level (NAP). Data source: (AHN, 2023)

Clays of the Maassluis Formation, shallow marine deposits of Late Pliocene to Early Pleistocene (Gelasien) age, are often considered the hydrogeological base for most of the country

(Dufour, 1998), although they form an aquitard not an aquiclude. In the east and southwest of the country, where this formation is absent, clays of Eocene and Oligocene age form the hydrogeological base, which approaches more the status of an aquiclude (Figure 1.5). The base of the overlying Pleistocene-Quaternary deposits varies from less than 10 m below mean sea level (bmsl, NAP) in the east of the country, to deeper than 450 m bmsl in the northwest (Dufour, 1998).

During later stages of the Quaternary, glaciation phenomena invaded the North Sea basin, including the Netherlands, and reshaped the landscape. Three glaciations have reached the present Netherlands (Zagwijn, 1986). During the Middle Pleistocene Elsterian glaciation, retracting glaciers formed narrow and deep tunnel-valleys, that locally incised the older sediments to depths of 150 m (Cohen, et al., 2014). These valleys were filled by fine, silty sands and heavy clays (glacio-lacustrine sediments) (TNO-NITG, 2023). The extent of this formation is limited to the north and northeast of the country.

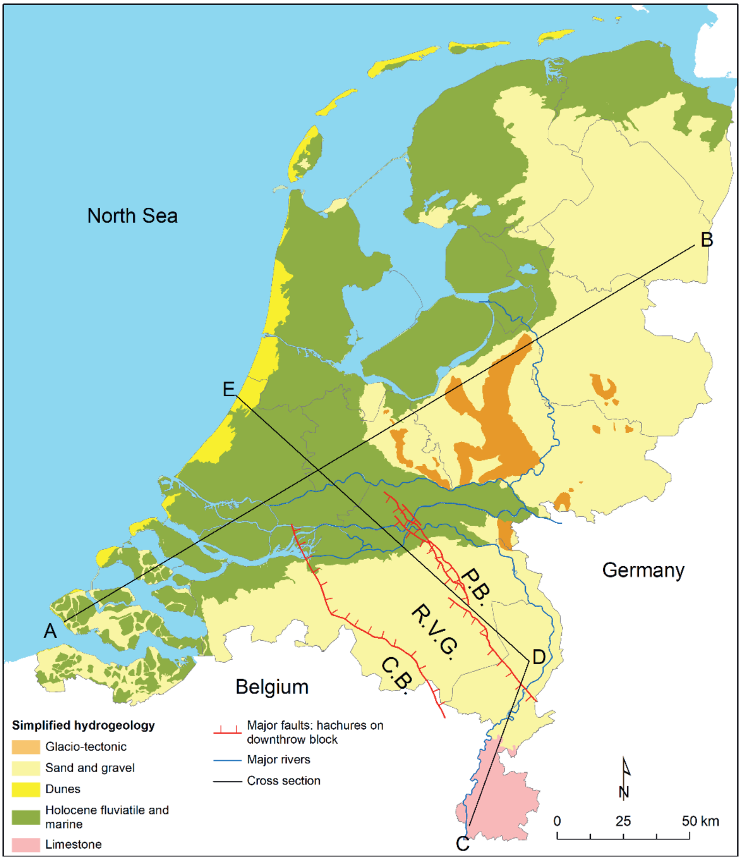

Figure 1.4: Simplified hydrogeology of the Netherlands. A-B and C-D-E: cross sections . R.V.G.= Roer Valley Graben, C.B.=Campine Block, P.B.=Peel block

During the Middle Pleistocene Saalian glaciation, glaciers covered the northern half of the country. The continental ice sheet formed moraine deposits (glacial till) at its base. At the edges of the ice sheet, deep glacial basins and high ice-pushed ridges were formed (Figure 1.4). These glaciotectonic ridges comprise older, mainly Early Pleistocene, sediments, which are tilted and locally steeply dipping (Van den Berg & Beets, 1986). During the last, Late Pleistocene Weichselian glaciation, glaciers did not reach the Netherlands, but the peri-glacial conditions resulted in aeolian deposits of cover-sands and loess and the formation of river dunes. The interglacial periods were relatively warm. The Eemian interglacial was characterized by sea levels that rose higher than today. Saalian glacial basins were flooded, and marine sands and clays were deposited in these basins (Laban & Van der Meer, 2011).

The end of the ice ages resulted in a steady sea level rise in the North Sea basin. The Holocene of the Netherlands is characterized by alternating marine transgressions and (minor) regressions in the low lying west and north of the country, and the formation of extensive river deposits in the valleys of the major rivers. Coastal regressions and transgressions are reflected in the sometimes-thick sequences of Holocene peat and clay in the west and north of the country (Bennema, 1954; Weerts, et al., 2005; Hijma, 2017). These deposits form a confining layer on top of the more pervious Pleistocene sediments. Along and between the major rivers, fluviatile clays cover the main aquifers (Figure 1.4).

Geology and topography determine the groundwater regime to a large extent. Major aquifers are formed by Pleistocene sediments that are present in most of the country. Groundwater levels are generally high, from near surface to 100 m below surface in the highest parts of the country (Dufour, 1998). In higher parts of the country, infiltration and downward groundwater movement dominate. Groundwater seepage, either from greater depths or from adjoining surface water bodies, is more dominant in the lower parts of the country. The deep polders in the west of the country and the reclaimed land (among others in the IJsselmeer) are kept dry by pumping out seepage. These polders cause lowered hydraulic heads over large distances. The dunes along the coast have a special hydraulic regime, as freshwater lenses suppress ingressing sea water. Tilting of the glaciotectonic hills has caused a strong anisotropy between horizontal and vertical flow. In combination with steeply dipping clay and loam strata, this results in a more complex hydrogeological regime. The only fresh limestone and karst aquifers are found in the southeast, where thick chalk deposits occur at shallow depths (Figure 1.4 and Figure 1.5).

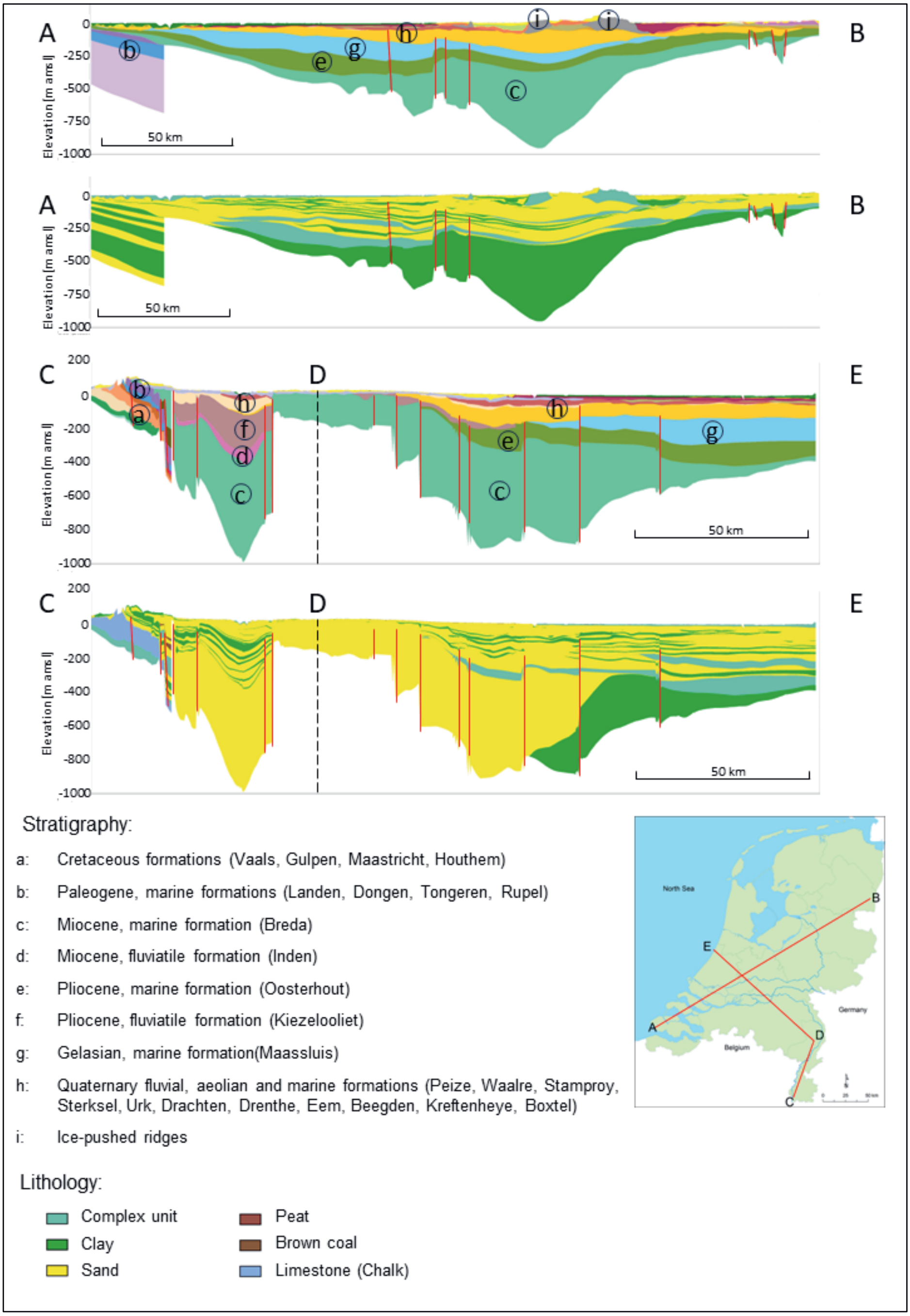

Figure 1.5: Stratigraphic cross sections and lithology. Cross sections are derived from the Digital Geological Model (DGM v2.2) and the hydrogeological model REGIS II v2.2, made available by TNO-National Geological Survey.

1.5 Aim and research questions

The previous sections clarify that insight in subsurface and groundwater temperatures, their spatial distribution and change in time is crucial to groundwater management and optimum use of the subsurface e.g. for underground thermal energy storage. The aim of this thesis is to improve the understanding of groundwater temperatures, their spatiotemporal distribution and drivers of groundwater temperature evolution in the Netherlands. The most important drivers of groundwater temperature change are climate change, land use change, in particular urbanization, and underground thermal energy storage. Based on this, the following main research questions were formulated:

1. How are groundwater temperatures distributed in the Netherlands, and how are the mapped patterns explained?
2. What are the regional temporal trends in groundwater temperature. How are these trends related to changes in land use, climate and groundwater management or exploitation?
3. What is the impact of urbanization on subsurface and groundwater temperatures?
4. What is the impact of aquifer thermal energy storage (ATES) on local groundwater temperatures? Is this impact related to hydraulic and thermal heterogeneity of the subsurface?

1.6 Thesis outline

The main body of this thesis consists of four chapters. Chapter 2 deals with the regional patterns and trends in groundwater temperatures and the drivers of change. Various aspects of these patterns and trends are studied by field measurements, both groundwater samples and temperature-depth profiles, data of abstracted groundwater at public supply well fields and numerical simulations. Numerical simulations have concentrated on (the evolution) of the ground surface temperatures under various types of land use, and on the identification and explanation of the groundwater temperature patterns in various parts of the country.

Chapter 3 presents a case study of the effects of urbanization on subsurface temperatures in the city of Amsterdam. This city is ideal to study the effects of urbanization, as it has expanded since the Middle Ages in a near-concentric pattern, which has largely remained unchanged. Therefore, certain parts of the city can be linked to a specific building period. The temperature evolution of the subsurface of this city has been explored by field measurements that are matched with a numerical temperature model, simulating the expansion from Middle Ages to modern times.

The monitoring and modelling of an ATES system and its impact of the groundwater temperatures is the subject of chapter 4. Temperature was monitored between start-up of the system in 2008 and 2012, in the ATES wells, various monitoring wells within the radius of influence of the system, and nearby background monitoring wells. A calibrated regional flow model was set up. The hydraulic effects and thermal impact of the ATES system were modelled with two detailed site models, the results of which were compared with the monitoring data. The two models involved different levels of heterogeneity in hydraulic and thermal parameters. It was shown that including the fine-scale heterogeneity is important to accurately model the impacts of the ATES system.

Fine-scale heterogeneity of hydraulic and thermal properties of the subsurface is further studied in chapter 5. This chapter deals in particular with how such fine-scale heterogeneity can be derived from commonly used geophysical borehole logging and other data. The detailed interpretation of such data provided insight in the variability of thermal parameters within a hydrogeological homogeneous aquifer. Insight in the heterogeneity of the thermal parameters is essential, not only for accurate modelling of the impacts of ATES systems, but also for interpretations of the natural thermal field e.g. in climate reconstruction or the study of vertical groundwater movements.

Chapter 6 presents a synthesis in which the main findings and highlights of the previous chapters are brought together and placed in a broader perspective.

Chapter 2

Regional patterns and trends in groundwater temperature with drivers of change

Abstract

Groundwater temperature (GWT) is a crucial parameter for the physical and chemical quality of groundwater. GWT is determined by the (semi) equilibrium between heat flow from the Earth's interior and ground surface temperature (GST). The GST depends on climatological characteristics and land cover. It is, therefore, variable in place and time. Climate change and land use change affect GST, subsurface and groundwater temperatures.

In this chapter, the spatiotemporal variability of the GWT is investigated in a novel way. Previous studies mapped temperatures at various depths by means of temperature-depth (TD) profiling. Here, apart from (repeated) TD profiling, use is made of time series of groundwater sample temperatures and temperatures of abstracted groundwater at public supply well fields (PSWFs). The groundwater samples are taken in a standardized manner. Field temperatures of samples from depths between 20 and 35 m below ground level (T20-35) are selected. Only time series of 4 samples or more are considered. The averages of T20-35 show a clear regional pattern. This pattern is confirmed by the PSWFs water temperatures, although these mix large quantities of groundwater from a greater depth interval.

Trend analysis of time series of T20-35 reveals dominantly increasing trends, in particular in areas of groundwater infiltration (downward flow). In the west of the country, T20-35 is more stable. This is, in part, explained by more prominent upward flow to deep polders. The use of T20-35 proves to be a valuable tool for screening and trend analysis of GWT. Groundwater samples in national and provincial monitoring networks are collected on a large scale and over longer periods of time, as such providing an additional investigation technique to TD profiling.

Regional patterns and trends are analyzed and explained by studying characteristics and trends of GST. GST is often directly linked to the surface air temperature (SAT). The differences between GST and SAT (GST-SAT offsets) are considered characteristic for land cover types. The GST and GST-SAT offsets are derived from field data, interpretive numerical simulations of TD profiles and a surface-atmosphere radiation balance (SARB) model for various types of land cover and locations in the Netherlands, covering the 1965-2020 period. This reveals that GST and GST-SAT offset for similar land covers are variable across the country due to regional variations of SAT and radiation (combined in the potential evaporation) and precipitation. Based on the model outcome for various locations and land covers, maps of GST and GST-SAT offset have been constructed. Comparison with the T20-35 distribution shows the relation between the GST trends and the T20-35 patterns. Field observations and model results confirm the rising trend in GWT.

Locally, the GWT distribution is perturbed by large-scale groundwater abstraction at PSWFs or by infiltration from major rivers. Examples of these features are presented and discussed.

2.1 Introduction

Climate change induced stresses imposed on groundwater quantity and quality receive increasing attention (Stuyfzand et al., 2007; Smith et al., 2023). Large-scale spatiotemporal changes in GWT are less studied and little is known about how groundwater responds to surface warming across spatial and temporal scales (Benz et al., 2024). Satellite-derived land surface temperatures (LST) and a global data set of GWT were used by Benz et al. (2017a) to demonstrate that evapotranspiration and snow cover impact the offset between LST and GWT globally. Benz et al. (2024) have simulated current and projected groundwater temperatures at the global scale, showing a conservatively projected increase in GWT of over 2°C that at the depth of the groundwater table between 2000 and 2100. However, GWT and temperature trends vary substantially by geographic region.

In this chapter, regional spatiotemporal patterns of subsurface temperatures in the Netherlands are investigated, using field data from (i) temperature measurements in groundwater samples from both monitoring wells and public supply well fields (PSWFs), and (ii) temperature-depth (TD) profiles in groundwater observation wells. TD measurements in the period 1976-2018, especially by Van Dalfsen (1981, 1983), Kooi (2008), Bense et al. (2017) and Bense & Kurylyk (2017) provided the basis on which this chapter is building. Pioneer Van Dalfsen produced isotherm maps for 25 m depth intervals from 25 to 250 m below ground level (m bgl), based on 577 TD profiles. He recognized regional patterns, including anomalous areas such as ‘heat sinks’, with relatively low temperatures, and areas with relatively high subsurface temperatures (Figure 2.1).

Low GWT areas (termed “heat sinks” by Van Dalfsen) were explained by Van Dalfsen by the downward groundwater flux in topographically high areas where infiltration dominates. Advective heat transfer of groundwater flowing along its path from recharge to discharge areas and lateral changes in thermal conductivity due to geological structures of relatively large scale, were recognized as causes of relatively high subsurface temperatures (Van Dalfsen, 1981). Repeated TD profiling in later decades was used to analyze the spatial variability in subsurface warming on a decadal scale by Kooi (2008) and to quantify vertical groundwater flow (Bense & Kurylyk, 2017).

The aim of this chapter is to analyze regional patterns and trends in groundwater temperature in the Netherlands, and to interpret them in terms of main drivers. A new approach was applied to investigate the temperature distribution of the shallow groundwater and recent trends in GWT. GWT trends are usually explained by increasing SAT as a result of climate change through GST-SAT coupling. Here the regional differences and changes in time in GWT, as a result of (changes) in GST-SAT coupling, are studied. The drivers behind the evolution of GST and GST-SAT offsets are explored by surface-atmosphere radiation-balance (SARB) modeling.

Figure 2.1: Isotherms [ºC] at 25 m below ground surface, based on Van Dalfsen (1983), with locations of TD-profiles measured by Van Dalfsen.

2.2 General data

2.2.1 Land use

GST and GST-SAT offset is usually assumed to be related directly to the land surface cover (e.g. Beltrami, 2001; Mann & Schmidt, 2003; Beltrami & Kellman, 2003; Kooi, 2008; Dědeček, et al., 2012; Visser, et al., 2020). This implies that spatial variations and temporal changes in land use result in different offsets. Land use and land use changes in the Netherlands are derived from land use datasets, e.g. the LGN, receiving updates every 3 to 6 years since 1986 (Hazeu, 2014), or data sets from the Central Bureau of Statistics, dating back to 1989 (Central Bureau of Statistics, 2022). For older historical data, sources like Klein Goldewijk (2016) and Van Lier (1991) were consulted. The present land use is shown in Figure 2.2.

Figure 2.3 shows that from the year 1900, the acreage of natural terrain in the Netherlands decreased continuously. The area covered by forest was more or less stable in the first half of the 20th century and increased slightly in the second half. Agricultural terrain increased in the first half of the last century mainly by bringing natural areas under cultivation. In the second half of the 20th century, the acreage used for agricultural purposes increased mainly due to reclamation projects.

Figure 2.2: Land use (2010). Source: Central Bureau of Statistics (2022).

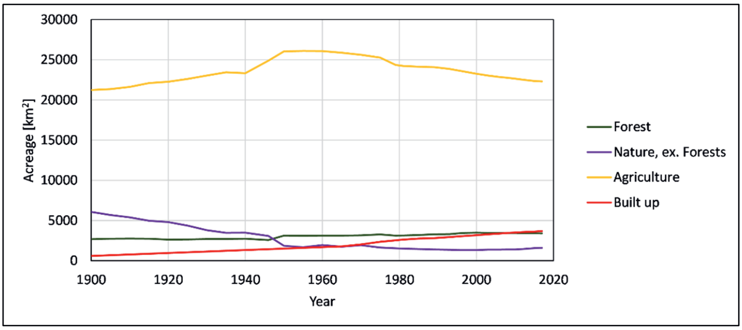

Figure 2.3: Change in land use between 1900 and 2018.

Data source: Central Bureau of Statistics (2023)

Approx. two-thirds (70% in 1997 and 66% in 2017) of the land surface of the Netherlands has an agriculture use. In 2020, almost 20,000 km^2 of agricultural land was grassland, i.e. almost 60% of the land surface of the country. Nearly 15% of the country is covered by forest or open natural terrain, whereas 11% is built-up (buildings, roads). Of the remaining 14% of the land surface, approx. half is used for arable farming and greenhouses, the other half by parks, green spaces etc. The most prominent land cover types in the Netherlands to be considered are, therefore, grassland, forest and built-up terrain.

2.2.2 Climate

Sluiter (2012) shows significant regional differences in the 1991-2010 climatological parameters, including SAT. Some of the regionally variable parameters that influence the radiation balance and precipitation data are summarized in Table 2.1. The regional ranges of these parameters are derived from the maps in Figure 2.4. Since these ranges stem from spatial interpolations, also the actual data for five meteorological stations that are used in this study are included in this table. The station data and regional data differ in some cases due to interpolation of the regional patterns.

Table 2.1: Regional variation of annual means of some components in the radiation balance and precipitation. Meteorological station names and their local data are put between brackets.

	SAT [°C]		Net radiation [KJ.cm^{-2}]		Precipitation [mm]		Pot. Evaporation [mm]	
Region:	1981-2010	1991-2020	1981-2010	1991-2020	1981-2010	1991-2020	1981-2010	1991-2020
Northeast	9.3-9.6	9.6-9.9	355-360	360-365	825-850	850-875	550-560	570-580
(Eelde)	(9.4)	(9.8)	(351)	(361)	(807)	(801)	(546)	(566)
Northwest	9.9-10.2	10.2-10.5	380-385	385-390	825-850	825-850	590-600	610-620
(De Kooy)	(10.1)	(10.5)	(383)	(392)	(766)	(782)	(599)	(619)
Central	9.9-10.2	10.5-10.8	350-355	370-375	875-900	875-900	570-580	590-600
(De Bilt)	(10.2)	(10.6)	(354)	(365)	(827)	(850)	(559)	(581)
Southwest	10.5-10.8	10.8-11.1	385-390	395-400	775-800	800-825	610-620	630-640
(Vlissingen)	(10.8)	(10.2)	(386)	(398)	(738)	(755)	(615)	(639)
Southeast	10.2-10.5	10.5-10.8	365-370	375-380	800-825	775-800	580-590	600-610
(Maastricht)	(10.3)	(10.7)	(367)	(378)	(768)	(753)	(585)	(607)

Table 2.1 and Figure 2.4 illustrate that the northeast of the country has the lowest average air temperature. Net radiation is low in the northeast and high along the North Sea coast. Temperature and net radiation differences are expressed in the Makkink potential evaporation (Hooghart & Lablans, 1988). Average precipitation shows a highly variable pattern (Figure 2.4), with relatively high amounts of precipitation on the Veluwe and Utrechtse Heuvelrug and northeast of the country . The west is also relatively wet, due to prevailing southwestern and northwestern winds carrying moist air from the Atlantic Ocean and North Sea. Strong urbanization, such as in in the west of the country, is associated with higher air temperatures, water vapor levels and convective precipitation. In combination with air

pollution aerosols, acting as nuclei for raindrops formation, this results in relatively high amounts of precipitation (Fan et al., 2020).

Infiltration of precipitation and groundwater recharge depend, besides surficial runoff, mainly on the precipitation surplus over the actual evapotranspiration. Figure 2.5 shows that between 1960 and 2020, in the Netherlands, approximately the same amount of rain fell during spring and summer (April-September) (49%) as autumn and winter (October-March) (51%).

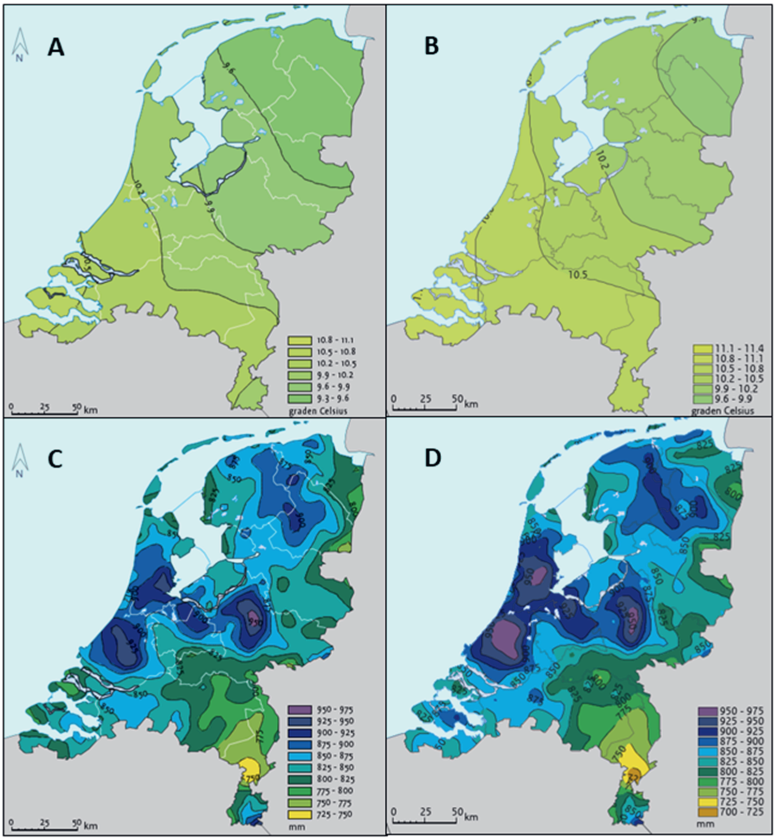

Figure 2.4: Average annual temperature [ºC] 1981-2010 (A) and 1991-2020 (B), average annual precipitation [mm] 1981-2010 (C)and 1991-2020 (D). Data source: KNMI (2023)

During summer, it rains less often, but the showers have a higher intensity. This may cause higher surface runoff and less infiltration, compared to the winter season. Evapotranspiration is low and the surplus of rainfall over the potential evapotranspiration is high during winter. Groundwater recharge is, therefore, mainly concentrated in the winter season. Precipitation on paved surfaces and in built up environments is largely discharged as surface runoff, which does not allow much infiltration. During the winter season, soils can be frozen, not allowing recharge. This condition is relatively rare in the Netherlands, especially since the 1990’s. Between 1900 and 1989, an average of 3.3 cold waves (consecutive 5 days periods with a maximum temperature below 0ºC) per decade occurred. Since 1990, this average has decreased to one cold wave per decade. Infiltration of cold precipitation during winter is likely to play a role in the low GWT zones, as postulated by Van Dalfsen (1981). Not due to more rainfall during winter, but as a result of a higher surplus of precipitation over evapotranspiration.

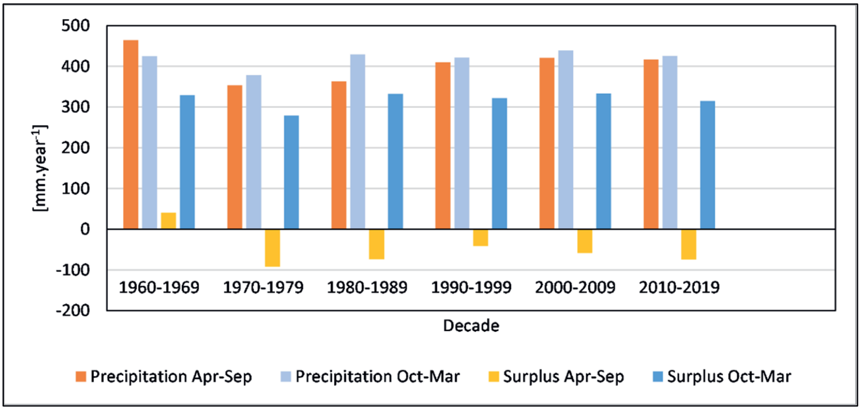

Figure 2.5: Average annual precipitation and precipitation surplus over potential evapotranspiration (Makkink) in De Bilt per decade.

Climate scenarios for the years 2050 and 2100 (KNMI, 2023b), foresee an increase in winter precipitation of 4-7% in 2050 to 4-24% in 2100. Summer precipitation, on the other hand, is expected to decrease, by 2-13% in 2050 and 2-29% in 2100. The precipitation distribution in time will, therefore, change significantly, and more infiltration (groundwater recharge) can be expected to occur during the cold season. This may lead to a reduction, or even decrease, of the subsurface temperature increase due to increasing SAT.

The temperature history in De Bilt from 1706 to 2021 is displayed in Figure 2.6.

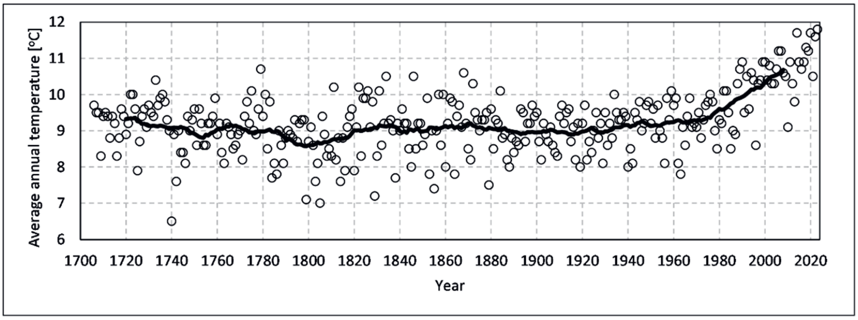

Figure 2.6: Average annual air temperatures at De Bilt, 1706-2023. The solid line is the 30-year centered moving average.

This long-term temperature reference record was constructed by the Royal Netherlands Meteorological Institute for De Bilt (Labrijn, 1945; Labrijn, 1948; KNMI, 2014). A relation between (the evolution of) climatological/meteorological parameters, including SAT, with GST and GWT is postulated.

2.2.3 River water temperatures

River water temperatures increase due to higher air and run-off temperatures and use of river water as cooling water. Climate change results in retracting glaciers and less snow in the source areas of the Rhine (De Vries et al., 2013), resulting in lower amounts of meltwater in summer. Temperature of the rivers Meuse and Rhine between 1965 and 2020 is plotted in Figure 2.7A. It shows a consistent rise in this period, with slopes of 0.033 and 0.021°C.year^{-1} for Meuse and Rhine respectively. This corresponds to an average temperature increase of 0.7 and 0.4°C between 1991 and 2011. High river water levels and infiltration into the aquifers generally occur in winter and spring (~November-May) (Breukel et al., 1992), when water temperatures are lowest (Figure 2.7B). Winter and spring water temperature of the major rivers increases at the same rate as the average annual and summer water temperature (Fig.2.7B).

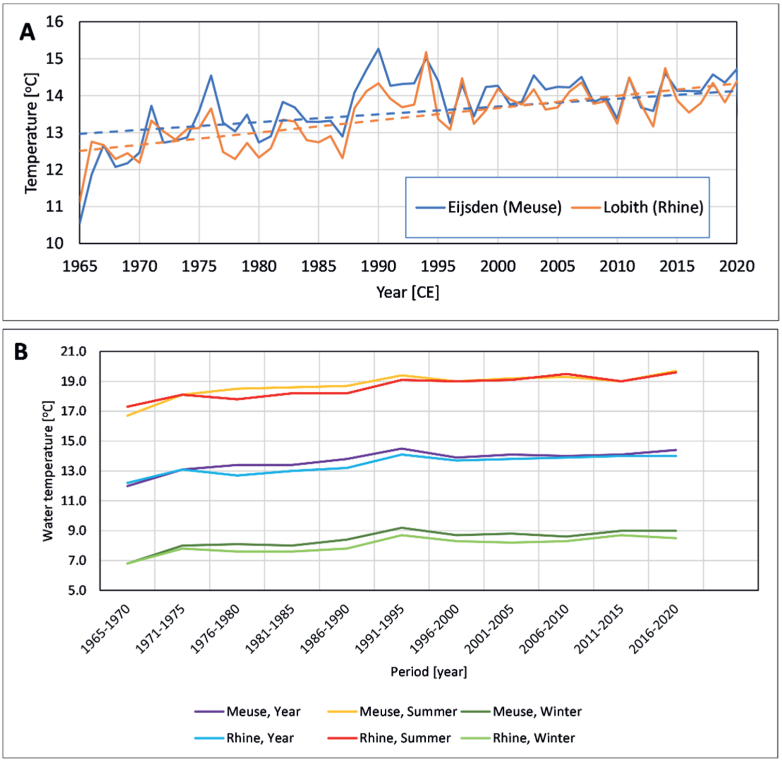

Figure 2.7: (A) average annual river water temperatures of the river Meuse (at Eijsden) and the river Rhine (at Lobith). Linear trend lines are dashed. (B) Seasonal averages (1965-2020) of river water temperatures. Data source: Rijkswaterstaat (2023).

Buitink et al. (2023) reported that according to the future (up to 2150) climate scenarios, discharge of the Rhine and Meuse are expected to increase in winter and spring and decrease in (late) summer. This implies that the average temperature of infiltrating river water is hard to predict.

2.3 Regional GWT distribution and trends

2.3.1 Materials and methods

Groundwater sample temperatures

Field measurements of 13,838 groundwater samples, taken from piezometers at 712 locations in the Netherlands, were retrieved from the national groundwater database (TNO Geological Survey of The Netherlands, 2020). The samples were taken between 1908 and 2012 from depths ranging from 12 to 396 m bgl. The median sampling depth is 23 m bgl.

The average groundwater temperature in piezometers with screened depths between 20 and 35 m bgl (T20-35) was calculated for 383 locations with at least 4 field measurements of the sample temperature between 1991 and 2011 (Figure 2.8 and Table 2.2). A minimum sampling depth of 20 m bgl minimizes the effect of seasonal fluctuations of the subsurface temperature (usually down to ~15 m bgl in the Netherlands). The median number of observations per location is 7. Unrealistic field temperatures (all temperatures below 5°C and above 17°C) were discarded.

The average temperatures do not show a significant linear relation with the sampling depth in the 20-35 m depth range ($p=0.6$), and, therefore, despite different sampling depths, intercomparison of the samples is possible.

Sampling of the wells, belonging to provincial or national monitoring networks, is done in a standardized manner as of 1991, described in Netherlands standard (NEN) 5744 (Normcommissie 390 09 "Bodemkwaliteit", 1991) as of 1991, National Technical Agreement (NTA) 8017 (2008) from 2008, and NTA 8017:2016 nl from 2016 (nen.nl). Samples in this study were collected according to NEN 5744 (1991-2008) and NTA 8017 (2008) (2008-2011). The sampling procedure of these two protocols remained unchanged and involves pre-flushing the piezometer with at least three times the water filled volume of the piezometer at a low flow rate, to prevent turbulence and gas bubbles, until pH and electrical conductivity are constant. The sampling pump intake is positioned at the piezometer screen depth (this was changed later, in 2016, to 1 m above the well screen). The temperature is recorded at the moment the sample is taken.

Most piezometers have a screened section length of 1 or 2 m. Assuming a 0.05 m piezometer diameter and water column height inside the piezometer of 20 m, the pre-flush volume is 118 liters, two thirds of which flow from the aquifer into the well. This volume of water flows from a more or less cylindrical body around the piezometer screen, as most aquifers in the Netherlands consist of horizontally stratified sediments with a horizontal permeability exceeding the vertical permeability. A screen length of 1 m and an effective porosity of the aquifer of 35% result in a cylindrical area with a radius of 0.27 m. The sample temperature is, therefore, representative for the depth and direct vicinity of the piezometer screen.

Environmental sampling of the piezometers is normally done with an above ground peristaltic pump. These pumps do not emit heat to the sample. Maximum sampling depth of a peristaltic pump is approx. 9 m. The mean lowest groundwater level (MLGL) in the Netherlands is generally <5 m bgl (Figure 2.9). The MLGL at the T20-35 observation locations (Figure 2.10) has a P50 of 1.6 m and P95 of 5.4 m bgl. Six samples (1.6%) had a MLGL >9 m bgl, possibly requiring the use of in-line centrifugal electrical pumps, causing a somewhat higher sample temperature.

Figure 2.8: Groundwater sampling locations, meteorological stations, lysimeter and river gauging locations.

Table 2.2: T20-35 observation point characteristics.

Top of screen [m bgl]	No.
20-25	350
26-30	28
31-35	5

Year	No. Start	No. End
<1991	0	0
1991-1995	365	0
1996-2000	6	60
2001-2005	1	52
2006-2010	11	255
>2010	0	16

Land use	No.
Agriculture	179
Built up (incl. roads)	101
Forest	73
Other natural terrain and parks	26
Greenhouses	4

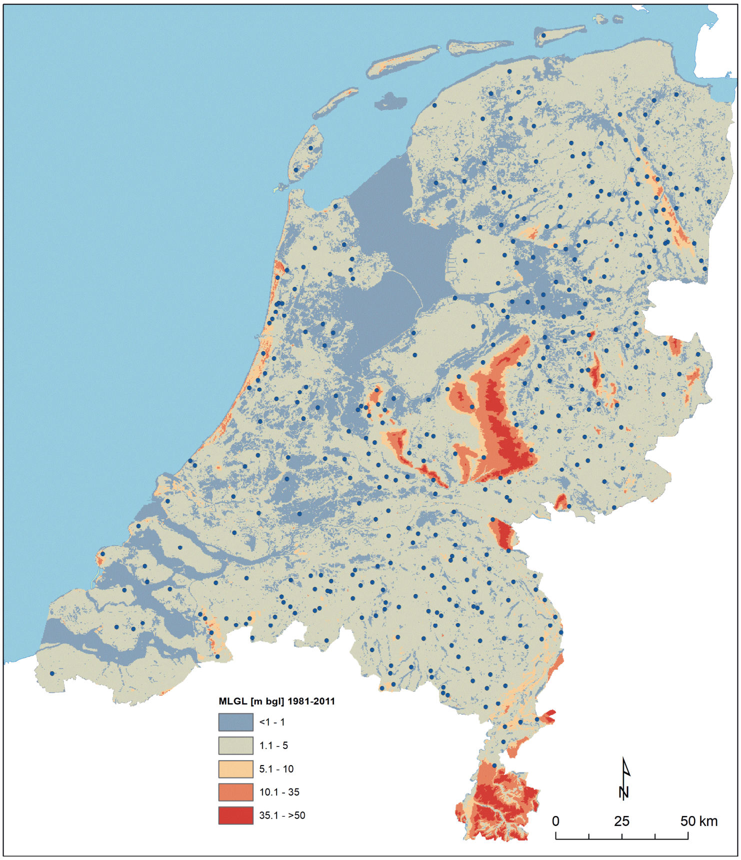

Figure 2.9: Mean lowest groundwater level (1981-2011) relative to ground level. Data source: LHM (Stowa / NHI, 2023)

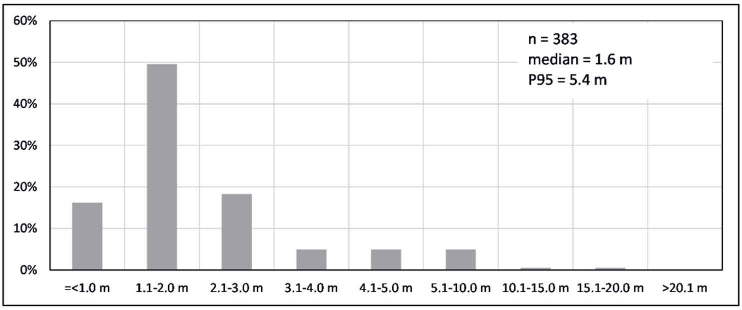

Figure 2.10: Mean lowest groundwater level relative to ground level (1981-2011) at T20-35 observation locations.

The sample undergoes a temperature change during the flow through the sampling tube to the above ground flow cell, where the temperature is measured. This potential sample temperature change was estimated with a numerical radial FE model encompassing a 20 m deep and 2 m radius aquifer section. A 20 m long 58 mm diameter PVC piezometer (with 4 mm wall) and 16 mm PE sampling tube (with 2 mm wall) were modeled in the center of the aquifer section. The aquifer temperature was assumed to increase linearly from 12ºC to SAT between sampling depth (20 m bgl) and ground surface. A SAT range of 5-30ºC and groundwater levels (GWLs) between 1 and 20 m bgl were applied. The water column level inside the piezometer equaled the GWT of the aquifer.

By pre-flushing, the water inside the piezometer is replaced with groundwater with GWT at sampling depth. During sampling, the temperature of the water column and air column inside the piezometer adjust slowly to the surrounding aquifer and air temperature, and the sample tube temperature by conduction. Calculated deviations of sample temperature at ground level from the GWT at sampling depth are presented in Figure 2.11.

At P95 MLGL, calculated temperature changes introduced by the upward transport of the groundwater sample is generally <0.1ºC at SAT between 5-30ºC. Deeper groundwater levels result in larger deviations. A very low GWL (20 m bgl) and uncommonly high SAT (30ºC) resulted in a maximum 0.19ºC temperature increase of the sample. The change in water temperature during the upward transport to the sample vessel is in most circumstances <0.1ºC and considered negligible.

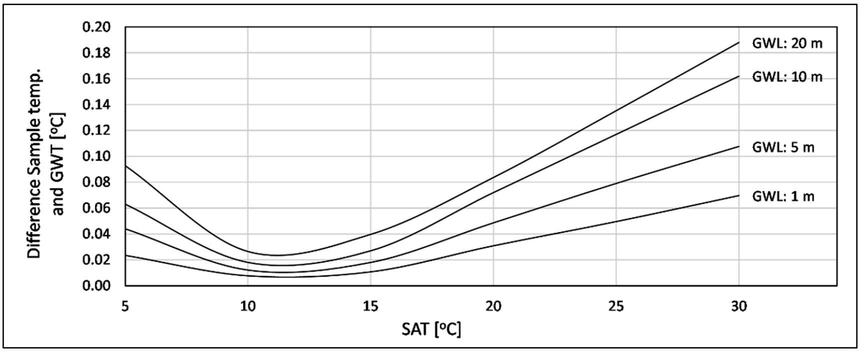

Figure 2.11: Estimated deviations of sample temperature from GWT as function of groundwater level below land surface (GWL).

Colombani et al. (2016) compared three temperature logging methods for several 18-24 m deep wells. They used open borehole temperature logging (OBL) and temperature measurements at 1 m well screen sections that were isolated by straddle packers. Water was pumped from the isolated sections and temperature logging was done inside the well (MLS-IW) or above ground (MLS-AG). In the MLS approach, an in-line electrical centrifugal pump, placed above the packers, was used. The results illustrate the effect of heat dissemination by the electrical pump, especially in the MLS-AG measurements when a less permeable section was pumped during a longer time. No temperature effect of the transport to the above ground temperature sensor is discernable from the results, as this is obfuscated by the pump effect.

Trend analysis of groundwater sample temperature

The Mann-Kendall test (Mann, 1945; Kendall 1975) was used to statistically assess if there is a monotonic trend of sample temperatures over time, and at which level of statistical significance. An upward trend means that the sample temperatures consistently increase over time. A downward trend indicates the contrary. The trend may be linear or not. The Mann-Kendall test is a non-parametric (distribution-free) test and can be applied even on small numbers of samples (Meals et al., 2011). The procedure is best viewed as exploratory (Hirsch et al., 1982). It is most appropriately used to identify piezometers where changes are significant or large, and to quantify these findings.

The parameter 'S' of the Mann-Kendall test indicates whether the temperature trend vs. time is generally decreasing (negative S-value) or increasing (positive S-value). The significance or confidence level determines whether the trend is statistically significant. Typically, a significance level of 0.05 (95% confidence) is used to test the null hypothesis that there is no trend in the data. At low absolute S-values and low confidence level, there is either no trend or a stable situation. The coefficient of variation (COV) was used to distinguish between both situations. The confidence levels and classification suggested by Aziz et al. (2003) were applied in this study (Table 2.3).

Table 2.3: Mann-Kendall trend classification (Aziz et al., 2003).

Mann-Kendall statistic	Confidence in the trend	Trend
$S>0$	>95%	Increasing
$S>0$	90%-95%	Probably increasing
$S>0$	<90%	No trend
$S\leq0$	<90% and COV≥1	No trend
$S\leq0$	<90% and COV<1	Stable
$S<0$	90%-95%	Probably decreasing
$S<0$	>95%	Decreasing

2.3.2 Results and discussion

A total of 383 observation wells has 1-2 m long screens at depths between 20 and 35 m bgl. These observation wells provided 2893 temperature readings (T20-35), collected between 1991 and 2011, and yielding a time-series of at least 4 measurements.

The average number of observations is 8 in an average time period of 13 years. The T20-35 values per piezometer show a normal distribution between a minimum and maximum of 5.7 and 16.6°C, with a median of 10.5°C (Figure 2.12A). The T20-35 values are plotted against time in Figure 2.12B. The trendline shows an increase of T20-35 with time.

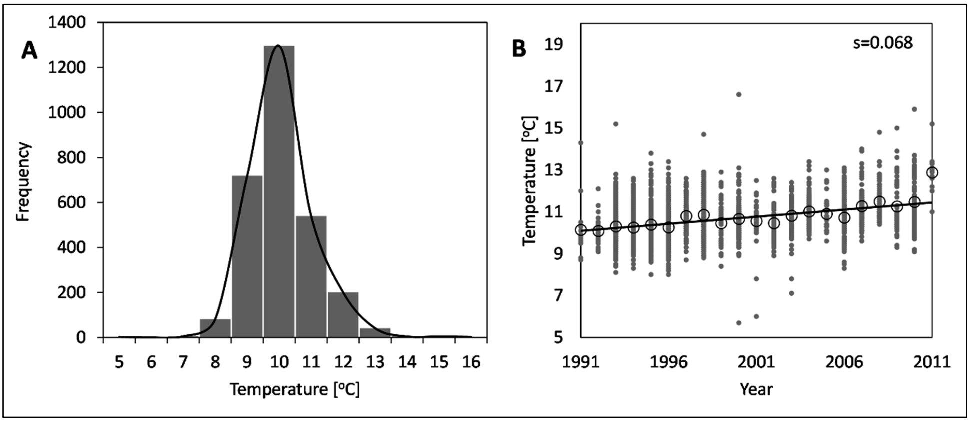

Figure 2.12: Frequency distribution of T20-35 observed in 1991-2011 (A) with their temperature trend during 1991-2011 (B). The dots in B represent individual measurements. The open circles are the average values per year. The solid line is the linear trendline fitted on the individual observations. "s" represents the slope of the trendline.

Regional pattern

The spatial distribution of the average T20-35 in the period 1991-2011 is plotted in Figure 2.13. Contours of T20-35 have been constructed by the inverse distance weighted method. Measurements and contours reveal a clear regional pattern, with the lowest groundwater temperatures occurring in the northeast of the country and the highest in the southeast. Figure 2.13 shows clear similarities, but also differences, with the isotherm map for 25 m depth by Van Dalfsen (1983) (Figure 2.1). The low-temperature areas ('heat sinks'), such as the topographically high Veluwe area, show very prominently on Van Dalfsen's map and can also be recognized in Figure 2.13. However, since the groundwater levels in these areas are generally deep, relatively few groundwater samples were taken from depths between 20 and 35 m bgl. The maps by Van Dalfsen show more data points in the 'heat sinks', revealing lower temperatures (<9°C) than found in the currently studied groundwater samples. Other topographically high areas include Het Gooi (central Netherlands) and Sallandse Heuvelrug and Achterhoek (in the east of the country), parts of which are shown in Figure 2.13 as 'heat sinks'. Van Dalfsen collected less data points in the Sallandse Heuvelrug and Achterhoek regions, and this 'heat sink' is lacking in his maps. 'Heat sinks' have been explained by Van Dalfsen by the fact that these high areas are groundwater recharge (infiltration) zones. The high topography and deep groundwater levels, in combination with sandy soils lead to high infiltration rates. Furthermore, Van Dalfsen postulated that the cold season between October and April is associated with most recharge, leading to advection of relatively low temperature water to great depths.

Another similarity between the Van Dalfsen maps (Figure 2.1) and Figure 2.13 is the region with low T20-35 in the north-east of the country. This area is topographically relatively high as well, and a correlation with groundwater recharge may be surmised.

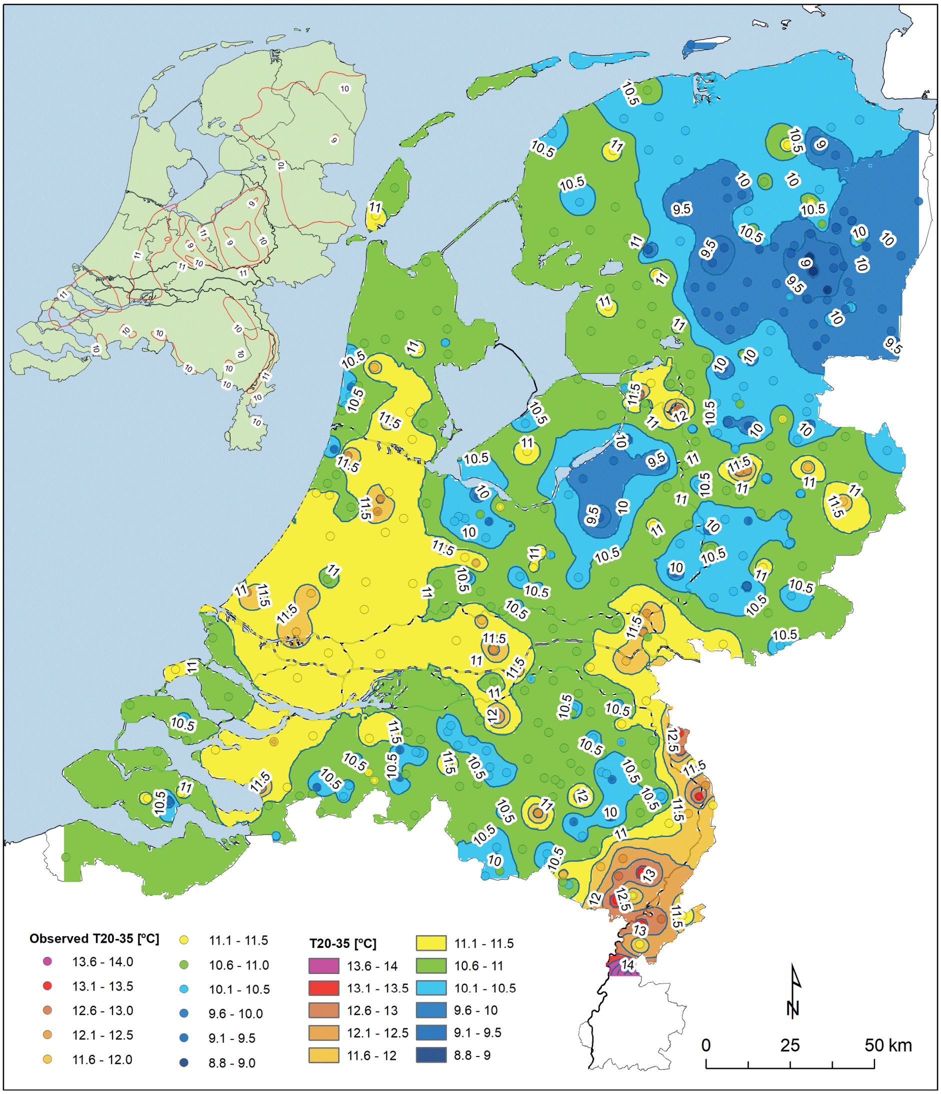

Figure 2.13: Spatial distribution of T20-35 observations and interpolated T20-35 contours. No data in SE (South Limburg) due to high land surface altitude and deep groundwater table. Inset map: T20 isotherms by Van Dalfsen (1983) (Figure 2.1).

The main differences between the isotherms in Figure 2.13 and Figure 2.1 are found in the areas with relatively high T20-35. Zones with temperatures >11°C were mapped by Van Dalfsen in the west and south-west. Figure 2.13 suggests a far larger expanse of high temperatures (>11°C) in the west. The west of the country is characterized by high groundwater levels and seepage in deep polders. Most precipitation is discharged through surface runoff and shallow drainage. The high precipitation rates in this part of the country are therefore not expressed in a low T20-35. The area has a relatively high building density (Figure 2.2) and largely coincides with the presence of the most extensive urban heat islands (Figure 2.14 and Klok et al. (2012)). The GST-SAT offset can be as high as 4.5°C in urban environments (Visser et al., 2020). The temperature anomaly in a shallow (15-25 m bgl) aquifer between city center and outskirts can be as high as 2.9°C (Hemmerle, et al., 2022). The percentage of built-up areas has doubled (from 6 to 12%, Figure 2.3) between 1970 and 2015, in particular in the west of the country. The larger expanse of the T20-35>11°C zone is likely to be related to progressive urbanization since Van Dalfsen's measurements.

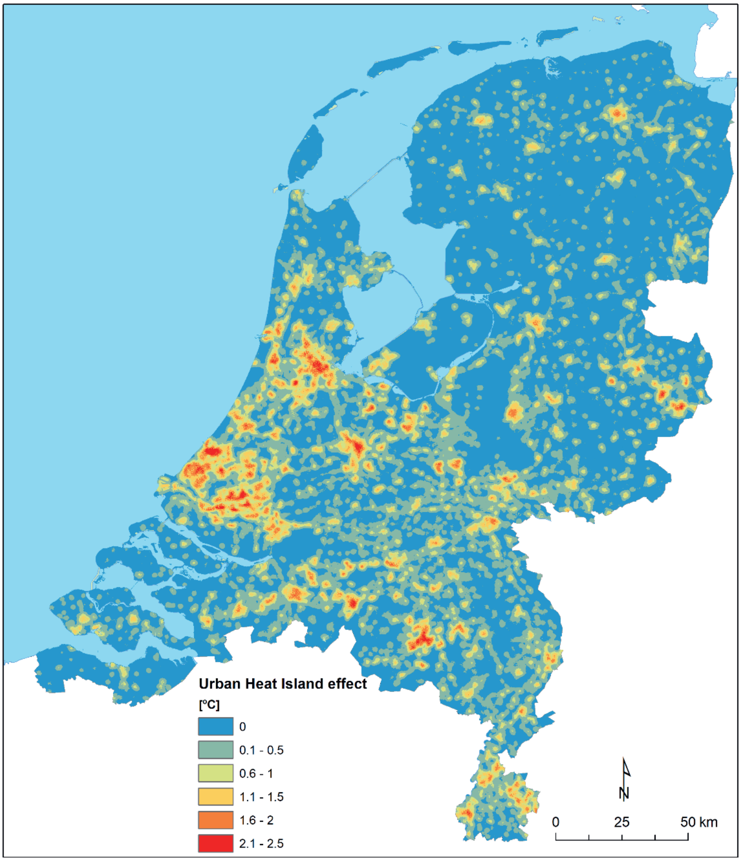

Figure 2.14: Urban heat island effect (difference in average annual temperature with surrounding countryside, year 2017). Map data source: Stichting Climate Adaptation (2023)

The highest T20-35 are found in the southeast of the country. These temperatures, exceeding 12°C, are not related to greater sampling depths. The single highest T20-35 in this area is found in an urban and highly industrialized area. However, the high T20-35 values appear in Figure 2.13 in a larger region, where also Van Dalfsen mapped an anomalously warm area, albeit with smaller extent. The southeast of the country receives significantly less rain and has more dry days (170-175 days, 1991-2020 average) than the high-precipitation areas. This relatively dry area overlaps the high T20-35 zone. A relation between little precipitation, less recharge of relatively cold rainwater and limited post-precipitation evaporative cooling and the high T20-35 in this region seems apparent.

Trends

Figure 2.12B shows an increasing trend ($p<<0.001$) for T20-35 values in time. During the 1991-2011 period, annual averages of all sample temperatures increased 0.06°C per year, or 1.2°C in 20 years. This is related to the accelerated increase of SAT and GST since approx. 1980 (Figure 2.6). As T20-35 responds to changes of SAT with some delay and is attenuated with depth, the GWT signal reflects SAT changes in previous decades. During the period 1981-2000, SAT increased by 1.4°C (De Kooy, Vlissingen) to 1.6°C (De Bilt, Eelde, Maastricht). The annual average increase of T20-35 for all samples, therefore, broadly reflects the effect of SAT forcing.

Trends of T20-35 are calculated for the 383 piezometers with temperature time series of at least 4 observations. The results are tabulated in Table 2.4. The spatial distribution of the temperature trends is depicted in Figure 2.15A. Most locations with increasing T20-35 trends are located in the east and south of the country where infiltration prevails (Figure 2.15B). Authors like Taniguchi et al. (1999) and Ferguson et al. (2006) have demonstrated that, apart from heat conduction, also groundwater flow is instrumental in conveying GST changes into the subsurface, which explains the dominance of increasing trends in the infiltration areas. In the west of the country, stable temperatures or no discernable trends dominate. This is partially caused by less prominent infiltration. Thick Holocene deposits, mainly low-solidity peat and clay, cover the west and north of the country. Low thermal diffusivity of these sediments is a second aspect that explains why increasing GST has not yet resulted in increasing T20-35 trends in the west of the country.

Table 2.4: Temperature trend statistics: no. of observations and percentage of discernable trends.

Trend	Total	Infiltration	Seepage
Increasing	134 (57%)	105 (44%)	29 (12%)
Probably increasing	48 (20%)	34 (14%)	14 (6%)
Stable	52 (22%)	32(14%)	20 (8%)
Probably decreasing	2 (1%)	1 (0%)	1 (0%)
Decreasing	1 (0%)	0 (0%)	1 (0%)
Total	237 (100%)	172 (73%)	65 (27%)

Seepage is most pronounced along major rivers (exfiltration) and deep polders (Figure 2.15B). In valleys of smaller streams in topographically high areas and the deep polders, the seepage is fed by deeper groundwater flow. It is, therefore, expected that seepage is less influenced by recent changes in GST. Along infiltrating major rivers, shorter flow path lines to the adjoining polders occur. Therefore, T20-35 in seepage areas under influence of the major rivers is expected to be more influenced by river water temperatures than by GST evolution. This, however, cannot be discerned from T20-35 data or GWT trends. Locations with not statistically significant T20-35 trends prevail in the deep polders and along the lower reaches of the major rivers.

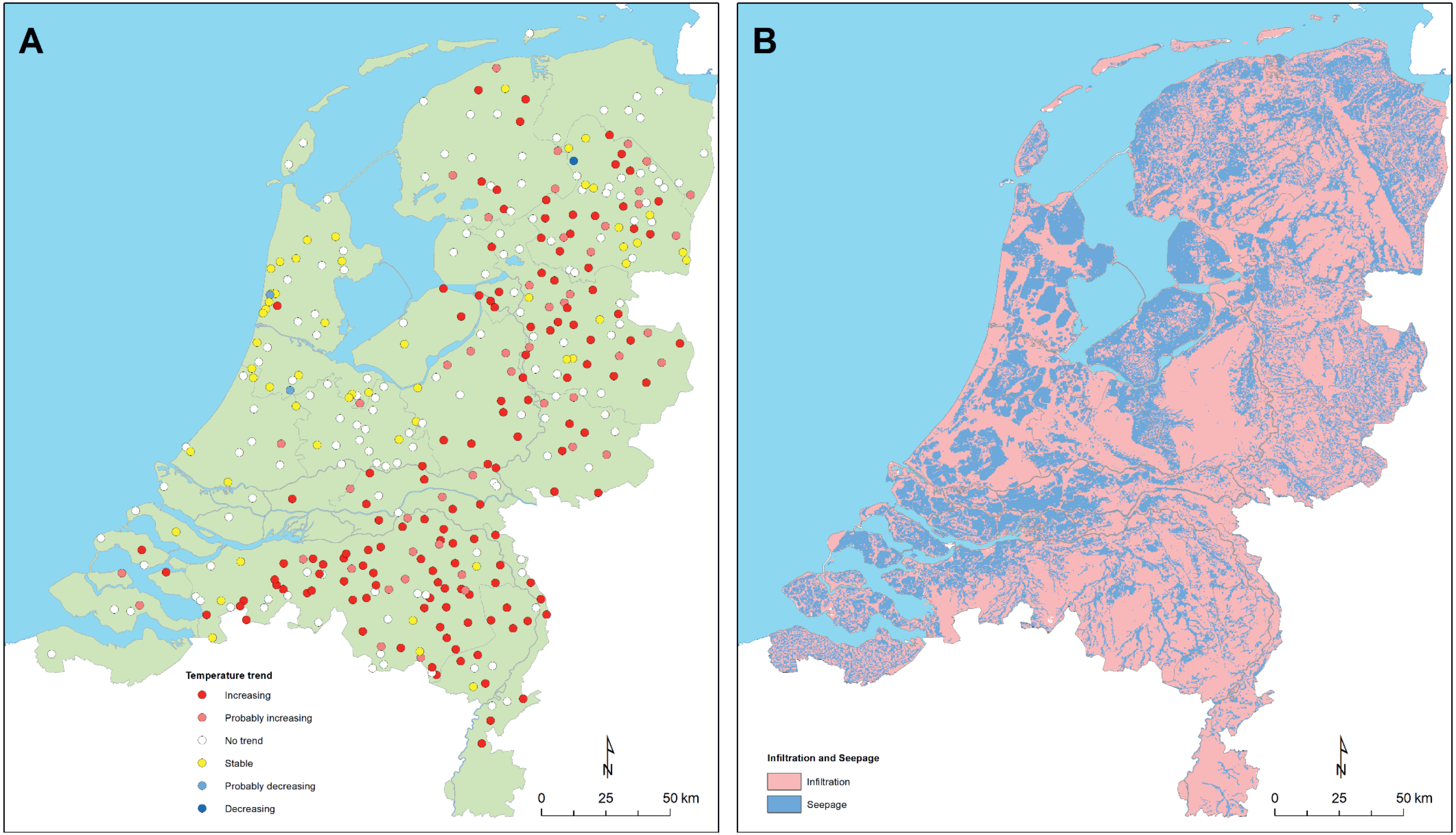

Figure 2.15: A: T20-35 trends, B: infiltration and seepage, derived from the national groundwater model (LHM) (Stowa / NHI, 2023).

2.4 PSWF water temperatures and trends

2.4.1 Materials and methods

GWT data of the mixed raw water produced by public supply well fields (PSWFs) in the Netherlands are retrieved from the so-called KIDAP database (Mendizabal & Stuyfzand, 2009). The database contains data on the characteristics of all PSWFs (e.g. well screen depth, aquifer type, annual extraction rate), and the chemistry and temperature of the raw (untreated) groundwater, spanning a period from 1898 to 2002. For backgrounds and hydrochemical elaborations reference is made to Mendizabal et al. (2011). Temperature data of abstracted groundwater provides an extra source of information of GWT at various depths and from various types of aquifers. Trends in water temperatures are analyzed using the same Mann-Kendall trend analysis techniques as for groundwater samples (section 2.3.1).

2.4.2 Results and discussion

Produced water temperatures

Temperatures of abstracted groundwater at PSWFs are available for 1931-2002 (although 82% of the observations stems from 1981-2002), averaged values of which are depicted in Figure 2.16. The 94 phreatic groundwater PSWFs concentrate in the eastern half of the country and topographically higher parts of central Netherlands (Figure 2.16A), at average depths of approx. 27-80 m bgl. The average GWT per station varies between 8.8 and 13.5°C, with a median of 10.2°C. The temperatures and temperature range are very similar to the T20-35 in these parts of the country.

The 102 deeper (>80 m bgl), (semi) confined groundwater PSWFs (Figure 2.16B) are associated with higher GWT, ranging from 9.8°C to 17.9°C, with a median of 11.5°C. The two highest average temperatures of 16.3°C and 17.9°C are detected in the deepest well fields (275 to 300 m bgl), both situated in the R.V.G. All but one PSWFs with GWT>13°C are situated in the R.V.G. and are relatively deep (130-300 m bgl), tapping the Kiezeloöliet Formation (unit f of cross section C-D in Figure 1.5). The depth explains the high GWT.

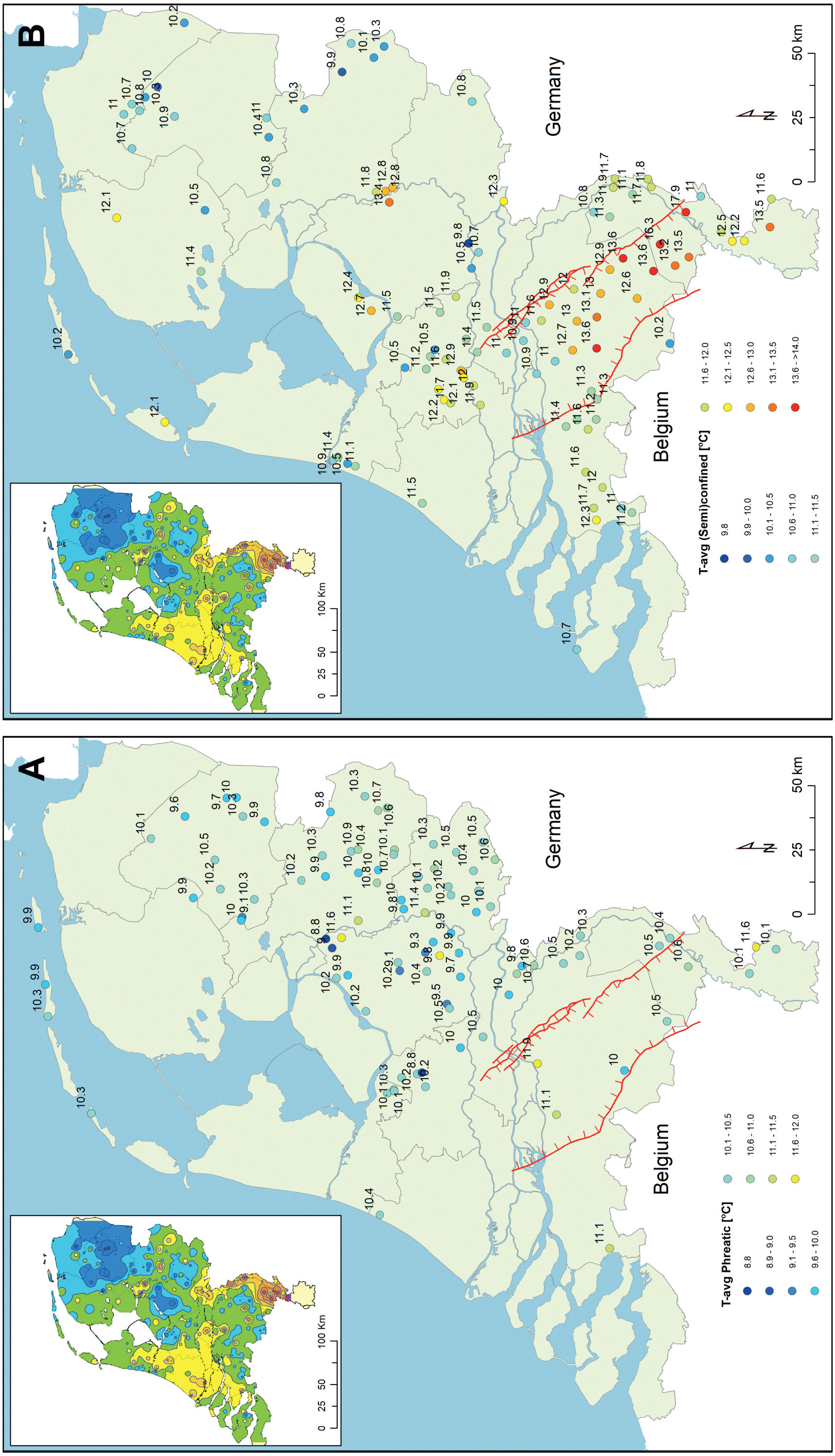

Figure 2.16: A: average temperatures of abstracted phreatic (~27-80 m bgl) groundwater at PSWFs (1931-2002), B: average temperatures of abstracted semi-confined (~80-140 m bgl) groundwater at PSWFs (1931-2002). Inset maps: T20-35 distribution (Figure 2.13).

The 14 PSWFs that abstract riverbank filtrate (RBF) are shown in Figure 2.17. These PSWFs are located along the lower branches of the rivers Rhine and Meuse. There are 3 PSWFs in the east with RBF temperatures between 10.7 and 11.6°C. This is well below the annual average river water temperature of the Rhine (Figure 2.7).

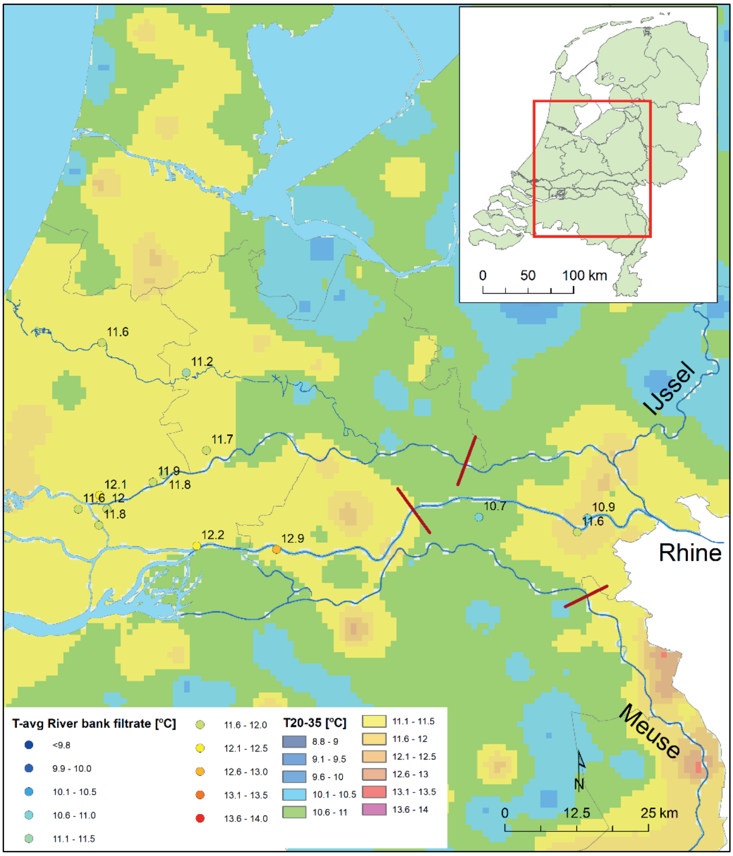

Figure 2.17: Average temperatures of abstracted riverbank filtrate at PSWFs. The red lines indicate the approximate location where the rivers change from gaining to losing river regimes.

The upper reaches of the rivers are (on the average) gaining streams. The lower reaches are losing streams. In the upper reaches, infiltration from the river only takes place during high water levels. The approximate location, based on isohypses of the upper aquifer derived from LHM (Stowa/NHI, 2023), where the river regime changes from generally gaining to losing is indicated in Figure 2.17 by a red line across the river. The RBF temperatures of the upstream PSWFs is similar to or even slightly lower than the interpolated T20-35 values at these locations and do not reflect the relatively high annual average river water temperatures of the Rhine. The percentage RBF in the produced water of these PSWFs is relatively low (29-66%), compared to the admixed autochthonous groundwater (Stuyfzand et al, 2006).

TD profiles measured at three locations along the upper branches of the Rhine are depicted in Figure 2.18. Locations of the TD profiles are shown in Figure 2.19. TD profile B40B0434 is logged in the floodplain of the river (between levee and winter dike), the other two beyond the winter dike. The average temperature at the three locations between 20 and 50 m bgl was 10.4, 10.9 and 11.9°C, well below the average annual river water temperature (Figure 2.7). A TD profile measured at B40B0434 in May 2011, approx. 4 months after high water levels and flooding of the flood plain in January 2011, shows the influence of infiltrating river water with low winter temperatures. Two other TD profiles measured at this location in the summer of 2010 and autumn of 2018 show that low winter infiltration temperatures are completely attenuated by then. No increase of the temperatures below the seasonal zone between October 2010 and September 2018 was observed. Infiltration with higher (summer) water temperatures is, therefore, unlikely to affect the GWT at these locations. Similar temperatures between 20 and 50 m bgl are observed at the other two locations along the river beyond the winter dike. The shape of TD profile B40B0420 shows signals of increasing GST, due to built-up environment, but apparently not as an effect of infiltrating warm river water.

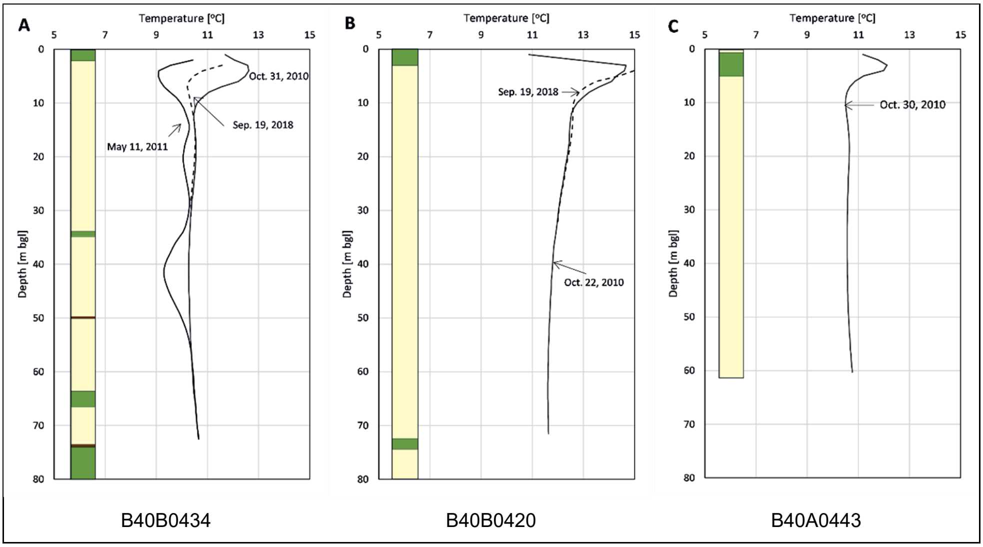

B40B0434 B40B0420 B40A0443

Figure 2.18: TD profiles at the river Rhine (Pannerdensch Kanaal and Neder-Rijn). (A): location in the floodplain ~1000 m from the river summer bed, (B) 350 m beyond the winter dike 1500 m from the river course, (C) beyond the winter dike 500 from the river. The columns on the left show the lithology of the borehole: yellow=sand; green=clay; dark brown=peat. Locations are shown in Figure 2.19B.

The majority of the RBF PSWFs is located farther downstream. These PSWFs abstract 18-100% RBF, with an average of 74% (Stuyfzand et al., 2006), and temperatures of 11.2°C to 12.9°C (11.8°C median). The rivers at the downstream PSWFs are mainly infiltrating (losing streams). The RBF temperatures are higher than the interpolated observed T20-35 along the rivers. This indicates that RBF temperatures of the downstream PSWFs are affected by the relatively high river water temperatures.

It is concluded that along the upper reaches of the major rivers, the GWT and T20-35 is only temporarily influenced by river water temperatures during high river water levels. In the lower reaches of the rivers, where year-round infiltration dominates, higher river water temperatures are reflected in higher RBF temperatures of the PSWFs. The lateral extent of this influence cannot be established from the T20-35 data as observation wells used are located too far from the river (>1 km).

Temperature trends of water from PSWFs

Temperature data from 449 PSWFs were extracted from the KIDAP database. Of these, 263 PSWFs have time series of abstracted water temperatures that are long enough to be analyzed by trend analysis. A statistically significant trend is found for 173 locations. Only one time-series is available for artificially infiltrated water in the coastal dunes, and is omitted in the results of Table 2.5.

Table 2.5 shows that most of the riverbank filtrate (category U) and abstracted surface water (category O) are subjected to (probably) increasing temperatures. A smaller fraction has stable temperatures, but no (probably) decreasing trend is seen. This reflects the increasing river water temperatures (Figure 2.7).

Table 2.5: Trends in drinking water abstraction temperatures (1931-2002). n=no. of time series, excluding the time series with no trend.

Type	Source	Avg.depth [m bgl]	Age [years]	n	Increasing	Probably increasing	Stable	Probably decreasing	Decreasing
A	Phreatic	40-80	2-200	61	30%	18%	36%	8%	8%
B	(Semi) confined	80-140	20-25.000	71	27%	11%	48%	6%	8%
K	Limestone	100-150	2-200	14	21%	0%	43%	21%	14%
O	Surface water	0	0-1	6	33%	33%	33%	0%	0%
U	Riverbank filtrate	30-70	1-50	5	40%	40%	20%	0%	0%

The largest percentage of the abstracted phreatic groundwater (category A) temperatures is also (probably) increasing. The fraction stable temperatures almost equals the percentage of (probably) increasing temperatures. Deeper (semi) confined (category B) abstracted groundwater shows somewhat lower percentages of (probably) increasing temperatures and a larger fraction of stable temperatures. (Probably) decreasing trends form a minor fraction for both types of groundwater abstraction. The effect of increasing GSTs on GWT is delayed and attenuated with depth. The shallower and younger groundwater is more influenced by recent GST increase, and the deeper, older groundwater is less affected. However, for both categories, an increasing trend in temperatures is evident for many locations (38-48%).

The majority of the temperatures of groundwater produced from limestone aquifers (category K, pink area in Figure 1.4), is stable. However, for this category, a significant portion shows (probably) decreasing temperatures and a smaller portion increasing temperatures. Most of these well fields were relatively shallow (~15-25 m). In recent decades, some, but not all, of the well fields were adapted by utilizing or drilling deeper wells. Deeper wells (if not too deep, to approx. 50 m bgl) could tap cooler water that is less influenced by recent GST increase. However, this does not explain all decreasing trends.

2.5 Interpretation of TD profiles

2.5.1 Materials and methods

Field measurements

In the 1970’s and 1980’s, TD logs were collected by Van Dalfsen, using a platinum resistor (100Ω) thermometer, mounted at the lower end of a probe, connected to a (>500 m long) cable. Various TNO (National Geological Survey)-produced probes were used in this period. Calibration showed a precision of ~10^{-2} ºC. The calibrated correction factor per probe was applied on the measured values. Instrumental drift was checked by repeatedly measuring temperatures in the same deep, undisturbed well.

A total of 24 logs was selected from TD profiles measured by the author between 2009 and 2012 as part of the present research (Figure 2.19). These logs have a measurement interval of 1 m, and temperatures were measured in a similar way as those by Van Dalfsen. The logging instrument, manufactured at the VU University Amsterdam, consists of a thermistor sensor (type DC95) mounted on a small-diameter probe equipped with spacers and attached to a microprocessor, logger and power source by an electric wire. The relative accuracy of the thermistor is ~10^{-2} °C. Comparison with a calibrated thermometer showed the thermistor had an absolute error of -0.16ºC (temperature too low) for temperatures in the range 4ºC to 31.5ºC. The field measurements were corrected for this error. The repeatability (precision) of the temperature measurements for ‘undisturbed’ wells was about 10^{-2} ˚C. Hence instrumental drift was negligible.

In 2018, additional data were collected in collaboration with Wageningen University & Research, using a RBR soloT instrument, calibrated to an accuracy of $2 \cdot 10^{-3}$ ºC, with a temperature resolution of <5.10^{-4} ºC and a time constant of 1s (www.rbr-global.com).

Numerical interpretation of TD profiles

TD profiles (Figure 2.19) were interpreted using a numerical 1D model. The model concept and process is schematically depicted in Figure 2.20. The scriptable finite-element code FlexPDE (www.PDESolutions.com) was used to solve the equations for conductive heat flow and groundwater advective heat flow. Forward modeling allowed to analyze drivers and magnitude of the evolving subsurface temperatures.

The model domain encompasses the upper 200 to 250 m of the subsurface. The hydrogeological stratification is modeled by simplifying the geology into any combination of horizontal sand, clay, loam or peat layers. The litho-stratigraphy is derived from the geological bore logs of the observation wells, sometimes supplemented (for the deeper parts) by information from (hydro)geological models such as TNO Geological Survey of the Netherlands REGIS II V2.2 (available through www.dinoloket.nl).

The vertical groundwater flux through the model domain is simulated by imposing a fixed flux on the model. The initial fixed flux was derived from the (calibrated) national groundwater model LHN

(Stowa/NHI, 2023). Assuming a uniform vertical flux is an over-simplification of the normally decreasing gradient with depth. The model results obtained here made it clear that the initial fixed flux needed adjustments to account for this over-simplification.

At the bottom of the model, a Neumann-type boundary condition is imposed, representing an upward heat flow from deeper strata. This heat flow is constrained by fitting deeper, linear parts of the TD profiles with the model results.

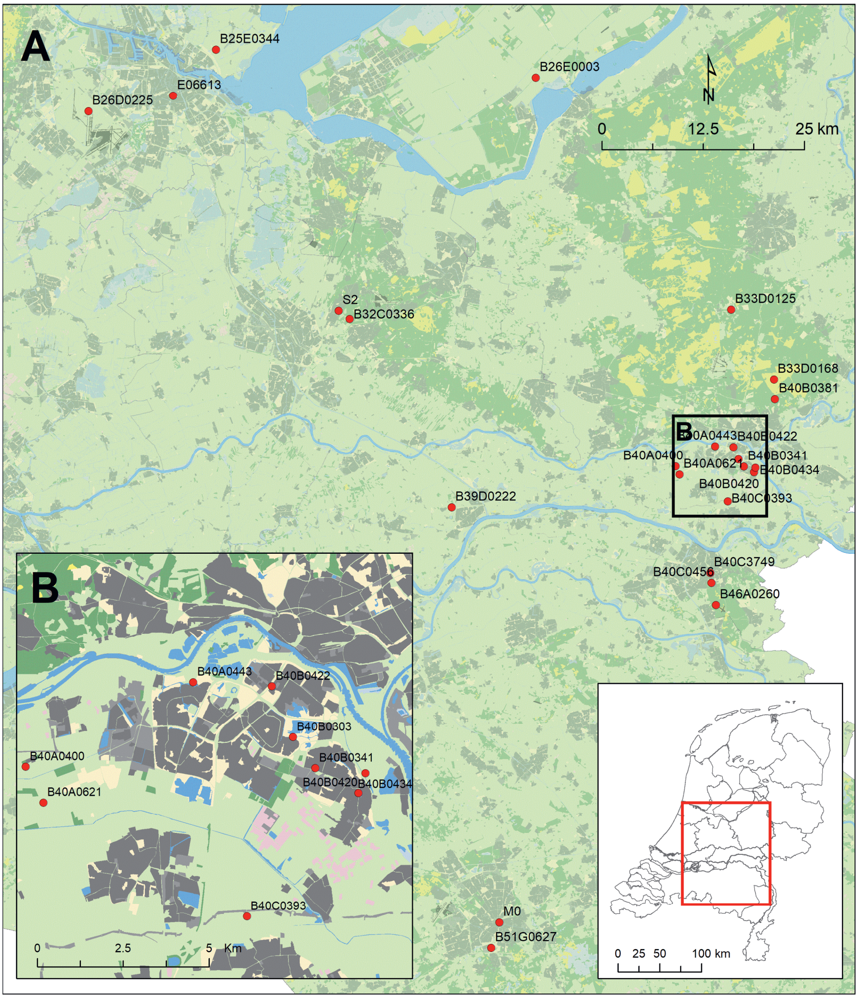

Figure 2.19: Selected TD profiling locations. Locator map shows the map extent (A) in the Netherlands. The black rectangle in the main map shows the extent of the detail map (B).

The temperature history for De Bilt from 1706 to the year of TD profiling was used as SAT (Figure 2.6). The use of this long SAT time series ascertains proper starting conditions of the model period of interest (approx. last century). The modeled heat flow is forced by the GST evolution at the top of the model. Average annual SAT data for De Bilt (central Netherlands, Figure 2.8) is considered to be representative for the country.

The GST usually tracks the SAT closely, but is offset, depending on land use and ground surface cover. This offset (GST-SAT) is derived by matching the field data with the simulated temperatures. Present and historical land cover data are used to assess the plausible offset ranges and temporal offset changes. The GST (as SAT plus offset) is imposed as a Dirichlet-type top boundary condition. The offset is changed interactively, until a good fit between measured and simulated temperatures is reached. The FlexPDE model solved the transient conduction-advection heat-flow equation in the Cartesian z-direction (depth). The form of Eq. (2.1) permits the use of vertical variations in k (Kooi, 2008):

$$c_b \rho_b \frac{\partial T}{\partial t} = \frac{\partial}{\partial z}\left(k \frac{\partial T}{\partial z}\right) - c_w \rho_w q_z \frac{\partial T}{\partial z} \tag{2.1}$$

where k =thermal conductivity [W.m^{-1}.K^{-1}], z=depth [m], T=temperature [°C], t=time [s], q_z=Darcy flux in vertical direction [m.s^{-1}], c_w and c_b=specific heat of resp. water and the bulk aquifer (solid and water) [J.kg^{-1}.K^{-1}], ρ_w and ρ_b=density of resp. water and bulk aquifer (solid and water) [kg.m^{-3}].

The bulk volumetric heat of the aquifer is defined as the weighted mean of the volumetric heat of water, $c_w\rho_w$, and the solid matrix, $c_s\rho_s$, with φ=total porosity:

$$c_b \rho_b = \varphi c_w \rho_w + (1 - \varphi) c_s \rho_s \tag{2.2}$$

Quartz is assumed to be the major solid constituent of the aquifers, with c_s=830 J.kg^{-1}.K^{-1}. The bulk density of water is taken to be 1,000 kg.m^{-3}. The bulk density of the aquifer is the weighted mean of the bulk density of water and quartz (2,650 kg.m^{-3}). This resulted in the initial model parameters used for the three types of lithologies shown in Table 2.6, which also shows the minimum and maximum k applied during the fitting process. The thermal properties of peat in the Holocene top layer are the averages of the values reported by Gnatowski (2016). Deeper peat occurrences were attributed clay properties.

Table 2.6: model parameters

Parameter:	φ [-]	$c_b\rho_b$ [MJ.m^{-3}.°C^{-1}]	k [W.m^{-1}.°C^{-1}]		
		Avg	Initial	Min	Max
Water (at 10°C)		4.2	0.58		
Sand (fine sand to gravel, saturated)	0.35	2.9	2.4	2.0	2.9
Sand (fine sand to gravel, 5% water)	0.35	1.4	0.5*		
Clay (clayey sand to clay, saturated)	0.50	3.1	1.4	1.2	1.8
Peat (at field capacity)	0.60	3.5	0.5	0.5	0.5
Limestone (chalk, low solidity, saturated)	0.54	3.1	1.2		
Limestone (high solidity)	0.00	2.4	3.0		

*: (Nikiforova et al., 2013)

An initial value of the vertical groundwater flux (q_z) is assumed to be equal to the net groundwater recharge or discharge. The groundwater recharge and discharge rates are available from various calibrated national and regional models (Stowa / NHI, 2023).

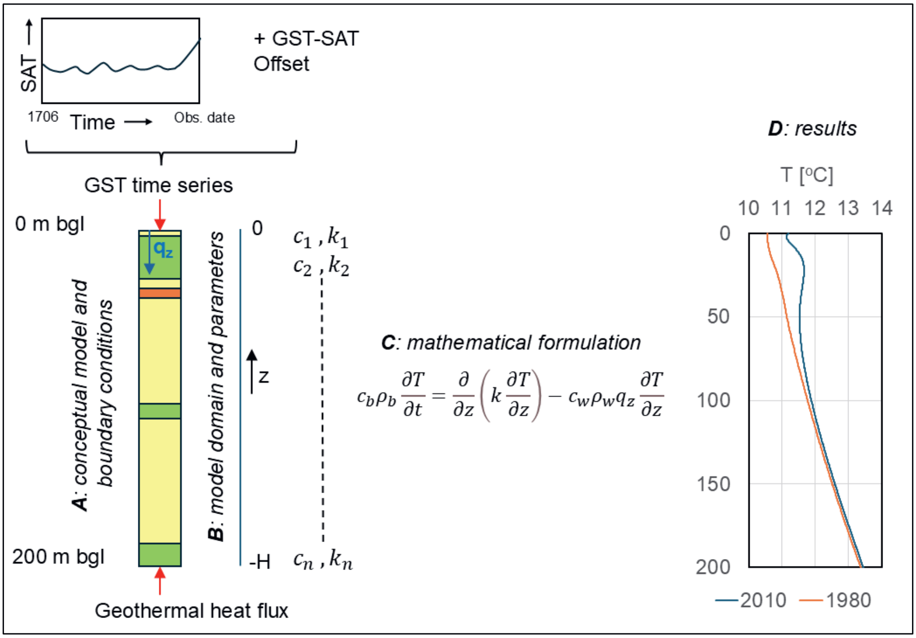

Figure 2.20: Schematic presentation of 1D modeling of TD profiles.

2.5.2 Results and discussion

Forward modeling, simulating observations of subsurface temperatures in (repeated) TD profiles, provides local evidence of changing subsurface temperatures and GST-SAT offsets. Some of the TD profile interpretations also reveal effects of other drivers, such as large-scale groundwater abstraction for drinking water production or ATES systems. Measured TD-profiles and modeled interpretations are shown in Figure 2.21 through Figure 2.24. Some of the model results of the fitted TD profiles are tabulated in Table 2.7.

The TD profiles under natural forest and heather vegetation show low GST-SAT offsets (Table 2.7A and Figure 2.21). These offsets are negative. The low offsets of natural vegetation locations are in part explained by the fact that the offset is modeled for SAT at meteorological station De Bilt, which may not be the same as the local SAT. De Bilt is representative for B32C0336. However, the other locations are farther away from De Bilt, and meteorological station Deelen is more representative for these locations. The 1980-2010 average annual SAT for De Bilt and Deelen are 10.1 and 9.7. The 2010-2011 GST-SAT offsets that are compensated for these SAT differences are still negative (included in Table 2.7 with an asterix suffix).

The locations with a grass cover (Table 2.7B and Figure 2.22) show slightly positive GST-SAT offsets. Offsets of two grass covered locations where repeated TD profiling was done show an increase in time. The TD profiles collected in urban environments (Table 2.7C and Figure 2.23) reveal the highest GST-SAT offsets.

The GST-SAT offsets derived for the 6 TD profiles that are perturbed by large-scale groundwater abstraction (Table 2.7D and Figure 2.24) or nearby ATES systems (Table 2.7E and Figure 2.24), confirm the pattern of low offsets near or under trees and somewhat higher offsets for grass covered surfaces. The TD profile taken at the only completely paved location (M0) could not be fitted, due to the large temperature anomaly caused by a nearby ATES system.

TD profile at location B40B0303 is near PSWF Ir. Sijmons in Arnhem. Groundwater is abstracted here since 1980. This is reflected in the TD profile measured by Van Dalfsen in 1980, not showing perturbation (van Dalfsen, 1981) (Figure 2.24). TD profiles measured in 2010 and 2018 show clear perturbations at the level of the abstraction wells screened sections. The modeled TD profiles show the extrapolation of the subsurface temperatures to these dates when no increased vertical and horizontal groundwater flow would have occurred. Below the screened depth, the temperatures have increased more than would be expected. This is due to the seepage of deeper water (“thermal upconing”). On the other hand, temperatures at the screened depth, are lower than expected, due to the onflow of relatively cold water from topographically high Veluwe, north of the location. The TD profiles logged at B40A0400 and B39D0222 only show slight perturbations of the temperatures around the screened depth. Groundwater is being abstracted at these locations since respectively 1961 and 1970, but at various depths and rates. At location B39D0222, water was originally abstracted from a shallow depth (~10 m). More recently, only deeper aquifers are being exploited. These deep (>70 m), large-scale PSWFs have a limited impact on the T20-35.

Another type of perturbation is due to nearby ATES systems. This type is illustrated by TD profiles at locations B40C3749, B51G0696, and M0 (Figure 2.24). Near these locations, ATES systems are operational since respectively 2010, 2005, and 1993. The ATES system near M0 is a high-temperature storage system, operating with injection temperatures up to 30°C. The perturbations by the ATES systems are causing large deviations from the modeled TD profiles, which are based on fitting the pre-operational temperatures. For M0, only one TD profile is available, but the ambient subsurface temperature was reported to range between 12 and 14°C to a depth of 85 m bgl. It is obvious that at these locations the T20-35 is perturbed by several °C to even more than 10°C.

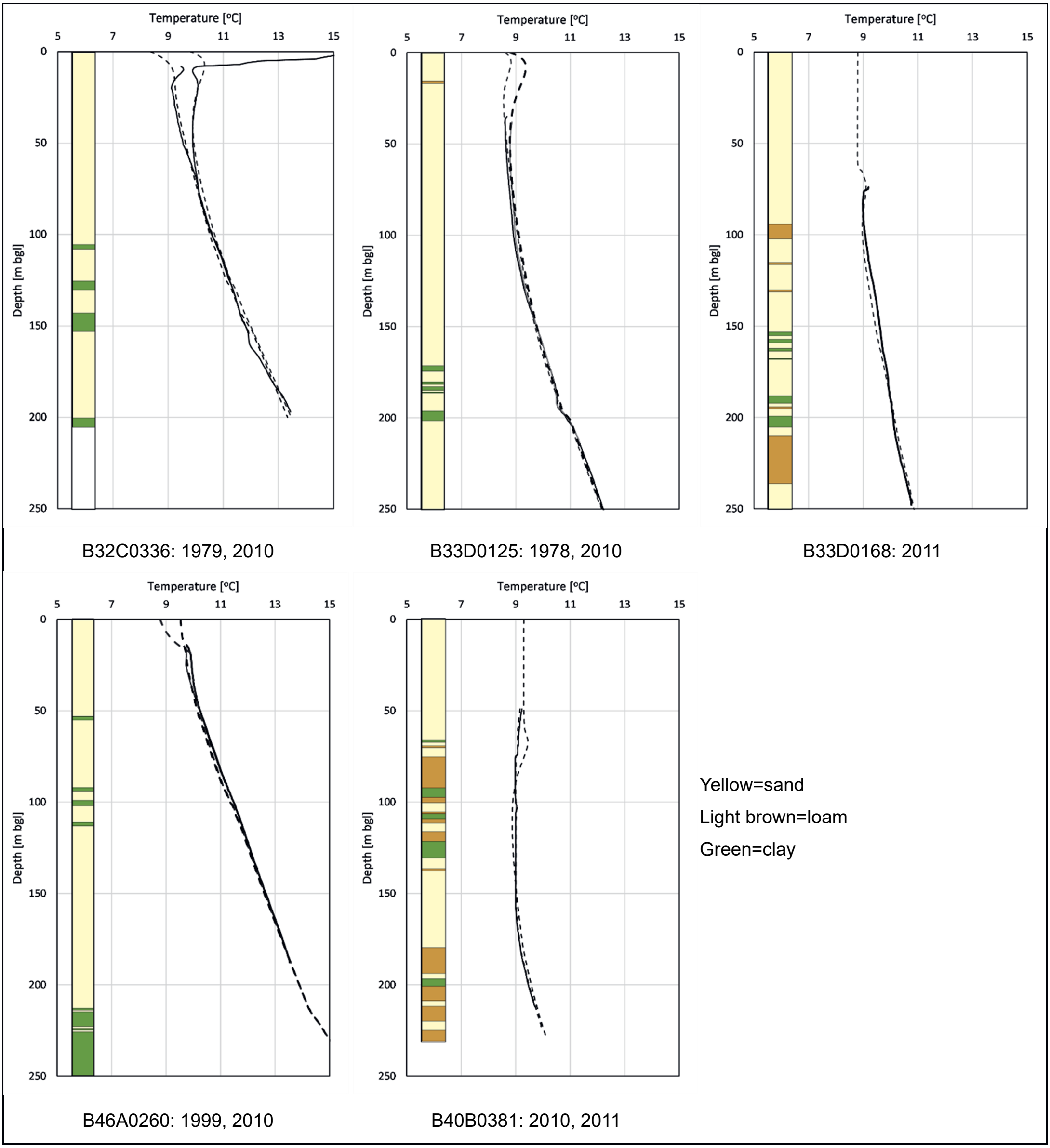

B32C0336: 1979, 2010

B33D0125: 1978, 2010

B33D0168: 2011

B46A0260: 1999, 2010

B40B0381: 2010, 2011

Figure 2.21: Measured TD profiles (solid lines) in areas with forest and natural vegetation, and synthesized profiles (dashed) in different years.

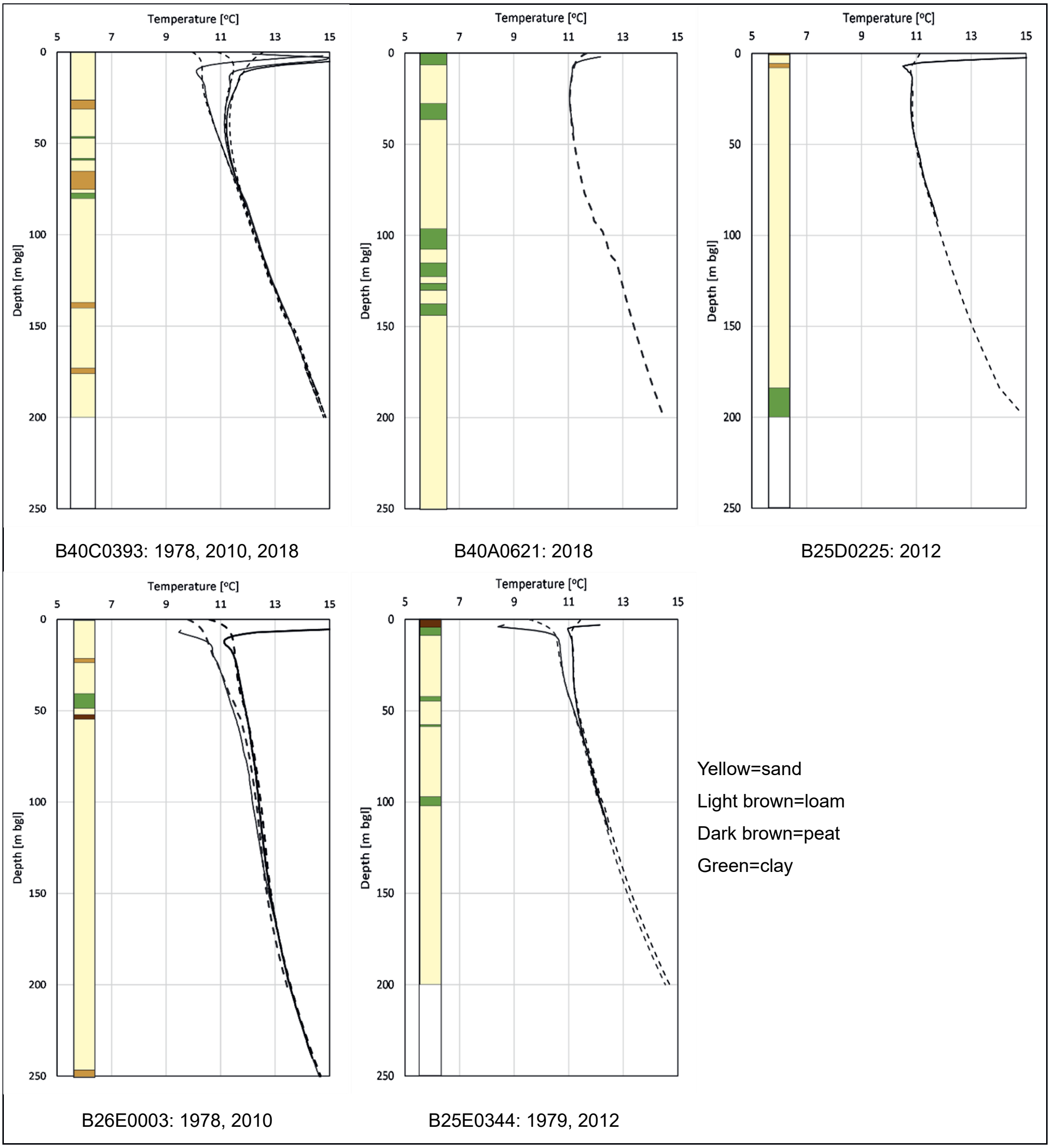

B40C0393: 1978, 2010, 2018

B40A0621: 2018

B25D0225: 2012

B26E0003: 1978, 2010

B25E0344: 1979, 2012

Yellow=sand

Light brown=loam

Dark brown=peat

Green=clay

Figure 2.22: Measured TD profiles (solid lines) in grass covered area and synthesized profiles (dashed) in different years.

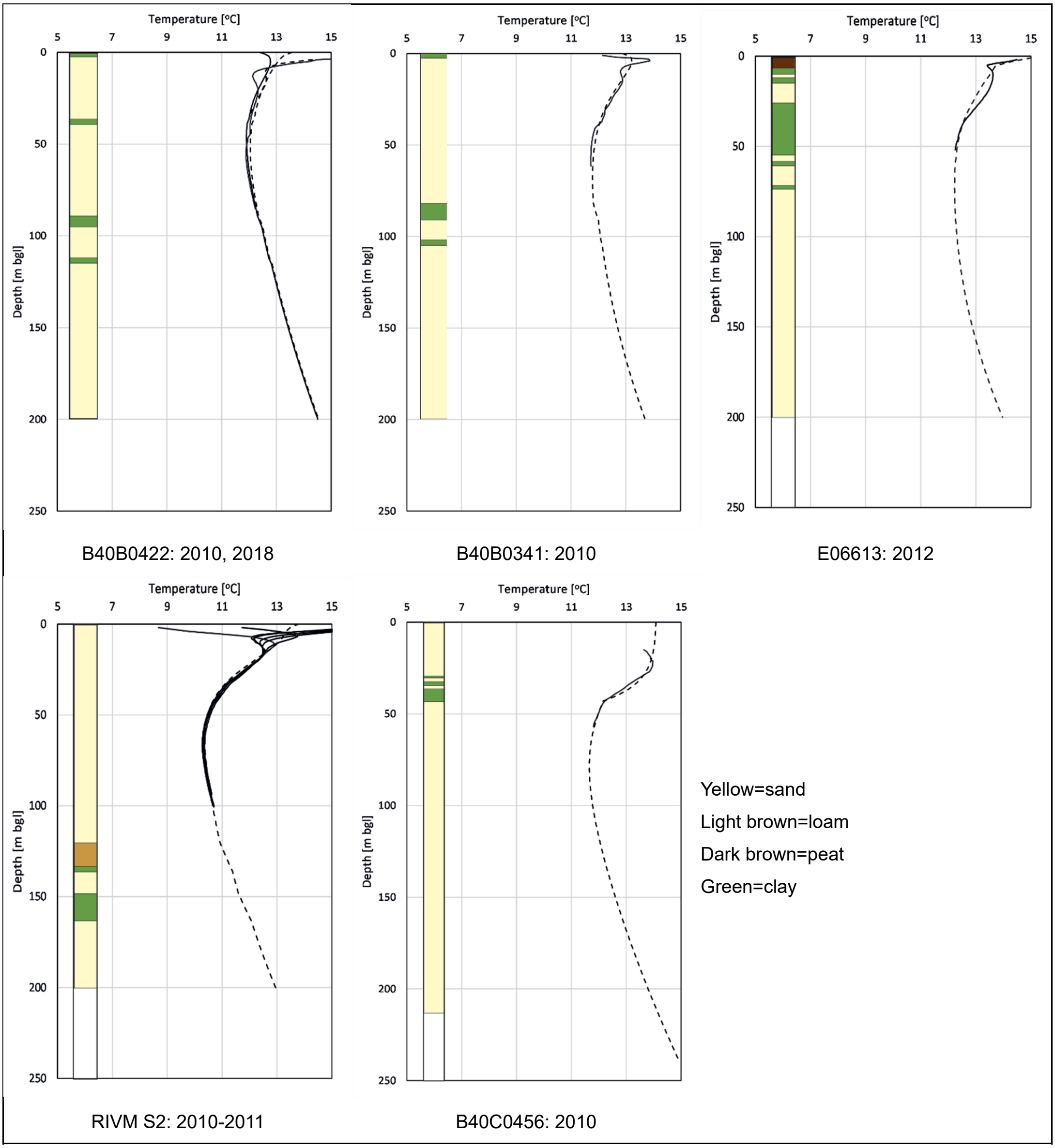

B40B0422: 2010, 2018

B40B0341: 2010

E06613: 2012

RIVM S2: 2010-2011

B40C0456: 2010

Figure 2.23: Measured TD profiles (solid lines) on urban locations and synthesized profiles (dashed) in different years.

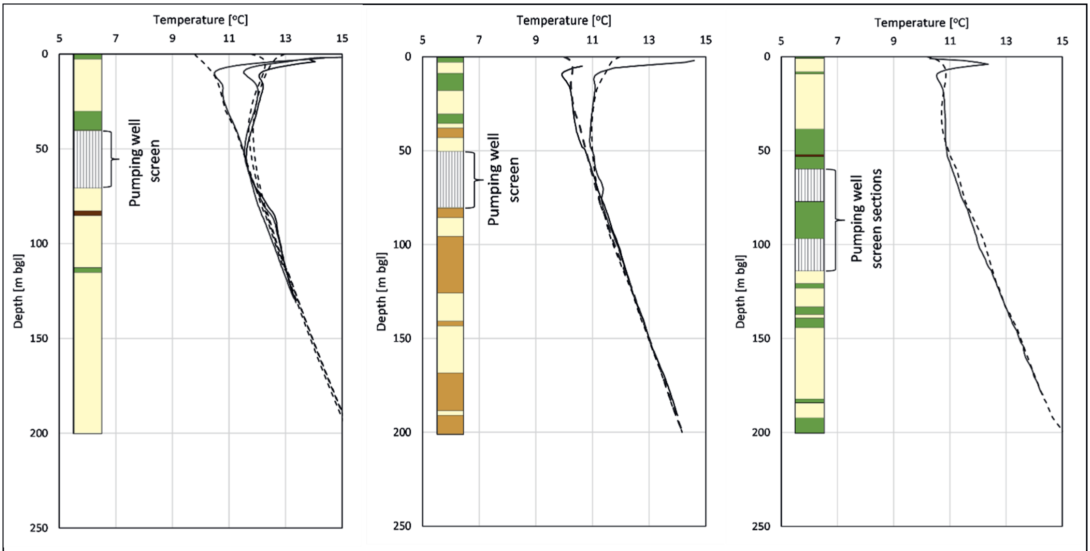

B40B0303: 1980, 2010, 2018

B40A0400: 1981, 2018

B39D0222: 2010

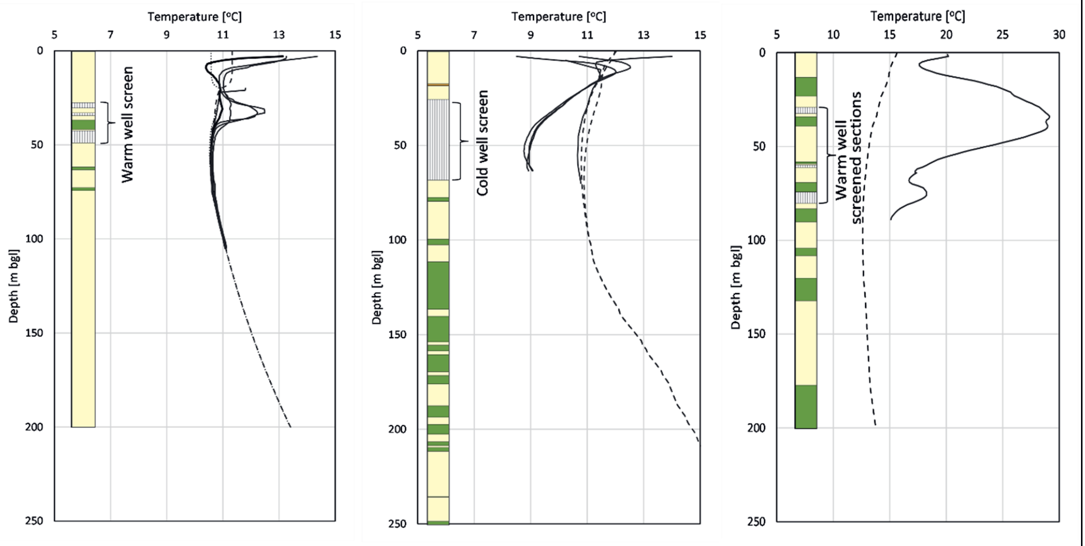

B40C3749: 2010, 2011, 2012

B51G0696: 2003, 2010, 2012

M0 Heuvel Galerie: 2012

Figure 2.24: Measured perturbed TD profiles (solid lines) and synthesized profiles (dashed) in different years. The columns on the left represent the lithology (yellow: sand; light-brown: loam; green: clay; dark-brown: peat).The hatching indicates the screened sections of the groundwater abstraction and ATES wells.

*Table 2.7: TD profile characteristics. The GST-SAT offsets with * suffix are compensated for inter-station differences in SAT.*

Location	Borehole	Land cover	GST-SAT [°C]				
			1978-1980	1999	2006	2010-2011	2018
A: topographically high terrain with natural vegetation							
Bilthoven	B32C0336	Forest (pine)	-0.4			-0.4 -0.4	
Hoenderloo	B33D0125	<1950: Forest (pine); >1950 Grass	-0.8			-0.8 -0.4*	
Brandtoren	B33D0168	Dense heather vegetation				-1.1 -0.7*	
Malden	B46A0260	Forest (pine)		-1.1		-1.1 -0.7*	
Rozendaal	B40B0381	Forest (pine)				-0.6 -0.2*	
B: topographically low terrain with grass vegetation							
Bemmel	B40C0393	Grass	0.6			1.0	1.5
Schiphol	B25D0225	Grass / Farm yard				0.5	
Zunderdorp	B25E0344	Grass / Farm yard	0.8			0.8	
Betuwe	B40A0621	Grass				0.6	
Flevoland	B26E0003	Grass	0.4			0.7	
C: urban							
Arnhem	B40B0422	Urban				2.5	2.5
Huissen	B40B0341	Urban				2.8	
Nijmegen	B40C0456	<1960 Grass; >1960: Built up				4.2	
Bilthoven	RIVM-S2	<1990: Grass; >1990: Parking				3.9	
Amsterdam	E06613	<1880 Grass; >1880: Built up				4.7	
D: perturbations due to drinking water abstraction							
Ir. Sijmons	B40B0303	Grass				1.9	
Fikkersdries	B40A0400	Grass				0.9	
Kerk-Avezaath	B39D0222	Grass and trees				0.3	
E: perturbations due to ATES							
Radboud	B40C3749	Parking lot, deciduous trees				0.7	
PHTC	B51G0696	Road side, grass				1.4	
Heuvel Galerie	M0	Parking lot, paved.				No fit	

2.6 Numerical modeling of the effect of shallow limestone occurrence

The thermal high in the southeast could be associated with the major faulting (some of the major faults are shown in Figure 1.4) and the vertical displacement of pre-Pleistocene formations in the Cenozoic Roer Valley Graben (R.V.G.), and adjoining Campine (C.B.) and Peel (P.B.) blocks. Luijendijk et al. (2010) found a local thermal anomaly of >10°C in 1000-1500 m deep wells in the north-western part of the rift basin. The most likely cause was the upward flow of water along faults.

Isotherm maps of the deeper subsurface (200 m bgl and more) by Gies et al. (2021) do not show a thermal anomaly in the high T20-35 region. This may be due to the temperature interval used, obscuring more subtle differences. Records of geothermal heat flow are made available by the Global

Heat Flow Data Assessment Group (Fuchs et al., 2023). In the southeast of the country, these data are scarce, but show a relatively low heat flow (in the range of 50-60 $mW.m^{-2}$), compared to data points north of the anomalous area (75-100 $mW.m^{-2}$). Heat flow data from the German part of the Rhine Valley Graben fall in the same low range. A locally higher geothermal heat flow does not explain the high T20-35.

Although hydrothermal convection and seepage of groundwater from deep formations along fault planes (e.g. Bense, 2004; Bense & Kooi, 2004; Luijendijk et al., 2010; Bonte et al., 2013), or in karstified carboniferous limestones (Bonté, 2012) may play a role, this is unlikely to explain the regionally high GWT at shallow depths. Most high T20-35 are concentrated in the RVG. Hydraulic heads of the deep aquifers (>160 m below ground level) in the RVG dropped since the 1970's by several meters, due to deep open-cast brown-coal mining in Germany (Dufour, 1998). This has reduced seepage from deep aquifers in the RVG. Deep seepage, therefore, is less likely to have caused the regionally occurring high T20-35 values measured between 1991 and 2011.

Effects of different thermal properties of deep seated, older formations cannot be excluded beforehand. Carboniferous rocks, belonging to the Dinantian Zeeland Formation (Table 1.1), occur at a relatively shallow depth in parts of the thermally anomalous area (Figure 2.25). The Zeeland Formation comprises limestones (comparable to the Carboniferous Limestone Supergroup in the UK). The effect of various depths to the limestone and various thermal characteristics of the rock has been modeled.

2.6.1 Materials and methods

Medium to high solidity (one minus fractional porosity) limestones have a lower to slightly higher thermal conductivity than that of water saturated sand of the aquifers (Robertson, 1988); approx. 1.2 $W.m^{-1}.^{o}C^{-1}$ at a solidity of 0.46 to approx. 3.0 $W.m^{-1}.^{o}C^{-1}$ at a solidity of 1.0. The specific heat capacity of limestones varies between 680 and 880 $KJ.m^{-3}.^{o}C^{-1}$ (Clauser, 2011). Not-karstified massive limestone with approx. zero porosity has a density of 2760 to 2770 $kg.m^{-3}$ (Clauser, 2011). Maastrichtian chalk that occurs in the subsurface in the southeast of the Netherlands (Figure 1.4), has a very high porosity 54% (Quist & Tolboom, 2017). The effect of various depths of limestone below strata with thermal capacities comparable to that of water saturated sands (Upper and Lower North Sea Groups), was investigated by forward modeling with a 2-layer version of the 1D heat-transport model described in section 2.5.1. The model domain is extended to 2000 m bgl. Advection by groundwater flow is ignored in this model (set to zero). A constant heat flux of 60 $mW.m^{-2}$ (Fuchs et al., 2023) is imposed on the bottom boundary of the model, while temperature at the top of the model is fixed at $10^{o}C$. The model simulated a period of 10,000 years.

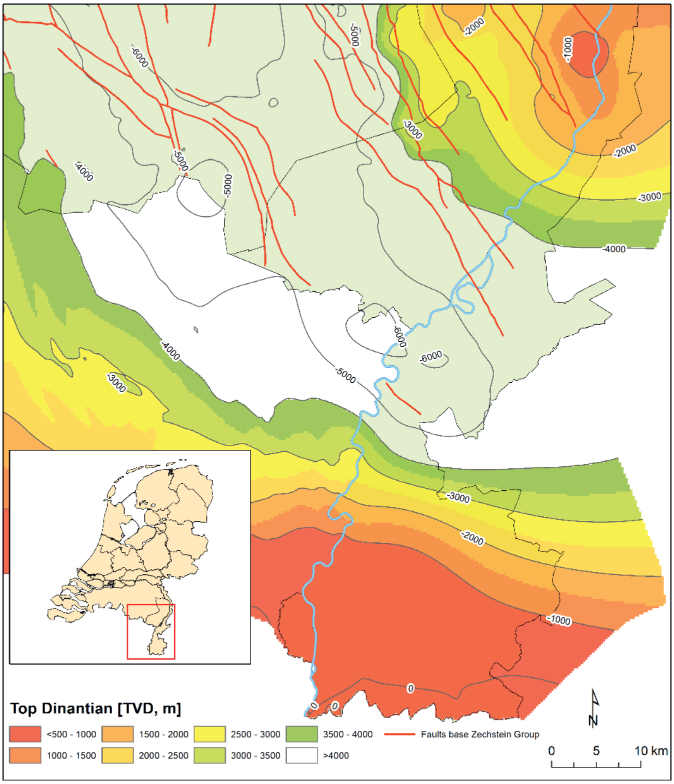

Figure 2.25: Top of the Dinantian in the southeast Netherlands, including the Carboniferous Limestone Group. Inset: locator map showing the map extent in the southeast of the Netherlands. Data source: NLOG, Nederlands Olie- en Gasportal (2023)

2.6.2 Results and discussion

The results (Figure 2.26A) show a temperature increase at 20 m depth (T20) and 100 m depth (T100) of respectively 0.13ºC and 0.66ºC with deceasing low solidity limestone depths. Decreasing depths of high thermal conductivity limestone (high solidity) results in T20 and T100 decrease with 0.04 and 0.22ºC. A shallow occurrence of low-conductivity rock in the thermally anomalous area could, therefore, explain a small contribution to the higher T20-35. A shallower position of high solidity limestone with a high thermal conductivity even results in a lower T20 and T100. Vertical flow of groundwater along fault planes remains a likely cause of local thermal anomalies (Bense & Kooi, 2004), but provides no satisfactory explanation for the high T20-35 values in larger stretches of the southeast of the study area.

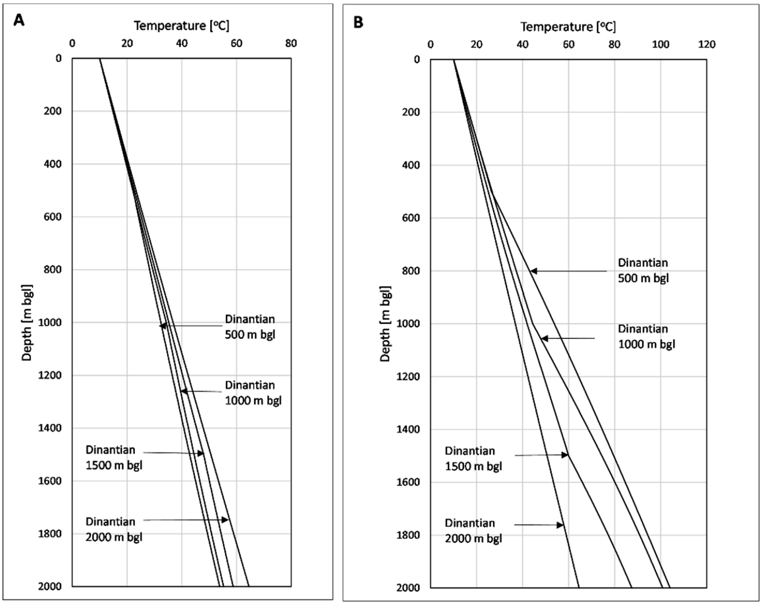

Figure 2.26: Simulated TD profiles for various depths to the Dinantian limestone. (A) and (B) with volumetric thermal capacities of the limestone of 1880 and 2430 KJ.m^{-3}.K^{-1}, respectively. The thermal conductivity of the limestone = 3.0 W.m^{-1}.°C^{-1} for (A) and 1.4 W.m^{-1}.°C^{-1} for (B).

2.7 GST-SAT offsets from field data and SARB modelling

A surface-atmosphere radiation-balance (SARB) model is used to simulate the GST-SAT offsets for various types of land cover and geographical locations.

2.7.1 Materials and methods

Following international standards, surface air temperature (SAT) is measured at Netherlands meteorological stations at 1.5 m above an open grass field (KNMI, 2000). Ground surface temperature (GST) is measured at four meteorological stations at 5 cm below the surface (Figure 2.8). The ground surface temperature (GST) and surface air temperature (SAT) offset, ΔT(GST–SAT), is defined as the difference between the temperature measured at the depth of 2 to 5 cm below the surface and the air temperature measured at 1.5 m above the surface (e.g. Lembrechts, et al., 2021).

Global maps of soil temperature (0-5 cm depth) were published by Lembrechts et al. (2021) at a 30 arc-second scale (~1 km^2). The maps were produced, using the offset between in situ soil temperature measurements and coarse-grained 1981-2020 air temperature estimates from ERA5-Land (https://Climate.Copernicus.eu). These maps provide insight in the global variations and dynamics of soil temperature but turn out to be less useful for the analysis of the spatial patterns of T20-35 in the Netherlands. The annually averaged GST range provided for the Netherlands is 7.8-10.7°C, which is well below the average SAT (Figure 2.6), whilst positive GST-SAT offset values are expected for the majority of the Netherlands' land surface. The effects of urban heat islands are also not reflected in these maps. For these reasons, the global maps were not used, and the following approach was applied to analyze the GST, GST-SAT offsets and regional patterns.

Grass GST observations

On a national scale, grassland (meadows) is the most important land cover. The landcover of meteorological stations is grass with a canopy height of 4 to 10 cm (KNMI, 2000). At four meteorological stations, hourly SAT data and 6-hourly GST data are collected since 1981 (De Bilt) and 1990 (Wilhelminadorp, Marknesse, Nieuw-Beerta) (Figure 2.8). These data are available through the data dissemination site of the Royal Netherlands Meteorological Institute (KNMI, 2023a). Daily averages of GST and SAT were calculated and were used to derive daily and annual averages of GST and GST-SAT offsets for grass covered surfaces.

Natural terrain GST observations

Near Castricum (Figure 2.8), at the west coast of the Netherlands, four lysimeters were operational from 1940 till 1999. The lysimeters are situated approximately 2.100 meters from the North Sea coast on calcareous dunes (Stuyfzand, 1987). One lysimeter (no.1) was left barren (dune sand). The other lysimeters are located in areas covered with dune vegetation (shrubs) (no.2), deciduous forest (oaks) (no.3) and coniferous forest (black pines) (no.4). At these four locations, subsurface temperatures have been measured thrice daily between 1941 and 1961 at depths of 0 (say: 0-5), 10, 25, 50 and 100 cm. Van der Hoeve (2011) summarized these, and the air temperature data into half-yearly (“summer”, May-October, and “winter”, November-April) averages.

Surface-atmosphere radiation balance (SARB) modelling of the GST

Field data, such as described in the previous sections, are representative for specific locations and periods of time. Climatological and surface conditions show spatiotemporal variations. These variable conditions do not only include SAT, but also incoming and outgoing radiation, wind, cloudiness, precipitation and evapotranspiration. These parameters determine the radiation balance and temperature of the ground surface. It should, therefore, be anticipated that the radiation balance and GST also show spatiotemporal variations. This aspect is investigated by applying a surface-atmosphere radiation-balance (SARB) model for five locations in different parts of the country and three types of land cover: an asphalt paved surface, grassland and forest. The respective sites are the meteorological stations Eelde, Den Helder, De Bilt, Vlissingen and Maastricht (Figure 2.8).

The applied radiation balance model is described in detail in Chapter 3 (Appendix 3.2). The model concept and process is schematically depicted in Figure 2.27. Hourly meteorological data from 1965 to 2021 of the five meteorological stations are used as input for this radiation balance model. For asphalt pavement, the model described in Chapter 3 is left unchanged with the appropriate parameters for this surface.

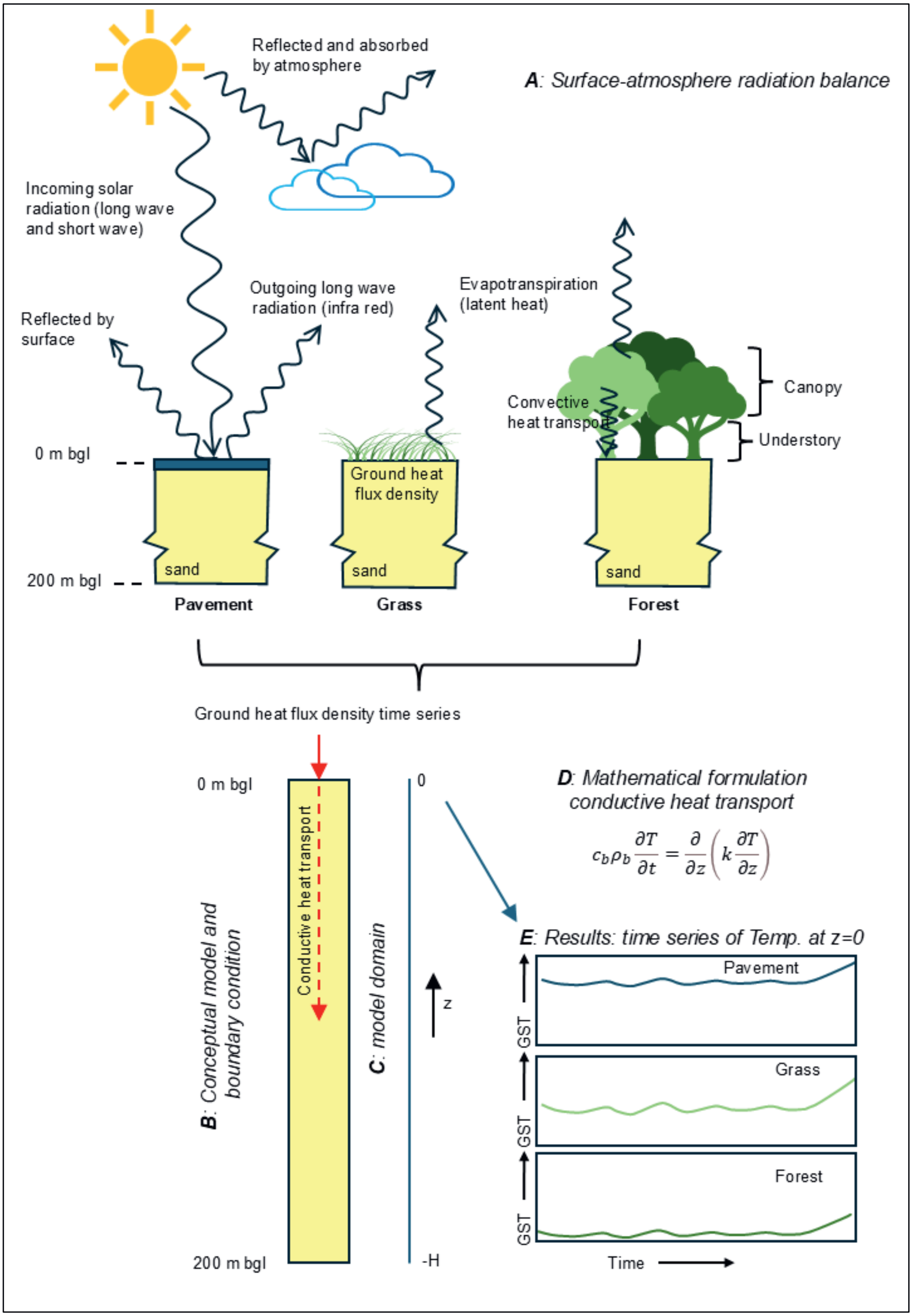

Figure 2.27: Schematic presentation of the SARB model.

For vegetated surfaces, the model is elaborated as follows. For grass surface, an extra (canopy) layer is added to the top of the model domain. The following parameters are applied to the canopy layer. The albedo was lowered to 0.23 as reported by Bosveld et al. (2020). The roughness length for momentum was reported to be 0.01 m by Duynkerke (1991). However, later studies such as by Verkaik (2006) and Sterl (2018) suggest a higher roughness length on the basis of which 0.03 m is chosen. The leaf area index (LAI) for grass is 0.58 (Duynkerke, 1991), with a vegetation height of 0.05 m and an estimated volume fraction of vegetation of 0.006. The volumetric heat capacity of the grass is estimated 0.5 MJ.m^{-3}.K^{-1}, based on a density of the biomass of 440 kg.m^{-3} and a specific heat capacity of 1200 J.kg^{-1}.K^{-1} (Jayalakshmy & Philip, 2010). The thermal capacity and conductivity of the canopy layer are the weighted averages of the thermal capacity and conductivity of grass and air.

Evaporation

A latent heat flux in the form of heat of evaporation from vegetation to air is added to the ground heat flux density calculation. The evaporation of a vegetated surface consists of transpiration by the plants, evaporation of the water intercepted by the vegetation canopy (interception evaporation) and evaporation from the ground surface (soil evaporation).

Potential evapotranspiration (Makkink), reported for the five meteorological stations on a daily basis, is used. The derivation of the parameters in the Makkink method implicitly integrates the interception evaporation (Massop et al., 2005). The theoretical ‘crop factor’ (being the ratio between the actual evaporation and potential evaporation for a certain vegetation) for a well-watered grass, therefore, is 1.0. However, comparative studies of actual evaporation and Makkink potential evaporation show that for grass and trees the ‘crop factor’ is different for dry and wet canopy situations. In forests, interception evaporation can equal the transpiration (Droogers, 2009). For the Castricum lysimeters 2-4, transpiration and interception evaporation accounted for 75% or more of total evaporation (Stuyfzand & Rambags, 2011). Massop et al. (2005) quote measured annual average evaporation values in a dense Douglas fir forest of 317 mm.year^{-1} interception evaporation and 363 mm.year^{-1} transpiration. Dolman et al. (1996) found a much lower interception evaporation in back pine forest of 185 mm. year^{-1}. For agricultural crops and grass, an annual average interception evaporation of 100 mm is reported (Massop, et al., 2005).

Elbers et al. (2009) provide an overview of measured actual evaporation and Makkink potential evaporation for various types of vegetation at 12 locations in the Netherlands. The ‘crop factor’ for grass varied from approx. 0.7 to 1.0, the highest values occurring during wet periods and including interception evaporation. For coniferous forest (black pine), this factor varied between approx. 0.6 (dry situation) and 0.8 (wet situation, including interception evaporation). Deciduous forest (poplar) and mixed forest showed higher ‘crop factors’ between 0.8 and 1.0. Based on these data, a ‘crop factor’ of 0.8 was chosen in the radiation balance model for both grass and forest, being a reasonable average, including the interception evaporation.

Respiration and transpiration by grasses is strongly (exponentially) temperature dependent. At a soil temperature of approx. 5ºC, respiration is only a fraction of that at optimum temperatures (Joseph et al., 2014; Romero & Dukes, 2016; Göbel et al., 2019). Studies of grass respiration consider it to be negligible at temperatures below 5ºC. Assuming that the soil temperature under grass is approx. 0.5ºC higher than air temperature, transpiration of grass is negligible at air temperatures below 5.5ºC. Evapotranspiration requires energy from incoming radiation (Feldhake & Boyer, 1986). The fraction of the daily sum of (incoming) global radiation at hourly intervals at air temperatures of 5.5ºC or higher is multiplied with 80% of the daily potential evapotranspiration, to derive the hourly actual evapotranspiration. The heat of evaporation, as a function of the air temperature, is used to calculate the latent heat flux on an hourly basis. Between 5 and 50ºC, the heat of vaporization of water is linearly related to the SAT (Sato et al., 1991):

$$L = 1000 \times EV_{act} \times (2501.1 - 2.38 \times SAT) \tag{2.3}$$

with L=heat of vaporization in J.m^{-2}.h^{-1} and EV_{act}=actual evaporation in mm.h^{-1}.

A realistic modeling of the ground surface temperature of a forest is challenging and beyond the scope of this study, as a forest comprises various layers consisting of canopy and understories. Haesen et al. (2021) describe the tree canopy in forests as a thermal insulator that buffers sub-canopy microclimatic conditions. They conclude that across Europe the sub-canopy air temperatures are on average 2.1°C lower in summer and 2.0°C higher in winter than free-air temperatures. The heat balance of the canopy and understories depends on many factors, such as the tree species, height, etc. Therefore, a simplified approach (hence “forest” model) is followed by assuming a canopy height of 35 m, with an understory height of 10 m. These are added as extra layers to the top of the model domain. The canopy heat balance assumes evapotranspiration of 80% of the potential evapotranspiration (Elbers, et al., 2009) at air temperatures of 5ºC and higher. This is more applicable for coniferous forests than for deciduous forests, as the latter stop transpiring during the cold season, when the trees are leafless. Schilperoort et al. (2020) studied the thermal stratification and decoupling of a Douglas fir canopy and understories by high resolution DTS (distributed temperature sensing) vertical temperature profiles. They showed that most of the time, the atmosphere of the understory is stable and little, or no convection takes place. Therefore, two “forest” model approaches are followed in the present study. In the first approach, there is no vertical wind speed (convection) in the understory between the canopy and forest floor, simulating decoupled vegetation layers. In the second approach, the vertical wind speed in the understory is arbitrarily taken to be 10% of the reported wind speed for the station, allowing advective heat transport between the canopy and ground surface.

A fraction of soil moisture evaporates before being taken up by plant roots or infiltrates to depths below which no significant evaporation takes place (0.1 m in wet, low energy environment, (Sprenger et al., 2017) to ~0.5 m in sandy, arid environments (Oerter & Amundson, 2016)). In a dense Douglas fir forest, average annual soil evaporation of 32 mm.year^{-1} was found (Massop et al., 2005). For grass, the soil evaporation is 82 mm.year^{-1} (Boers & Noij (ed.), 1996).

During summer, evaporation is dominated by transpiration and interception evaporation, whilst during winter interception evaporation dominates. The model approach assumes the actual evaporation to be zero at SAT<5.5ºC. The average total potential evaporation at days with SAT<5.5ºC amounts to 8% of the total annual potential evaporation (meteorological station De Bilt, 1958-2023). This implies that the sum of interception evaporation and soil evaporation that is ignored by the model as a percentage of the total actual evaporation is in the order of 3% for grass, 4% for black pine forest and 6% for dense Douglas fir forest. This is assumed acceptable for the explorative modeling.

Precipitation

Precipitation influences soil temperature (GST) and the dynamics of the GST in several ways. Precipitation in the Netherlands is more or less evenly distributed between summer and winter seasons (Figure 2.5). Snowfall is relatively rare. At De Bilt 477 days with a snow cover of 1 cm or more occurred between 1965 and 2023 (average of 8 days per year). The last 30 years (1993-2023), this average decreased to 6 days per year. A snow cover increases the surface albedo to 0.9 for freshly fallen snow to 0.4 for old snow (Willeit & Ganopolski, 2018). Uniform temperatures throughout the snowpack at 0°C are most likely to exist during the ablation period and during periods of snowmelt (USACE, 2024). For days with a closed snow cover, the calculated GST was adjusted to 0°C.

In Japan, Fukuoka (1969) found the rainwater to be cooler than the ground surface, with temperature differences up to 4°C in January to 9°C in July. The difference decreases with the total monthly precipitation. Experimental data show that the precipitation temperature signal only influences shallow soil temperatures and rapidly weakens after two months (Song, et al., 2020). High frequency observations of GST, SAT and precipitation in Prague were analyzed by the Granger causality test (Cermak & Bodri, 2018). The analysis did not reveal any evidence of Granger causality for precipitation to GST-SAT offsets on a daily scale of aggregation, except for asphalt pavement. Strong evidence of causality was found on an hourly scale of aggregation for all land cover types except for the sand surface cover. The drivers of this causality, however, are only partly explained. The GST of grass decreased very strongly even before the onset of the rain. This is explained by the cloudiness associated with the rainfall events, decreasing incoming radiation. Evaporative heat loss for paved surfaces only exists when standing water is present (Herb, et al., 2018). Bakema et al. (2022) analyzed the dynamics and changes in soil temperatures at the four soil temperature monitoring sites (Figure 2.8). Global radiation did not explain the dynamics of soil temperature. Precipitation only explained a minor part of the dynamics. The uncertainty in rainwater temperatures, the lack of unambiguous evidence of GST and rainfall coupling and the fact that cloudiness associated with rainfall is already a part of the radiation balance model led to the choice to leave rainwater cooling of the surface (either by low rainwater temperatures or by evaporation from pavements) out of the calculations.

A third aspect related to rainfall is infiltration. E.g. Taniguchi et al. (1999) demonstrated that the vertical downward flux of groundwater conveys surface temperature signal to the subsurface by advection. In general, the more rainfall the higher infiltration rate can be expected. Except when the rainfall is discharged by surface runoff. It was tested here whether incorporating q_z of Eq. (2.1) would yield realistic GST values. q_z was taken to be the hourly amount of precipitation minus the calculated hourly actual evapo(transpi)ration when precipitation exceeds the actual evapo(transpi)ration. Otherwise, $q_z = 0$. For tarmac q_z is always zero. The results for the grass cover in De Bilt deviated strongly from actual measured GSTs (see following section 2.7.2), whilst model results with $q_z = 0$ provided a good match. Therefore, in further calculations q_z was set to zero.

2.7.2 Results and discussion

GST-SAT offset from field data

Data from the soil temperature observation stations with grass cover are listed in Table 2.8 and the observed GST time series are depicted in Figure 2.28. The impact of climate change on soil temperatures at the four stations has been analyzed by Bakema, et al. (2022). They concluded that the GST at these locations increased between 1.2 and 1.8ºC during the past 40 years.

Table 2.8: Average GST and GST-SAT offset at four soil temperature observation stations.

Station	Period	Avg. GST [ºC]	Avg. GST-SAT [ºC]
De Bilt (Center)	1981-1990, 1992-2023	11.3	0.84
Marknesse (NE, polder)	1990-2023	11.0	0.84
Wilhelminadorp (SW)	1990-1999, 2001-2013, 2018-2023	11.9	0.94
Nieuw-Beerta (NE, Uplands)	1990-1999, 2002-2023	10.8	0.96

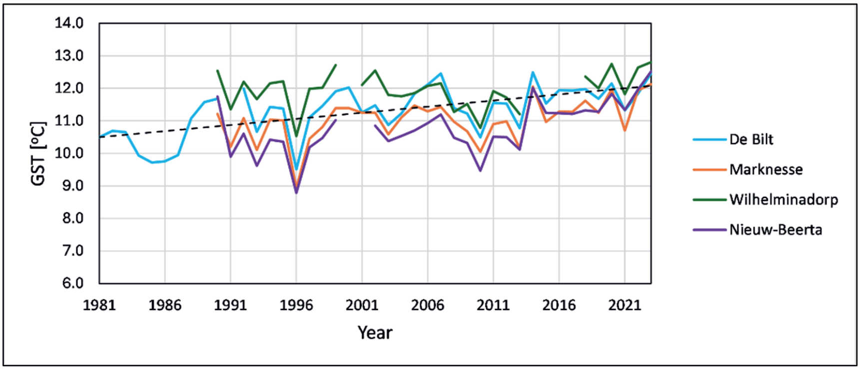

Figure 2.28: Ground surface temperatures at four meteorological stations. The dashed line is the linear trend line for the ground surface temperature at De Bilt.

The historic lysimeter data from Castricum provide GSTs for bare soil, shrub vegetation and deciduous and coniferous forests in various stages of development (newly planted to maturing). The GST-SAT offsets derived from these data are summarized in Table 2.9. Bare soil has the highest (annual) offset, while offsets of the vegetated surfaces is clearly related to the vegetation type and cover percentage. Compared to other land covers, forest has a significant effect on the GST and, therefore, subsurface temperatures. The GST-SAT differences are expressed clearly, although more subdued, in temperature differences of the drainage water of the lysimeters (Table 2.10).

Table 2.9: Vegetation cover [%] and average offset between GST and SAT [ºC].

		Lysimeter 1 (bare sand)		Lysimeter 2 (shrub)		Lysimeter 3 (oak)		Lysimeter 4 (pine)	
		Cover	GST-SAT	Cover	GST-SAT	Cover	GST-SAT	Cover	GST-SAT
1944-1954	Winter	0.5	-0.6	75.3	0.3	57.5	-0.1	66.6	-0.2
	Summer	0.5	5.7	75.3	4.0	57.5	5.0	66.6	3.0
	Year	0.5	2.9	75.3	2.3	57.5	2.6	66.6	1.6
1955-1961	Winter	1.0	n.a.	98.0	0.5	94.3	0.5	95.0	-0.4
	Summer	1.0	n.a.	98.0	5.4	94.3	1.2	95.0	0.0
	Year	1.0	n.a.	98.0	3.0	94.3	0.9	95.0	-0.1

Table 2.10: Weighted averages of the temperature of drainage water of the 4 lysimeters (after Stuyfzand, 1987).

	Lysimeter 1 (bare sand)	Lysimeter 2 (shrub)	Lysimeter 3 (oak)	Lysimeter 4 (pine)
1980-1989	9.5	8.2	8.1	7.6
1990-1998	11.1	9.3	9.4	9.4

GST and GST-SAT offset results from SARB modelling

The effect of regional and temporal differences in meteorological parameters on GST and the GST-SAT offset has been assessed by a radiation balance model for three types of land cover and for meteorological forcing records of five meteorological stations in different parts of the country. The model results are summarized in Table 2.11 per decade and for the entire 1965-2020 period. For the same type of land cover, significantly different GSTs are found for different locations in the Netherlands. The differences in GST are partly explained by the regional differences of SAT, but GST-SAT offsets show regional variations as well. SAT, therefore, is not the only explaining variable.

For all land cover types and periods, the lowest simulated GST is found at Eelde. The highest GST for an asphalt covered surface is found at the Vlissingen location. For grass covered surface and “forest” with convection in the understory, Maastricht displays the highest GSTs. The GSTs for a “forest” with a decoupled canopy only show marginal differences between five locations (0.3ºC). The low GST for all types of land cover, in combination with relatively high precipitation and infiltration at Eelde explains the low T20-35 in the northeast of the country.

The long-term (1965-2020) average GST shows the largest variation between the locations for asphalt and “forest” with convection in the understory. In both cases the maximum inter-station difference is 2.5ºC. The stations with the highest insolation (De Kooy and Vlissingen) at the west-coast of the Netherlands, exhibit high GSTs for the land cover types with a low albedo. The inter-station differences in GST-SAT offset are generally smaller, varying between 1.1 to 1.5ºC. For most land cover types, the lowest GST-SAT offset was calculated for De Bilt, in the central part of the Netherlands. The locations with the highest net radiation (De Kooy and Vlissingen) show the highest GST-SAT offsets for asphalt. This shows that applying a uniform GST-SAT offset in estimates of GST for similar land cover types in different parts of the country can introduce an error of more than 1ºC.

Table 2.11: Average simulated GST [°C] and GST-SAT offsets [°C], based on radiation balance.

Period:	1970-1980		1981-1990		1991-2000		2001-2010		2011-2020		1965-2020	
	GST	GST-SAT	GST	GST-SAT	GST	GST-SAT	GST	GST-SAT	GST	GST-SAT	GST	GST-SAT
Asphalt												
Eelde	13.5	4.9	13.4	4.5	13.8	4.5	14.4	4.5	14.1	3.9	13.8	4.5
De Kooy	15.1	5.8	15.3	5.8	15.4	5.4	16.0	5.4	15.8	4.9	15.5	5.6
De Bilt	13.8	4.5	14.2	4.5	14.5	4.4	15.0	4.5	15.1	4.2	14.4	4.4
Vlissingen	15.6	5.5	16.1	5.8	16.5	5.7	16.8	5.6	17.1	5.5	16.3	5.6
Maastricht	14.1	4.7	14.7	5.0	15.2	4.9	15.4	4.8	16.1	5.0	15.0	4.9
Grass												
Eelde	9.6	1.0	9.7	0.8	10.2	0.9	10.8	0.9	11.2	1.0	10.2	1.0
De Kooy	10.4	1.2	10.6	1.0	11.0	0.9	11.4	0.9	12.0	1.2	11.0	1.1
De Bilt	9.9	0.6	10.3	0.6	10.7	0.6	11.0	0.5	11.5	0.5	10.6	0.6
Vlissingen	10.9	0.8	11.2	0.9	11.7	0.9	12.1	0.9	12.7	1.1	11.6	0.9
Maastricht	11.2	1.8	12.0	2.2	12.5	2.2	13.0	2.4	13.4	2.3	12.2	2.0
“Forest”, decoupled canopy												
Eelde	8.8	0.2	9.0	0.1	9.4	0.1	9.4	-0.4	9.8	-0.3	9.2	-0.1
De Kooy	9.2	-0.1	9.2	-0.3	9.6	-0.5	9.6	-0.9	9.9	-0.9	9.4	-0.5
De Bilt	9.0	-0.4	9.2	-0.5	9.6	-0.6	9.5	-1.0	9.8	-1.1	9.3	-0.7
Vlissingen	9.3	-0.8	9.4	-0.9	9.7	-1.1	9.7	-1.5	10.0	-1.6	9.5	-1.2
Maastricht	9.0	-0.4	9.4	-0.4	9.8	-0.5	9.9	-0.7	10.0	-1.1	9.5	-0.6
“Forest”, convective understory												
Eelde	10.1	1.5	10.1	1.2	10.5	1.2	11.0	1.2	11.0	0.9	10.5	1.3
De Kooy	11.	2.1	11.4	1.9	11.7	1.6	12.1	1.5	12.5	1.7	11.8	1.9
De Bilt	10.8	1.4	11.0	1.3	11.2	1.1	11.5	1.0	12.3	1.3	11.3	1.2
Vlissingen	12.1	2.0	12.3	2.0	12.7	1.9	13.0	1.8	13.3	1.7	12.6	1.9
Maastricht	12.4	3.0	12.9	3.2	13.4	3.1	13.6	2.9	13.6	2.5	13.0	2.8

Regression analysis of annual averages of simulated GST and windspeed, SAT, global radiation (Q), precipitation, cloudiness, relative humidity, and (Makkink) potential evapotranspiration (EV) showed statistically highly significant ($p<<0.001$) relations between simulated GST and SAT, Q and EV for all surfaces and stations. The GST-EV relation was also statistically highly significant for asphalt, although EV does not play a role in asphalt SARB calculations. This is explained by the fact that EV (Makkink) is based on SAT and Q. Coefficients of determination (Table 2.12) demonstrate a strong to very strong correlation between SAT and simulated GST for asphalt and grass. For forest, the correlation is less strong. Although Q and simulated GST show a weak to medium correlation, the influence of this parameter, and derived EV, on GST cannot be ignored.

Table 2.12: Coefficients of determination between annual averaged simulated GST and meteorological parameters.

	Asphalt			Grass			"Forest" (decoupled understory)		
	SAT	Q	EV	SAT	Q	EV	SAT	Q	EV
De Bilt	0.85	0.41	0.57	0.86	0.44	0.58	0.64	0.21	0.29
De Kooy	0.72	0.23	0.41	0.85	0.36	0.57	0.77	0.15	0.32
Eelde	0.49	0.20	0.33	0.87	0.30	0.49	0.69	0.07	0.18
Maastricht	0.83	0.54	0.64	0.81	0.43	0.56	0.49	0.22	0.30
Vlissingen	0.81	0.53	0.67	0.93	0.47	0.64	0.69	0.22	0.34

Time series of modeled GST values for a grass covered surface at De Bilt, Vlissingen and Eelde are aggregated into yearly averages and compared with observed values of nearby soil temperature observation locations (De Bilt, Wilhelminadorp and Nieuw-Beerta) in Figure 2.29. The calculated GST-SAT offsets match literature values and data from the soil temperature observation locations. The grass land GST-SAT offset for De Bilt (0.6ºC) approaches the 1981-2023 measured value (0.8ºC, Table 2.8). At Vlissingen and Eelde, calculated and observed GST-SAT offsets are exactly the same (0.9 and 1.0ºC, Table 2.11) as observed at nearby soil temperature observation locations Wilhelminadorp and Nieuw-Beerta (0.9 and 1.0ºC, Table 2.8).

On the average, the calculated GST at De Bilt is too low. Simulation including a vertical groundwater flux (q_v) results in systematically lower GSTs and larger RMSE. This demonstrates the heat discharge to the subsurface by infiltration. This effect is overestimated in the calculations as no surface runoff is taken into account. Underestimation of the GST can also be attributed to an overestimation of the latent heat loss by evapotranspiration. Potential evapotranspiration only occurs when the grass has an optimum (unlimited) water supply. The summer (April-September) precipitation deficit is highly variable but shows an increasing trend since approx. 1980. The actual evapotranspiration is strongly reduced when the vegetation experiences water stress in the summer.

The GST and GST-SAT offsets of the two types of "forest", either with decoupled understory or with convective heat transport in the understory, differ by several degrees. The average of the two offset values, assuming that both situations occur half of the time, is well below 1ºC, as can be expected for both mature deciduous and conifer forest (e.g. lysimeter 3 and 4 in Castricum, Table 2.9). The range between the two "forest" types matches the free air and sub-canopy air temperature differences reported by Haesen et al. (2021) for all European forests (-2.1 and +2.0ºC). The TD profiles, however, reveal that for natural vegetation the lower GST-SAT offset (decoupled canopy) is more realistic for pine forest and densely heathered land. The canopy temperature affects the GST less for the decoupled canopy situation. The model with a convective understory probably calculates a too high canopy temperature and the assumed interception evaporative cooling may be too low. Therefore, the model results for "forest" with a decoupled canopy are more representative for the landcover type forest.

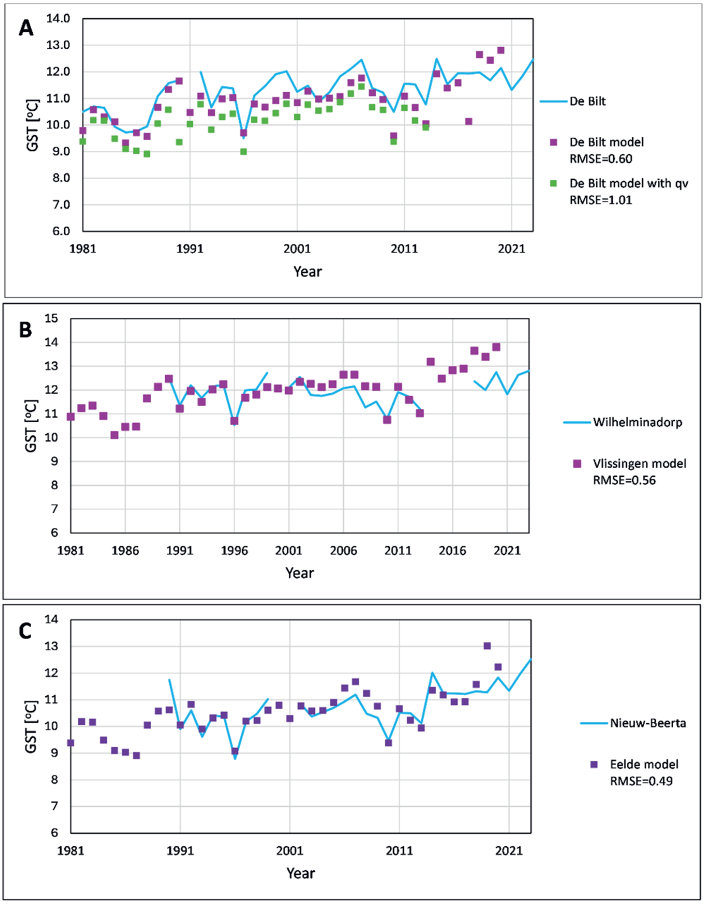

Figure 2.29: Observed and modeled GST for a grass covered surface at or near De Bilt (A), Vlissingen (B) and Eelde (C). RMSE = residual mean square error.

The land use in Figure 2.2 has been converted into a regular 1 km^2 grid. Voronoi polygons are constructed for the five meteorological stations used. The dominant land use type per grid cell is designated a GST, as per Table 2.11, and by assigning one of the meteorological stations by the Voronoi polygons. For the land use type forest (mainly pine) the GST-SAT offset for “forest” with decoupled canopy is applied. For the land cover dry nature, the SAT of the representative meteorological station, plus an offset of 2.9°C is used. This offset is derived from the bare soil and shrub lysimeter data (Table 2.9). This way, synthesized GST and GST-SAT offset maps have been constructed (Figure 2.30). The interpolated T20-35 contours are also plotted on these maps, revealing a regional correlation between T20-35 and simulated GSTs.

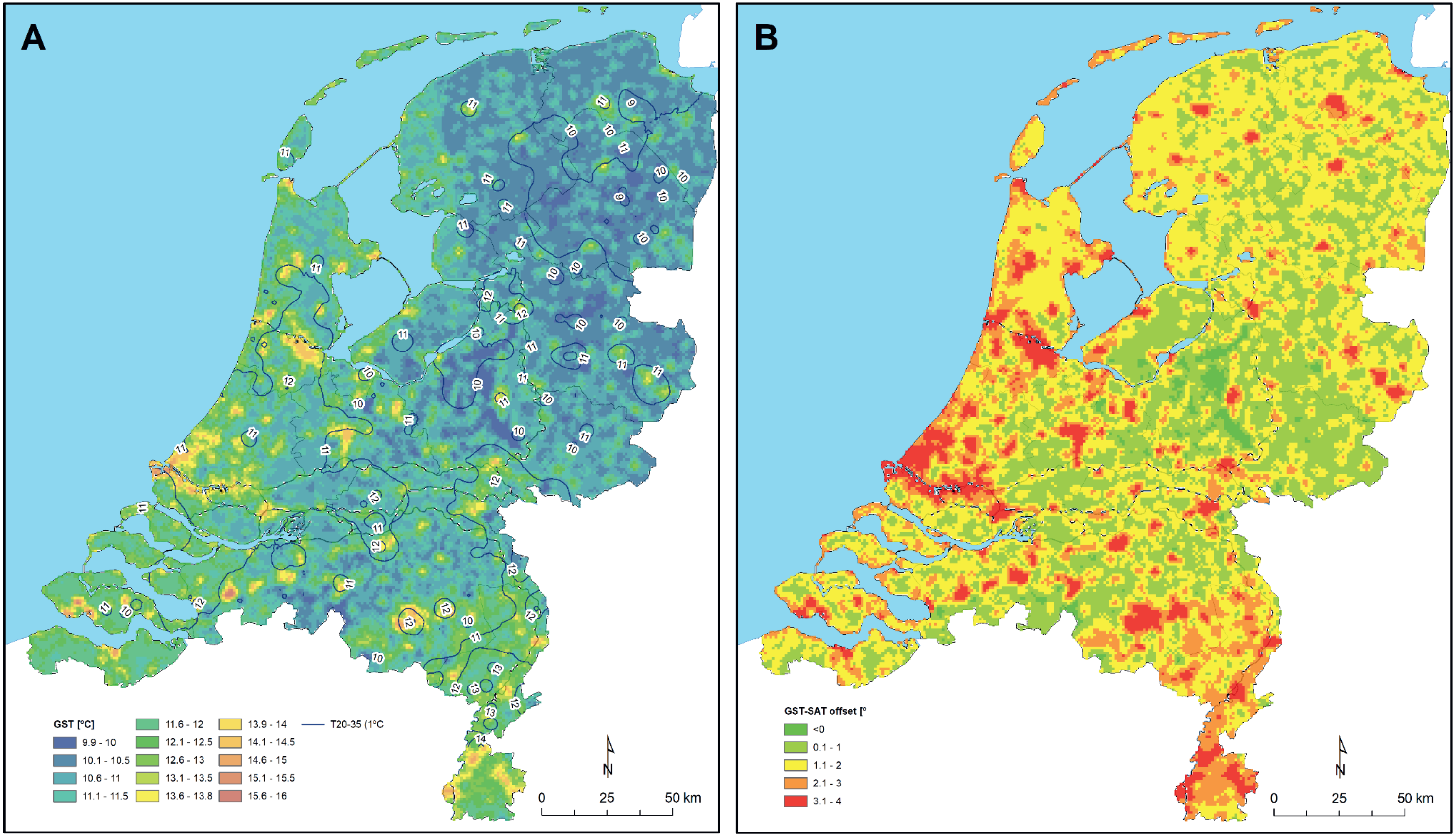

Figure 2.30: A: Simulated GST and observed T20-35 contours (1°C interval). B: Simulated GST-SAT offsets.

The relation between the observed T20-35 and simulated GST values is illustrated in Figure 2.31. The p-value of the regression analysis between these two parameters is extremely low (<<0.001), indicating highly significant test results (Johnson, 2013). It is concluded that the simulated GST and measured T20-35 values show a statistically highly significant relation.

Lowest and highest T20-35 areas are explained by the low and high GST occurring in these zones, in combination with high and low precipitation. It is concluded that the GST is not a simple sum of SAT and a uniform GST-SAT offset per land cover type. This offset differs per location and land cover type, depending on the radiation balance and rainfall.

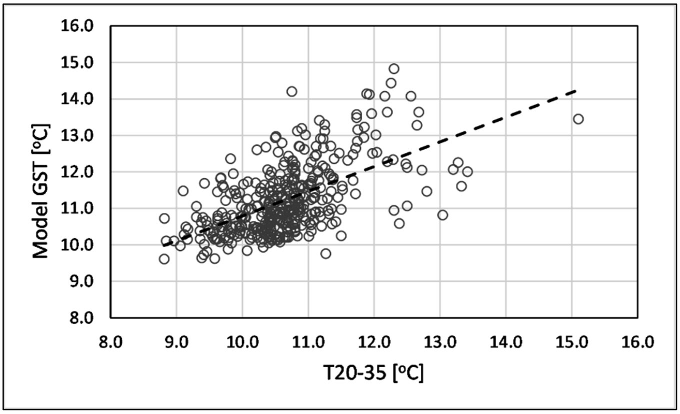

Figure 2.31: Relation of observed T20-35 and simulated GST. The dashed line is the fitted linear regression line. n=378, R^2=0.34, p=2.2E^{-35}.

Model results suggest that climate change (change in ground surface energy balance) results in a change in GST-SAT offset. Both determine the top boundary condition of the soil-groundwater system and, therefore, also contribute to the GWT trend. The evolution of air temperatures in the Netherlands during the past century as a result of climate change is shown in Figure 2.6. The increase of air temperatures has accelerated since approx. 1980 and results in a rise of the GSTs and changing GST-SAT offsets (Table 2.11). The progressive increase of modeled GST is displayed in Figure 2.32. At all locations and for all land covers, SAT and GST increase in the 1965-2020 period. In most cases, GST rises slower than SAT. This results in a slight decrease of the GST-SAT offset in time.

The modeled GST trend is quantified in Table 2.13. These results imply that GST increased in all parts of the country in the 1965-2020 period, albeit at different rates for different locations and land covers. This is, in part, observed in GWT trends.

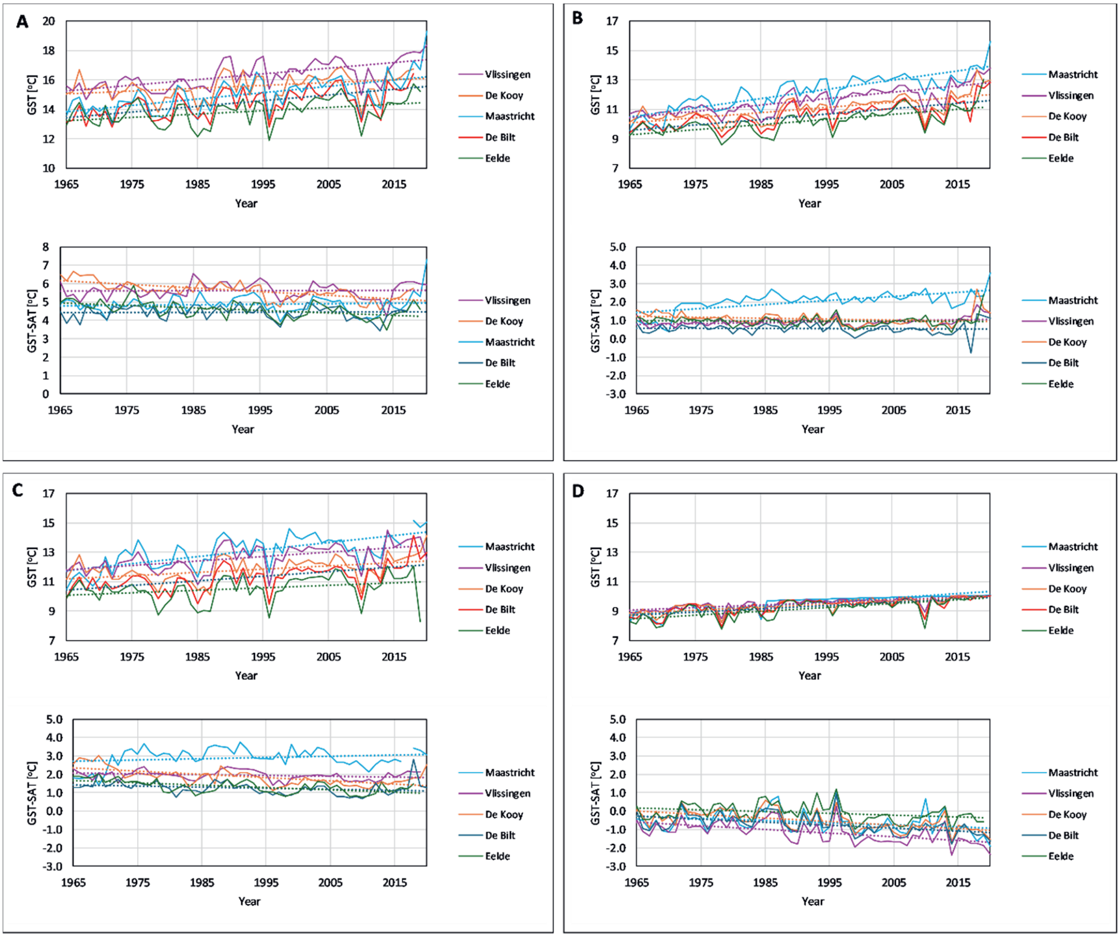

Figure 2.32: Simulated GST and GST-SAT offsets for five locations in the Netherlands on an hourly basis, annual averages for 1965-2020. The solid lines show the annual averages, the dashed lines are linear trendlines. A: asphalt pavement; B: grass cover; C: "Forest" with convective understory; D: "Forest" with decoupled canopy.

Table 2.13: Synthesized average GST increases for five locations and different land covers. s=slope of the fitted linear regression line [ºC.year^{-1}], ΔT0=average GST increase between 1965 and 2020 [ºC.year^{-1}].

	Asphalt		Grass		"Forest", decoupled canopy		"Forest", advective understory	
	s	ΔT0	s	ΔT0	s	ΔT0	s	ΔT0
Eelde	0.017	0.9	0.037	2.1	0.026	1.4	0.019	1.0
De Kooy	0.014	0.8	0.035	1.9	0.020	1.1	0.022	1.2
De Bilt	0.034	1.9	0.037	2.0	0.022	1.2	0.032	1.8
Vlissingen	0.039	2.1	0.043	2.4	0.018	1.0	0.031	1.7
Maastricht	0.044	2.4	0.062	3.4	0.029	1.6	0.042	2.3

2.8 Conclusions and recommendations for future research

The temperature of groundwater samples, taken at a specified depth range below the seasonal zone in a standardized manner, provides good insight in the spatiotemporal variation of subsurface temperatures. When using groundwater sample temperatures as an indicator for groundwater temperature (GWT), it is recommended that the sampling is carried out according the applicable protocol for environmental sampling, using a peristaltic pump, and during periods that both surface air temperature (SAT) and ground surface temperature (GST) are >5°C and <25°C.

The GWT between 20 and 35 m below ground level (T20-35) obtained this way, shows clear regional patterns and trends in time. T20-35 varies with 3°C between the northeast and southeast of the country. Areas with low T20-35 are linked to areas with low calculated GSTs, based on the radiation balance and precipitation rates, and high T20-35 areas are related to high calculated GST zones.

A second aspect that plays an important role in the T20-35 distribution, is the groundwater recharge rate. In areas where infiltration (groundwater recharge) prevails, low T20-35 values are found. The highest T20-35 values coincide with parts of the country with the lowest annual rainfall. In the west of the country, with high annual precipitation rates, the precipitation does not lead to high infiltration rates, as this region is mainly characterized by groundwater seepage and high building densities, leading to surface runoff. Strong urbanization of the west of the country is reflected in the high calculated GSTs and observed high T20-35 values.

The 1991-2011 average of all T20-35 data shows an increase by 1.2°C. The results of the trend analysis of the T20-35 values reveal a strong relation with infiltration or seepage. In the infiltration zones, increasing trends prevail. In seepage zones, stable T20-35 values are dominant. (Probably) decreasing trends are negligible (~1% of the trends).

River water temperatures are steadily increasing over time, in both summer and winter. This is not (yet) reflected in the T20-35 observations near the major rivers. This can be explained by the distance of the observation points beyond the winter dikes (>1 km). Temperatures of abstracted river bank filtrate, on the other hand, exhibit a statistically significant rising trend.

Increasing trends of the temperature of abstracted groundwater are also observed at most phreatic PSWFs, and in a smaller portion of the deeper (semi)confined PSWFs. This illustrates the fact that the increasing GST signal propagates slowly and is attenuated with depth. A relatively large percentage of the well fields tapping limestone aquifers in the southeast of the country show declining water temperatures. Complex flow patterns through Tertiary sediments to karstified or fractured limestone and the lack of TD profiles in this area makes this inexplicable without further research.

Increasing SAT and calculated GSTs at the five selected locations and four land cover types, explain the increasing T20-35 trends. (Repeated) TD profiling confirms the calculated ranges and changes in GST-SAT offsets in time for various land cover types and parts of the country. The use of uniform GST-SAT offsets per land cover type for various parts of the country in forward or reverse modeling of the subsurface temperatures will, therefore, produce less accurate results.

Climate change forces subsurface and groundwater temperature to increase through higher GSTs, being a result of higher SAT and insolation. The higher surface temperatures are conveyed to the subsurface by conduction and advection through infiltration of precipitation. Climate scenarios for the Netherlands predict increasing winter precipitation in the period up to 2100, while summer precipitation will decline. Evapotranspiration (mainly related to SAT and radiation) will also increase. More winter precipitation results in more groundwater recharge with relatively cool infiltrating water. Increase of evapotranspiration yields higher loss of latent heat from the surface. These processes may compensate to some extent the GST rise that results from higher SAT and incoming radiation. However, as these processes are already ongoing and the majority of the T20-35 trends are increasing, it is likely that the net result is warming of the subsurface. The net effect of changing SAT, precipitation rates and patterns, radiation and evapotranspiration, which may amplify or partly compensate each other, is not easily assessed and requires further study and modeling.

Even more difficult to assess aspects of climate change are changes in vegetation and agricultural practices. For example, the felling of coniferous forests is sometimes promoted as a measure to prevent high evaporative groundwater losses, or to raise biodiversity. This, however, results in higher GSTs and warming of the subsurface and groundwater. Farming practices could also change, due to climate change. Different types of crops, which require less water during the growing season, and other agricultural practices could result in less crop transpiration and, thus, possibly higher GSTs. Ongoing urbanization will increase GST and subsurface temperatures.

The radiation balance models applied in this study could be extended with the future climate scenario’s to further assess the impact of climate change on subsurface temperatures. New campaigns of groundwater sampling and temperature measurements, combined with (repeated) TD profiling will enhance the finetuning and calibration of these models.

Chapter 3

Impacts of progressive urban expansion on subsurface temperatures in the city of Amsterdam (the Netherlands)[1]

Abstract

Subsurface temperatures are substantially higher in urban areas than in surrounding rural environments; the result is a subsurface urban heat island (SUHI). SUHIs and their drivers have received attention in studies world-wide. In this study, a well-constrained data set of subsurface temperatures from Amsterdam, the Netherlands, is presented. The study demonstrates that, through modeling of centuries-long (from 14th to 21st century) urban development and climate change, along with the history of both the surface urban heat-island temperatures and ground surface temperatures, it is possible to simulate the development and present state of the Amsterdam SUHI. The results provide insight into the drivers of long-term SUHI development, which makes it possible to distinguish subterranean heat sources of more recent times that are localized drivers (such as geothermal energy systems, sewers, boiler basements, subway stations or district heating) from larger-scale drivers (mainly heat loss from buildings and raised ground-surface temperatures due to pavements). As these findings have consequences for the assessment of the shallow geothermal potential of the SUHIs, it is proposed to distinguish between (i) a regional, long-term SUHI that has developed over centuries due to the larger-scale drivers, and (ii) local anomalies caused by anthropogenic heat sources less than one century old.

3.1 Introduction

The subsurface urban heat island (SUHI) is the phenomenon of elevated subsurface temperatures in urban areas. In part, SUHIs can be regarded as the subsurface thermal imprint of the meteorological urban heat island (UHI) that causes elevated ground-surface temperature, but anthropogenic heat sources (such as basement heating, underground thermal energy storage, sewers, and district heating) provide additional control on the development of a SUHI. Temperature-depth (TD) profiles obtained from borehole records allow one to describe the subsurface extent of SUHIs. Examples of case studies that use such descriptions include mid-latitude cities in Canada

---

[1] Published slightly modified as: Visser, P.W., Kooi, H., Bense, V. & Boerma, E., 2020. Impacts of progressive urban expansion on subsurface temperatures in the city of Amsterdam (The Netherlands). Hydrogeology Journal 28:1755–1772.

(Ferguson & Woodbury 2004), Japan (Benz et al. 2018; Taniguchi et al. 2007; 2009), and Europe (e.g., Benz et al. 2015; Epting & Huggenberger 2013; Menberg et al. 2013b; Mueller et al. 2018). In contrast to the UHI, the SUHI is a significant store for heat which accumulates at shallow depths and only slowly diffuses deeper into the subsurface. Consequently, the SUHI is often more pronounced than the UHI in terms of thermal intensity (Benz et al. 2017b). The heat that is stored in SUHIs could be retrieved by geothermal energy systems (GES) and used for the heating of buildings, and in that way contribute to the offset of carbon emissions (e.g., Allen et al. 2003; Zhu et al. 2010; Menberg et al. 2013b; Menberg et al. 2015; Benz et al. 2015, García-Gil et al. 2015; Bayer et al. 2016; Epting et al. 2017). Bayer et al. (2019) review and categorize available studies on the geothermal potential of the urban subsurface. However, the long-term geothermal potential of a SUHI is expected to depend on the current extent, intensity and processes that maintain the SUHI (Benz et al. 2018). The latter are still poorly quantified because the development of SUHIs underneath major cities has been occurring in many instances over time-scales of centuries during which the evolution of surface heat fluxes and/or subsurface temperatures is typically unknown. Chen et al. (2019), for example, characterize the spatiotemporal dynamics of anthropogenic heat fluxes due to rapid urban expansion over the past 20 years in China.

Groundwater temperature observations are the only means to map the lateral extent of a SUHI, whilst relatively deep (e.g. at least tens of meters) TD profiles taken in boreholes are required to characterize the depth extent of a SUHI. From TD profiles, past fluctuations in surface heat flux can be retrieved using inverse modeling techniques (Beltrami 2002). However, repeated TD observations, ideally separated by decades or more (Kooi, 2008; Bense & Kurylyk 2017), allow one to directly estimate site-specific heat fluxes from the surface into the SUHI under a range of urban surface cover types (Benz et al. 2018). At the scale of entire cities, numerical modeling of coupled heat transport and groundwater flow, calibrated with observed temperatures and hydraulic head data, has been used to assess the geothermal potential of the SUHI (e.g., Mueller et al. 2018). The Mueller et al. (2018) study only considered the present-day thermal state using a model period of 2010-2015 CE (Common Era, hereafter applying to all dates in this article). Zhu et al. (2014) simulated the development of the SUHI of the city of Cologne, Germany, by numerical modeling of groundwater flow and heat transport. However, detailed simulations of spatial development of the city and potential heat sources were beyond the scope of their study and an idealized hot spot of fixed size, representing the city center, was defined. In contrast, the present study uses recent TD observations, not only to define the current thermal state, but to reconstruct the spatiotemporal characteristics of the subsurface temperature field of the city of Amsterdam, the Netherlands, as a function of the history of urban expansion using a transient heat flow model covering a time span of several centuries, between 1350 and 2012 CE.

In order to better understand SUHI development since the onset of urban expansion, a particularly detailed subsurface-temperature data set from the city of Amsterdam has been analyzed. The TD data have all been collected in the same manner, with one instrument, in similar monitoring wells at the same depth of 20 m below ground level (bgl) (and deeper). Furthermore, location-specific surface air temperatures, and hydrogeological and auxiliary data have been collected.

Amsterdam was developed in a staged manner over the past centuries, where well-defined periods of urban expansion can be distinguished. Through an analysis of TD profiles inside and outside the city, using a numerical model, it is found that these stages can be identified at the present day as a thermal zonation in subsurface temperature patterns.

The numerical model, coupling groundwater flow and heat transport, covers a two-dimensional section parallel to the regional groundwater flow direction, stretching 10 kilometers from the city center to the rural outskirts of the city, and to a depth of 750 m.

The numerical model is used to investigate if a heat transport model of the subsurface of Amsterdam, linked to a surface model for the ground surface temperature (GST) that reflects the spatial-temporal development of urban expansion, results in a modelled SUHI that is consistent with the observations. This study provides novel insights into the interplay between urban expansion and the development of a SUHI. These insights will allow improved simulation of the present and future states of SUHIs, which provides important input for the assessment of the geothermal potential of SUHIs.

3.2 Study area and thermal data

The city of Amsterdam is a medium-sized western European city and the capital of the Netherlands (Figure 3.1a). The city, in 2019, had a population size of ~820,000 people. Amsterdam is, compared to many other European cities, a relatively young city, with origins dating to the early 14th century.

3.2.1 Urban expansion

The first stone building in Amsterdam was erected in 1295 (the Oude Kerk). The 14th century city comprised only approx. 40 hectares (ha) and is located in the present-day city center. The city gradually expanded around this city center, south of the River IJ, to approx. 60 ha by 1450. Between 1450 and the end of the 16th century, there was virtually no growth of the city. Between the end of the 16th century and the first quarter of the 18th century, the city grew to almost 700 ha; this forms the present-day historical part of the city with the many concentric canals illustrating the stages of expansion.

The city’s expansion has been carefully recorded by the municipality (Figure 3.1a) illustrating how Amsterdam went through a period of bloom in the 17th century, experiencing rapid expansion. However, in the 18th and until halfway through the 19th century, further expansion was very sparse. Only from the mid-19th century, further urban expansion of the areas surrounding the city occurred, but in a staged manner.

The 2017 built-up surface of Amsterdam comprised approx. 7,900 ha, while paved surfaces occupy approx. 1,700 ha. Green spaces, agricultural terrain and natural habitat account for 6,900 ha, and water bodies account for 5,500 ha, in the municipality of Amsterdam.

3.2.2 Thermal data

Surface air temperature

From two locations in the study area (Figure 3.1a), long-term time-series of surface air temperature (SAT) are available (Figure 3.1b). One series was recorded in the Amsterdam city center (Stadswaterkantoor) starting in 1785 but which was discontinued in 1961 (KNMI 2014b). At Schiphol airport, air temperature has been recorded since 1951. Additionally, a long-term (1706-present) temperature reference record (Figure 3.1b) has been constructed by the Royal Netherlands Meteorological Institute (KNMI 2014a) for the town of De Bilt, 36 km from the city center (Figure 3.1a). Engelen et al. (2001) constructed average annual temperature data for the Netherlands dating back to the 8th century. Figure 3.1b shows a section of the Van Engelen et al (2001) data series and the KNMI (2014a) 1706-present temperature record.

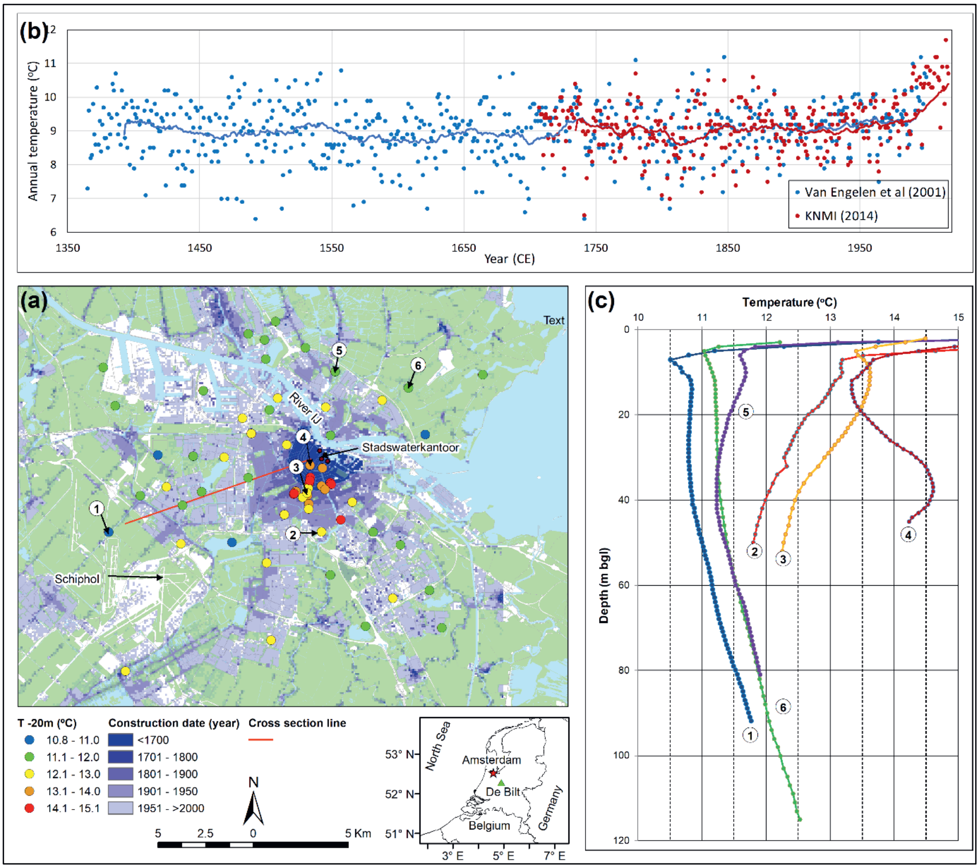

Figure 3.1: (a) Map of the city of Amsterdam (the Netherlands) indicating stages of urban expansion since the 18th century and observed groundwater temperatures at 20 m depth (T_{-20m}). (b) Average annual air temperatures (dots) and 30-year running average of annual air temperatures (solid lines). (c) Temperature-depth (TD) curves.

Auxiliary data

- Short-term air temperature records are available from 14 semi-professional amateur stations in the city (see Appendix 3.1).
- The long-term (1990-2015) canal water temperature at two locations in the city center is 0.2 to 0.9 °C higher than the urban SAT (IHW 2019) (see Appendix 3.1).
- Stichting Bouwresearch (1985) showed that heat losses through uninsulated floors to ventilated crawl spaces resulted in an average crawl space temperature of 12 °C. Due to ventilation with outside air, the crawl space temperature is only slightly higher than the outside temperature (~ urban SAT).

Subsurface temperature data

Groundwater temperature data for the subsurface below Amsterdam and its vicinity were collected in 2012 by the author and E. Boerma (Figure 3.1a,c). This was possible through the presence of boreholes equipped with piezometers that allowed the collection of TD data. The measurements were done by carefully lowering a temperature probe into a piezometer tube to record temperature at depth intervals of one meter. The narrow diameter (diameter 50 mm or 38 mm) of the tubes reduced the risk of convection in the bore (Sammel 1968). At six locations (1-6, Figure 3.1c), relatively deep TD profiles could be obtained up to 45-115 m.

At 63 other locations in the area (Figure 3.1a), temperature was measured, in similar piezometers, at a depth of 20 m below the surface (T_{-20m}). The depth of 20 m is well below the zone where significant seasonal fluctuations of temperature occur for typical conditions in the Netherlands (Bense & Kooi 2004).

3.2.3 Hydrogeology

Amsterdam is set in an essentially flat landscape built upon loosely consolidated sedimentary deposits of Holocene age that have a thickness of 10-20 m. These overlay a stack of Quaternary and Tertiary sedimentary deposits that reach to a depth of ~450 m, where stiff marine clayey deposits of Miocene age are reached (TNO 2012; Beets & Beets 2003). The latter is widely regarded (e.g. Dufour, 1998) as the hydrological base, not allowing much, if any, groundwater movement. The subsurface is schematized in Figure 3.2a, in which also the hydraulic parameters of the various strata are given.

Surface water levels and phreatic water levels follow the polder water levels (Figure 3.2b) closely. The river IJ runs north of the city center with a water level of 0.4 m below mean sea-level and a water depth of approx. 11 m. At the southwest end of the cross-section line in Figure 3.1a, the Haarlemmermeer reclaimed lake area lies about 4.5 m below mean sea-level. Before reclamation of the Haarlemmermeer, the regional groundwater flow south of the River IJ was directed to this river. Due to the reclamation of the Haarlemmermeer in the 19th century, this gradient was gradually reversed to the southwest (Figure 3.2c).

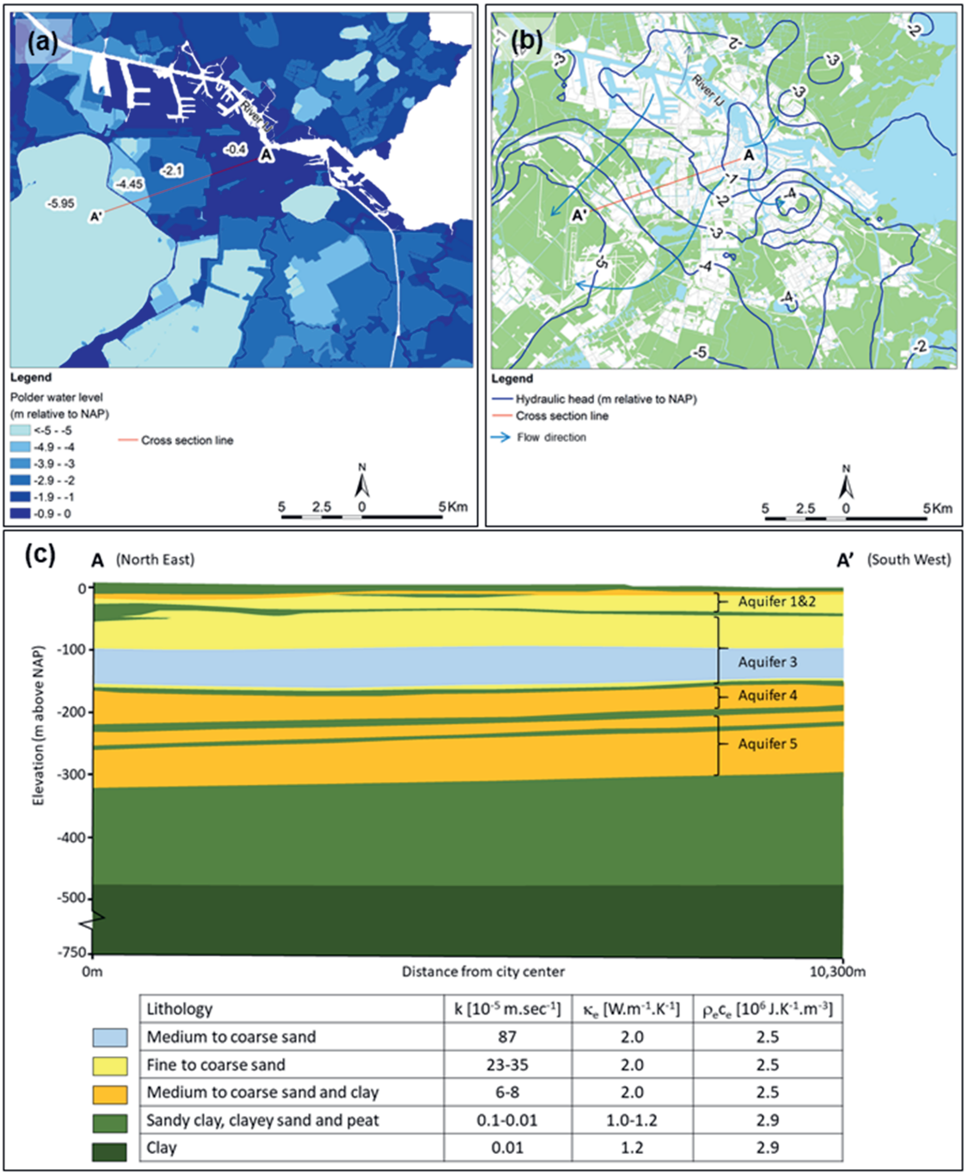

	Lithology	k [10^{-5} m.sec^{-1}]	κ_e [W.m^{-1}.K^{-1}]	$\rho_e c_e$ [10^6 J.K^{-1}.m^{-3}]
🟦	Medium to coarse sand	87	2.0	2.5
🟨	Fine to coarse sand	23-35	2.0	2.5
🟧	Medium to coarse sand and clay	6-8	2.0	2.5
🟩	Sandy clay, clayey sand and peat	0.1-0.01	1.0-1.2	2.9
■	Clay	0.01	1.2	2.9

Figure 3.2: (a) polder water levels (= approx. surface water levels) in m relative to the ordnance datum (NAP = approx. sea level), (b) isohypses of hydraulic head in m relative to NAP in aquifers 1&2 (see a) and the inferred groundwater flow direction, (c) Geological cross section along line A-A' (after TNO 2012), with lithology, hydraulic and thermal parameters of the strata.

3.3 Data Analysis and modeling

The available data from Amsterdam outlined above allow one to interpret the evolution of the suburban heat island underneath the city in relation to urban expansion, regional climate warming and groundwater flow.

3.3.1 Suburban temperature distribution

The deep TD data (Figure 3.1c) confirm the presence of a SUHI underneath Amsterdam. Temperatures inside the city limits are distinctly elevated as compared to the temperatures outside these limits.

Comparison of the historic SAT series for both the Amsterdam city center (Stadswaterkantoor; KNMI 2014b) and De Bilt (KNMI 2014a) shows that between the late 18th century and mid-20th century the Amsterdam temperatures have consistently risen by an average of 1.1 ^{o}C and with a maximum of 1.8 ^{o}C (Figure 3.1b). The 1951-2014 temperature time series of the Schiphol Airport meteorological station tracks the De Bilt series very closely; the averages for the periods 1951-2014 (9.9 ^{o}C) and 1985-2014 (10.4 ^{o}C) are just 0.1 ^{o}C higher at Schiphol. The substantially higher temperatures in the Amsterdam city center are, therefore, most likely an expression of the UHI effect. The period where SAT was measured at both Schiphol and the Amsterdam city center (1951-1964) shows that the difference between these two stations is also about 1.1 ^{o}C. The Schiphol SAT is therefore used to extrapolate the city center temperatures to more recent times using the same offset. Recent measurements of amateur semi-professional meteo stations in the city center (see Appendix 3.1) suggest that this is a reasonable approach. The SAT time series are used to reconstruct the GST development in time as is explained in section ‘Numerical modeling’.

The TD profiles (Figure 3.1c) show a concave shape, characteristic of increasing ground surface temperatures (Kurylyk et al. 2019). For location 6 (Figure 3.1a), comparison with an older temperature log shows that temperatures have increased to a depth of approx. 62 m in the period 1979-2012.

The measured minimum and maximum T_{-20m} are respectively 10.8 ^{o}C and 15.1 ^{o}C. The mean is 12.5 ^{o}C with a 1.1 ^{o}C standard deviation, resulting in a 95% reliability interval of approx. 10.3 to 14.7 ^{o}C. T_{-20m} values below 11.0 ^{o}C are found near the city limits. These temperatures are only marginally higher than the long-term average SAT for Schiphol and, therefore, considered to be the (rural) background temperature. In this study, the SUHI intensity is defined as the T_{-20m} minus the rural background temperature (11 ^{o}C). T_{-20m} values between 11 and 13 ^{o}C are found scattered over all built-up areas of the city. All T_{-20m} higher than 13 ^{o}C are concentrated in and near the city center.

Figure 3.3 suggests a degree of correlation between the urban expansion age and the built-up density (fraction of the surface occupied by buildings and pavements) with the T_{-20m} around the observation point. Almost all T_{-20m} >13 ^{o}C are found in the parts of the city that were built before 1900 CE, whilst also highest T_{-20m} values are associated with the higher built-up densities. Figure 3.3b considers the data from the city quarters that were built after 1870 CE in more detail, further illustrating the T_{-20m} relation with the built-up density. Although the data set is limited in size, the lower T_{-20m} values appear to be related to the lowest built-up densities. This illustrates the interplay between the age of the urban expansion and built-up densities. Thirdly, it can be expected that the UHI effect is the strongest in the city center, where also the oldest quarters are found.

This analysis leads to the hypothesis that the development of the SUHI can be construed from the urban expansion history and built-up densities. To do so, the delayed and attenuated temperature rise with depth in response to urban expansion has to be taken into account. The modeling of the development of the SUHI of Amsterdam is presented in the following section.

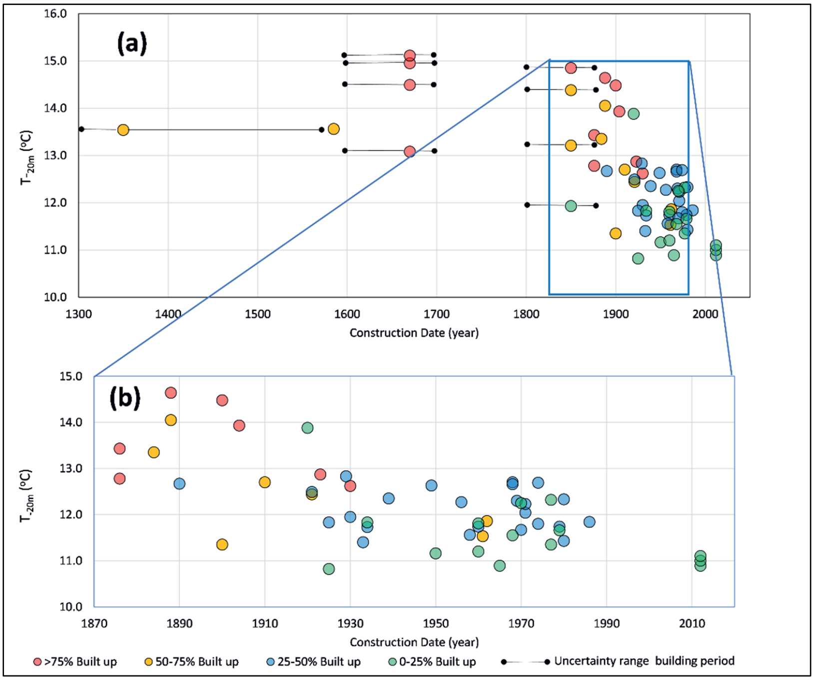

Figure 3.3: (a) T_{-20m} plotted against date of urban expansion. The colors of the symbols represent the percentage of the surface in a 100 m radius covered by buildings and paved surfaces. (b) T_{-20m} for the younger city quarters, built after 1870. The locations built after 2012 have been plotted at 2012.

3.3.2 Numerical Modeling

A numerical model to describe the development of the temperature distribution underneath the city of Amsterdam from 1350 to 2012 was considered. A two-dimensional cross-sectional model that is aligned parallel to the regional direction of groundwater flow (cross section location in Figure 3.1a) was developed.

Groundwater and heat flow equations

The scriptable finite-element code FlexPDE (PDESolutions; Bense & Kooi 2004) was used to solve the groundwater flow equations and advection-diffusion equation for heat flow (Stallmann 1963; Kurylyk et al. 2019).

Model domain and layers

The model domain is 10,300 m wide and stretches to a depth $z=-750$ m. The ground level is assumed to be constant over the model domain.

The model comprises 16 layers of alternating sand and clay with variable hydraulic and thermal properties. A schematic presentation of the layers and their properties is given in Figure 3.2c. The thermal properties are based upon literature values (Kooi 2008) or in-situ measurements on similar sediments (Witte et al. 2002). The hydraulic properties are derived from the national hydrogeological database DinoLoket (TNO, 2012).

Hydraulic boundary conditions and groundwater flow

Only horizontal flow is modelled. Recharge at the surface is therefore implicitly neglected. This is considered reasonable as the top strata comprise clay and peat layers with a very low vertical hydraulic conductance and a thickness of almost 20 m at the northeastern end of cross section A-A' to approx. 7 m at the southwestern end. This, in combination with intensive surficial drainage, limits vertical infiltration and makes it negligible compared to the vertical flow q_x. This can be shown as follows.

Apart from the River IJ, surface waters comprise mainly shallow canals around the city center. The canals have an average depth of 2.6 m (to 3 m below sea level) and an average water level of 0.4 m below sea level (Figure 3.2a). The hydraulic head in the aquifer below the Holocene layers in the city center is approx. 1 m below sea level. This results in a hydraulic gradient below the canals of 0.05 m m^{-1} over 13 m of Holocene strata. With a vertical hydraulic conductivity of 1.16E^{-8} m s^{-1}, and an effective porosity of 0.2, this results in a vertical flow (q_z) of 2.9E^{-9} m s^{-1}.

On the other hand, the present day horizontal hydraulic gradient in the aquifers below the Holocene strata is approx. 5E^{-4} m m^{-1}, while the minimum horizontal permeability and effective porosity are 7E^{-5} m s^{-1} and 0.35, respectively. This results in a horizontal groundwater flow (q_x) of 1E^{-7} m s^{-1}, demonstrating that q_x is at least several orders of magnitude larger than q_z.

Horizontal groundwater flow is based upon the uniform hydraulic gradient that is determined by the different hydraulic heads at both ends of the domain. A gradient of approx. 10^{-4} m m^{-1} is directed towards the River IJ (northeast) between 1350 and 1849. First, this gradient was induced by drainage towards the IJ (north of the cross section). In the early-17th century, reclamation of deep polders north of the River IJ increased this gradient. From 1849 to 1852, reclamation of the Haarlemmermeer lake on the southwest end of the cross section gradually reversed the hydraulic gradient into that direction. Nowadays, a groundwater divide is located approximately below the River IJ. The hydraulic heads close to the IJ are well below the river level (>1 m vs. 0.4 m below sea level), indicating a high hydraulic resistance of the deposits at and below the river bottom. The reversal of the hydraulic gradient direction was simulated by stepwise lowering of the hydraulic head on the southwest domain boundary until the hydraulic gradient was about the present-day value of 5×10^{-4} m m^{-1} to the southwest.

Thermal boundary conditions

The northeastern vertical boundary and the model bottom have been assigned fixed temperatures that are calculated from a constant initial vertical geothermal gradient and initial GST. The initial GST is taken as 9.1 ^{o}C, being the average 1329-1349 SAT (Van Engelen et al. 2001) minus 0.5 ^{o}C. The background geothermal gradient is 0.025 ^{o}C m^{-1}. The southwestern model domain edge has a flux (Neumann) boundary condition in the form of $\rho_b\, c_b\, q_x\, T$, where ρ_b [kg m^{-3}] and c_b [J kg^{-1} ^{o}C] are respectively the (bulk) density and specific heat of the solid-fluid medium, T [^{o}C] is the temperature, q_x [m sec^{-1}] is the x-component of specific discharge.

The model top has been assigned a spatiotemporal variable ground-surface temperature (GST). The GST history is constructed from the following components:

(a) The time-dependent autonomous or 'rural' SAT;
(b) The UHI effect, which takes effect after urban expansion. Added to the 'rural' SAT, this yields an 'urban' SAT;
(c) An offset between SAT and GST that depends on the land cover, which varies with time.

The 'rural' SAT history is taken from the long-term records given by KNMI (2014a) and Engelen et al. (2001). From the city margins to the city center, the UHI effect is increased stepwise from 0.7 to 1.1 ^{o}C. This graduated UHI effect is based on the average 2014 air temperatures measured along the cross section by semi-professional amateur stations (see Appendix 3.1) and the consistent difference between the De Bilt, Schiphol and Stadswaterkantoor time series. At the rural southwest extreme of the model domain, the UHI effect is nil.

GST usually tracks the seasonal fluctuation of SAT but tends to be systematically higher than SAT with the offset depending on land surface conditions (Mann & Smidt 2003). Before the building period, the GST is assumed equal to the average annual SAT plus 0.5 ^{o}C, being a reasonable rural SAT-GST offset (e.g. Dědeček et al. 2012, Kooi 2008). After the building period, the offset is assumed to depend on the building period and the position relative to the city center.

The urban SAT-GST offset is based on the 'built-up density' history as follows. The model domain is horizontally divided into 400 to 800-m long sections that coincide with discrete building periods. The SAT-GST offset per top boundary section is time-dependent and calculated as area-weighted values for green spaces (including surface water), roads and buildings (comparable to Taylor & Heinz 2009). Surface water was assumed to have the same SAT-GST offset at green spaces. The water temperature of the canals in the city center is 0.2 to 0.9 ^{o}C higher than the urban SAT (see Appendix 3.1), which is comparable to that of green spaces.

A surface-atmosphere radiation balance (SARB) model has been set up to calculate the SAT-GST offsets and ground heat flux for various pavement types under specific climatological conditions of the Amsterdam city center (see Appendix 3.2). The inferred offset for brick was used for roads constructed before 1925 and the offset for asphalt was used for roads that were constructed since 1925.

The present-day temperatures in living spaces in the Netherlands average approx. 20 ^{o}C. One century ago, an ambient living space temperature of 15 ^{o}C was normal. For work spaces the temperatures vary between 12 and 18 °C (e.g. Montijn 2000; Palmer & Cooper 2012; Kuijer & Watson 2017). For uninsulated flooring, the maximum temperature ranged between 14 and 16 °C, due to a 2 °C m^{-1} vertical temperature gradient in living spaces (Stichting Bouwresearch 1985). Most buildings in Amsterdam have basements, cellars or crawl spaces. The basements and cellars were rarely heated. In fact, these were often used as storage rooms and had temperatures of ~11 °C (Montijn 2000). Only recently, semi-basements of the 17th century buildings are being converted into living and working spaces and may be heated.

Only where floor heating is applied with uninsulated floors, the crawl space temperature approaches the living space temperature (Stichting Bouwresearch 1985). Floor heating is not very common. Therefore, the ground temperature below buildings is assumed to be approx. 2.5 °C higher than the urban SAT for the building periods before 1960. After that date, central heating became common, and it is assumed that this resulted in higher living-space temperatures and a 5.0 °C higher ground temperature below buildings. For the building period after 2000, it must be assumed that better floor insulation resulted in a lower (4.0 °C) difference.

A GST increase due to emplacement of a new urban surface cover (e.g. paving of the surface) or construction of a building propagates into the subsurface primarily by diffusion. This implies that the temperature rise at depth occurs with a delay relative to the surface change and that the amplitude is smaller than, or attenuated relative to the GST change, over long time periods (e.g. Lesperance et al. 2010).

Initial conditions

Initial conditions are calculated as a steady-state simulation representing the pre-1350 temperature distribution and groundwater flow. A horizontal hydraulic gradient of 10^{-4} m m^{-1} directed northeast, a surface temperature of 9.1 °C and a geothermal gradient of 0.024 °C m^{-1} were imposed on a steady-state version of the model. The results of this model run were used as initial conditions for the transient 1350-2012 simulations.

3.4 Results

Figure 3.4 depicts the modelled GST history for various pavement types under the meteorological conditions of the city center of Amsterdam for the period 1990-2014 (method detailed in Appendix 3.2). Table 3.1 summarizes the average GSTs for these pavement types over this period together with the modelled component contributions: rural SAT, the UHI effect and the SAT-GST offset. The results show that GST differences associated with pavement type are expected to be about 1.2 °C. The offsets for brick and asphalt were used to represent the SAT-GST offset for roads before and since 1925.

Table 3.1: Summary of the predicted GST and contributing components for the city center.

Pavement type	1990-2014 rural SAT [°C]	UHI effect [°C]	SAT-GST Offset [°C]	GST [°C]
Long-term SAT, Schiphol	10.4	-	-	-
Long-term SAT	-	+1.1	-	-
Asphalt pavement	-	-	+4.1	= 15.6
Granite sett pavement	-	-	+3.2	= 14.7
Concrete pavement	-	-	+3.0	= 14.5
Brick pavement	-	-	+2.9	= 14.4

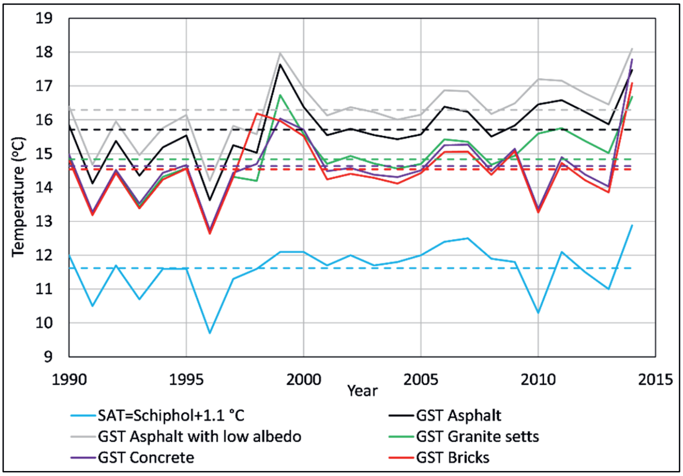

Figure 3.4: Calculated annual averages of road surface temperatures for an average city center SAT represented by Schiphol SAT + 1.1 °C. The dashed lines in corresponding colors show the 1990-2014 averages of the temperatures.

Figure 3.5 presents the calculated area-weighted offset between the rural SAT and the local GST (Figure 3.5d) for the model transect.

The historically minimum rural SAT was 6.4 °C in both 1491 and 1740 (Van Engelen et al. 2001) (Figure 3.1b). Taking the SAT-GST offset for the oldest part of the city center (Figure 3.5b and d) into account, the urban GST in these years would have been 10.1 °C. The present-day compounded SAT-GST offsets vary from 0.9 to 4.5 °C (Figure 3.4d). For the period 1990-2014, this results in average GSTs from 11.3 °C at the city margins to 14.9 °C for the section between distances 7300 m and 7800 m, that were built up around year 2000 (Figure 3.5b) with 88% buildings and 6% (asphalt) roads (Figure 3.5c).

The spatio-temporal development of the GST has been implemented as the thermal top boundary condition of the coupled groundwater and heat transport model, resulting in TD distributions for the years 1350-2012. Figure 3.6a-g shows the calculated distribution of temperature in the top 200 m of the model domain at selected times. Figure 3.6h shows the calculated T_{-20m} values along the cross section at four selected years. At the positions indicated with dashed vertical lines in Figure 3.6g, synthetic TD profiles have been calculated for the situation in 2012.

Figure 3.7a shows the calculated TD profiles at various distances together with the measured profiles. Figure 3.7b gives the relative frequency of measured and calculated T_{-20m} values for the year 2012. The offsets between rural SAT and GST generally decreases with distance to the city center, apart from the zone between line km 7300 and 7800, where a maximum offset of 4.5 °C is calculated. This zone has the highest building intensity and very little green space.

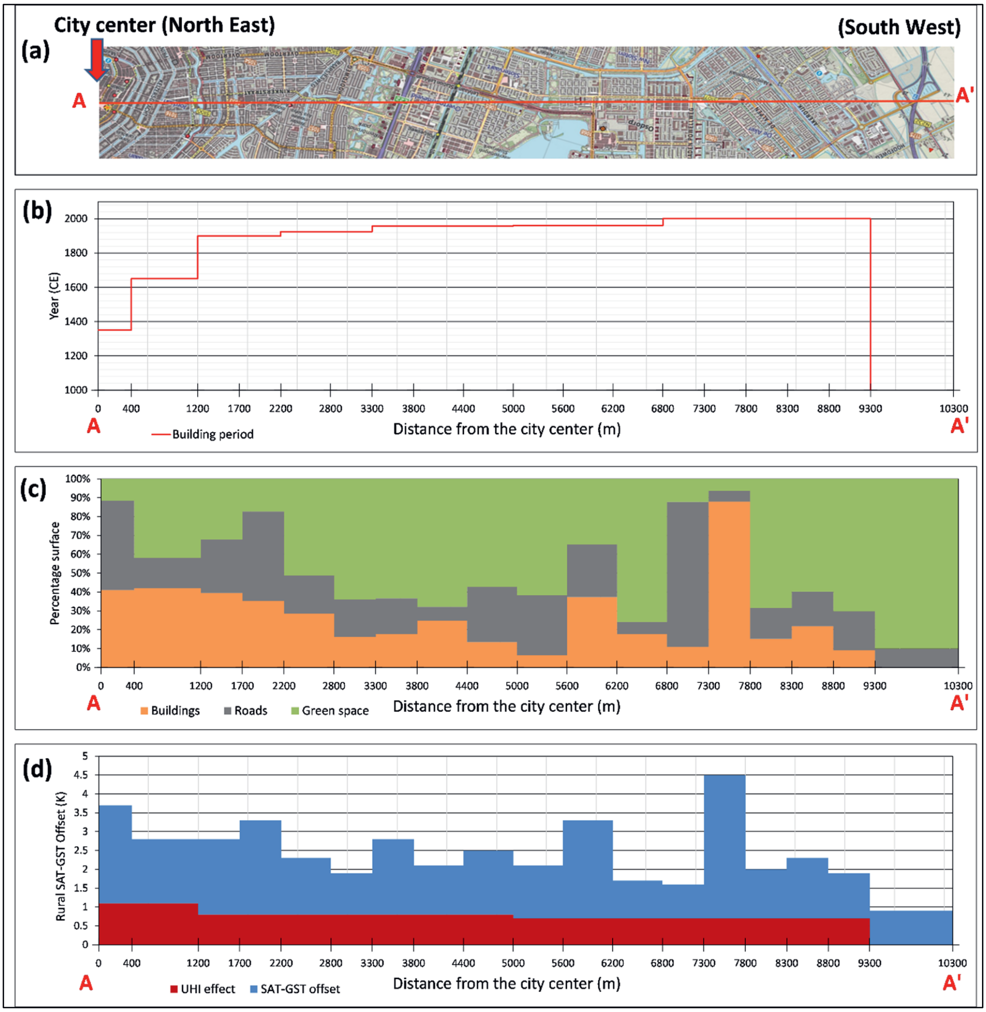

Figure 3.5: (a) Cross section line A-A' plotted on the present-day topographical map, (b) Building periods of the sections along line A-A', (c) Percentages of space occupied by buildings, roads and green space, and (d) UHI effect and total compounded offset between the rural SAT and GST of the sections along line A-A'.

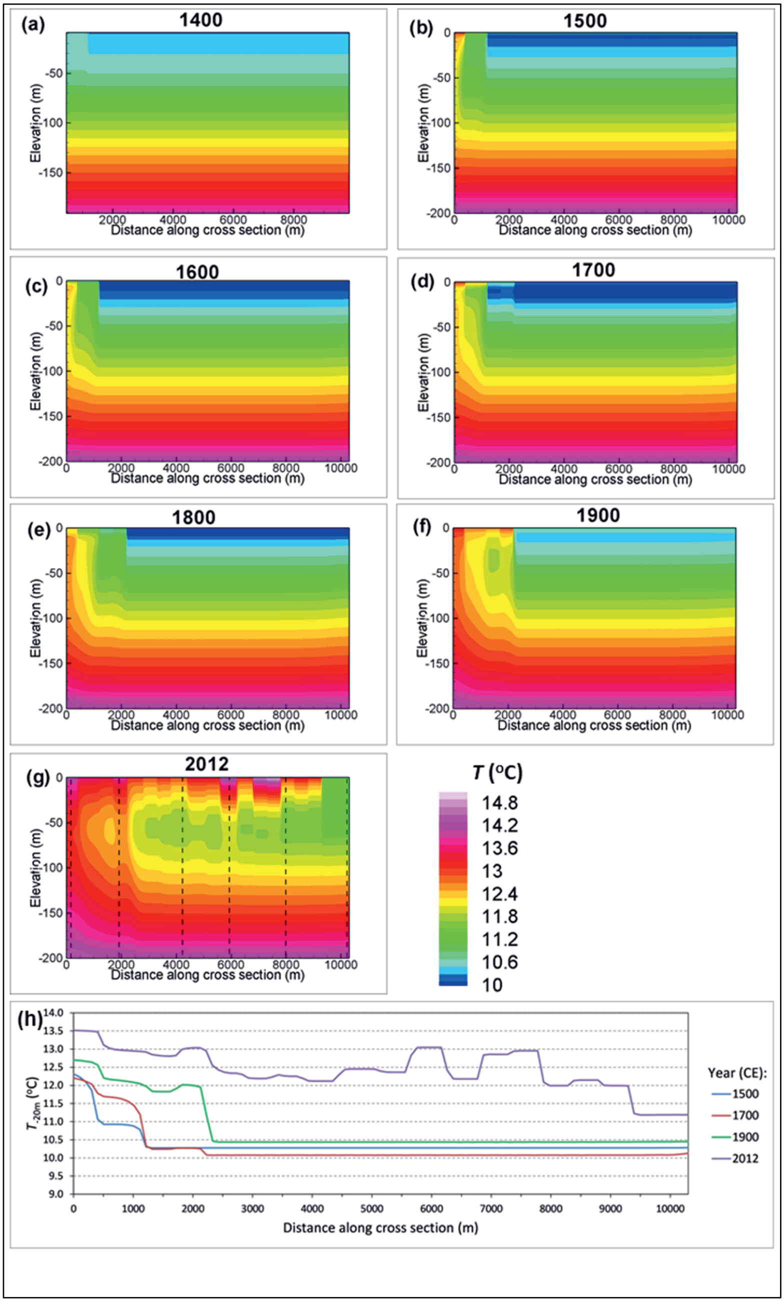

Figure 3.6: Calculated temperatures at selected times (a-g) along the cross section in Figure 3.5. The northeast end of the cross section is on the left, the southwest end is on the right. The dashed vertical lines in panel (g) are the locations of the synthetic TD profiles in Figure 3.5. (h) Calculated T_{-20m} distribution along the cross section in four selected years.

3.5 Discussion

The Amsterdam T_{-20m} observations (Figure 3.1a), with a maximum of 4.1 °C above the background temperature, appear to compare very well with other cities. However, studies in other cities have recorded the subsurface temperatures at variable depths, as well above and below the seasonal zone. This biases the comparison with the present study. The SUHI effects reported are, for example, 5 °C in Winnipeg in Canada (Ferguson & Woodbury 2004; Zhu et al 2010; Zhu et al 2014) and 3.5°C for Istanbul in Turkey (Yalcin & Yetemen 2009). Taniguchi et al. (2007) and Huang et al. (2009) demonstrated that SUHIs exit in various Asian cities. In Basel (Switzerland) the mean temperatures in the saturated zone were found to be approx. 5 °C higher than the average annual SAT (Epting 2013). In various German cities the inferred difference between highest and lowest observed groundwater temperatures is 4 to 8 °C (Zhu et al 2010; Menberg et al 2013a, b, c; Menberg et al 2015; Benz et al 2015a). Locally, subsurface temperatures have been raised to an even larger extent by groundwater heat pump systems or warm water injection (e.g. Zaragoza (Spain) at 8 °C and more [García-Gil et al 2014]).

The observed maximum T_{-20m} values are less than the expected maximum GST (Figure 3.1). This may indicate that the propagation of elevated urban GSTs and attenuation with depth constrain the T_{-20m} to values below the maximum of 15.6 °C based on the urban SAT and SAT-GST offset.

The synthetic-road surface temperatures, shown as predicted GST values in Table 3.1, are probably over-estimations. The low asphalt albedo used is not likely to occur as the asphalt surface is usually covered with chippings with a higher albedo. Furthermore, the albedo of asphalt surfaces increases with the age of the surface. In the city, the insolation of the road surfaces is often reduced due to a limited sky view factor and heat may be discharged by surficial run off and evaporation of precipitation. Therefore, the calculated road surface temperatures are maximum values. This may also explain the lower observed T_{-20m} values compared to the maximum GST. It is recommended to collect long-term surface temperature data at various types of surfaces in the city center to validate and fine-tune the modeling approach described in Appendix 3.2.

The calculated temperature distributions in Figure 3.6 clearly reflect the staged urban expansion in the shifting of the front of higher temperatures to the right end (southwest) of the cross section. Between the end of the 16th century and the late-19th century, little urban expansion took place. Groundwater flow was directed to the northeast and, therefore, the thermal front only moved marginally due to conduction. After 1900, fast urban expansion raised the subsurface temperatures widely in the model, but over a lesser depth than in the older parts of the city. The effect of the groundwater flow is obvious from a slight rightward tilting of the thermal fronts.

The calculated TD profiles in Figure 3.7a show, as expected, the concave deviation of the curves from the straight deeper end of the curves at larger depth for the older urban expansion stages. The calculated TD profiles fit in the measured ranges, supporting the suitability of the approach. However, it is recommended to repeat the TD logging and T_{-20m} measurements in the future to be able to validate the model. Validation of the model would allow the use of the model to predict the future thermal state of the SUHI.

To model and describe the spatiotemporal development of the SUHI, the model domain has been scaled down to generalized sections of 400 to 800 m long. Therefore, a direct comparison of the measured and synthesized profiles will never result in a ‘perfect’ fit. Site specific developments that cannot be incorporated in such a model influence the local TD profiles. Although no direct comparison is possible, the calculated TD profiles appear to have systematically slightly higher temperatures than the observed TD profiles. A possible over-estimation of the GST, as discussed above, may play a role in this as well. The high temperatures in the deeper part of the observed curve 4 (Figure 3.7a) must have been caused by lateral advection from a deep-seated heat source. This was possibly the subway station, which had been constructed in the years preceding the measurements, only 10 m from the piezometer and at a depth of approx. 25 m bgl, although other sources, like an underground thermal energy storage (UTES) system, cannot be excluded.

The distribution of the T_{-20m} values, as a measure of the SUHI intensity, is rather well explained by the model, as demonstrated by the relative frequency distribution of these observations (Figure 3.7b). The distribution of the calculated T_{-20m} values on the cross section compares well with measured T_{-20m} values at random locations. It is remarkable that in both histograms, two peaks occur. The calculated values peak at temperatures that are about 0.5 °C higher than where the peaks in observed values occur. This suggests that the calculated values may be a slight over-estimation of the actual values. The same could be read from the fact that the calculated TD profiles (Figure 3.7a) seem to indicate higher temperatures than the observed TD profiles.

The range of the calculated T_{-20m} values is narrower than that of the measured values. Figure 3.6h shows the calculated T_{-20m} distribution along the cross section, with a maximum of 13.5 °C. The eight observed T_{-20m} values above 14.0 °C were all found in a relatively small area, just south of the city center. The land cover at these locations is not different from comparable observation points and the high T_{-20m} values can, therefore, not be explained by locally higher SAT-GST offsets. All these observation points are located very close (10-20 m) to buildings with deep boiler basements, subway stations or district heating, and a link with these sources can be assumed. These individual anthropogenic heat sources were not included in the model. Four T_{-20m} observations between 13.5 and 14.0 °C are also located near similar potential heat sources but could not be linked unequivocally to known sources.

This leads to the observation that the maximum T_{-20m} on a regional (model) scale, that can be explained from the urban expansion history and land cover, is 13.5 °C. The TD observations, however, are only representative of a small subsurface volume around the observation well. These differences in scale explain, at least in part, deviations between the maximum modeled and observed T_{-20m} values. The T_{-20m} observations between 13.5 and 14.0 °C may suggest that the lower value is a slight underestimation of the actual maximum. Values above 14 °C can be linked to localized anthropogenic heat sources and have no great extent. The actual maximum SUHI intensity at 20 m depth is, therefore, only between 2.5 and 3.0 °C for Amsterdam. Locally, e.g. close to buildings with deep boiler basements, the T_{-20m} values are higher, but these are very local effects.

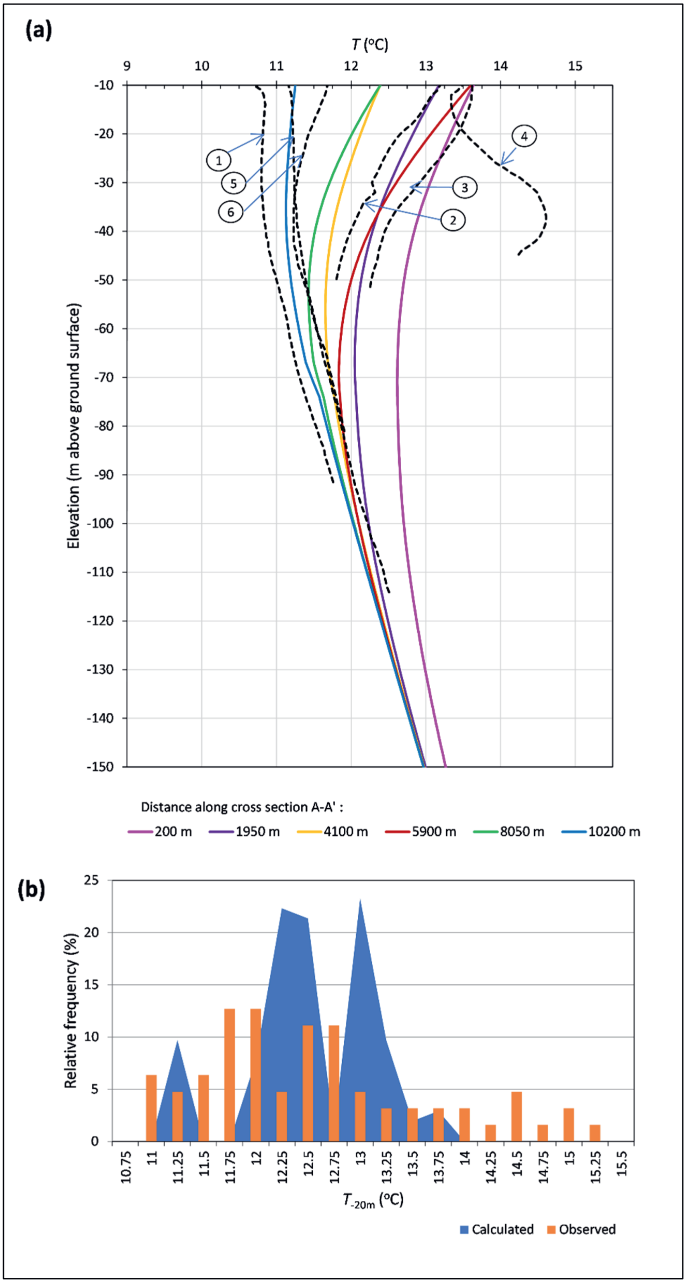

Figure 3.7: (a) Synthesized TD profiles at selected distances along the cross section (solid lines), and measured TD profiles (dashed lines). The locations of the calculated profiles are indicated in Figure 3.6g. The circled numbers at the measured TD profiles correspond to the locations in Figure 3.6a. (b) Relative frequency distributions of the observed T_{-20m} values (n=63) and calculated T_{-20m} values (n=103) at 100 m intervals along cross section A-A'.

One aspect that may, at least in part, explain the difference with other studies is the observation depths. Menberg et al. (2013a) concluded that elevated GST and heat loss from basements are dominant factors in groundwater temperature anomalies in the city of Karlsruhe (Germany) at the groundwater surface between 3 and 8 m bgl. Ferguson & Woodbury (2004) used the same 20-m observation depth as used in the present study to investigate the Winnipeg SUHI. Based on their measurements and numerical modeling, they concluded that the highest temperatures occur close to buildings, and that several hundreds of meters from these buildings, the difference with the background temperature was only a few tenths of a degree. Their conclusion is that heat loss from buildings is the major source of the Winnipeg SUHI.

Bidarmaghz et al. (2019) studied by numerical modeling the amount of heat from basements released to the ground and concluded that this constitutes a significant percentage of the total heat loss from buildings, particularly in the presence of groundwater flow. In that study, basements were assumed to be kept at 18 °C throughout the year. Benz et al. (2015b) used satellite-derived land-surface temperatures in combination with building densities and basement temperatures to estimate regional groundwater temperatures below German cities. Basement temperatures were estimated to be 17.5 ± 2.5 °C. Bayer et al. (2016), by inversion of TD logs from three locations in the suburbs of Zurich (Switzerland), derived temperatures of 15-16 °C below basements of buildings, whereas Zhu et al. (2014) carried out a numerical modeling of groundwater flow and heat transport to simulate the SUHI development of the city of Cologne (Germany) in the past 110 years, and applied a GST increase up to 15 °C for the built-up areas. The basement temperatures in these studies, and therefore the heat loss from buildings, are higher than estimated for Amsterdam, where only semi-basements and crawl spaces prevail, with much lower temperatures. In Amsterdam, therefore, the contribution of buildings to the higher ground temperatures, appears to be much less and in the same range as that of the pavements.

The development of the SUHI of Amsterdam shows that temperatures at depths that are of interest for GES systems (existing systems are located between 25 and 230 m bgl, with averages between 90 and 147 m bgl) are up to 2 °C higher in the parts of the city that were built before 1900 and that these temperatures have increased rapidly in more recently urbanized areas. Increases of these temperatures to 13 °C against a 11 °C background temperature must be expected, thus limiting the cooling capacity of these systems. A lesser cooling capacity may result in higher groundwater demand during the cooling cycle of ATES systems and higher return temperatures. A self-strengthening effect may be the consequence.

3.6 Conclusions

Simulation of the SUHI of Amsterdam by modeling the SAT, UHI, GST relations and offsets based on historical data, results in a realistic distribution of subsurface temperatures that compare well to measured TD profiles and T_{-20m} values. This is, to the authors' knowledge, the first case where a long-term (centuries) urban development, studied in relation to climate change, along with the history of both the surface urban heat-island temperatures and ground surface temperatures, has been modeled to simulate the SUHI of a city.

This simulation sheds light on the relative contributions of the drivers that play a role in this long-term process. It shows that distinction can be made between a regional SUHI effect and localized higher temperature anomalies. The drivers of the regional SUHI are higher GSTs due to pavement and heat loss from buildings. The GST history is related to the SAT history and UHI effect and the history of the land cover (e.g. Kooi 2008; Bayer et al. 2016).

The data illustrate the relationship between T_{-20m} and the age of the urban expansion and building density. It can be expected that the UHI effect is the strongest in the city center, where also the oldest quarters are found. The model results show that these relations and the development of the SUHI can be construed from the urban expansion history and building density.

The maximum regional SUHI intensity in Amsterdam ranges between 2.5 and 3.0 ^{o}C, which is much less than for comparable (similar latitudes and sizes) cities around the world. This difference is caused by omitting high subsurface temperatures associated with localized subterranean heat sources like boiler basements, UTES systems etc. as part of the regional SUHI. The local sources are relatively recent features and have a relatively local impact (horizontal and vertical). The regional SUHI is caused by processes that find their origin in urban developments that started centuries ago.

The distinction between a regional SUHI and localized heat sources has implications for the calculations of the (exploitable) geothermal potential of the SUHI, as done in some other studies (e.g. Menberg et al. 2015; Bayer et al. 2019; Epting et al. 2018).

Appendix 3.1: Auxiliary temperature data

Air temperature observations

Available air temperature observations in Amsterdam, Schiphol and De Bilt are summarized in Table 3.2.

Table 3.2: Average surface air temperatures (SAT) of meteorological stations in Amsterdam and De Bilt.

			Annual average minimum SAT (ºC)				Annual average SAT (ºC)				Annual average maximum SAT (ºC)			
Station name	Period	Avg. SAT	2011	2012	2013	2014	2011	2012	2013	2014	2011	2012	2013	2014
Buiksloterbreek	2000-2014	11.1	8.4	7.9	7.5	9.4	11.5	10.8	10.3	12.3	15.1	13.6	13.6	15.8
Oud West	-	-	-	-	-	9.7	-	-	-	12.4	-	na	na	15.5
Holendrecht	2009-2014	10.6	7.8	7.3	6.9	8.9	11.1	10.6	10.0	12.1	14.9	13.9	13.4	15.5
Amsterdam DL	2012-2014	11.3	-	8.8	8.2	9.7	-	11.3	10.8	11.8	-	14.3	13.9	15.2
Nieuwmarkt	-	-	-	-	-	10.0	-	-	-	12.7	-	na	na	16.1
Westerpark	-	-	-	-	-	9.8	-	-	-	12.4	-	na	na	15.5
Oostzanerwerf	2013-2014	12.3	-	-	8.2	10.8	-	-	11.1	13.6	-	na	14.5	14.1
Amstelveen Noord	2013-2014	11.6	-	-	6.9	8.0	-	-	10.7	12.5	-	na	15.3	18.6
Oostzaan	2012-2014	11.5	-	8.2	7.7	9.6	-	11.2	10.7	12.7	-	14.8	14.4	16.4
Westzaan	2012-2014	11.3	-	7.5	7.0	9.1	-	10.9	10.3	12.6	-	15.1	14.7	17.2
Zaandam	2010-2014	11.5	8.3	7.7	7.3	9.3	12.1	11.5	10.9	12.7	16.8	16.3	15.4	16.7
Amstelveen Westwijk	2009-2014	10.7	7.8	6.9	6.5	7.9	11.8	10.7	10.3	11.6	16.9	15.5	15.1	16.2
Zaanstreek	2011-2014	11.6	9.3	8.7	8.2	10.0	11.9	11.2	10.8	12.7	15.2	14.4	14.2	16.1
Badhoevedorp	2012-2014	11.4	-	8.4	7.4	9.3	-	11.4	10.4	12.3	-	14.6	13.6	15.7
Schiphol Airport	1951-2014	9.9	7.2	6.5	6.1	8.2	11.0	10.4	9.9	12.1	14.8	14.0	13.5	15.9
De Bilt	1951-2014	9.8	6.7	6.2	5.6	7.6	10.9	10.4	9.8	11.7	15.0	14.3	13.7	15.7

Canal water temperatures

The surface water in Amsterdam is being sampled by the Water Authority on a regular basis (at least once monthly) (IHW 2019). Water samples are taken at 0.5 m below the water surface and the water temperature (T_w) is registered. From these data, long-term temperature series could be constructed for two locations in the city center. For the Amstel canal, time series are available for 1990-1999 and 2003-2015. For the Keizersgracht canal, continuous records from 1990-2015 are available. The monthly averages of the surface water temperatures for these periods are compared with the SAT of the same period in Table 3.3.

The surface water temperatures are, however, biased as during the coldest months fewer observations were made. No observations are available when the water is frozen. On the other hand, more sampling was done during warm periods, due to the concern for the water quality. This results in an over-estimation of the average water temperature. When it is assumed that during the winter months for which observations are lacking the water was frozen, the overall average water temperature drops to 11.8 °C, which is marginally higher than the urban SAT.

Table 3.3: Average water temperature (T_w) and urban SAT - 1990-2015(°C)

Month	T_w , Amstel Canal (Magere Brug)	T_w, Keizersgracht Canal (Molenpad)	Avg. all measurements	Avg. SAT, Schiphol	Urban SAT	T_w - urban SAT
Jan.	4.5	4.8	4.7	3.8	4.9	-0.2
Feb.	4.8	4.5	4.6	4.0	5.1	-0.5
Mar.	6.7	6.3	6.5	6.5	7.6	-1.1
Apr.	10.0	10.6	10.3	9.6	10.7	-0.4
May	15.4	15.1	15.2	13.2	14.3	1.0
Jun.	17.8	17.7	17.8	15.6	16.7	1.0
Jul.	20.2	20.6	20.4	17.9	19.0	1.4
Aug.	21.0	20.6	20.8	17.8	18.9	1.8
Sep.	17.0	16.8	16.9	14.9	16.0	0.9
Oct.	12.6	12.5	12.6	11.2	12.3	0.3
Nov.	8.2	8.7	8.5	7.4	8.5	0.0
Dec.	4.8	5.3	5.1	4.4	5.5	-0.4
1990-2015	12.6	12.5	12.5	10.5	11.6	0.9

Appendix 3.2: Pavement GST from radiation data

The GSTs of various pavement types under the metrological conditions of the city of Amsterdam were modeled. In this modelling exercise, a surface-atmosphere radiation-balance (SARB) model was used to calculate a ground heat flux for various pavement types. The calculated ground heat flux is imposed on the top boundary of the 1D version of the heat transport model described in section '*Numerical modeling*'. For the asphalt surface model, the upper 0.2 m has been assigned thermal properties of an asphalt road surface. For granite-sett, brick and concrete surface coverings, this depth was respectively 0.10, 0.07 and 0.05 m. The respective thermal properties of the road surfaces were derived from Herb at al. (2006). Below the surface cover and to a depth of 0.8 m, dry sand is assumed, simulating the road bed that is present below road surfaces.

The radiation balance model calculates the ground heat flux density (*G*) as follows:

$$G = -H_{ga} + \mathrm{Rl}_{ag} - \mathrm{Rl}_{ga} + \mathrm{Rs}_{ag} - \mathrm{Rs}_{ga} \tag{3.1}$$

where *H* is the sensible heat flux density, Rl the long-wave radiation and Rs the short-wave radiation. The subscripts ga and ag denote fluxes directed from the ground to atmosphere and from atmosphere to the ground, respectively. The energy demand of vegetation (the latent heat flux by evaporation and energy use for temperature rise of vegetation) is ignored in this approach to modeling pavements.

One-hour-interval meteorological data from Schiphol Airport for 1990-2014 were used. The city center air temperature was synthesized by the Schiphol SAT plus 1.1 °C. The following relationship (Stewart 1994) was used to quantify the sensible heat flux

$$H_{\mathrm{ga}} = \frac{\rho_{\mathrm{a}} \times C_{\mathrm{p}} \times (T_{\mathrm{R}} - T_{\mathrm{a}})}{r_{\mathrm{h}}} \tag{3.2}$$

where r_{h} is the resistance to heat transfer from the surface, ρ_{a} is air density, and C_p is the specific heat capacity of air at constant pressure. T_R and T_a denote the radiometric surface temperature and air temperature (measured at several meters above the surface). Bennett (2004) evaluates various methods for determining the excess resistance from heat r_h.

In the present study, the method described by Voogt & Grimmond (2000) is adopted, in which the resistance term is calculated as $r_h = r_{am} + r_T$, where r_{am} is the aerodynamic resistance for momentum, and $r_T = r_b + r_r$, with r_b being the bulk aerodynamic excess resistance and r_r is the radiometric excess resistance. The aerodynamic definition is:

$$KB^{-1} = \ln\left(\frac{z_{0\mathrm{m}}}{z_{0\mathrm{h}}}\right), \qquad r_{\mathrm{T}} = \frac{B^{-1}}{u_*} \tag{3.3}$$

where, K is the Von Kármán constant and u_* is the friction velocity. B^{-1} is a dimensionless parameter. z_{om} and z_{oh} are the roughness lengths for momentum and heat. The roughness length for momentum required in this approach has been chosen as 1 m (Bennett 2004). Based on Högström (1985) and

Voogt & Grimmond (2000), the Von Kármán constant has been set at 0.4. The roughness length for heat can be approached as follows:

$$z_{0\mathrm{h}} = z_{0\mathrm{m}}\left[7.4e^{\left(-2.46\mathrm{Re}_*^{0.25}\right)}\right] \tag{3.4}$$

where $\mathrm{Re}_* = \frac{z_{0\mathrm{m}}\, u_*}{\upsilon}$ is the roughness Reynolds number, with a kinematic molecular viscosity υ of 1.461 x 10^{-5} m sec^{-1}.

For the downward and outgoing atmospheric (long-wave) radiation, the methods described by Holtslag & Van Ulden (1980) are applied:

$$\mathrm{Rl}_{\mathrm{ag}} = L_0^+ + 60N_{\mathrm{t}} \tag{3.5}$$

where N_{t} is the total cloud cover and

$$L_0^+ = 5.31 \times 10^{-13} \times {T_{\mathrm{a}}}^6 - 20 \tag{3.6}$$

with T_{a} being the air temperature at screen height (2 m).

$$\mathrm{Rl}_{\mathrm{ga}} = \varepsilon\sigma T_{\mathrm{R}}^4 \tag{3.7}$$

where ε is the emissivity of the Earth' surface and σ is the Stefan-Boltzman constant.

The net incoming shortwave radiation is the incoming shortwave radiation minus the reflected radiation. The incoming radiation is measured directly at Schiphol meteorological station. The reflected radiation depends on the surface albedo. Wide ranges for the asphalt and concrete pavement albedos are cited in literature and previous studies (e.g. Wang 2015). The albedo of asphalt is assumed to be 0.17. For comparison reasons, also a low asphalt albedo of 0.10 is applied. The albedo for granite setts and concrete is 0.30 and 0.32 for bricks.

The latent heat flux is ignored in this model. The surfaces considered are paved surfaces and no evapotranspiration from vegetation on these surfaces is assumed. Negligence of evaporation from the surface may result in an over-estimation of the surface temperatures. Snow cover, resulting in a higher albedo and thermal insulation of the ground surface, has not been taken into account either. In the urban environment, hardly any prolonged periods with a thick snow blanket covering pavements are expected to occur and the effect of a snow cover is assumed to be negligible.

Chapter 4

The thermal impact of aquifer thermal energy storage (ATES) systems: a case study in the Netherlands, combining monitoring and modeling[2]

Abstract

Results are presented of a comprehensive thermal impact study on an aquifer thermal energy storage (ATES) system in Bilthoven, the Netherlands. The study involved monitoring of the thermal impact and modeling of the three-dimensional temperature evolution of the storage aquifer and over- and underlying units. Special attention was paid to non-uniformity of the background temperature which varies laterally and vertically in the aquifer. Two models were applied with different levels of detail regarding initial conditions and heterogeneity of hydraulic and thermal properties: a fine-scale heterogeneity model which construed the lateral and vertical temperature distribution more realistically, and a simplified model which represented the aquifer system with only a limited number of homogeneous layers. Fine-scale heterogeneity was shown to be important to accurately model the ATES-impacted vertical temperature distribution and the maximum and minimum temperatures in the storage aquifer, and the spatial extent of the thermal plumes. The fine-scale heterogeneity model resulted in larger thermally impacted areas and larger temperature anomalies than the simplified model. The models showed that scattered and scarce monitoring data of ATES-induced temperatures can be interpreted in a useful way by groundwater and heat transport modeling, resulting in a realistic assessment of the thermal impact.

4.1 Introduction

Aquifer thermal energy storage (ATES) provides a means for storage and retrieval of energy in the subsurface and reduction of the use of fossil fuels. ATES is a form of seasonal energy storage using one or more pairs of groundwater wells. Groundwater is abstracted from one half of the wells and used for cooling or heating (e.g. houses, commercial buildings, green houses), depending on the season. Subsequently, the warmer or cooler return water is re-injected through the other well(s). The following season, the abstraction and injection directions are reversed. The aquifer is used as a storage medium for the excess seasonal heat and cold (Tsang, 1978; Kannberg, 1982; Lee, 2013).

---

[2] Published slightly modified as: Visser, P.W., Kooi, H. & Stuyfzand, P.J., 2015. The thermal impact of aquifer thermal energy storage (ATES) systems: a case study in The Netherlands, combining monitoring and modeling. Hydrogeology Journal 23: 507–532

In the Netherlands, the number of ATES systems has grown exponentially to over 2,200 in 2015 since their introduction in 1987 (estimates on the basis of data from provincial authorities). In 2010, 200 Mm^3 of groundwater were utilized for ATES in the Netherlands (CBS, 2011). Most ATES systems require a groundwater permit. The licensing procedure includes an impact assessment, which involves the modeling of hydraulic and thermal effects of the system.

The exponentially growing number of ATES systems has led to increasing demand and political pressure to allow these systems inside groundwater protection zones. In the Netherlands, approximately 61% (762 Mm^{3}year^{-1}) of all drinking water is produced from groundwater, riverbank filtrate and artificially recharged surface water (Geudens, 2010), which is abstracted at 206 public supply wells fields that were active in 2010 (Mendizabal et al., 2011). The public supply well fields are situated in groundwater protection zones that encompass the 60-day, 25, 50 or 100 year travel times for water from infiltration at the surface to the wells (Commissie Bescherming Waterwingebieden, 1980; Wuijts et al., 2007). ATES systems are not permitted within these groundwater protection zones in 8 of 12 provinces, and only permitted under specific conditions in 3 provinces (Wuijts et al., 2007).

One of the main concerns regarding ATES systems is the impact on groundwater quality, and the ensuing potential risk to the drinking water supply (Bonte et al., 2011a, 2011b). At present, these impacts and risks are poorly understood, and relevant process knowledge needs to be greatly expanded if licensing policy and regulation are to be changed. ATES systems are thought to affect groundwater quality in various ways, including mixing of originally stratified hydrochemistry induced by the abstraction and injection cycles (Bonte et al., 2010), and induced leakage through confining units.

In addition, modifications of the aquifer thermal conditions caused by ATES systems are also expected to impact water quality via the temperature-dependency of aquifer microbiological and hydrochemical processes (Bonte et al. 2011a, 2011b). Stable groundwater microbiological quality is important where groundwater is a source for drinking water supply and changes in temperature alter the composition of microbial communities (Zog et al., 1997, Wallenstein & Hall, 2012; Bonte et al., 2013) by affecting the growth and survival of micro-organisms (Madigan et al., 2012). Bonte et al., (2013) have shown for sands of the Sterksel aquifer that various chemical effects are temperature induced, such as the (in)congruent dissolution of silicates (K-feldspar), resulting in increased levels of K and Si, increasing DOC due to desorption and SOM mineralization, and desorption from iron oxides, believed to be responsible for increasing concentrations of As, B, Mo, V, and Be.

Comprehensive understanding of the thermal impact of the ATES systems on the utilized aquifers is, therefore, a fundamental element for risk (being the product of the probability and impact) assessment. The present study focuses on these thermal impacts.

The thermal impact is a change in the temperature conditions of the aquifer or the groundwater regime. The spatial extent over which this impact occurs is named thermal affected zone (TAZ) by some authors (e.g. Staufer et al., 2013; Lo Russo et al., 2014) or temperature affected areas (TAA) (Hähnlein et al., 2013). However, an accurate and unique definition of this zone does not appear to exist at present.

Ideally, the thermal impact would be defined by the temperature ranges where demonstrated negative impacts on groundwater quality occur. However, this is impractical at present as these processes are not well understood and still subject to ongoing research. Therefore, in many assessments for ATES systems, which are rarely published in main-stream literature, the thermal impact is defined as the temperature changes greater than an arbitrary threshold (e.g. 0.5°C) above and below the natural background temperature. The impact is commonly evaluated through pre-operational predictive modeling where background temperature is usually assumed constant throughout the aquifer and the thermal impact is evaluated as uniform over the storage aquifer thickness.

The fact that once operational, a high percentage of ATES systems do not perform as expected in terms of thermal efficiency and thermal balance (IF Technology BV, 2007), strongly suggests that the pre-deployment models developed for licensing purposes provide rather poor tools for predicting actual thermal impacts. Few studies are available where the actual temperature development and the influence of the subsurface characteristics were evaluated for a relatively long period after system deployment. Recent examples were presented by Bridger & Allen (2010; 2014) for the Agassiz ATES system in western Canada and by Sommer et al. (2014) for Utrecht University (UU) campus ATES system in the Netherlands. Other studies relate to the simulation of relatively short durations of system use or short duration (injection) experiments (Papadopulos & Larson, 1978; Tsang et al., 1981; Buscheck, 1983; Dwyer & Eckstein, 1987; Xue et al.,1990; Palmer et al., 1992; Molson et al., 1992; Vandenbohede et al., 2009 and 2011).

Allen et al. (2014) recognize aquifer heterogeneity as a critical aspect for understanding coupled flow and heat transport. Bridger & Allen (2010; 2014) and Sommer et al. (2014) investigated the role of heterogeneous hydraulic and thermal properties of the aquifer in the development of the thermal anomalies. Bridger & Allen (2010; 2014) compared the performance of a homogeneous, single layer model and a layered aquifer model. The warm water plume extent in the single-layer model was found to be most sensitive to vertical anisotropy and the hydraulic gradient. A higher hydraulic gradient resulted in an elongated and farther-reaching thermal plume compared to the base case. Increase of the hydraulic gradient resulted in an increase of the plume length in the flow direction, while the width and thickness decreased. In the layered model, simulated temperatures were found to be sensitive to a combination of well screen placement and layering. Preferential transport along high permeability layers resulted in longitudinal plume distortion, and overall higher short-term efficiencies. The warm water plume that formed after injection reached significantly farther in the layered model. The thermally impacted zone and the effect of the heterogeneity on the extent of this zone were not explicitly quantified. During short-term storage, the low permeability layers at screen intervals of the warm water injection well retained higher temperatures. This probably explains the higher short-term efficiencies.

Measurements conducted by Sommer et al. (2014) from 2010 till 2012 revealed unequal distribution of flow rates over different parts of the well screen and preferential flow due to aquifer heterogeneity. The aquifer was modeled by a single layer with homogeneous hydraulic and thermal parameters. Both observed (averaged over the vertical extent of the storage aquifer) and simulated temperatures at various monitoring wells show periodic increases and decreases of the subsurface temperatures of more than 3 degrees at distances 10 to 25 m from the ATES wells. However, the extent of the thermally impacted zones was not the focus of this study and is not reported.

This chapter adds to the currently limited set of observation-based case studies of the temperature development in storage aquifers through a detailed investigation of the thermal impact of an ATES system in Bilthoven, the Netherlands (Figure 4.1). The study involves monitoring of the thermal impact in observation wells and modeling of the 3-dimensional temperature evolution of the storage aquifer and over- and underlying units. In contrast to previous studies (e.g., Bridger & Allen (2014); Sommer et al. (2014)), focus here is on the thermal impact of the ATES system (extent of the thermally impacted zone, maximum and minimum temperatures reached, and temporal variability) rather than on ATES system efficiency. The objective of the study is to evaluate the significance of two factors that influence the impact: (a) complexity associated with the non-uniformity of the "natural" background temperature (both horizontally and vertically), and (b) storage aquifer heterogeneity. The impact under actual operating conditions is also compared to the predicted impact for the design operating conditions.

4.2 Background

The following sections provide information on the study area, followed by a description of the ATES system and the hydrogeology of the site.

4.2.1 Study Area Description

Location

In 2007, the provincial authorities of the province of Utrecht licensed an ATES system at the RIVM (the National Institute for Public Health and the Environment) in Bilthoven (Figure 4.1).

Bilthoven is located northeast of the city of Utrecht in the central part of the Netherlands, approximately 6.5 km northeast of the city center and 3 km from the outskirts of the city. The land surface of the RIVM site is approximately 3.5 m above mean sea level (amsl). Almost 10 km to the east, the topographic elevation increases to over 50 m amsl on the ice-pushed ridge of 'Het Gooi' and the 'Utrechtse Heuvelrug'. This higher area is mainly covered by forest. To the west, Bilthoven borders a low polder landscape, mainly occupied by meadows and surface waters, where the terrain drops to elevations around mean sea level and at the lowest point 4 meters below mean sea level (bmsl).

In 1953, the RIVM moved to the present location in Bilthoven. The oldest buildings date from the early 1950's and are low, barrack like brick stone buildings. The ATES system is designed for cooling and heating of the Cohen building, built in 1988 and modified in 1992, and building G22, which was built in 2008 (Rijksgebouwendienst, 2012).

The wells of the RIVM ATES system are located west of the Cohen building (Figure 4.2) at the RIVM compound.

The RIVM ATES system is located at the border of the 100-year travel time "attention zone" and near the 50-years travel time groundwater protection zone of the Beerschoten public water supply well field (Figure 4.1 and Figure 4.2). The Beerschoten well field consists of 16 wells. Seven of these wells are screened within the same depth range as the RIVM ATES system (screens from 51-71 m bsl to 84-103 m bsl). The other nine wells are screened in a deeper aquifer (approx. 155-175 m bsl). The well field is licensed to abstract up to 8 Mm^3 per year.

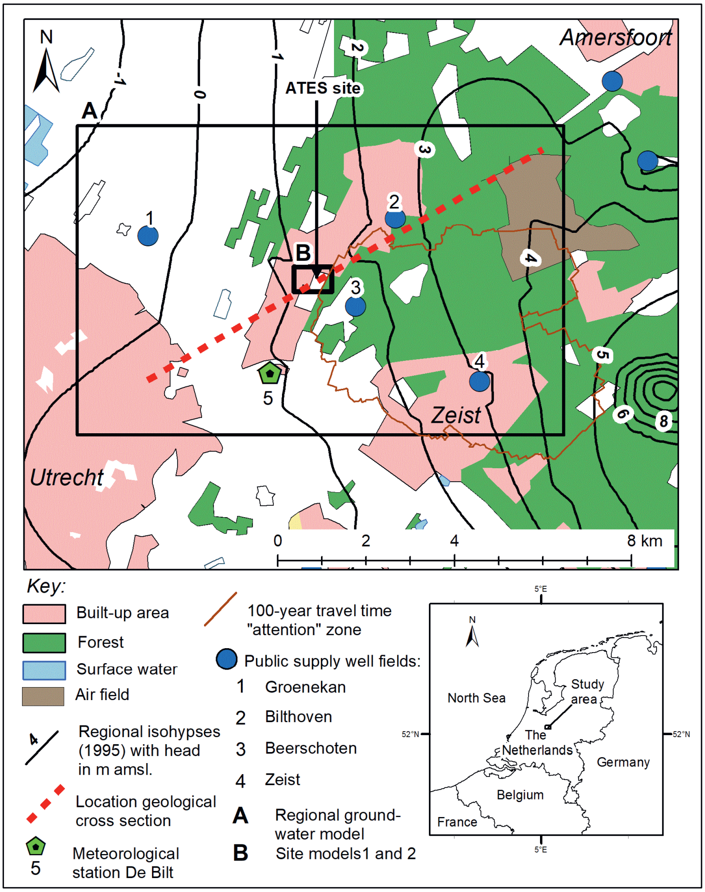

Figure 4.1: Location of the ATES site and its environs (Source of the isohypses: TNO Geologische Dienst Nederland, 2012c).

The RIVM ATES System

The ATES system at RIVM consists of four wells: two wells that are used to inject and abstract cold water (“cold” wells, labelled C in Figure 4.2) and two wells that are used to inject and abstract warm water (“warm” wells, labelled W in Figure 4.2). The wells are placed along a 230 m long transect running north-northeast to south-southwest. Information on depths of screens and casings is summarized in Table 4.1.

Screens have a 315 mm diameter, with 0.75 mm slots. The annulus of the boreholes was filled with gravel (2-5 mm grain size) from the bottom of each borehole up to 2-3 meters above the top of the highest well screen. On top of the gravel pack, 3-4 meters of Mikolit (bentonite) clay was placed. The remainder of the borehole annulus was filled with gravel (1.0-1.6 mm grain size) and Mikolit.

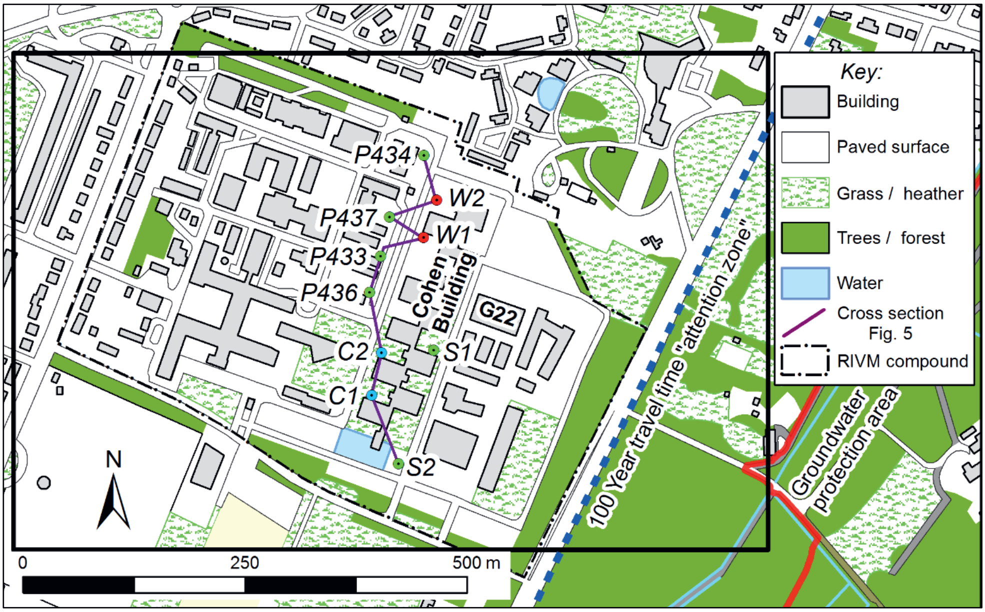

Figure 4.2: Lay-out of the ATES system (cold (C) and warm (W) wells), monitoring wells (P), piezometers (S).

Table 4.1: Summary of ATES well construction details. Depths are m below ground level.

	C1	C2	W1	W2
Casing1	0-55	0-47	0-55	0-48
Screen1	55-75.5	47-73	55-100	48-83
Casing2	75.5-78.5	73-78	-	83-87
Screen2	78.5-103	78-96	-	87-106
Casing3	103-104	96-97	100-101	106-107
Max. borehole depth	105	110	104	109

The groundwater permit for the ATES system allows abstraction and re-injection of groundwater to a maximum of 216,000 m^3 annually and 312 m^3 per hour (Province of Utrecht, 2009). The actual volumes of groundwater abstracted and re-injected in the period 2008-2011 ranged between 33,720 m^3 (2010) and 232,490 m^3 (2008). The average design injection temperatures were set at 17°C (with a maximum of 25°C) in summer and an average of 8°C (minimum 6°C) in winter. Based on these temperatures and flow rates, it was calculated that 2,000 MWh of energy would be stored through the system annually (Royal Haskoning, 2007). The ATES system has been in operation since January 2008. Design and actual abstraction volumes and injection temperatures for the period 2008-2011 are summarized in Table 4.2.

Table 4.2: Summary of the RIVM ATES system design and actual operating regime.

Year	Season	Design abstraction / injection volume (m^3)	Design injection temperature (°C)	Actual abstraction / injection volume (m^3)	Actual injection temperature (average*) (°C)
2008	Winter	108,000	8	107,000	7
2008	Summer	108,000	17	22,000	17
2008-2009	Winter	108,000	8	201,000	7
2009	Summer	108,000	17	23,000	17
2009-2010	Winter	108,000	8	3,000	7
2010	Summer	108,000	17	31,000	17
2010-2011	Winter	108,000	8	3,000	7
2011	Summer	108,000	17	42,000	15
2011	Winter	108,000	8	26,000	7

*: time-based average

Figure 4.3 illustrates the pumping regime of the ATES wells, in relation to the number of days with maximum air temperatures greater than 18°C (meteostation De Bilt; location Figure 4.1). The figure shows that in the first months of 2008 and in the winter season 2008-2009 an excess of cold water was injected compared to the amount of warm water injected in the summer seasons. This was caused by the fact that in 2008 the cooling system of the Cohen building was not yet adapted for the use of the ATES system. In order to restore the thermal balance of the aquifer, in the following two winter seasons a limited amount of cold water was injected, and an excess of warm water was injected from the spring 2009 until the winter of 2011.

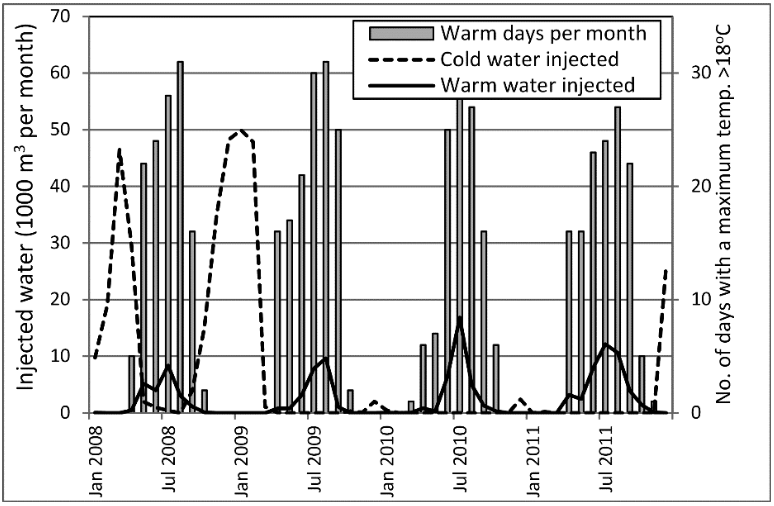

Figure 4.3: Cold and warm water injection periods and number of warm days (days with a maximum air temperature of over 18°C).

The RIVM ATES system has been licensed for a period of five years on condition that intensive monitoring of the system should allow an evaluation of the effects and the licensing policy after this period of five years. Furthermore, the license demands that a long-term closed energy balance of the re-injected water should be strived for, and that an imbalance should not exceed 15% in any period of five years or 10% in a 10-years period.

Monitoring of the ATES system was done with existing piezometers (P433, P434, P436, P437) that belonged to a groundwater abstraction system constructed and abandoned in the 1980's. The P-monitoring wells each consist of nested piezometers installed at various depths in a single borehole. The bottom 1 meter over the piezometers is perforated. The deepest piezometer of each monitoring well is used for temperature logging. The depths of these piezometers is respectively 140.5, 101.0, 98.5, 96.5 m. Two additional piezometers (S1 and S2) were placed as "sentry wells", approximately on the boundary of the zone that could be influenced by the re-injected water. The depth of these piezometers is 60 and 94 m. The lower 1 m of the piezometers is screened. These existing wells were used in the present study.

Geology and Groundwater

Figure 4.4 provides a schematic cross section of the geology. The geology of the site is described here on the basis of the site boreholes and boreholes and the geological model available in the database DINOloket of TNO Geological Survey of the Netherlands (TNO Geologische Dienst Nederland, 2013).

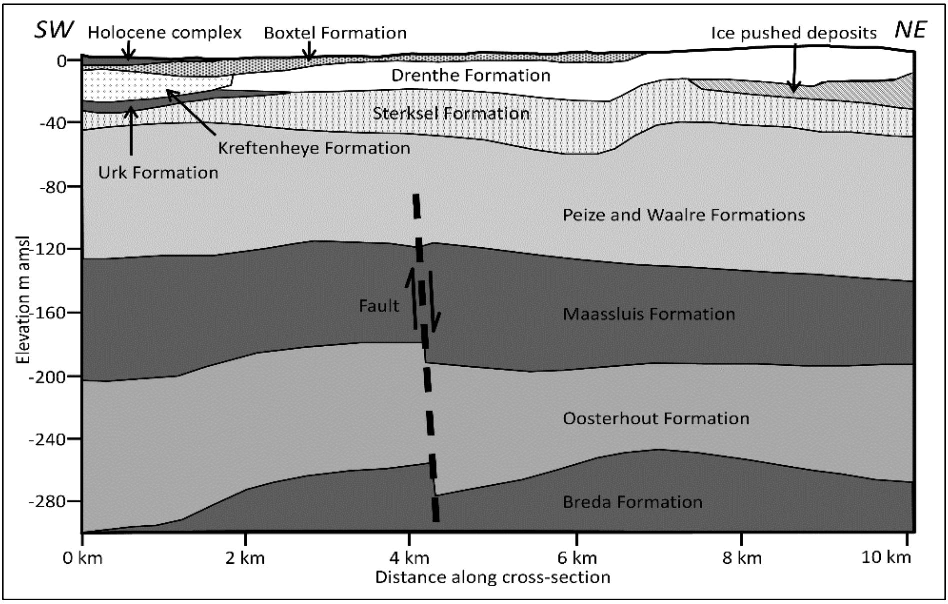

Figure 4.4: SW to NE geological cross section.

From a depth of around 270 m below mean sea level (bmsl), very thick (to a depth of almost 600 m bmsl) marine clay deposits of the Miocene Breda Formation are found. These clays form the base of the hydrogeological system of the area and are overlain by sandy Pliocene deposits of the marine Oosterhout Formation to a depth of approximately 190 m bmsl. The Oosterhout sands are generally very fine with interspersed clay layers.

The Tertiary deposits in turn are overlain by early Pleistocene alternating marine sands and clays of the Maassluis Formation, which is found from a depth of approximately 117 m bmsl. In the nearby Beerschoten public supply well field, nine of the abstraction wells have been drilled in the sandy strata of this formation. The alternating sand and clay layers are ten to several tens of meters thick.

The RIVM ATES system is situated within the aquifer formed by interfingering sands and gravels of the Peize and Waalre Formations. Seven of the Beerschoten public supply wells are also situated within these formations. These deposits are laid down by early Pleistocene river systems from the east (Peize Formation) and the (proto) Rhine (Waalre Formation) and are found from a depth of approximately 49 m bmsl. At various levels in these formations, thin (several meters thick) clay layers are found.

On the site itself, the Peize and Waalre sands are separated from the phreatic aquifer by a several meters thick clay layer or sandy clays of the mid-Pleistocene alluvial Sterksel Formation. Away from the site, this layer pinches out. To a depth of approximately 19 m bmsl, the Sterksel Formation consists of fine sands.

The Sterksel sands are overlain by coarse sands of the Drenthe Formation. These sands are glaciofluvial deposits that originate from the ice-pushed ridge that is found to the east of the site. Ice-pushed, tilted deposits are found overlying the Sterksel Formation from 2.5 km northeast of the site. These tilted deposits consist mainly of the fluvial sands, gravels and clay layers of the mid-Pleistocene Urk Formation. The flanks of this ice-pushed ridge are covered by the glaciofluvial deposits of the Drenthe Formation, which pinch out 3 km to the west of the site.

Where the Drenthe sands pinch out to the west, fluvial deposits of the Urk and Kreftenheye Formation are found interfingering with these glaciofluvial sands and a thin layer of windblown cover sands of the Boxtel Formation increases in thickness. From approximately 2.5 km to the southwest, Holocene surficial deposits of clay and peat occur with increasing thickness to the southwest.

Faults with a (limited) vertical displacement are present in the Breda through Sterksel sequence of formations. The Breda Formation shows a number of northwest to southeast trending (echelon) faults as well east as west of the site. Faulting in more recent Tertiary to Pleistocene deposits is limited to areas southwest of the site. A fault in the Sterksel Formation southwest of the site may have influenced the thickness and vertical position of the Sterksel clay layer.

The strata as found to a maximum depth of 140 m below ground level at the site have been interpreted and depicted in Figure 4.5. The median grain sizes in the boreholes drilled at the site, obtained from 1m interval samples, have been interpolated and show a sequence of clays, sands and gravel lenses. The local hydrogeological base is formed by the clays of the Waalre Formation. The overlying Peize and Waalre deposits grade from medium fine grained to coarse sands, with some gravel lenses at various depths and form a confined aquifer. The Sterksel Formation above these deposits is generally fine to medium fine grained, with a semi-confining clay layer around wells C2, P434 and P435. The overlying Drenthe and Boxtel sands are medium fine to coarse grained and form an unconfined aquifer.

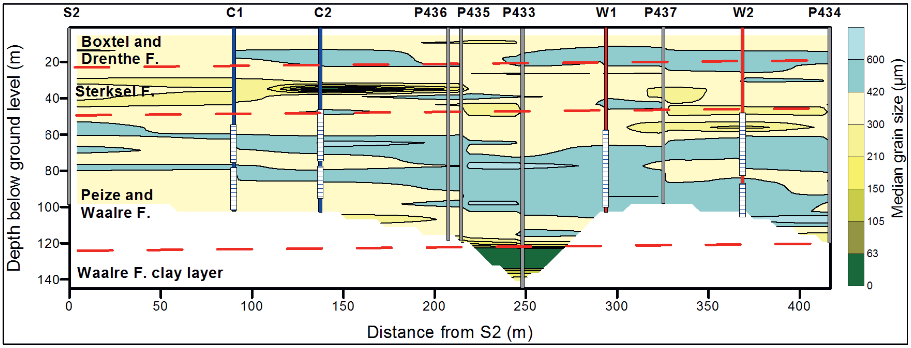

Figure 4.5: Cross section of interpolated median grain sizes (in µm) along wells at the ATES site. The red dashed lines indicate the approximate boundaries of the litho-stratigraphic units.

Existing groundwater isohypse (equipotential) maps indicate a regional groundwater flow from the ice-pushed ridge in the east, to the polder area in the west (Figure 4.1). Measurements at the ATES site between 2010 and 2012 (monitoring wells S1, S2, P433, P434, P436 and P437) showed groundwater levels varying seasonally between 1.1 and 1.7 m amsl (1.6-2.2 m below ground level). A downward component of groundwater flow is inferred at the site from the fact that hydraulic head at depths > 95 m bgl is about 13 cm lower than the head at depths < 20 m bgl when the ATES system is not operating.

The four public supply well fields present within a radius of 5 km from the ATES site extract groundwater from various depths between 50 and 180 m bmsl. The groundwater abstraction at these well fields, and in particular the larger well fields Beerschoten and Groenekan, creates a groundwater divide at or near the ATES site, groundwater east of the ATES system flowing to the Beerschoten well field and west of the site flowing in the direction of the Groenekan well field.

Higher salinity, brackish groundwater exists at deeper levels (1,000 mg L^{-1} chloride concentrations at approximately 250 m depth). The higher densities of these waters are not expected to influence groundwater flow conditions at the depths considered in the present study. Groundwater abstracted from the public supply well fields above this zone contains chloride concentrations ranging between 20 and 38 mg L^{-1} (Vitens 2012).

4.2.2 Data and Methods

General Approach

The thermal impact assessment of the ATES system involved the following general steps. First, the background temperature field was studied using temperature logs for the monitoring wells. Second, information on the actual thermal impact of the system was obtained by frequent temperature logging in the ATES wells and monitoring wells for several years since system operation started. Third, the thermal impact was modeled using the borehole temperature data, ATES operational data, and a broad set of hydrogeological data. Two site models (area shown in Figure 4.2) were developed with different levels of detail regarding representation of the background temperature field and the hydraulic and thermal properties (heterogeneity). A larger scale regional groundwater flow model (area shown in Figure 4.1) was used to determine appropriate boundary conditions and initial hydraulic parameters for the site models.

Groundwater flow, solute transport and heat transport calculations were performed with the model code SEAWAT (version 4), a coupled version of MODFLOW and MT3DMS designed to simulate three-dimensional, variable-density, variable-viscosity saturated groundwater flow (Thorne et al. 2006; Langevin et al. 2008; Hecht-Méndez et al. 2010). Temperature dependency of the fluid density and viscosity were included in the calculations. Although density effects are of negligible importance because the temperature differences for the present ATES system are relatively small, the differences in dynamic viscosity at these temperature ranges cannot be ignored.

Background Temperature Field

The background temperature field is complex and non-uniform (both horizontally and vertically). This temperature field forms (a) the reference situation for thermal impact assessment and (b) initial and boundary conditions for the thermal modeling. The background temperature field of the ATES site was constrained using monitoring wells where repeat temperature logs collected in the present study (2010-2012) showed stable temperature conditions at depths corresponding to the storage aquifer. Background temperature data were also obtained from older temperature logs obtained by the drilling contractor involved in ATES system construction. These logs were measured on October 1, 2008, and April 7, 2009, in monitoring wells P433, P434, P435, P436 and P437. Although these logs also were measured after the system operation had commenced in January 2008, they also reflect the undisturbed temperature field as the zone of influence of the ATES system is unlikely to have reached the location of these wells at the times of logging (as was confirmed by the later modeling and logging).

Figure 4.6a depicts selected temperature logs (summer 2010) for observation wells where ATES impact is absent at the time of the logging. The profiles all display a distinct C-shape with minimum temperatures occurring at depths between 50 and 80 m. This pattern indicates that marked GST warming within the past several decades (e.g., Pollack & Huang, 2000; Taniguchi et al., 1999) has taken place on the premises of the RIVM, inducing downward heat flow and progressive subsurface warming. At depths of 100 m and more, the thermal gradient appears to gradually approach ‘normal’ values representative of upward conductive heat transport from deeper crustal layers. In the upper 20 m, the profiles show the influence of GST change during the past few years, including the “surficial zone” with high-amplitude ‘wiggles’ reflecting seasonality.

Apart from these general characteristics, inspection of Figure 4.6 shows that the background thermal regime in the study area varies horizontally, in particular up to depths of about 80 m. These inter-well differences most likely reflect differences in local GST histories associated with surface conditions (Ferguson & Woodbury 2004, 2007; Kooi 2008; Cermák et al. 2012).

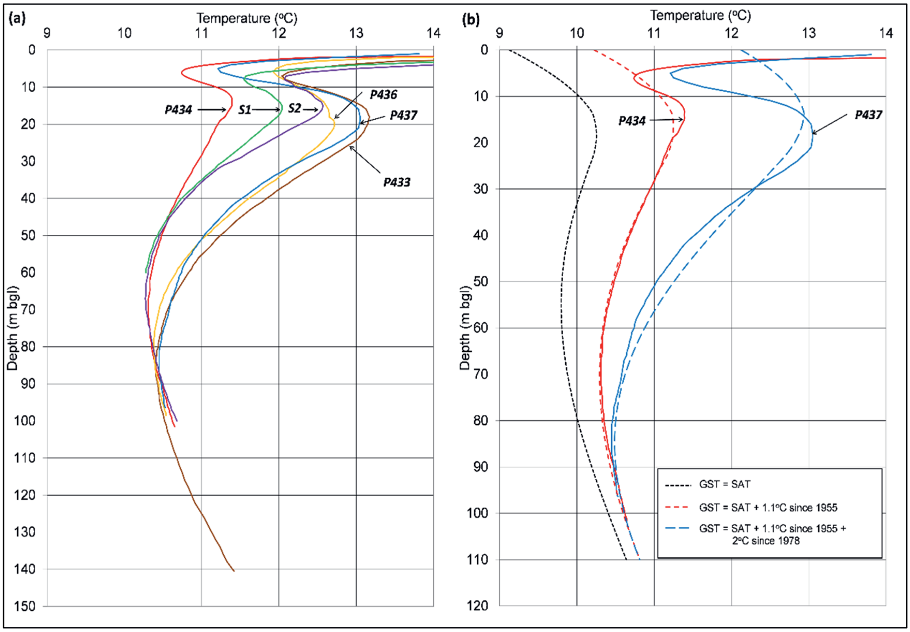

Figure 4.6: (a) Measured background temperature logs at the monitoring wells and (b) comparison of measured background temperature logs at some of the monitoring wells (solid lines) and modeled temperature profiles (dashed lines). GST=ground surface temperature, SAT=surface air temperature.

The lowest subsurface temperatures to a depth of 80 m bgl are found in P434. This monitoring well is located at the edge of the RIVM compound and underneath trees, close to buildings dating from the 1950's. The profiles of wells S1 and S2 show higher temperatures at depths shallower than 40 to 50 m bgl. This suggests a relatively recent GST increase at these points. This can be explained by the location of these wells near the Cohen building (built in 1988) and a parking lot (constructed in the early 1990's). The other temperature logs (wells P433, P435, P436, P437) show increased temperatures compared to P434 to a depth of 80 m bgl. These monitoring wells are all located closer to the center of the compound that has been built up since 1953, with some building renovations in the 1970's. Overall, the subsurface temperature distribution appears to be strongly related to the building developments on the site.

In the storage aquifer (approximately 50 – 100 m bgl) lateral temperature differences are largest at the top (10.5 - 11.3ºC). Vertically averaged temperatures range from 10.4ºC (P434, S2) to 10.7ºC (P437).

Dedicated Temperature Monitoring for Impact Assessment

Between June 2010 and March 2012, repeat temperature logging was completed in all monitoring wells and in the ATES wells. A total of 120 logs were obtained with a measurement interval of 1 m. Temperature was measured with a thermistor sensor (type DC95) mounted on a small-diameter probe equipped with spacers and attached to a microprocessor, logger and power source by an electric wire. Relative accuracy of the thermistor, which is important to accurately record the temperature-depth trend in each log, is about 0.01°C. Comparison with a calibrated thermometer showed the thermistor had an absolute error of about of -0.16°C (temperature is too low) for temperatures in the range 4°C to 31.5°C. The data presented here were not corrected for this systematic error of the instrument. The repeatability of the temperature measurements for 'undisturbed wells' was about 0.01°C. Therefore, instrument drift was considered to be negligible.

In addition to the logging, the deepest piezometer of well P437 was equipped with 5 "GeoBead^{TM}" sensors (Alert Solutions BV). These multi-sensors were placed at the depths 25, 50, 65, 80 and 95 m below ground level and attached to a GPRS telemetry system. The temperature measurements of the sensors, however, showed a too large difference with the manual measurements and a substantial drift in time. Therefore, the temperature readings of the GeoBeads^{TM} have not been used.

ATES Operational Data

Operational data of the ATES system were obtained from the building management system. These included the amounts and average temperatures of water abstracted and re-injected on a monthly basis for the period 2008-2011. For the period 2010-2011 these data were also available at a temporal resolution of 8 minutes.

Regional Groundwater Flow Model

Design

The regional groundwater model covers a 7 x 11 km^2 area (Figure 4.1). Seven model layers were used: layer 1 aggregates the sands of the Boxtel, Drenthe, Kreftenheye, Urk and Sterksel Formations; layer 2 the Sterksel clay; layer 3 the Sterksel sand; layers 4 and 6 the Waalre clays; and 5 and 7 the Peize/Waalre sands. The base of the model corresponds to the top of the low-permeability Maassluis Complex. The geometry of the formations was obtained from TNO Geologische Dienst Nederland (2012b).

A uniform cell size of 100m x100m was used resulting in 53,900 model cells. The initial hydraulic conductivities (horizontal conductivities for the aquifers, and vertical conductivities for the aquitards, with initial anisotropy factors of 5 for the aquifers and 10 for the aquitards) were averaged from data from the regional geohydrological information system REGIS (TNO Geologische Dienst Nederland, 2012b).

Drainage patterns were derived from topographical map information and modeled with the MODFLOW river package (Harbaugh et al. 2000). The north-western corner of the model area represents a polder with a dense network of ditches which were represented by drains at a level of 0.5 m below ground level. Recharge was differentiated according to the land cover/use using 26 different zones. Head was specified along the lateral boundaries with values based on the regional isohypse map (Figure 4.1). 55 wells were incorporated representing public water supply well fields and other permanent abstraction wells. Average abstractions for the period 1990-2000 were used for each well, derived from provincial groundwater records. Steady state conditions were simulated.

Calibration

Average groundwater levels and hydraulic heads of 113 piezometers (source: TNO Geologische Dienst Nederland, 2012a) for the period 1990-2000, prior to the ATES system operation, were used as targets for calibration and sensitivity analysis. Calibration parameters were the horizontal and vertical hydraulic conductivities of the model layers and the recharge in the recharge zones. Calibration involved repeated automated sensitivity analysis, followed by manual adaption of the most sensitive parameters. The calibration aimed at overall low residuals of calculated and measured heads, with the lowest residuals around the ATES site.

Figure 4.3 lists the initial and calibrated hydraulic conductivities. Calibrated recharge values ranged from less than 0.33 mm day^{-1} for built-up areas and roads, and 0.045 mm day^{-1} for forests up to 1.5 mm day^{-1} for parks and grassland.

Table 4.3: Initial and calibrated hydraulic conductivities of the regional model.

	Initial conductivity (m day^{-1})		Final conductivity (m day^{-1})	
Layer no.	horizontal	vertical	horizontal	vertical
1	10	3	35	10
2[a]	0.01	0.001	0.1	0.04
3	20	5	4	2
4[a]	0.01	0.001	0.1	0.015
5	20	5	50	25
6[a]	0.01	0.001	0.1	0.04
7	10	3	22	7

[a]: conductivities in the zones where this layer is clayey, otherwise the conductivity of the overlying or underlying layer was assigned.

The statistical parameters for the calibration are:

Residual mean:	-0.02 m;
Residual standard deviation:	0.14 m;
Absolute residual mean:	0.11 m;
Residual sum of squares:	2.12;
RMS error:	0.14
Scaled RMS error:	0.05

The residuals fall within 10% of the range of the observations at the targets, which is 2.60 m. For the layer comprising ATES storage aquifer and within a radius of 2 kilometers from the ATES site, all residuals were less than 0.10 m. Only at the Beerschoten well field at 1,500 m to the southeast, slightly higher residuals (0.11 to 0.17 m) were found near the abstraction wells.

The flow pattern in the ATES storage aquifer shows that the ATES system is located on a groundwater divide; east of the system, the flow is directed south to southeast, west of the system, the flow is directed southwest to west.

Site Models

General design characteristics

The site models encompass a model area of 850x560 m^2 in map view (Figure 4.2); at least several hundred meters beyond thermally impacted zones. The main design features of the two site models are described in detail below and summarized in Table 4.4. Site Model 1 has the same layering as the regional model, with the exception of the top layer of the regional model, which was split into two layers, such that the specified top boundary temperature is more confined to the surface in the site model. Site Model 2 was more detailed in terms of vertical resolution, vertical and horizontal heterogeneity and the top thermal boundary condition.

Table 4.4: Site Models 1 and 2: key design characteristics

Model characteristic	Site Model 1	Site Model 2
Cell size (map view)	5x5 m^2	5x5 m^2
Model layers	8 layers, variable thickness	60 layers, each 2 m thick
No. of cells	152,320	1,142,400
Top boundary temperature	Uniform and temporally constant	2 zones of which the GSTs are time dependent as explained in following paragraphs.
Initial temperatures	3 zones in storage aquifer layer, based on observed lateral variation. Other layers have a uniform mean value.	3 zones in all 60 layers, based on observed lateral variation.
Hydraulic conductivity	Copied from regional model	Varying per cell, based on 3D interpolation of grain-size data.
Heat capacity	Single values for sand-rich and clay-rich zones (2).	Uniform, based on variations in geophysical logs and empirical relations.
Thermal conductivity	Lithology-based literature values for sand-rich and clay-rich zones (2).	Values based on geophysical logs and empirical relations aggregated into 7 zones.

Hydraulic boundary conditions, initial condition and stresses

Fixed heads were imposed along the western and the eastern boundary and a general head boundary (GHB) condition along the northern and southern boundaries. The GHB was applied to allow for time dependent heads due to a pumping station to the southeast and another ATES system to the north. The hydraulic heads were derived from the regional groundwater flow model. The heads from the regional model cells at a distance of 300 m north and south of the model edges were used as GHB control heads. The GHB conductances were calculated from the grid cell face surface areas perpendicular to the cross-boundary flow, the hydraulic conductivity of the model layer in which the cell is located and the distance to the GHB head. In the SEAWAT simulations, the GHB elevation was set to the center of the cell. The initial head field in the site models was set uniformly to 0 m amsl (approximately 3.5 m bgl).

The recharge distribution assigned to the top of the models was copied from the regional model. As no drainage features occur within the area of the site models no other boundary conditions were required at the top boundary.

The ATES wells were incorporated in the model by entering the top and bottom levels of the screened sections. For the wells with multiple screened sections, the abstraction/injection rates for each section was calculated as a fraction of the total rate equal, by multiplying the total rate by the fraction of the total transmissivity of the screened aquifer material. The monthly abstraction/injection volumes for the period 2008-2011 were used in the heat transport simulations. The 8-minute resolution time series for the period 2010-2011 was used to calibrate the storage properties of the site models (see following section).

Hydraulic conductivity and storage properties of the site models

In Site Model 1, the hydraulic conductivity of the model layers was copied from the regional groundwater flow model. In Site Model 2, a fine-scale heterogeneous permeability was introduced.

The grain-size-permeability correlation of Shepherd (1989) was used to assign the hydraulic conductivity distribution of Site Model 2. First the median grain size of the sand fraction (the fraction >63 µm) was recorded in 1 m intervals for the ATES and monitoring wells and a number of additional boreholes within the model area. These medians were estimated in the field with a ‘sand ruler’. The values were subsequently interpolated over the model domain by the inverse distance weighting and converted to hydraulic conductivity with the Shepherd correlation. The two parameters in this correlation (a coefficient and a grain size exponent) were optimized (to respectively 4700 and 1.66) so that the effective transmissivities of the aquifers in the site model were consistent with the calibrated transmissivities of the regional model.

Figure 4.7 displays the inferred permeabilities for borehole P433. The median grain size – permeability relation for the site lies close to that of channel deposits (Shepherd, 1989), which is consistent with the fluvial depositional history of the formations at the site. Incorporation of subsurface heterogeneity in Site Model 2 resulted in the storage aquifer permeability widely ranging between 18 and 132 m.day^{-1} for the sandy strata, with locally lower and higher permeabilities for respectively loamy/clayey and gravelly strata, whereas in Site Model 1 the storage aquifer comprised two permeabilities of 55 and 60 m.day^{-1} (Figure 4.7).

Storage properties of the site models were assumed to be uniform within the model domains. Specific storage and specific yield were initially set at 1E^{-5} m^{-1} and 0.20 respectively, and optimized in model calibration of the site models for two periods when the ATES system was in use.

For period 1 (19-22 July 2011) water was injected through the ‘warm’ wells and water abstracted through the ‘cold’ wells from morning until the evening (respectively from-to: 08:56-18:56 hrs.; 09:52-18:32 hrs; 09:04-18:40 hrs.; and 11:44-18:16 hrs. with an interruption between 14:24-17:12 hrs.) . During the evening and night, the ATES system was not operational. Monitored heads in the storage aquifer at P437 (recorded at 8-minute intervals using GeoBead^{TM} pressure loggers) was used as calibration target. The observed heads were simulated with Site Model 1. This necessitated a small adjustment of the horizontal and vertical hydraulic conductivity of the storage aquifer from respectively

50 and 25 m day^{-1} to respectively 55 and 27 m day^{-1}. The specific storage remained unchanged for all layers at 1e10^{-5} m^{-1}. The specific yield was increased to 0.25. After these adjustments, the calculated and measured peaks of the hydraulic head show a good agreement as shown in Figure 4.8.

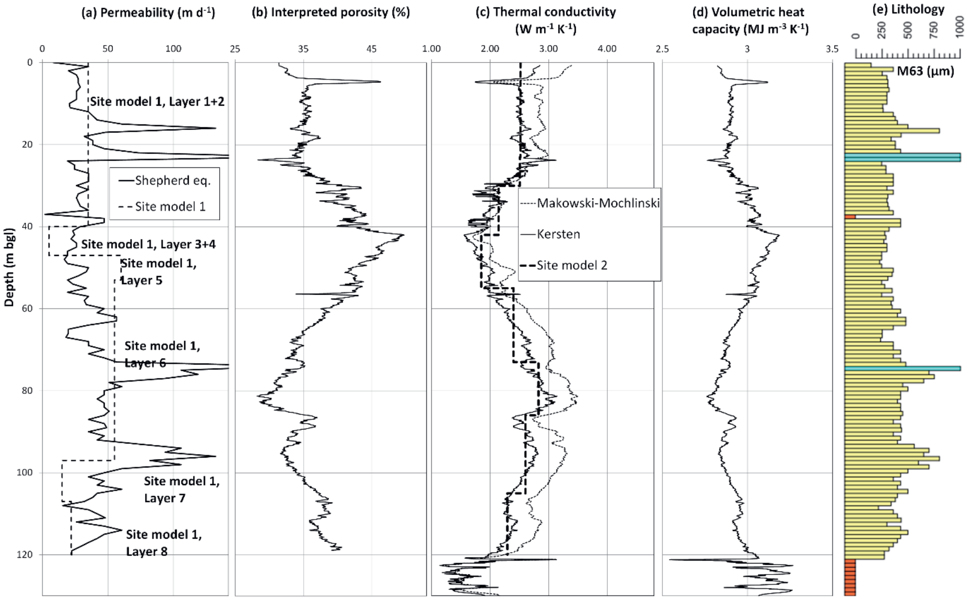

Figure 4.7: (a) Inferred permeability, (b) porosity, (c) thermal conductivity, (d) volumetric heat capacity, and (e) lithology for borehole P433 (yellow=sand, blue=gravel, and orange=loam). The width of the lithology symbols in panel e indicates the median grain size.

For period 2 (15-18 August 2011, from respectively 09:08-18:12 hrs.; 09:32-19:32 hrs.; 08:44-18:12 hrs.; and 11:40-17:40 hrs.) head data for wells P433, P434 and S1 (recorded at 10-minute intervals, using Diver^{TM} pressure transducers from Schlumberger Water Services) were used as targets. These heads were simulated with both Site Model 1 and Site Model 2 as a verification. Figure 4.9 shows that the calculated heads at monitoring wells P433, P434 and S1 for this period show a good agreement with the high frequency logs of the heads at these wells for both site models, demonstrating that the translation of the transmissivity of the simple Site Model 1 into highly variable and heterogeneous permeabilities of Site Model 2 was successful.

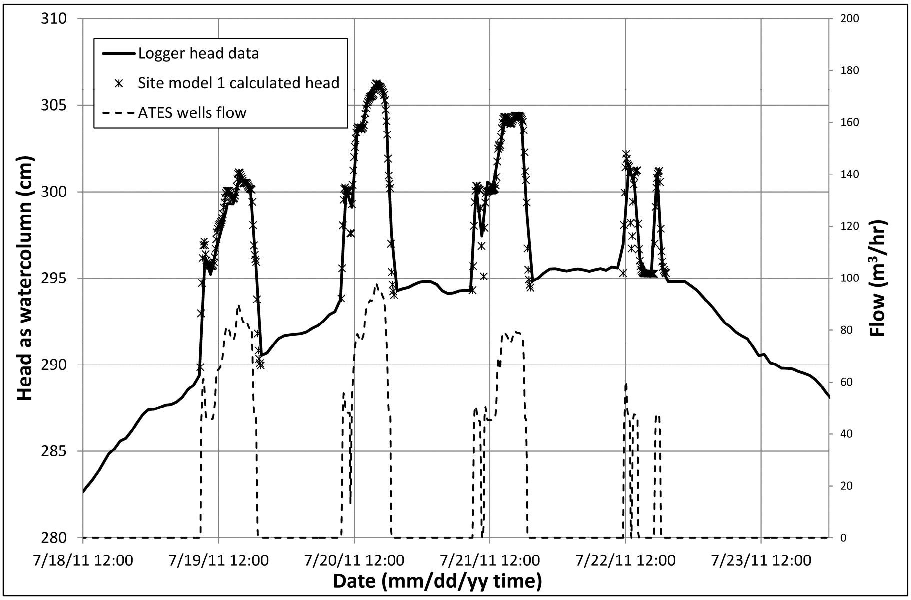

Figure 4.8: Verification of Site Model 1 with hydraulic heads at P437, July 2011.

Porosity

The total porosity was derived from geophysical borehole logging data and grain size analysis of nearby boreholes. Geophysical log data were available for the "P" monitoring wells (Figure 4.2) and grain size-data for the boreholes of the Beerschoten well field (Figure 4.1). Clay content for the monitoring wells was derived from the gamma ray (GR) logs and information about the maximum clay content in the logged formations, and using Larionov's equation (Larionov, 1969). A regression of the relation of the clay and silt content in the Beerschoten boreholes showed these quantities to be strongly correlated for the formations studied. This also enabled the assessment of silt content with depth.

The Humble equation (Winsauer et al., 1952) was used to derive the porosity from the long normal (LN) electrical resistivity. The sediment electrical conductivity depends on the porosity and porewater conductivity and the clay content. LN-resistivity was therefore first corrected for the clay content using the method described by Glover (2008) for laminar clays in sandy formations. Porewater electrical conductivity in the Humble equation was constrained using the national groundwater database DINOLoket (TNO Geologische Dienst Nederland, 2012a); a relationship was established for the depth-dependency of conductivity.

The total porosity as derived from the borehole geophysical log in P433 is depicted in Figure 4.7. The geophysical log interpretations show a clay and silt-rich section between 23 and 42 m bgl in borehole P433. Above and below this section, an average total porosity has been calculated of 35% and 37% respectively. The clay and silt-rich sections show porosities up to a maximum of 50%, with an average of approximately 45%.

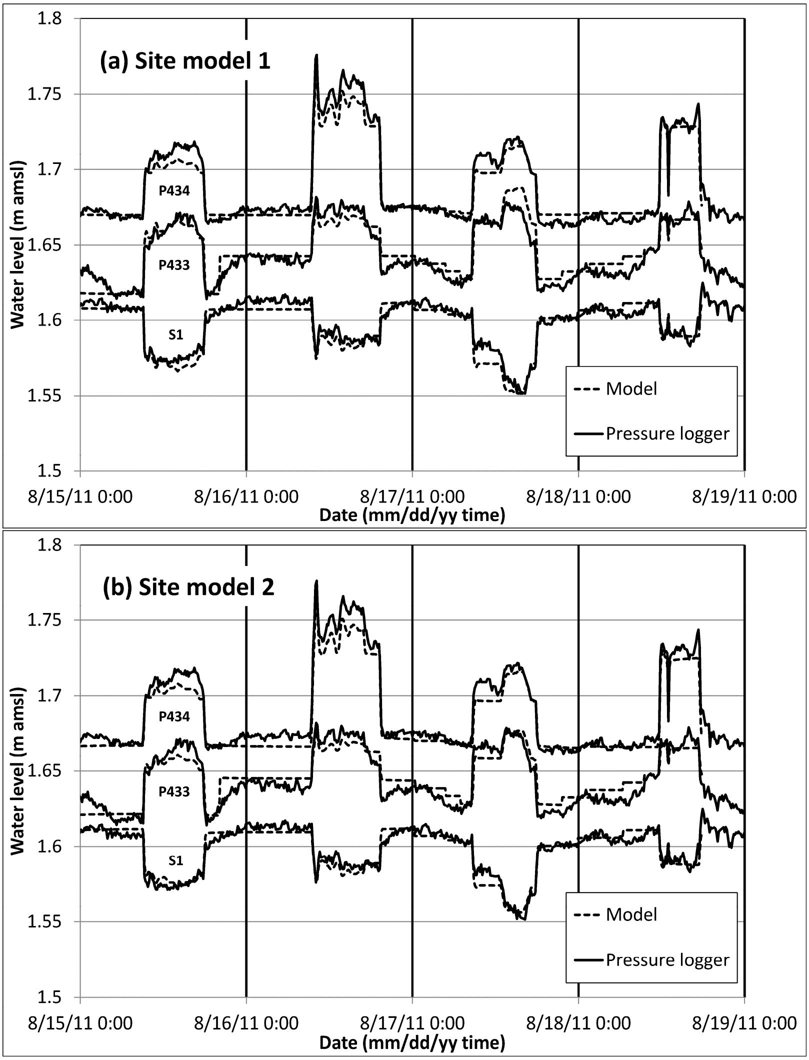

Figure 4.9: Verification of the (a) Site Model 1 and (b) Site Model 2 with hydraulic heads at P433, P434 and S1, August 2011.

Thermal properties of Site Model 1

Parameter values used to assign thermal properties are listed in Table 4.5. Bulk thermal conductivity and volumetric heat capacity values are linked to two basic lithological classes: sand and clay. The thermal conductivity values are representative values from the literature (Witte et al. 2002). Volumetric heat capacity for the two lithologies is calculated from simple mixing of the heat capacities of groundwater and sediment solids/minerals:

$$\rho_b c_b = \varphi \rho_w c_w + (1 - \varphi) \rho_s c_s \qquad (4.1)$$

where ρ is the density and c the bulk specific heat capacity of the aquifer (b), water (w) and solid matrix (s), and φ is the porosity.

Table 4.5: Heat transport parameter values used in Site Model 1

Parameter	Sand	Clay
Density of groundwater (kg m^{-3})	1000	1000
Density of solids/minerals (kg m^{-3})	2620 (quartz)	2700 (illite)
Total porosity (-)	0.37	0.45
Dry bulk density of aquifer (kg m^{-3})	1650	1485
Specific heat capacity of groundwater (J kg^{-1} K^{-1})	4190	4190
Specific heat capacity of matrix grains (J kg^{-1} K^{-1})	840	920
Bulk thermal conductivity (W m^{-1} K^{-1})	2.7	1.8

Thermal properties of Site Model 2

Bulk thermal conductivity (k, W.m^{-1}.K^{-1}) and volumetric heat capacity values for this model were based on geophysical logs, grain-size data, the inferred porosity (see previous section) and the empirical relations of Makowski & Mochlinski (1956) and Kersten (1949).

The Makowski & Mochlinski relation:

$$k = [\alpha_m \log w + \beta_m] 10^{0.00062 \rho_d} \tag{4.2}$$

where α_m and β_m are factors depending on the clay content *C* (%) as follows:

$$\alpha_m = (1.4241 - 0.00465 \text{ x } C) 10^{-1} \tag{4.3}$$

$$\beta_m = (0.4192 - 0.00313 \text{ x } C) 10^{-1} \tag{4.4}$$

The Kersten relation (Kersten, 1949) in metric units for unfrozen silt-clay soils:

$$k = [0.130 \log w - 0.0288] 10^{0.0006243 \rho_d} \tag{4.5}$$

And for unfrozen sandy soils:

$$k = [0.101 \log w - 0.0577] 10^{0.0006243 \rho_d} \tag{4.6}$$

In these equations w is moisture content (% of dry weight), and ρ_d is dry density (kg m^{-3})

These methods yielded high-resolution vertical profiles of thermal conductivity and volumetric heat capacity for the P-wells. The derived volumetric heat capacity of the aquifer shows relatively little variation between 2.8 and 3.2 MJ m^{-3} K^{-1} (Figure 4.7c). The parameters applied for Site Model 1 (Table

4.5) result in volumetric heat capacities of 2.9 and 3.1 MJ m^{-3} K^{-1} for respectively sand and clay layers and are comparable to those in Figure 4.7.

For the aquifer system between 1.8 and 120 m depth, the thermal conductivity according to respectively the Makowsi & Mochlinski (1956) and Kersten's (1949) equations average 2.7 and 2.4 $W.m^{-1}.K^{-1}$. The averages for the total aquifer agree with literature values and in-situ measured values of the thermal conductivity in the Netherlands (e.g. Witte et al., 2002). However, the vertical variation of the thermal conductivity is notably large, in particular given that the lithological log indicates a single aquifer.

The same analysis was performed for the other monitoring wells for which geophysical logs were available (P434, P435, P436 and P437). These analyses resulted in comparable values for thermal properties.

As the P-wells cluster in a small part of the model area, direct interpolation of the thermal property values over the model domain was deemed inappropriate. Instead, similarity of the profiles was used to construct a single simplified representative thermal conductivity-depth profile that was then assigned to the model cells. As the volumetric heat capacity showed relatively small variability the average value (2.9 $MJ.m^{-3}.K^{-1}$) was assigned uniformly to the model grid.

Thermal initial condition and boundary conditions

The initial temperature field for Site Model 1 is summarized in Table 4.6. But for the storage aquifer, all layers have a uniform temperature; a representative value for the model area. The three temperatures listed for the storage aquifer layer (6) were assigned to three zones (in map view) and reflect the lateral variation in temperature observed in the aquifer. This revealed that the high background temperature value corresponds to the RIVM compound that has been built up since the 1950's, the intermediate value to the more recently built up area around the Cohen building, and the low value to the remainder of the area which is dominated by green spaces (Figure 4.2). For Site Model 2, the 3-zone approach was used to assign initial temperatures to all 60 layers.

For both site models, temperatures at the east and west boundaries were imposed to stay fixed during model simulation time, which basically assumes the boundaries are far enough away from the ATES wells to not be influenced by or to influence the temperature development in the zone of interest. On the north and south sides of the model domain a general head boundary was applied, with a constant temperature at the control cells, such that the heat transport over these boundaries is determined by the groundwater flux and the horizontal temperature gradient. A zero heat flow boundary condition was used for the bottom boundary. Advective heat transport is nil as the vertical component of groundwater flow is zero at the base and conductive heat flow is therefore also zero. Although this is not realistic, it is of little consequence as simulated time periods are short (max 20 yrs.).

Table 4.6: Initial temperatures at Site Model 1.

Layer	Initial temperature (ºC)
1	11
2	10.8
3	10.8
4	10.8
5	10.6
6 (storage aquifer)	10.4, 10.5, or 10.58
7	10.5
8	10.8

At the top boundary of Site Model 1, a constant and uniform 'ground surface temperature' (GST) of 11°C was imposed. For Site Model 2, a time-dependent GST was used. These are monthly surface air temperatures (SAT) of the meteorological station at De Bilt (location in Figure 4.1; data: KNMI, 2012) with a constant temperature correction which reflects the GST-SAT offset. In general GST tends to be systematically higher than SAT depending on land surface conditions (e.g. Mann & Smidt, 2003). The GST-SAT offsets for the three zones were determined by forward modeling of the undisturbed (referring to ATES impacts) temperature logs of monitoring wells P434 and P437 where the meteo-record of De Bilt (1706 – time of logging) was used as the nominal (uncorrected) GST history (Kooi, 2008).

Figure 4.6b presents results of the modeling of the logs of P434 and P437. A GST equal to the annual SAT time series clearly underestimates the subsurface temperatures. For P434, a good fit was obtained by increasing the top temperature by 1.1°C from 1955 onwards. An additional offset of 2°C from the year 1978 onwards was inferred for P433, P436 and P437. No attempt was made to fit temperatures shallower than 20 m as these are sensitive to seasonal fluctuations.

Calculations

With the two site models, non-steady state calculations were performed of groundwater flow and heat transport for the period January 2008-December 2011. This period was split into 48 stress periods of one month length each. Time-based averages of abstraction and injection volumes and injection temperatures were calculated for the stress periods. Each stress period in turn, was divided into time steps with a length of 1 day (accumulating to 1461 time steps), which enabled calculation of heads and temperatures for a specific date.

Subsidiary calculations have been performed with both site models for 252 stress periods of 30 days each (accumulating to almost 21 years), and a pumping regime and injected temperatures as originally designed for the ATES system. This was done for the purpose of comparing actual operating impacts with the impact by operating the ATES according to the original design.

The model results of the site models were used to evaluate the thermal impact. This was done by:

- Mapping the horizontal extent of the thermally impacted zones beyond and below the “natural” background temperatures;
- Visualizing the vertical variability of the temperature field in cross sections.
- Graphing the temporal variability of storage aquifer temperature at a daily time scale and for annual averages.

The impact for actual operating conditions is also compared to the predicted impact of the ATES system under design operating conditions.

4.3 Results

4.3.1 Performance of the heat transport models

Figure 4.10 compares observed temperatures and calculated temperatures from both site models for the storage aquifer during the period from January 2008 to December 2011.

Operational details of the ATES system during this period are provided in Table 4.2 and Figure 4.3. In Figure 4.10a and b, logged temperatures (1 m vertical resolution) are averaged over the thickness of the storage aquifer. Figure 4.10c shows the temperature development at 75 m bgl (the middle point of the storage aquifer). The logged temperatures show that breakthrough of warm water only occurred at P433 and P437 (45 m and 52 m from the nearest warm well). No thermal breakthrough is observed at the wells monitoring the cold-water thermal plume (P436, S1, S2, see Figure 4.11d,e,f). The peak average temperature of the storage aquifer amounted to 12.04ºC, while the maximum recorded temperature in P437 was 12.3ºC.

For Site Model 1, the maximum deviation of the modeled temperatures from the measured average temperatures in the storage aquifer at P433 and P437 amounts to 0.16ºC above the actual temperatures for P437 and 0.21ºC below the actual temperatures for P433. Therefore, it can be concluded that this model simulates the temperature development in the storage aquifer reasonably well with a limited number of model layers and parameters.

For Site Model 2, the average temperatures in the storage aquifer shows a simulated peak temperature at P437 that is 0.24ºC below actual measured temperatures, but the temperatures at P433 are modeled accurately (deviation of 0.05ºC in the peak temperature). Figure 4.10c shows that for a specific depth of 75 m, the calculated peak level and timing of the highest temperatures in P437 and P433 are very close to those measured (deviations of respectively 0.02ºC and 0.15ºC in the peak temperatures). The onset of the temperature rise, however, appears to be too early in the model. The temperature logs of P437 show that until March 2011, temperatures in the parts of the aquifer above 75 m bgl were systematically higher than those below this depth. The temperatures calculated for the depth of 75 m, therefore, appear to be more representative for a shallower depth.

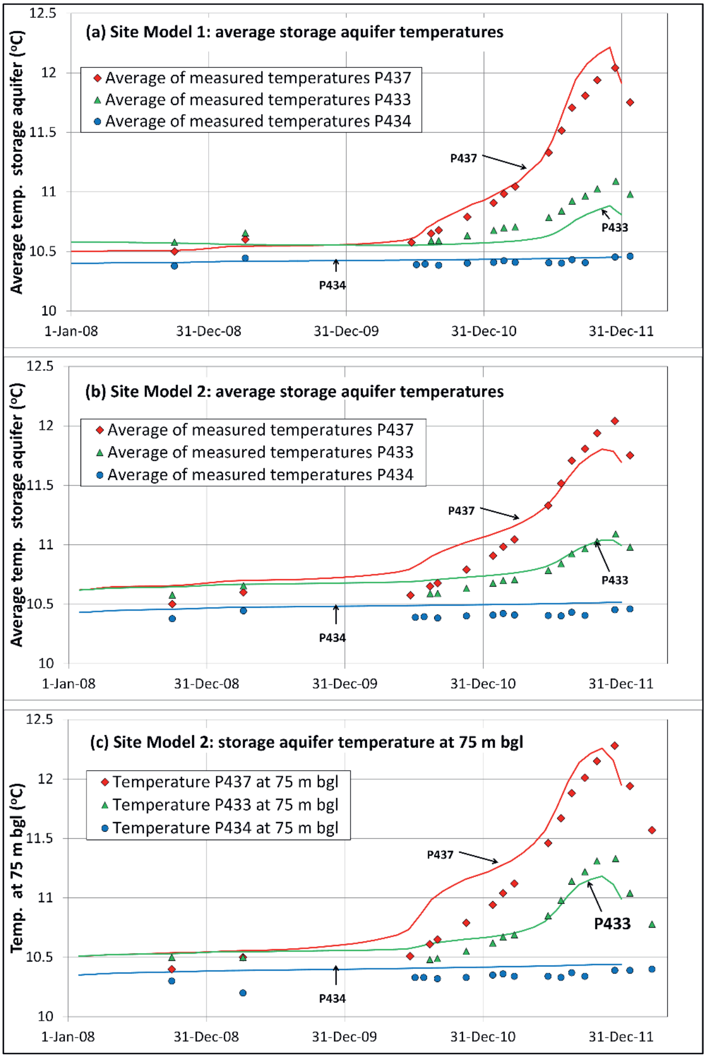

Figure 4.10: Modeled and averages of logged temperatures in the storage aquifer using (a) Site Model 1, and (b) Site Model 2. (c) Site Model 2, modeled and logged temperatures in the storage aquifer at 75 m bgl.

The temperature ranges observed at these monitoring wells and some measures of the goodness of the fit between the simulated and measured temperatures are given in Table 4.7. For all three cases discussed above, the RMS is lowest for P434. This is due to the limited temperature range observed in this monitoring well. The RMS values for the simulations of the temperatures at P437 and P433 show little difference between Site Model 1 and Site Model 2, in case the storage aquifer averaged temperatures are used. For the discrete depth of 75 m, the RMS values suggest a lower model accuracy for Site Model 2. That this is a reflection of overall lower accuracy of Model 2 is unlikely, however, because the goodness of fit varies strongly over short distance in the vertical for this model. The modeling efficiency (Loague & Green, 1991) shows that the temperature development at P437 is simulated accurately in all three cases (EF values approaching 1). The EF for the simulations of the temperature at P433 is significantly better for Site Model 2 than for Site Model 1. The EF for the simulations at P434 are relatively meaningless due to the low temperature range observed at the monitoring well.

Table 4.7: Measures of goodness of fit of the temperature calculations at three monitoring wells.

	Min. temp. observed (°C)	Max. temp. observed (°C)	Maximum error (°C)	Root Mean Square (RMS) error	Modeling Efficiency (EF)
Site Model 1:					
P437	10.5	12.0	0.21	0.11	0.96
P433	10.6	11.1	0.16	0.14	0.34
P434	10.4	10.5	0.05	0.03	-1.25
Site Model 2, storage aquifer temperatures averaged:					
P437	10.5	12.0	0.27	0.17	0.89
P433	10.6	11.1	0.12	0.06	0.86
P434	10.4	10.5	0.11	0.09	-16.33
Site Model 2, temperatures at 75 m bgl:					
P437	10.4	12.3	0.49	0.27	0.82
P433	10.5	11.3	0.30	0.19	0.63
P434	10.2	10.4	0.27	0.17	-14.83

Figure 4.11 shows that Site Model 2 reproduces the actual vertical temperature development for P433, P434 and P437 quite well. The largest deviations are found for the simulations of December 14, 2011, when the highest temperatures were measured in P437. The vertical section of the storage aquifer where these highest temperatures occur is thinner in the simulated temperature profiles than observed. This is probably due to the coarse grained, highly permeable strata between 94 and 100 m bgl (see Figure 4.5 and Figure 4.7) that may have caused higher injection rates in the deeper sections of the warm wells. Unfortunately, this could not be confirmed by the temperature logging of the warm wells because the piezometers in these wells only reach to 70.5 and 80 m bgl.

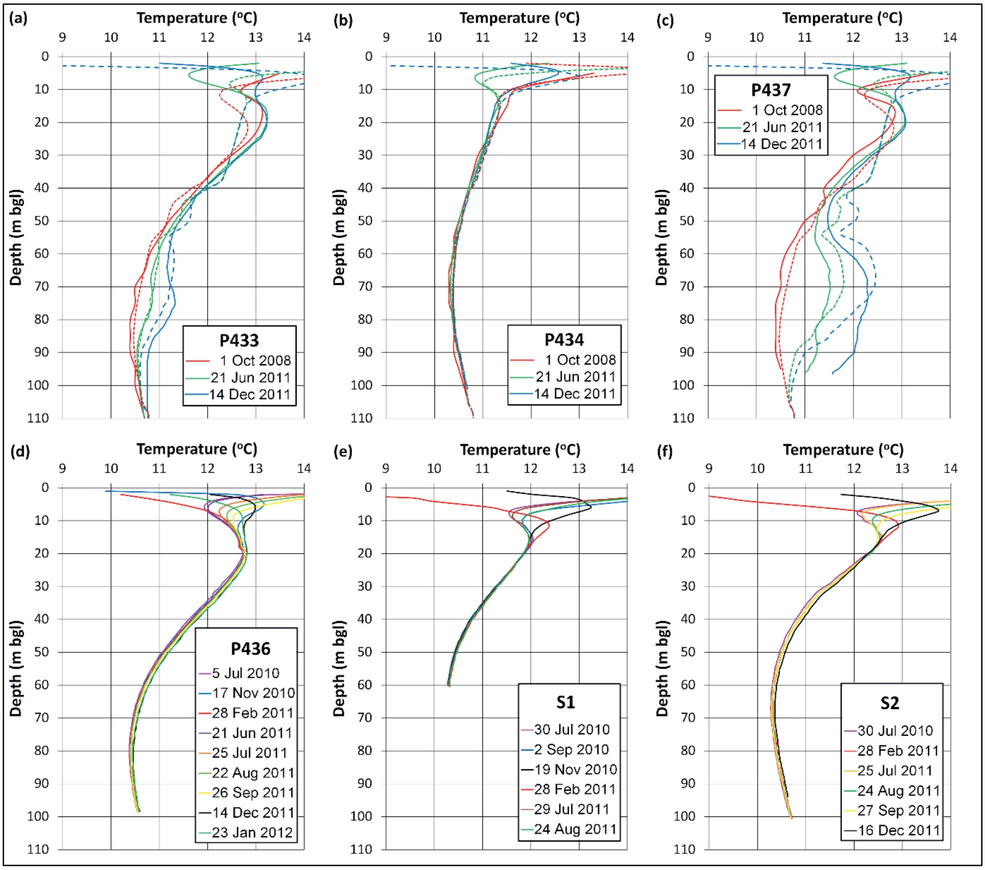

Figure 4.11: Comparison of logged (solid lines) and Site Model 2 simulated (dashed lines) temperature profiles at (a) P433, (b) P434, and (c) P437. No thermal breakthrough was observed in (d) P436, (e) S1 and (f) S2.

4.3.2 Thermal impact of the ATES system

Figure 4.12 displays storage aquifer temperatures predicted at the end of a cold well-injection period (31 March 2009; Figure 4.12a,d) and at the end of a warm well injection period (30 November 2011; Figure 4.12b,e) for both site models. By the end of November 2011, the largest extent of the warm water thermal plume was expected in the period considered (2008-2011). For Site Model 2, vertically averaged temperatures of the storage aquifer (between 50 and 100 m bgl) are contoured. Contours shown correspond to temperatures above the maximum (11.2°C) and below the minimum (10.3°C) background temperature of the aquifer. Site Model 1 calculates a larger horizontal extent of the cold-water thermal plume compared to the averaged temperatures of Site Model 2, while the warm water thermal plume extends farther in Site Model 2 compared to Site Model 1. For comparison, Figure 4.12c and f also display the impact predicted at 30 November 2011 for the design abstraction and injection rates and temperatures.

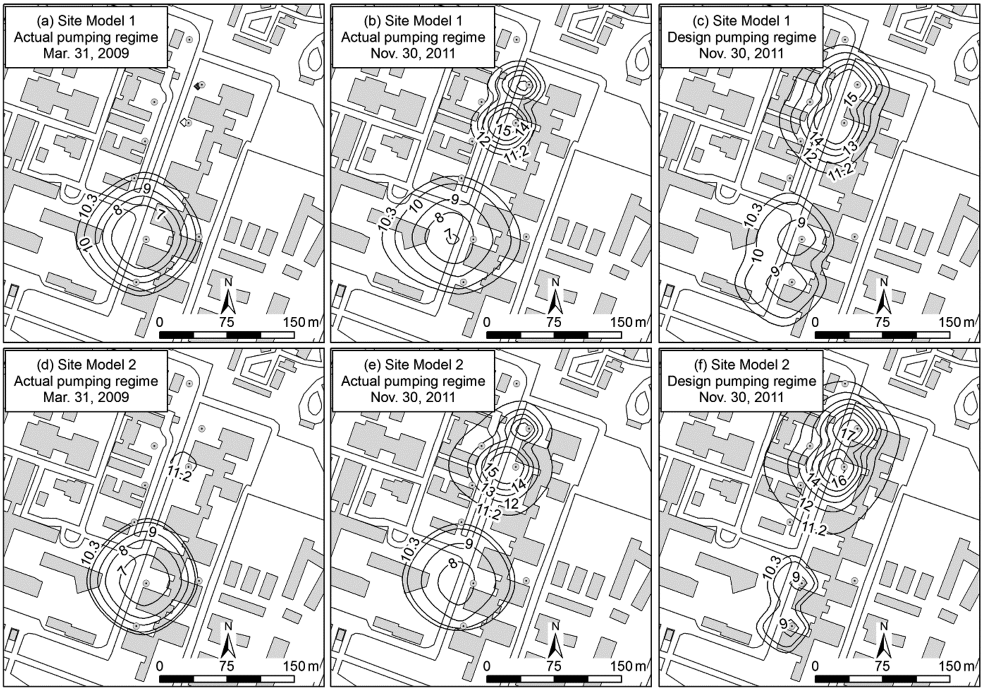

Figure 4.12: Calculated temperature contours for (a,b,c) Site Model 1 and (d,e,f) Site Model 2.

In Table 4.8, the horizontal extent of the cold and warm thermal plumes in both models are compared.

Table 4.8: Areas (m^2) occupied by the warm and cold thermal plumes in both site models

		Actual operating regime	
		Site Model 1	Site Model 2
Warm thermal plume			
	March 31, 2009	70	510
	November 30, 2011	5,850	10,770
Cold thermal plume			
	March 31, 2009	13,740	11,650
	November 30, 2011	14,930	11,210

Figure 4.13 depicts the predicted temperature field in the storage aquifer in vertical cross section as a function of distance from the warm well W1 in west-east for 30 November 2011. For Site Model 1 (Figure 4.13a) temperature in the storage aquifer only varies in the horizontal direction because of the single model layer representation of the storage aquifer. The result for Site Model 2 (Figure 4.13b) gives a more detailed representation of the temperature field, e.g. illustrated by the purple shades, representing the highest temperatures, that occur at 15 to 30 m west of the well at depths between 50 and 60 m bgl.

Similar to Figure 4.13, cross sections have been drawn through cold well C2 in Figure 4.14. This figure illustrates the effect of the vertical heterogeneity in Site Model 2 even more by the farthest spreading of the lowest temperatures in the zones around 50, 65 and 80 m bgl.

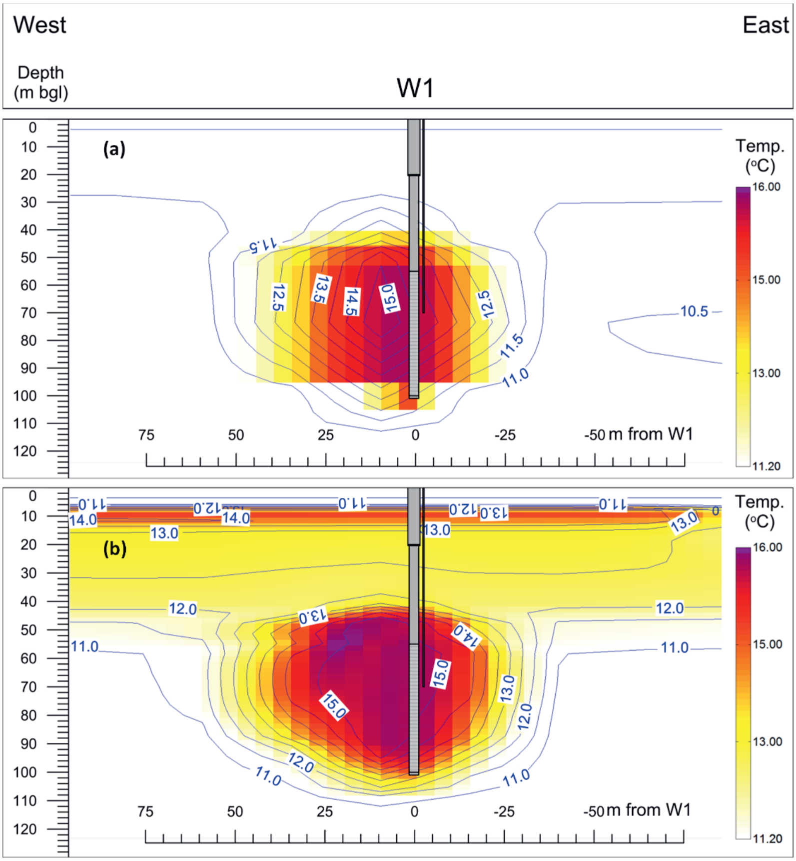

Figure 4.13: West to East vertical cross section through the warm water thermal plume around warm well W1 at November 30, 2011, as calculated by (a) Site Model 1 and (b) Site Model 2. The color shading gives the temperature for each model cell, while the blue lines represent the contoured temperatures.

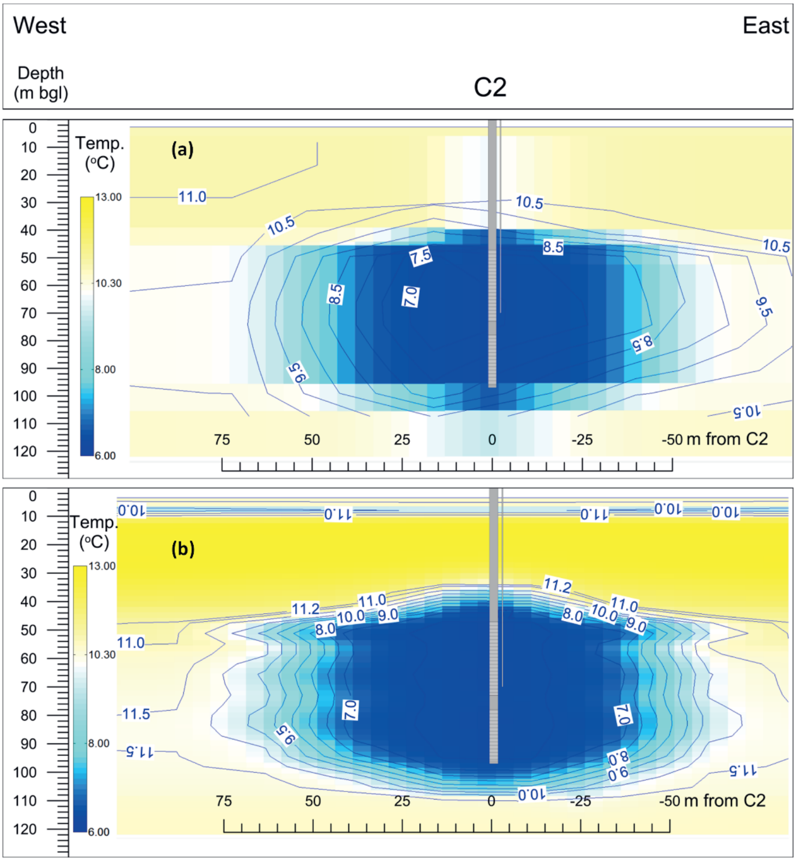

Figure 4.14: West to East vertical cross section through the cold water thermal plume around cold well C2 at March 31, 2009, as calculated by (a) Site Model 1 and (b) Site Model 2. The color shading gives the temperature for each model cell, while the blue lines represent the contoured temperatures.

Figure 4.15 gives the temporal history of aquifer temperature at various distances from the warm well in a westerly direction (same as the transects of Figure 4.13, west of the warm well). For Site Model 1 the temperature is that of the single layer which was used to represent the storage aquifer. For Site Model 2 the temperature evolution is shown as the vertically averaged storage aquifer temperatures. Figure 4.15a and b display the impact at daily temporal resolution; Figure 4.15c and d track the histories of annual average temperatures. In these graphs, the highest “natural” background temperature in the storage aquifer (11.2°C) is indicated by a horizontal dashed line.

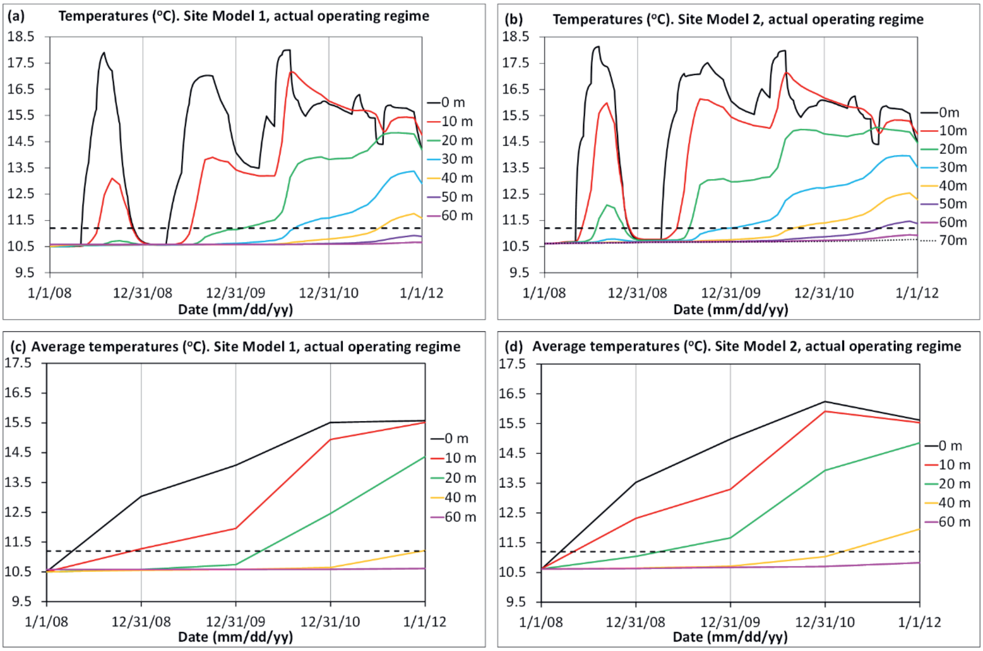

Figure 4.15: Fluctuation of the storage aquifer temperature at various distances from warm well W1, (a,b) on a daily basis and (c,d) as annual averages. The dashed line indicates the maximum pre-operational background temperature in the storage aquifer.

Table 4.9 lists the distance at which the predicted annual average temperature exceeds (by more than 0.1°C) the average background aquifer temperature. Predicted distances differ more than 10 m among the two site models. For purposes of comparison, the vertically averaged temperatures in the storage aquifer for Site Model 2 were used in Table 4.9.

Table 4.9: Extent of thermal impact by the end of 2011 on the basis of two criteria (in m from warm well W1).

	Design operating regime		Actual operating regime	
Criterion:	Site Model 1	Site Model 2	Site Model 1	Site Model 2
Exceedance of max. background aquifer temperature, calculated on a daily basis.	60	~70	40-50	50-60
Departure of annually averaged temperatures from average background temperature.	80	100	40-60	>60

Figure 4.16 shows the temporal vertical variations of the temperature in the storage aquifer, being the difference between the highest and lowest temperature in the aquifer, calculated at various distances west of well W1. The natural temperature range in the pre-ATES storage aquifer was 0.9°C. Within a short time after the ATES system started operating, this natural temperature variation in the

storage aquifer was exceeded up to 20 m from the well. After almost two years of operation, this exceedance of the natural temperature variation occurs at 30 m from the well, and during the following years, this distance keeps increasing.

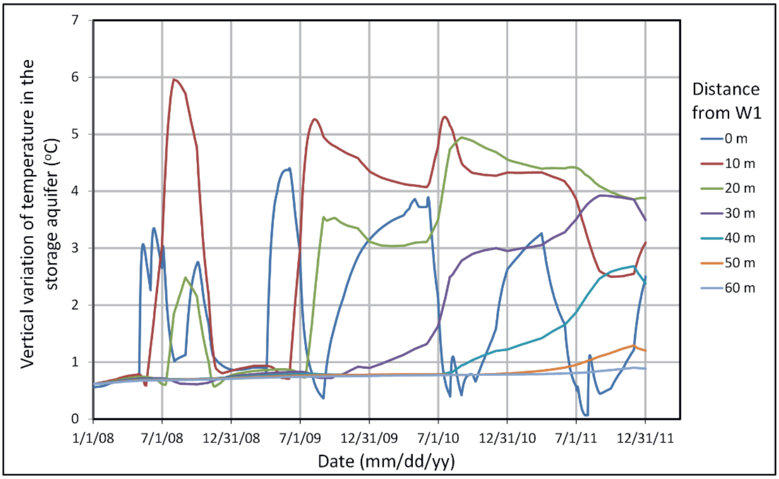

Figure 4.16: Vertical variation of the temperature in the storage aquifer at various distances west of W1 as calculated by Site Model 2.

4.4 Discussion

4.4.1 Comparison and General Applicability of the Model Approaches

Site Model 1 follows a widely applied modeling approach. Models applied in ATES impact assessments typically use a similar, simplified approach. Site Model 2, however, incorporates the interpretation of detailed grain size and geophysical data. These data will not always be readily available for modeling exercises. Both models simulate the actual condition realistically, due to the fact that many flow and transport parameters could be constrained and verified by means of a large set of available data.

The temperature development simulated with both models was in agreement with measured temperatures in monitoring wells when considering the vertically averaged temperatures in the storage aquifer. Site Model 2 is also able to realistically simulate the vertical temperature distribution in the storage aquifer. The temperature distribution calculated by this fine-scale heterogeneity model showed a significantly larger thermally impacted area by the warm water plume and a slightly smaller impacted area for the cold-water plume. A possible explanation is that around the 'warm wells' the more permeable zones are more pronounced and thicker, and the well screens of the 'warm wells' are placed such that these intersect the coarsest aquifer material more efficiently (Figure 4.5). The heterogeneous distribution of the coarser and finer aquifer material results in a higher than average permeability around the 'warm wells' in Site Model 2, while the permeability around the 'cold wells' is slightly lower than the homogeneous average value in Site Model 1. Site Model 1, therefore, underestimates the thermally impacted area of the warm water plume.

Site Model 2 requires a realistic initial temperature distribution and a dynamic and spatially varied GST. Depth-temperature logging is essential for verifying the models and determining the background temperature characteristics and SAT-GST relationships. These data can easily be obtained by logging or by the application of fiber optic distributed temperature sensing (FO-DTS) systems (Tyler et al., 2009).

Comparison of the results of models implementing the design operating regime of the ATES system with the actual operating conditions of the wells demonstrated that the actual abstraction and injection rates and injection temperatures are essential for carrying out reliable modeling of the actual temperature development and accurately evaluating the thermal impact of the ATES system. In the present case, injection and abstraction volumes and temperatures were aggregated into one-month stress periods. This proved to be detailed enough to accurately simulate the observed temperatures.

The subsurface heterogeneity in Site Model 2 is mainly expressed by highly variable hydraulic permeability and to a lesser extent by variations in the thermal conductivity, and volumetric heat capacity of the aquifer. Therefore, differences between the model outcomes of both site models are mainly attributable to variations in hydraulic properties and to a lesser extent to the variations in thermal properties.

4.4.2 Thermal Impact of the ATES System

It is obvious that the temperature changes induced by the ATES system are highly complex in the three spatial dimensions and time.

The spatial extent of the thermal impact has been delineated by mapping the areas with ATES induced temperatures higher and lower than those naturally occurring in the storage aquifer. Figure 4.12 shows the horizontal extent of the warm and cold-water thermal plumes. To facilitate comparison, the storage aquifer temperatures in Site Model 2 were averaged. The mapped warm water thermal plume extent was 1.8 times as large for Site Model 2 compared to Site Model 1 (Table 4.8). On the other hand, the cold-water thermal plume is smaller for Site Model 2.

However, when the vertical cross sections of the warm and cold water thermal plumes (Figure 4.13 and Figure 4.14) are viewed, it is obvious that in Site Model 2 these have variable lateral extents with depth. These cross sections show that at discrete depths the extent of anomalous low temperatures is also larger for Site Model 2 than for Site Model 1. In these zones, temperatures are found that are 0.5 to 1.0ºC lower than in Site Model 1. The largest extents of these anomalous temperatures occur at, or just below, depths with the highest permeabilities (Figure 4.7). The anomaly extends farthest around 80 m depth, and coincides with the highest permeability, the highest thermal conductivity and lowest volumetric heat capacity (although the variability of the latter was not modeled).

The heterogeneity of the subsurface, expressed in variations in hydraulic and thermal characteristics, can, therefore, not be ignored when assessing the actual extent of the thermal impact. Heat is more easily advected along more permeable layers, but aquifer heterogeneity also influences the distribution of the injection and abstraction rates over well screens and well screen sections. Simple models, like Site Model 1, are likely to be used for impact assessment. Site Model 1 underestimates the size of the warm thermal plume. Underestimation of the impacted zone may have implications for the licensing of ATES systems, and secondly has consequences for assessing the risk of interference between various ATES systems that are located close to each other.

The operating regime of the ATES system is another important factor in the size of the impacted areas.

Figure 4.15a and b show the progressive widening of the warm zone; points further from the ATES well gradually increase in temperature, but with a delay compared with points closer to the well. The dampening of fluctuations with distance can also be recognized. However, the curves show little cooling after 2009 with step-wise increases in temperature at distances greater than 20 m. A complete cooling of the aquifer to background temperatures occurred early 2009 during the second cold water injection cycle. The design operating conditions assumed a recovery after each injection cycle to temperatures 1 to 1.5°C below and above the background temperatures (Royal Haskoning, 2007). After 2009, this recovery was not achieved in the warm thermal plume near the ATES wells. This enhanced accelerated spreading of the thermal plume, as thermal ‘retardation’ is reduced due to the higher aquifer temperatures.

Site Model 2 shows systematically higher temperatures, first only near the warm well and progressively over a larger distance from the well. The differences between the two site models are rather large (up to 4.7°C at 10 m from the well to less than 1°C at more than 40 m), but otherwise difficult to characterize.

The vertical temperature variations in the storage aquifer at fixed distances from W1 have been calculated with Site Model 2 at various times. These variations are high just after commencement of the ATES operation and decrease in time when the vertical temperature distribution in the aquifer becomes more homogeneous. The farther away from the wells, the later the amplitude starts increasing and declining. Therefore, the vertical temperature differences in the aquifer do not represent a sustained change over an extended period of time and these temporal changes in temperature may be not the most significant indicators for the thermal impact.

Hydrochemical and microbiological changes may be expected to occur when the induced temperatures lie above or below the naturally occurring temperatures. However, it is also demonstrated here that the temperatures vary with the injection and abstraction cycles and that this amplitude changes with distance and in time. Processes may be induced by anomalous temperatures that are reversed when the temperature changes in the opposite direction with the next ATES operating cycle.

The annual average of the temperature, on the other hand, is a more stable parameter in time. The change in the average temperature of the aquifer may also be more significant for certain processes, like dissolution and microbiological changes. The modeling has demonstrated that the deviation from the background average aquifer temperature shows a gradual increase in magnitude and spatial extent both for the design operating regime and for the actual operating modus, but also significant differences in the calculated average temperatures between the two site models.

Further research of the temperature driven processes that may influence groundwater quality should provide more knowledge about which type of anomaly, deviation from the minimum and maximum temperatures or from the average aquifer temperature, is most significant for these processes. Possibly, both types of anomalies are significant for different types of processes.

4.4.3 Comparison With Other Recent Studies

The results of this work are consistent with several findings by Bridger & Allen (2014) (in the following abbreviated as BA) in their study of the Agassiz ATES system in Canada. Both modelling studies demonstrate the influence of aquifer heterogeneity on thermal breakthrough at specific distances of ATES wells and the variability of breakthrough with depth in particular. The latter was also inferred from observed vertical temperature variations in observation wells by Sommer et al. (2014) in Utrecht, the Netherlands. Both studies also predict a larger warm water plume for heterogeneous aquifer conditions. However, the longitudinal and vertical distortion of the warm water plume due to the aquifer heterogeneity is stronger for the aquifer studied by BA than for the aquifer at the RIVM site. This seems to be in part due to the different ATES operational regimes (cyclic operational regime for the RIVM system versus a discrete storage experiment for the Agassiz system), but probably is also caused by the larger range of hydraulic conductivity used in the model of BA (about 17 to 600 m day^{-1} versus 18 to 132 m day^{-1} for the present study).

The model used in this study seems to predict the observed variability of ATES induced temperatures with greater accuracy than the model of BA. It is speculated that this may be related to the different methods used for the assessment and representation of thermal property heterogeneity in the modeling. Both studies used grain size analysis for assessment of the hydraulic conductivity. Both studies also calibrated these with respectively ATES pumping cycles and a pumping test. However, in the present study thermal properties (including total porosity) were inferred through a detailed analysis of geophysical well logs and, therefore, possibly with greater accuracy than literature-derived representative estimates applied by BA. Furthermore, in contrast to BA and other studies (e.g. Sommer et al., 2014), but similar to Vandenbohede et al. (2011), in this model, temperature-dependency of dynamic viscosity of the groundwater was used.

Temporal and spatial variations of viscosity (and hence hydraulic conductivity) associated with the temperature ranges for the ATES systems up to a factor of 1.5 (Voss, 1984). These ratios may not be negligible and are comparable with the ranges for the hydraulic conductivity applied in the sensitivity analysis by BA.

The high vertical variability of the temperatures simulated in this heterogeneity model could only be attained by using a realistic background temperature distribution as an initial condition. In other studies (e.g. Bridger & Allen, 2014 and Sommer et al., 2014) a homogeneous initial temperature was applied.

The results confirm and highlight the recent finding by Sommer et al. (2014) that the actual thermal changes induced by ATES systems are sensitive to the actual operational regime of the system.

4.5 Conclusions

Lessons learned from the modeling of the studied ATES system are the following:

(1) The thermal impact is strongly controlled by actual operational conditions of the ATES system, which differed markedly from design conditions. Policy and decision makers should be aware of this limitation of pre-deployment impact assessments based only on design operational conditions, in particular if the ATES system is projected in the vicinity of sensitive groundwater uses, like drinking water supplies, or where interference with nearby existing systems may occur. In these cases, a sensitivity analysis should be carried out to evaluate the effect of ranges in hydraulic and thermal input parameters, but also operating conditions. For example, if under actual operating conditions there is a certain deviation from the design conditions, can it be expected that a thermal imbalance will develop and what will be the extent of the thermal impact then?

(2) Fine-scale heterogeneity was shown to be important to accurately model: (a) the ATES-impacted vertical temperature distribution and the maximum and minimum temperatures in the storage aquifer, and (b) the spatial extent of the thermal plumes. Predicted maximum and minimum temperatures were more than 1°C higher and 0.5 to 1.0°C lower for models that included fine-scale heterogeneity. The higher maximum temperatures are consistent with the findings of Bridger & Allen (2014). Fine-scale heterogeneity increased the predicted spatial extent of the warm water thermal plume by a maximum of more than 80%, based on vertically-averaged aquifer temperatures. Not using fine-scale heterogeneity underestimates the thermal plume extent. Designs of ATES systems should probably be more conservative in this respect.

(3) The relatively large pre-ATES-system horizontal and vertical temperature variations of the storage aquifer (caused by spatially varying land-cover and its historical changes) were required to model a vertical temperature distribution that approached the observed temperatures. The vertical temperature distribution is important for accurate thermal impact assessment.

(4) The methods used to quantify both hydraulic and thermal parameters from various borehole data (logs, samples) provide effective, albeit relatively elaborate means to construct realistic thermal impact models, which account for fine-scale heterogeneity in these parameters.

(5) Fine-scale heterogeneity cannot be mapped or modeled without detailed and accurate lithological logging of boreholes, describing the grain size and clay content, or sampling and sieve analysis. Geophysical borehole logging provides a helpful tool to investigate the subsurface heterogeneity and to derive thermal and hydraulic parameters. These techniques could be applied at least at the ATES wells. However, to spatially map the heterogeneity of the storage aquifer, data from more boreholes are required. In the present case, data of eleven boreholes that covered the extent of the thermal plumes were used to realistically construct the subsurface heterogeneity. It is not realistic to expect such a data density for every projected ATES site. Therefore, the uncertainty in models assessing the ATES thermal impact could be addressed to some extent by sensitivity analysis.

(6) Scattered and scarce monitoring data of ATES-induced temperatures can be interpreted in a useful way by groundwater and heat transport modeling. This study shows that regular temperature logging in at least three monitoring wells (P433, P437, and P434), in two of which a thermal

breakthrough was observed, enabled the interpretation of the development and extent of the warm thermal plume.

4.6 Outlook

The quantification of the thermal impact of ATES systems, in spatial extent, temperature ranges and temporal variations, could benefit from more case studies in which both monitoring results and modeling efforts are being combined. Monitoring can be intensified when easily available and relatively cheap monitoring techniques are available. The use of fiber optic (FO) cables with distributed temperature sensing (DTS) systems is one example. FO cables could be introduced into the subsurface by relatively cheap techniques, e.g. in combination with cone penetration tests (CPT), that could be used to gather detailed subsurface information as well. A disadvantage of CPTs is the limited depth that can be reached (generally some tens of meters). Hermans et al. (2012) and Hermans et al. (2014) have demonstrated that time-lapse electrical-resistivity and self-potential tomography could be applied for thermal plume monitoring in a warm water injection test in a sandy aquifer at relatively shallow depth. Further research should focus on the applicability of these and other existing techniques and the development of new techniques for subsurface temperature monitoring.

Secondly, the three-dimensional mapping of the subsurface heterogeneity is a challenge. This study shows that data from conventional geophysical well logging can be applied in a useful way. Further research could focus on these and additional techniques to enhance research of the subsurface heterogeneity.

The effects of temperature changes on groundwater quality need to be further investigated for various types of aquifers and hydrogeological conditions. A presently unresolved and potentially relevant issue is whether thermal impact needs to be addressed/evaluated from a Eulerian or a Lagrangian perspective. Here temperatures were evaluated relative to the immobile aquifer solids (Eulerian reference frame). For processes that are related to the aquifer matrix, like dissolution or microbes that are attached to the aquifer matrix, this approach may be the most applicable. However, it may be considered that processes that take place in the dissolved phase, or activity of suspended microbes, would be better traced by applying a Lagrangian approach. The models applied here also assume an instantaneous transfer of the heat or cold carried by the groundwater throughout the entire matrix. This is confirmed by checking the calculated temperatures of the solid matrix with the calculated groundwater temperatures. On the scale of pores and the aquifer matrix of the heat transfer and related processes, this may be a simplification of the actual processes. These aspects require further study.

Chapter 5

Detailed assessment of thermal properties of the subsurface by means of standard geophysical borehole logging[3]

Abstract

Intensified use of the subsurface for thermal energy storage requires proper planning. Design and planning of underground thermal energy storage systems (UTES) requires insight in the thermal properties of the subsurface. Use of existing geophysical logs could be helpful to assess the thermal properties. The present study shows that use of publicly available 'standard' geophysical borehole logs can successfully be applied to derive the thermal properties of an aquifer.

Numerous empirical methods are available for estimating thermal conductivity and capacity of soil. These methods relate thermal properties to moisture content, (dry) bulk density, quartz and clay content of the soil. Some available empirical methods are utilized here to assess thermal properties of an aquifer for which lithological bore logs and geophysical logs are available. Geophysical logs with a high vertical resolution allow interpretation of the variability of thermal properties within an apparently homogeneous aquifer. Geophysical logs do not provide the required parameters by direct measurement. A method is presented here to infer porosity and moisture content, bulk density and clay content from "standard" geophysical logs, including natural gamma ray logs and long normal (LN) electrical resistivity logs.

Thermal properties of an aquifer with an existing aquifer thermal energy storage (ATES) system are evaluated. Interpretation of the thermal properties allows inter-comparison of the various empirical equations for thermal conductivity and reveals heterogeneity of thermal properties within an aquifer.

Results show that thermal conductivity, diffusivity and retardation vary by 100% or more in apparently uniform strata. This implies that average values for thermal properties should be considered with caution. Heterogeneity of the subsurface needs to be taken into account when designing and planning UTES.

---

[3] A version of this chapter has been re-submitted for publication after review on August 16 2024 as: Visser, P.W., Detailed assessment of thermal properties of the subsurface by means of standard geophysical borehole logging. Geothermics.

5.1 Introduction

Climate change and recent high energy prices necessitate the use of alternatives for fossil energy sources. As approximately 40% of the energy demand in the Netherlands comprises thermal energy, underground thermal energy storage (UTES) is a growing source for low-enthalpy sustainable heating and cooling of buildings. These systems store seasonal heat and cold from cooling and heating buildings, surplus heat from industrial processes, solar heat or heat and cold from surface water, in the subsurface. Aquifer thermal energy storage (ATES) systems store thermal energy in groundwater in aquifers. Borehole thermal energy storage (BTES) stores and abstracts seasonal heat and cold in the formation by closed loops (borehole heat exchangers), without extracting groundwater. Geothermal heat pumps (GHP), or ground source heat pumps (GSHP), use the relatively constant temperature of the subsurface for heating and cooling, without actually storing seasonal heat and cold.

The number of ATES systems increases and it is estimated that in the Netherlands approx. 2,800 ATES systems are operational. This number could increase to about 200,000 by 2050 (Amsterdam Institute for Advanced Metropolitan Solutions, 2019). ATES in the Netherlands uses aquifers between depths of 20 and 300 m for storing seasonal heat and cold. Also in other countries, the potential of UTES as a sustainable thermal energy source is high and numbers of these systems are growing (Bloemendal et al., 2015; Bloemendal, 2018; Fleuchaus et al., 2018; Hoekstra et al., 2020; Gluyas et al., 2020). Especially in urban areas large number of these systems are concentrated and this may lead to interference between systems and, therefore, less efficient use of the subsurface. For these reasons, proper planning and design of UTES and GHP systems is of utmost importance.

The planning, design and effect assessment of these systems is usually done through modeling groundwater flow and heat transport. E.g. Bulté et al. (2021), Todorov et al. (2020), Bakr et al. (2013), Zerihun et al. (2015). Thermal conductivity and volumetric heat capacity are important model and design parameters for both ATES and BTES systems. The effect of the heterogeneity of hydraulic and thermal properties of the aquifers has been pointed out in various studies, e.g. Sommer et al. (2013), and Chapter 4 of this thesis. These heterogeneities cannot always be assessed accurately from borehole descriptions only.

Thermal response test techniques have been used in various studies to measure the ground thermal properties (e.g. Witte et al., 2002). Developments in these techniques, like the hot wire method in combination with fibre optic temperature measurements, have yielded more thermal conductivity profiles to depths of 100 m and in varying geological environments (Fujii et al., 2009a; Fujii et al., 2009b). Synthetic vertical distribution of thermal conductivity data based on literature values has been applied by Focaccia (2012).

However, few published examples with high resolution data of the vertical distribution of the thermal properties from the Netherlands are available to serve as a reference. Therefore, an alternative approach, using available borehole logging data, is investigated and tested in this chapter in order to quantify the vertical differences in thermal characteristics at an ATES site. This analysis focuses on the grain size distribution, in particular the clay and silt fractions, the porosity and density of the various geological units. Use is made of publicly available geophysical bore logs (TNO

Geologische Dienst Nederland, 2022) to demonstrate that, with data available, the vertical distribution of thermal properties can be assessed in detail.

This chapter describes a method combining conventional geophysical borehole logging techniques and other borehole data, to derive a detailed description of thermal properties of the subsurface. Geophysical logging techniques have been used to assess the thermal properties of rock before, e.g. Hartman et al. (2005), Gasior & Prezelaskowska (2014), Fuchs & Förster (2013) and Hu et al. (2021). These existing studies aim at deep geothermal reservoirs and apply logging techniques that are current in the oil and gas industry, such as neutron logging of density and porosity. Logging techniques that are available for direct measurements of certain parameters of the aquifer that contribute to thermal properties include e.g. nuclear magnetic resonance (NMR) and neutron-density logging for measuring the water content, are not widely available or have not been applied often for shallow hydrogeological investigations for UTES systems. The main difference with previous studies, therefore, is in deriving porosity and aquifer density by means of available indirect measurements instead or more direct methods like neutron-density logging. Gamma-ray, self-potential and electrical resistivity logs are collected routinely and are available in large numbers (over 1,000) in public databases in the Netherlands for aquifers to 200 m below the surface. Interpretation of such logs is described in this chapter and provides a valuable tool for more accurate design and spatial planning of ATES and BTES systems.

5.1.1 Background of the site

Location

An ATES system is operational since 2008 at the National Institute for Public Health and Environment (RIVM) in Bilthoven, central Netherlands (Figure 5.1). The ATES system consists of two “warm” wells and two “cold” wells with screened sections between 47 to 106 m below ground level (m bgl). Near the ATES system wells, geophysical logging was carried out in five boreholes (B32C0433-B32C0437). These boreholes and loggings are used in this study to infer thermal properties of the ATES system aquifer. Boreholes B32C0239, B32C0327, B32C0519, and B32C0568 at approx. 1.5 km southeast of the ATES system and Borehole B32C0560 2.3 km northeast of the ATES system (Figure 5.1) are used to provide auxiliary data for interpretation of the geophysical logs and lithological data.

Hydrogeology

Strata, as found to a maximum drilling depth of 145 m bgl at the site, show a sequence of clay, sand and gravel shown in Table 1. Between 0 and 120 m bgl, sandy deposits make up the first aquifer, which is highly suitable for ATES systems.

Below 120 m bgl, aquicludes and thin aquifers are encountered, comprising Early-Pleistocene and Tertiary marine deposits of intercalated (fine) sands, clayey sand and clay. These deposits are less suitable for ATES. From approx. 240 m bgl, thick Tertiary clays form the hydrogeological base below which hardly any groundwater circulation occurs (TNO Geologische Dienst Nederland, 2022).

Groundwater level in the first aquifer at the site is 1.6 to 2.2 m bgl and the piezometric surface is dipping southwest (Chapter 4 of this thesis).

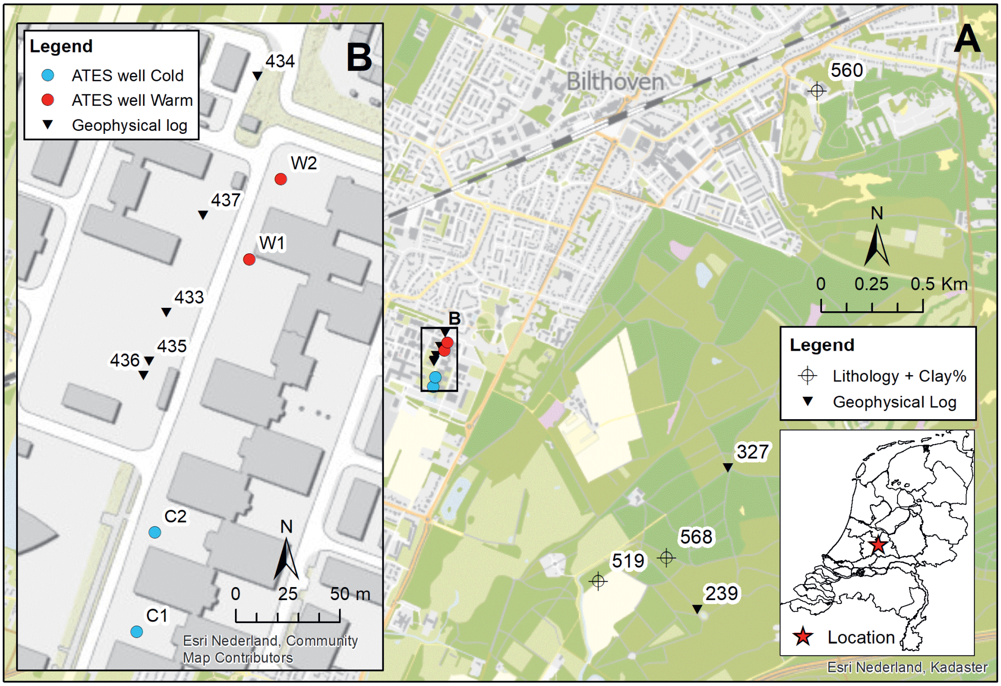

Figure 5.1: Location of the study area and boreholes, showing boreholes of which a lithological log, including clay and silt percentages are available (Lithology + Clay%), boreholes of which a lithological log and geophysical log are available (Geophysical log)and the ATES wells (A). Inset map (B) shows the study area around the ATES system. Complete borehole codes are B32C0, plus the number shown on the map.

Table 5.1: Lithostratigraphy, based on borehole B32C0433 (TNO Geologische Dienst Nederland, 2022) and TNO Geologische Dienst Nederland (2012).

From (m bgl)	To (m bgl)	Formation	Chronostratigraphy	Lithology
0	3	Boxtel	Middle-Pleistocene – Holocene	Aeolian sands, fine to coarse
3	22	Drenthe	Middle-Pleistocene	Glacial outwash sands, fine to coarse, locally loam or clay.
22	54	Sterksel	Middle-Pleistocene	Fluviatile sands, medium to coarse, locally gravelly, gravel and clay.
54	120	Peize and Waalre	Early-Pleistocene	Fluviatile sands, medium to coarse, locally clayey to gravelly, and clay.
120	>145	Maassluis	Early-Pleistocene	Marine sands, medium to coarse, and clay.

5.2 Methods and data

Thermal properties studied here include thermal conductivity, volumetric heat capacity and thermal retardation. Thermal conductivity controls conductive heat transport. Heat transport in the aquifer occurs both in groundwater filled pores and the solid matrix. Storage of thermal energy in the solid matrix of the aquifer retards the heat transport by groundwater flow (advection). This can be quantified by the thermal retardation and depends on volumetric heat capacities of the water and aquifer (Bloemendal & Olsthoorn, 2018; Gossler et al., 2019).

Thermal conductivity, volumetric heat capacity and thermal retardation are assessed by theoretical and empirical equations. Input for these equations comprises porosity, moisture content, dry density, and clay and silt content of the aquifer material. These input parameters are estimated with the help of geophysical logs as elucidated in the following sections. A schematic representation of the process of deriving the input parameters and calculation of thermal properties is presented in the flow chart in Figure 5.2.

First, clay content is calculated from natural gamma ray logs. Clay content is (1) an input parameter for thermal conductivity equations and (2) required to derive porosity. Secondly, porosity is assessed from electrical resistivity logs. Electrical resistivity of the aquifer is determined by the water content, water electrical conductivity, and electrical conductivity of the aquifer matrix. By assessing these parameters, the water content and, thus, porosity of the saturated parts of the aquifer is determined. Knowing porosity and clay content, thermal conductivity of the aquifer is calculated by three different (empirical) methods. Volumetric heat capacity and thermal diffusivity and retardation are also derived.

Data sources used for the assessment of thermal properties are given in section 5.2.1. Section 5.2.2 elaborates on the interpretation methods applied.

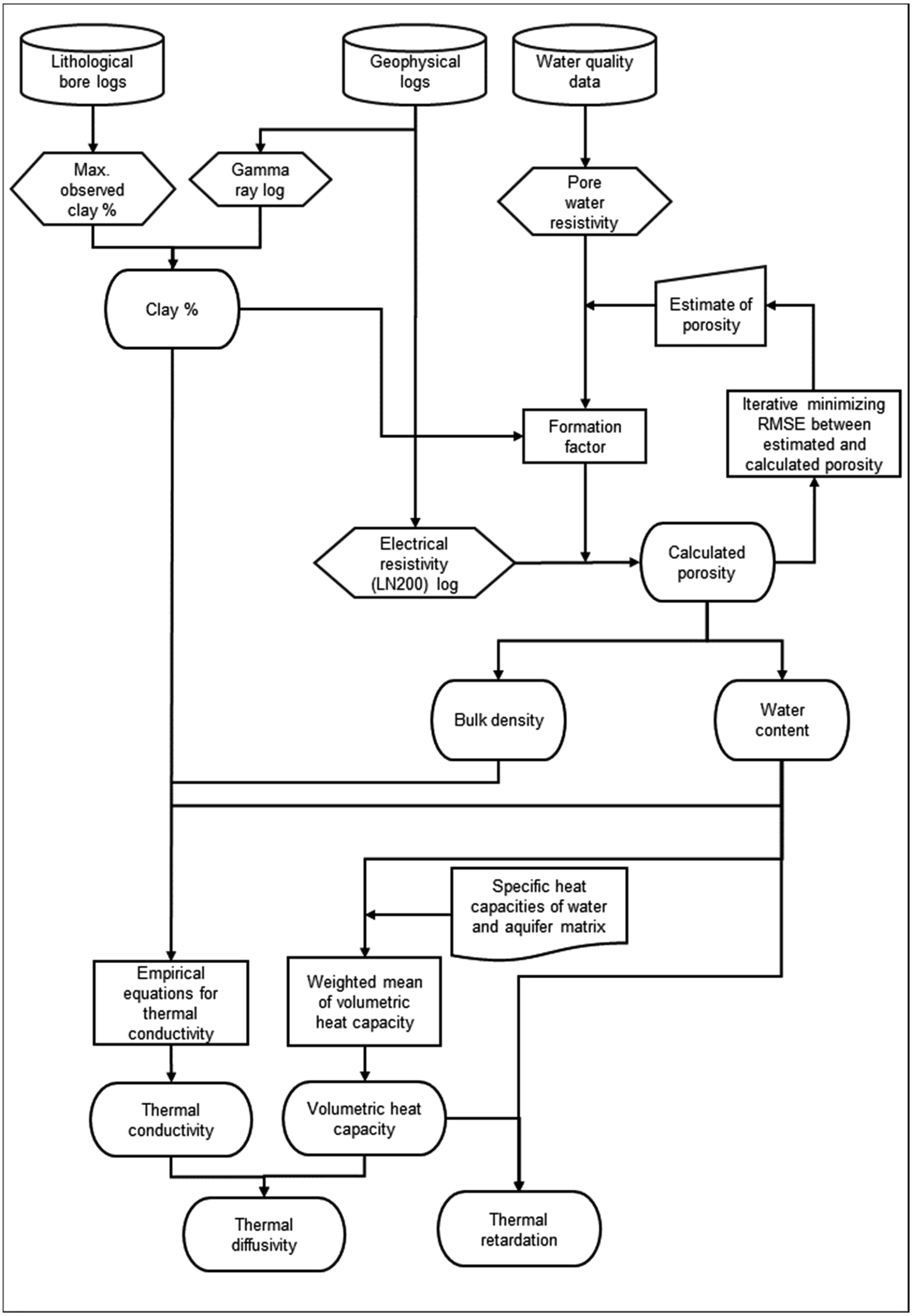

Figure 5.2: Flow chart of the process to derive thermal properties.

5.2.1 Data

Bore logs and geophysical logs

Lithological and geophysical logs were collected in the 1970's and 1980's near the location of the present ATES system in boreholes B32C0433-B32C0437 (Figure 5.1). These boreholes lack substantial clay layers, required to be able to correlate gamma ray readings with high clay percentages. Therefore, following auxiliary borehole logs in the vicinity of the study area are also used. Boreholes B32C0239, B32C0327, B32C0519, and B32C0568 were drilled 1.5 km southeast of the ATES system between 1973 and 2001. Borehole B32C0560 was drilled in 2000 2.3 km northeast of the ATES system (Figure 5.1). Stratigraphy and lithology of these boreholes are identical to that of the ATES site.

Lithological descriptions of boreholes B32C0433-B32C0437 have been made by the former National Institute for Water Supply (RID) (TNO Geologische Dienst Nederland, 2022). Borehole section intervals at which lithology is described are highly variable. Lithology of the auxiliary boreholes has been reported by TNO Geological Survey of the Netherlands (TNO Geologische Dienst Nederland, 2022). Details of the boreholes and available logs are given in Table 5.2. M63 is the median grain size of the sand fraction (63µm-2mm) (Van de Meulen et al., 2005). Caliper (Cal) is the uncased borehole diameter [mm]. Natural gamma ray (GR) measures the naturally occurring gamma radiation [counts per second, CPS]. SP is the self-potential [V], SN and LN are short normal resp. long normal resistivity [Ohm.m]. 20 and 40, resp. 100 and 200 represent the vertical distance (in cm) between the electrodes of the SN and LN probe.

Table 5.2: Available geophysical logs.

Borehole	Year	Max. logging depth [m bgl]	Lithology description interval [m]	M63	Silt and clay %	Geophysical logs available	Geoph. log interval [m]
Case study:							
B32C0433	1981	145	1.0	yes		Cal; GR; SP; SN20+40; LN100+200	0.02
B32C0434	1981	121	1.0-13.0	yes		Cal; GR; SP; SN20+40; LN100+200	0.02
B32C0435	1981	120	1.0-7.0	yes		Cal; GR; SP; SN20+40; LN100+200	0.02
B32C0436	1982	100	0.5-7.3	no		Cal; GR; SP; SN20+40; LN100+200	0.02
B32C0437	1982	103.5	1.0-7.0	yes		Cal; GR; SP; SN20+40; LN100+200	0.02
Auxiliary logs:							
B32C0239	1973	205	0.5-8.3	yes		Cal; GR; SP; SN20; LN100	0.02
B32C0327	1974	205	1.2-47.5	no		Cal; GR; SP; SN20; LN100	0.02
B32C0519	1995	200	1.0-7.0	yes	yes		
B32C0560	2000	280	0.5-8.0	yes	yes		
B32C0568	2001	280	1.0-10.0	yes	yes		

Groundwater conductivity

Ground water quality data, including the electrical conductivity EC_w, is collected from the national groundwater database DINOloket (TNO Geologische Dienst Nederland, 2022). Most recent observations (2005-2009) show a relatively high EC_w of the shallow groundwater. This is indicative of surficial influences on groundwater quality. In an urban environment, EC_w is influenced by road salting, urban runoff, sewage etc., but also by aerial deposition of nitric oxides and the like. Therefore, EC_w cannot be assumed to be constant in depth and time.

Between 1981 and 1982, when geophysical logs in the study area were collected, the boreholes were located at the edge of built-up terrain. By the end of the 1980's, the rural area east of the wells was built-up. This urbanization is reflected in the EC_w of groundwater in monitoring wells within two kilometers from the ATES site. EC_w measured in 2005-2009 is not representative for the 1981-1982 situation. Therefore, the fitted depth-EC_w relationship for measurements between 1952 and 1997 is taken as representative for the 1981-1982 period (Figure 5.3).

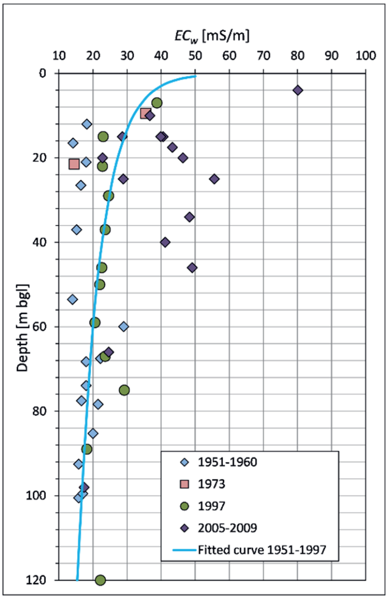

Figure 5.3: Development of the groundwater EC_w in time at various depths in the environs of the study site. Data source: TNO Geologische Dienst Nederland (2022).

Thermal properties

Between 2009 and 2011, the ATES system has been monitored and modeled in detail as described in Chapter 4. Temperature logging and model results suggested variable thermal properties (thermal conductivity and thermal capacity) between the upper parts of the aquifer (approx. 0-50 m bgl) and the lower part of the aquifer (approx. 50-120 m bgl). Lithological descriptions do not offer indications that could explain these differences in the thermal properties.

Most probable parameters explaining differences in thermal properties are porosity, bulk density, pore geometry and packing density. Significant differences due to different mineralogy between the formations making up these aquifers are not expected. Sand of formations present at the site to 120 m bgl mainly consists of quartz and feldspar, with a minor percentage of heavy minerals (De Mulder et al., 2003). Waalre Formation sands, present between approx. 50-120 m bgl, may have a low to moderate mica content (TNO Geologische Dienst Nederland, 2012). Presence of mica, with a low thermal conductivity, could result in a lower thermal conductivity.

5.2.2 Methods

First, the amount of clay is derived from gamma logs, as the clay content is required to infer porosity. Next, porosity is calculated, using electrical resistivity logs. Thermal conductivity, heat capacity, thermal retardation and diffusivity are calculated using these parameters (Figure 5.2).

Clay percentage from gamma ray logs

Clay content is inferred from natural gamma ray logs ($GR_{Log\ Signal}$) of the first 7 boreholes in Table 5.2 through the gamma ray index (I_{GR}). It only needs the response of the gamma ray log for a nearby known shale (or clay) body (GR_{Shale}) and a nearby known clean rock ($GR_{Clean\ Rock}$):

$$I_{GR} = \frac{GR_{Log\ Signal} - GR_{Clean\ Rock}}{GR_{Shale} - GR_{Clean\ Rock}} \qquad (5.1)$$

According to Larionov (1969), the shale volume fraction (V_{sh}) in Tertiary rocks (both consolidated and unconsolidated) can be calculated as follows:

$$V_{sh} = 0.083(2^{3.7 \times I_{GR}} - 1) \qquad (5.2)$$

Using $GR_{Clean\ Rock}$ and GR_{Shale}, I_{GR} is calculated for the gamma ray logs. Applying Eq.(5.2) results in V_{shale}. Using grain density and calculated porosity (following section), weight percentages of clay are calculated.

Porosity and dry density from resistivity logs

Porosity logs, e.g. neutron-neutron logs, or neutron-gamma logs, are not widely available, due to the fact that these logging techniques require the use of a (radioactive) neutron source. In the present case, use has been made of the resistivity logs to derive porosity as follows.

Archie (1942) proposed the interpretation of the results of resistivity logs, based on the empirical results, by defining a formation resistivity factor (F) as a function of porosity (φ) [fraction] and a cementation exponent (m):

$$F = \varphi^{-m} \qquad (5.3)$$

Or, as the cementation exponent cannot be simply derived, in terms of the resistivity of the fluid-filled porous rock (R_o) and water resistivity (R_w):

$$F = \frac{R_0}{R_w} \tag{5.4}$$

Winsauer et al. (1952) analyzed data from 30 samples. From these data, a correlation known as the Humble Equation, was developed:

$$F = 0.62\varphi^{-2.15} \tag{5.5}$$

Eq.(5.5) can be used for granular or soft rocks, e.g. sand(stone). The following three steps are required to determine the formation factor, based on R_o and R_w, corrected for matrix electrical resistivity.

Porewater resistivity (R_w)

Theoretically, the pore water resistivity R_w can be interpreted from the self-potential (SP) logs, in combination with electrical resistivity logs. However, this procedure is not straightforward. In the present study, R_w is determined as the reciprocal of the electrical conductivity of water samples (EC_w) from various boreholes and depths in the vicinity of the ATES system (see section 2.1.2).

Resistivity of the fluid filled porous rock (R_o)

R_o is read directly from the geophysical logs. The long-normal resistivity log (LN100 or LN200) value is deemed most representative of resistivity of fluid-filled porous rock surrounding the borehole, and less influenced by the drilling-mud filled borehole and filter cake on the borehole wall. With R_w known, the porosity can be estimated using Eq.(5.4) and Eq.(5.5).

Electrical resistivity of the matrix and clay content

Accuracy of estimating the amount of conductive pore water and nonconductive solid matrix is less where clays are present. As a rule of thumb, the Archie method should only be used when V_{sh} is smaller than 0.20 and the shale (clay) resistivity is larger than 8 Ω.m. Many different methods have been proposed to account for the conductivity of clay, e.g. the Waxman-Smits model (Waxman & Smits, 1968), the bi-component model, and modified Archie's equation (Lee, 2011; Choo et al., 2016). An overview of most common mixing models for electrical conductivity in porous media is given by Glover (2010).

Waxman & Smits (1968) developed an empirical relation, by measuring the electrical conductance on soil cores:

$$EC_o = \frac{1}{F} \times (EC_w + B.Q_v) \tag{5.6}$$

where EC_o [S.cm^{-1}] and EC_w [S.cm^{-1}] are the specific conductance of respectively the core and the pore water. B is the equivalent conductance of clay exchange cations (sodium) as a function of EC_w at 25°C [S.cm^2.meq^{-1}].

The parameter Q_v is the excess of surface charge per unit pore volume [eq.L^{-1}], or [96.32 x 10^6 C.m^{-3}] in SI units, where C represents Coulomb (Revil et al., 1998), or the volume concentration of clay exchange cations (Waxman & Smits, 1968). This parameter can be expressed as (Revil et al., 1998):

$$Q_v = \rho_s \times \left(\frac{1-\varphi}{\varphi}\right) \times CEC \tag{5.7}$$

with ρ_s = grain density [kg.L^{-1}] and CEC [eq.kg^{-1}] is the cation exchange capacity. Waxman & Smits (1968) suggested an empirical estimate of B:

$$B = 0.046 \times \left[1 - 0.6 \times exp\left(\frac{-EC_w}{0.013}\right)\right] \tag{5.8}$$

Clay-bearing strata at the site belong to the Sterksel and Waalre Formations, both Pleistocene fluviatile deposits of the Rhine basin, and (from approx. 120 m bgl) the Pleistocene, marine Maassluis Formation. Griffioen et al. (2016) show that in clay minerals of Pleistocene sediments of the Rhine basin illite dominates (35-40%), followed by vermiculite and smectite (both with 10-20%). Van der Veer (2006) quotes similar percentages for the marine clays in the Netherlands (30-40% illite, followed by 10-50% smectites and <5% to 20% vermiculite). Assuming a predominantly illite and smectite composition of the clay layers, ρ_s and CEC of the clay minerals are estimated.

The ρ_s of the clay minerals cited in literature varies between 2000 and 3070 kg.m^{-3}, while the CEC of the clay minerals is typically around 0.20-1.50 eq.kg^{-1} (Table 5.3).

EC_o is taken to be the reciprocal of the resistivity, reported in the logs as LN100 (boreholes B32C0239 and B32C0327) or LN200 (boreholes B32C0433-437). Porosity is the unknown, but related to F through Eq.(5.5). By first applying an estimated porosity in Eq.(5.7), F is derived and porosity calculated using Eq.(5.5). The estimated porosity in Eq.(5.7) is then changed iteratively, until it approaches calculated porosities throughout the profile by minimizing the root mean square error (RMSE).

The clay percentage corrected formation factor from Eq.(5.6) is used in Eq.(5.5) to derive the final estimate of the porosity. Dry density of the aquifer matrix is $(1-\varphi)$ ×2650 [kg.m^{-3}], 2650 [kg.m^{-3}] being the typical density of aquifer minerals (Robie & Bethke, 1962).

Table 5.3: Grain density and CEC of illite and smectite

	ρ_s illite (kg.m^{-3})	ρ_s smectite (kg.m^{-3})	CEC illite (eq.kg^{-1})	CEC smectite (eq.kg^{-1})
Bolt & Bruggenwert (1978)			0.40	
Appelo & Postma, (2005)			0.20-0.50; 0.16	0.81
Revil et al. (1998)	~2650 for clay minerals		0.09 (authigenic clay); 0.10-0.40; 0.16	0.70-0.81 (Na-montmorillonite); 0.80-1.50
Deer et al. (1966)	2600-2900	2000-2600		
Totten et al. (2002)	2600-2900 (av. 2750)			
Baeyens & Bradbury (2004)			0.075-0.205 (depending on the Na-concentration)	
Środoń et al. (2008)		2747-3070 (av. 2821)		0.81-1.23 (av. 1.04)

Thermal conductivity

Many empirical and theoretical relations between bulk density, moisture and clay content and thermal conductivity of soils have been developed in the past. Kersten (1949) collected empirical data for many soil types and produced equations for frozen and unfrozen silt-clay soils and sandy soils. The Kersten relation in metric units, as cited by Farouki (1981), Johansen (1975) and Becker & Fricke (1997), gives the soil thermal conductivity (k) [W.m^{-1}.K^{-1}] as function of the moisture content (w) [% of dry weight] and dry density (ρ_d) [kg.m^{-3}]:

Unfrozen silt-clay soils:

$$k = [0.130 \log w - 0.0288] \times 10^{0.0006243\rho_d} \tag{5.9}$$

Unfrozen sandy soils:

$$k = [0.101 \log w + 0.0577] \times 10^{0.0006243\rho_d} \tag{5.10}$$

Sandy soils used by Kersten comprised four natural sands, seven man-made sands and a sandy loam. Natural sands were silicious and feldspar sands and gravels. The sands are classified as moderately to strongly gravelly sands with less than 2.5% clay and silt. Fine soils (clay, silty clay loam, silt loam and sandy loam) contained 50% or more silt and clay.

Clay particles form bridges between sand grains. A certain clay content, therefore, increases thermal cnductivity of sandy soils. Makowski & Mochlinski (1956) developed an equation for thermal conductivity in soils, based on a semi-empirical mathematical model, that takes into account the clay content of the soil. This equation was put in the same form as Kersten's empirical equations for unfrozen soil materials:

$$k = [\alpha_m \log w + \beta_m] \times 10^{0.00062\rho_d} \tag{5.11}$$

α_m and β_m are factors depending on the clay content C [% dry weight] as follows:

$$\alpha_m = \ (0.14241 - 0.000465\ C) \tag{5.12}$$

$$\beta_m = \ (0.04192 - 0.000313\ C) \tag{5.13}$$

Equations like (5.9), (5.10) and (5.11) are often applied as an estimate of thermal conductivity. Rawat et al. (1982), for example, suggest that the Kersten's relation is observed to reasonably predict thermal conductivity of soils. Predictions by Makowski and Mochlinski's relation are not good but improve if the sum of silt and clay fractions is treated as clay fraction in the computation. Therefore, in this study, the Makowski and Mochlinski approach has been applied, with the sum of the silt and clay fractions representing C.

Moisture content and mineral fractions of the soil also influence thermal conductivity. This was accounted for by Johansen (1975). He introduced a normalized thermal conductivity, termed the Kersten number (K_e). Thermal conductivity of a soil then depends on thermal conductivity of the saturated and dry soil (k_{sat} and k_{dry}) and K_e:

$$k = \left(k_{sat} - k_{dry}\right) \times K_e + k_{dry} \tag{5.14}$$

k_{sat} and k_{dry} are derived from the porosity (φ), and the thermal conductivity of the soil solids (k_s):

$$k_{sat} = k_s^{(1-\varphi)} \times k_w^{\varphi} \tag{5.15}$$

$$k_{dry} = (0.135\rho_d + 64.7)/(2700 - 0.947\rho_d) \tag{5.16}$$

k_s is calculated as the geometric mean of the quartz content of the total solids Q and the thermal conductivities of quartz (k_q) and other minerals (k_o):

$$k_s = \ k_q^Q \times k_o^{(1-Q)} \tag{5.17}$$

k_q is taken as 7.7 W.m^{-1}.K^{-1}. k_o is 2.0 W.m^{-1}.K^{-1} for soils with $Q > 0.2$ and 3.0 W.m^{-1}.K^{-1} for soils with $Q \leq 0.2$ (Johansen, 1975). $k_w$is the thermal conductivity of water (0.579 W.m^{-1}.K^{-1} at 10^{o}C).

According to Griffioen et al. (2016) quartz usually accounts for over 70% of sands of the fluvial sediments. Based on this, the quartz fraction of sand is taken 0.7 and Q is calculated as the quartz fraction of sand, silt and clay.

The Kersten number K_e in Eq.(5.14) depends on the normalized soil water content S_r only. Lu et al. (2007) proposed an adaption of the model developed by Johansen (1975):

$$K_e = exp\left\{\alpha_j \left[[1 - S_r^{(\alpha_j - 1.33)}]\right]\right\} \tag{5.18}$$

$$k_{dry} = -a\varphi + b \tag{5.19}$$

in which α_j is a soil texture dependent parameter (0.27 for fine textured soils and 0.96 for sand) and a and b are empirical parameters. For $0.2 < \varphi < 0.6$ parameters a and b were found to be 0.56 and 0.51 respectively.

Considering that groundwater level in the present case study is 1.6 to 2.2 m bgl (see section 1.1), the soil below 2.2 m bgl can be considered to be saturated. This reduces K_e in Eq.(5.18) to 1 and k in Eq.(5.14) only dependent on k_{sat} in the Johansen model.

The models by Kersten (1949), Makowski & Mochlinski (1956) and Lu et al. (2007) have been applied to this study to estimate the thermal conductivity of the soil.

Volumetric heat capacity

Bulk volumetric heat capacity [J.m^{-3}.K^{-1}] of the aquifer (c_b) can be estimated from the porosity (φ) and the volumetric heat capacities of water (c_w) and solids (c_s) as follows:

$$c_b = \varphi c_w + (1 - \varphi)c_s \tag{5.20}$$

Water and solids volumetric heat capacities [J.m^{-3}.K^{-1}] are calculated by multiplying the specific heat capacity and bulk density. For water, the specific heat capacity is taken 4182 J.kg^{-1}.K^{-1}, with a specific density of 1000 kg.m^{-3}. The solids matrix of the aquifer is made up of mainly quartz and feldspar, with a minor percentage of clay. Specific heat of quartz, feldspar and the clay minerals ranges between 800 and 830 J.kg^{-1}.K^{-1}, while the typical specific density is 2650 kg.m^{-3} (Robie & Bethke (1962) and Table 5.3). The specific heat capacity and density of the solids are been taken to be that of quartz.

Thermal retardation

Gossler et al. (2019) distinguish between an apparent thermal retardation factor (R_{app}) and an effective thermal retardation factor (R_{eff}). If a local thermal equilibrium (LTE) is valid, R_{app} and R_{eff} are equal. At higher flow velocities (e.g. due to abstraction and injection of an ATES system) or larger particle sizes, the LTE may be non-valid. In this study, the effect of flow conditions have not been taken into account, and the thermal retardation has, therefore, been assumed to be equal to the apparent thermal retardation:

$$R_{app} = 1 + (1 - \varphi)c_s \times (\varphi c_w)^{-1} \tag{5.21}$$

5.3 Results and discussion

5.3.1 Clay volume and percentage

Previous studies using geophysical bore logs to derive thermal parameters like Hartman et al. (2005), Fuchs & Förster (2013) and Gasior & Prezelaskowska (2014) did not explicitly derive V_{sh}, but related laboratory measurements of thermal conductivity to the $GR_{Log\ Signal}$. Hu et al. (2021) calculated V_{sh} from the I_{GR}, similar to this study, but it remains unclear if the values set for GR_{Shale} and $GR_{Clean\ Rock}$ are actually measured in a pure shale body and clean rock, or how these values have been chosen.

In the present study area, no pure clay (or shale) body is reported in bore logs. Nearby auxiliary bore hole logs B32C0519 and B32C0568, 1.5 km from the site (Figure 5.1) and penetrating the same litho-stratigraphic units, report relatively high maximum clay percentages of resp. 40 and 45% (weight). $GR_{Log\ Signal}$ readings in auxiliary boreholes B32C0239 and B32C0327 vary between 15 and 61 counts per second (CPS). $GR_{Clean\ Rock}$ in these boreholes is, therefore, set to the minimum $GR_{Log\ Signal}$ logged in these boreholes (15 CPS). Highest $GR_{Log\ Signal}$ responses occur in a zone where high clay percentages were reported (between 120 and 130 m bgl). Assuming that highest readings (61 CPS) correspond to highest reported clay percentages (45%) in this zone, GR_{Shale} is estimated to be 117 CPS (i.e. 15 + 100% x (61-15)/45%).

Applying I_{GR} and Eq.(5.2) to the logs collected in the boreholes near the ATES system, results in V_{shale}. Using ρ_s and calculated porosity, weight percentages clay are inferred. Calculated clay percentages (weight) in B32C0239 and B32C0327 are comparable those reported for B32C0519 and B32C0568 (Table 5.4), although the depth intervals where the highest clay content occurs differ. Calculated clay percentages in the boreholes near the ATES site (B32C0433- B32C0437) are generally lower (Table 5.4). This is in accordance with the lithological descriptions of these boreholes, which report only sporadic and thin clay layers in the upper 120 m of the subsurface.

Table 5.4: Interpreted clay percentages (% weight).

Borehole	Min. clay%	Max. clay%	Median clay%	Average clay%
B32C0239	0	28.6	5.7	6.8
B32C0327	0	43.2	6.9	4.5
B32C0433	0	14.6	2.4	3.2
B32C0434	0	13.1	3.0	3.8
B32C0435	0	10.0	2.1	2.7
B32C0436	0	9.3	2.7	3.3
B32C0437	0	18.0	3.2	3.9

According to the Netherlands standard for classification of unconsolidated soil samples (NEN5104), valid at the time of the borehole descriptions, soil with C of 8% or more is classified as clay or loam. This constrains the calculated clay percentages for the sections classified as sand and gravel. C of 8% and higher has been shaded green in Figure 5.4. The sections that have been interpreted to be clay generally correlate very well with the lithological descriptions.

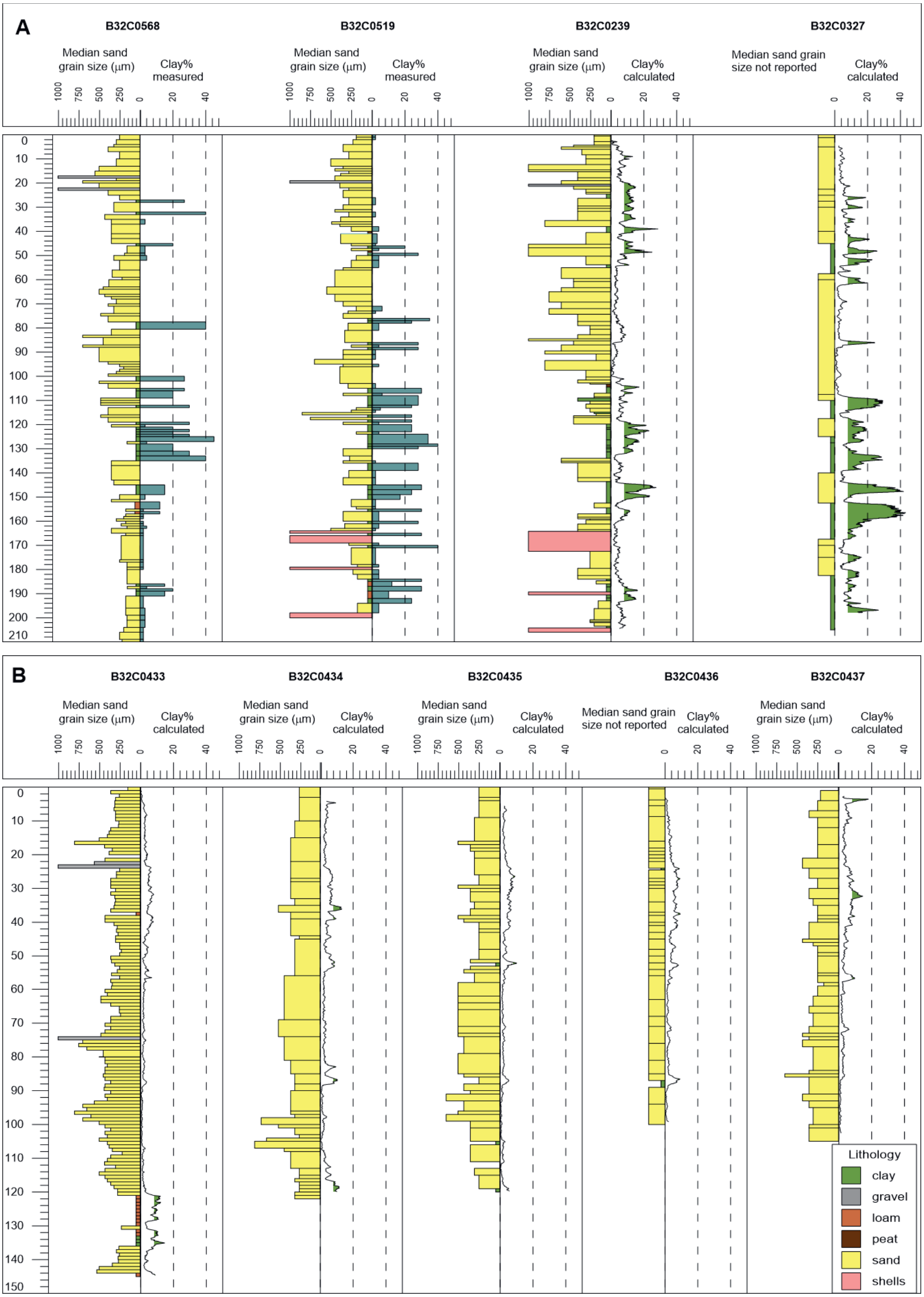

Figure 5.4: Median sand fraction grain size and calculated clay percentages. (A) Reference borehole, penetrating deeper clay strata. (B) Boreholes near the ATES wells. For B32C0327 and B32C0436 no median sand grain size is reported. The bars right of the lithological logs of B32C0568 and B32C0519 indicate the reported clay percentages.

In borehole B32C0239, the section between 20 and 50 m bgl shows calculated clay percentages that exceed 8% at most depths, whilst the lithological log only reports two clay layers and clayey, very coarse sand. The adjoining boreholes B32C0568 and B32C0519 show significantly more clay layers in this zone. It can be surmised that, possibly due to the coarseness of the sand and drilling technique (reverse circulation), the clay percentage in the samples from B32C0239 has been under-estimated in the borehole description.

The lithology of borehole B32C0327 has been classified by large depth intervals (several meters to tens of meters). It appears from the gamma log that in some sections clay layers occur that have been omitted in the borehole lithology description. Probably due to the fact that the drilling method applied (reverse circulation with airlift) does not allow very detailed lithological descriptions.

In boreholes B32C0433- B32C0437, very thin clay layers have been interpreted from the gamma logs. Not all of these layers have been identified in the lithological logs, or have been described over a lesser thickness. The boreholes have been drilled with the straight flush and airlift methods. These are not ideal methods for lithological descriptions of such thin strata.

5.3.2 Clay and silt percentages

Clay and silt percentages are strongly related in the deposits studied (Figure 5.5). The sum of the clay and silt fraction of the upper 145 m of boreholes B32C0519, B32C0560 and B32C0568 relates to the clay fraction as follows:

$$S + C = -0.08(C^2) + 5.57C - 0.75 \tag{5.22}$$

where, S is the silt percentage and C is the clay percentage. The coefficient of determination (R^2) is 0.95.

From Eq.(5.22) it is concluded that a grain size composition with more than 50% silt and clay is not found when the clay fraction is less than 8% (the orange rectangle in Figure 5.5). Therefore, it can be assumed that Eq.(5.10) is valid for sections with C< 8% at the site studied. For sections with C>8% Eq.(5.9) should be applied.

Eq.(5.22) also allows to derive $C + S$ from C (interpreted from natural gamma ray logs). The sum of clay and silt percentages has been applied in Eq.(5.11) as C.

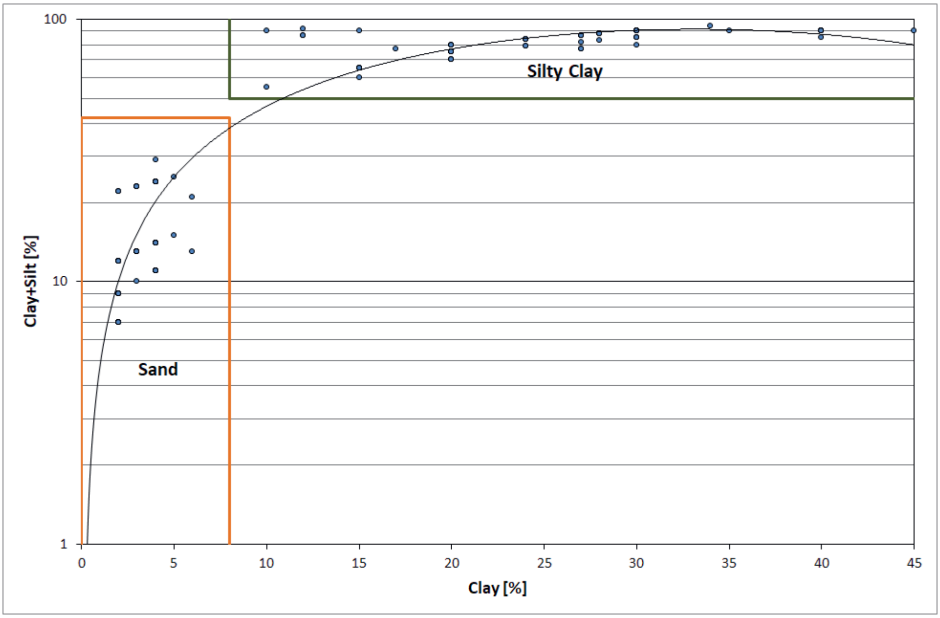

Figure 5.5: Correlation between C and $C + S$ percentages (weight) in boreholes B32C0519, B32C0560 and B32C0568.The orange rectangle indicates the boundaries of sand according to the Netherlands classification system. The green rectangle bounds silty clay. Plot data source: TNO Geologische Dienst Nederland (2022).

5.3.3 Porosity

Manger (1963) reported average porosities of unconsolidated Quaternary sediments to vary between 20.2% for gravel to 49.9% for very fine sand, 53.2% for silt and 62.9% for clay. Fahmi (1961) determined porosities between 31.3 and 44.4% for sands from the Netherlands with variable grain size and clay contents. Addition of artificial clay aggregates (up to 12% of clay) to sands increased porosity, compared to clean sands. Olsthoorn (1977) concluded that total and effective porosity of the unconsolidated sediments from which drinking water is being extracted in the Netherlands are more or less the same and equal approx. 38%. Vernes (2013) reported median porosities of Netherlands' unconsolidated sands between 33% (coarse sand) to 39% (fine sand). Sandy clays have median porosities between 28 and 59%. These data constrain the probability range for calculated porosities.

Use of the classical Humble equation (Eq.5.5) results in high calculated porosities, that exceed 40% in most sections of the boreholes. As most strata consist of medium to coarse sand, these porosities have to be deemed unrealistic. Applying the technique by Waxman & Smits (1968) results in lower porosities that fall within the ranges mentioned above. However, the porosities calculated this way are sensitive to the CEC in Eq.(5.7), that is used to estimate Q_v in Eq.(5.6). When the range of CEC values in Table 5.3 is used, unrealistic low porosities are calculated. Porosities that are within the ranges of the previous studies mentioned above, are found when a CEC lower than the characteristic CEC of illite or smectite is applied. That this is acceptable is discussed below.

Waxman & Smits (1968) reported a sharp, non-linear, increase of the soil core conductance with the electrolyte concentration at low equilibration solution concentrations. Surface electrical conduction at the clay-water interface is supposedly explained with the Stern theory of the electrical double layer (EDL) by Revil et al. (1998). They described that this type of conductivity is independent of the salinity in shaly sands with pore water concentrations above 10^{-3} mol.L^{-1}. Above this concentration, the Stern layer is saturated with sodium ions. In the present study, groundwater ionic strength (including all major cations and anions) is in the order of magnitude of 10^{-3} mol.L^{-1} or lower.

Recently, Qi & Wu (2022) showed that at the groundwater conductivities comparable to those in this study (in the range of 5 to 50 mS.m^{-1}), clay conductivity behaves non-linear with the pore water conductivity. At low salinities of the pore water in this study, clay (and, therefore, also the bulk) conductivity is not constant and obviously lower than that based on the characteristic CEC of illite or smectite. Qi & Wu (2022) developed a model by which the surface conductivity can be derived. However, clay conductivity in this model represents average conduction abilities of all the clay particles, which is dependent on many factors like clay type, clay fraction, clay aggregation extent, etc. Assuming that CEC in Eq.(5.7) is not equal to the characteristic clay mineral CEC, this parameter has been varied such that the calculated porosities fall within the range based on literature values. I.e. for the sand, not lower than 20% and porosities of around 37% in the coarse, clean sand sections. In clayey and silty sections of the logs, higher porosities (>40%) are calculated (Table 5.5). Two sections in B32C0239 and B32C0327 show calculated porosities <20%. These sections comprise the upper approx. 50 m of the two boreholes, where, based on the gamma-logs, the sand is interspersed with clayey layers. LN100 readings used to derive the bulk resistivity may, therefore, be less representative for the sandy sections only. In the upper 3 m of borehole B32C0437 an unrealistic porosity of >90% is calculated. LN200 in this section is low (around 15 Ohm.m), while C has a maximum of 18%. This results in a very high porosity. It is likely that an elevated EC_w of shallow groundwater, possibly caused by a sewer next to the borehole, causes low LN200 readings in this section. For this reason, the upper porosity values of this borehole are omitted in Table 5.5. Calculated porosity and lithology from lithological logs, are depicted in Figure 5.6.

Table 5.5: Porosity derived from resistivity logs with the Humble equation (Eq.5.5).

Borehole	Min. porosity (%)	Max. porosity (%)	Median porosity (%)	Average porosity (%)
B32C0239	12.3	49.9	26.4	26.5
B32C0327	15.7	58.3	33.0	31.9
B32C0433	20.8	47.7	31.7	32.0
B32C0434	26.3	43.6	35.3	34.8
B32C0435	20.0	48.9	29.5	30.6
B32C0436	23.3	45.7	34.1	34.1
B32C0437*	26.2	41.6	32.5	32.7

*: only below 6 m bgl

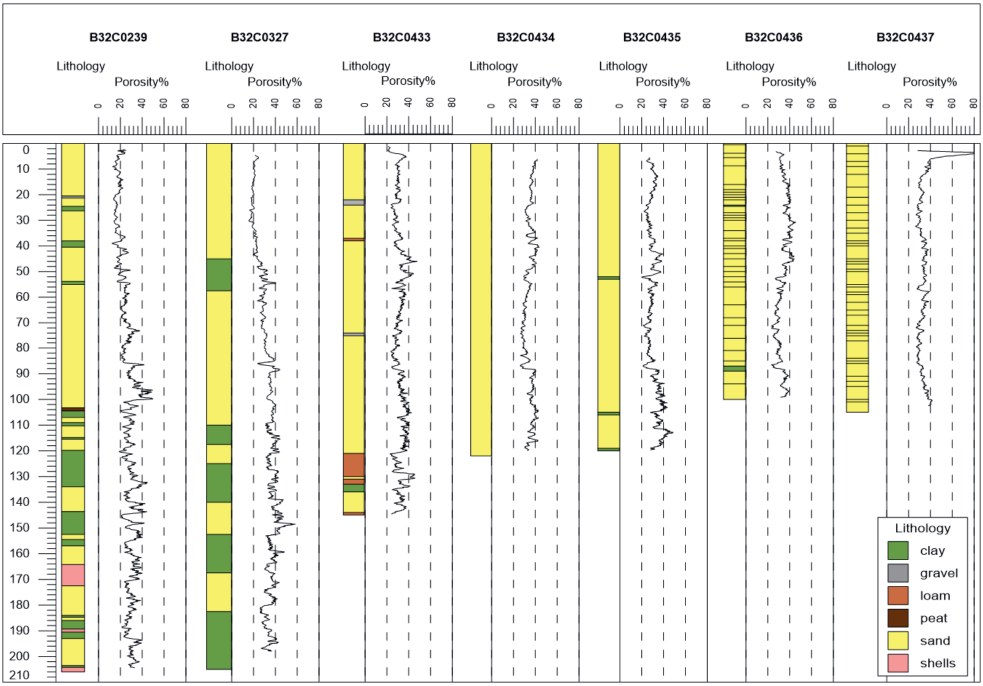

Figure 5.6: Lithological logs and calculated porosity. The scale bar on the left is depth in m bgl.

5.3.4 Thermal conductivity, thermal capacity, and thermal retardation

Literature values of thermal conductivity and volumetric heat capacity of various soils are widely available. A recent and comprehensive overview of thermal properties from international guidelines, a wide literature review and obtained from more than 400 direct measurements is given by Dalla Santa et al. (2020) (Table 5.6). Dalla Santa et al. (2020) recommend that in saturated conditions the highest of the “wet” values in Table 5.6 should be chosen. From this table it follows that the probability range for thermal conductivity of aquifer materials at the study site should be between 1.1 and 3.1 $W.m^{-1}.K^{-1}$.

Table 5.6: Thermal properties (minimum, maximum and recommended) reported in Dalla Santa et al. (2020) and Verein Deutscher Ingenieure (2000).

	From literature			Directly measured				UNIPD-Cheap GSHPs database		
	k [W.m^{-1}.K^{-1}]		c_b [MJ.m^{-3}.K^{-1}]	k [W.m^{-1}.K^{-1}]			c_b [MJ.m^{-3}.K^{-1}]	k [W.m^{-1}.K^{-1}]		
	min	max		min	max	Rec		min	max	Rec
Heterometric gravel with sand, wet	0.18	3.00		0.94	1.33	1.08		0.2	3.00	1.08
Gravel, water-saturated	1.6	2.5	2.4*							
Sand, water-saturated	2.0	3.0	2.2-2.9*							
Medium sand, wet	1.00	2.60	2.2-2.8	1.44	2.45	1.86	1.53-2.27	1.0	2.6	1.9
Silty sand/sandy silt, wet	1.20	2.25		1.24	2.06	1.56	1.85-2.48	1.20	2.25	1.62
Silt and clayey silt, wet	0.82	2.60	2.0-2.8	0.93	1.76	1.32	1.84-2.43	0.82	2.60	1.45
Clay/silt, water saturated	1.1	3.1	1.6-3.4*							
Till/loam	1.1	2.9								
Plastic clay, wet	0.60	1.90	2.0-2.8	0.87	1.39	1.03	0.62-2.67	0.60	1.90	1.10

*: source = Verein Deutscher Ingenieure (2000).

Vertical distribution of calculated thermal properties is shown in Figure 5.7.

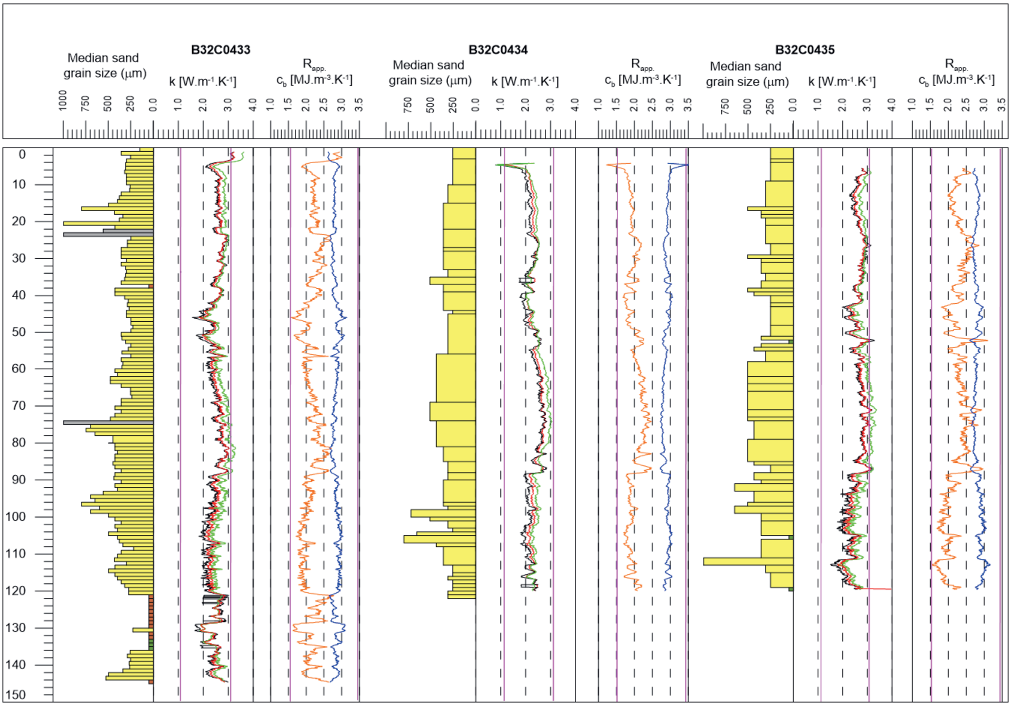

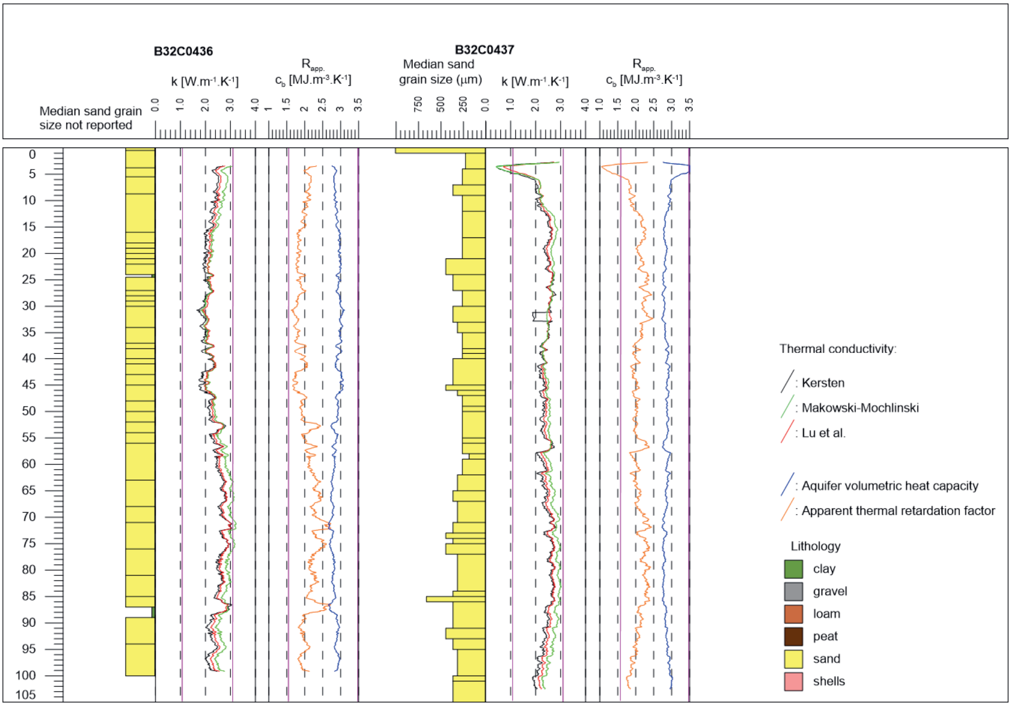

Figure 5.7: Calculated thermal properties. The scalebar on the left is depth in m bgl. The vertical cyan colored lines indicate probabilty intervals for k and c_b from literature (Dalla Santa et al., 2020).

Distribution of calculated thermal conductivities in the upper 100 m of the boreholes is illustrated by frequency plots in Figure 5.8 and is tabulated in Table 5.7. To allow comparing properties between boreholes, only data of the upper 100 m (the maximum depth of B32C0436) are used in Figure 5.8 and Table 5.7.

Table 5.7: Calculated thermal conductivity [W.m^{-1}.K^{-1}] to 100 m bgl.

B/H	Kersten-k					Makowski-Mochlinski-k					Lu et al.*-k				
B32C0 -	Min	Max	Med	Avg	SD	Min	Max	Med	Avg	SD	Min	Max	Med	Avg	SD
433	1.6	3.2	2.5	2.5	0.3	1.8	3.6	2.8	2.8	0.3	1.8	3.3	2.6	2.60	0.2
434	0.8	2.8	2.3	2.3	0.3	0.8	3.1	2.5	2.5	0.3	1.1	2.8	2.4	2.39	0.2
435	1.9	3.3	2.7	2.6	0.3	2.2	3.4	2.9	2.9	0.2	2.1	3.2	2.7	2.69	0.2
436	1.6	3.1	2.3	2.3	0.3	1.8	3.2	2.6	2.6	0.4	1.9	3.0	2.4	2.43	0.3
437	0.4	2.8	2.4	2.4	0.3	0.4	3.0	2.6	2.6	0.3	0.7	2.8	2.5	2.46	0.3

Calculated thermal conductivities do not exhibit a normal distribution (Figure 5.8). D'Agostino-Pearson tests show for all calculated thermal conductivity distributions a difference between the data sample and the normal distribution that is big enough to be statistically significant. Most frequency distributions exhibit a negative skewness (Table 5.8). Despite skewness of the frequency distribution, the standard deviation of calculated values (Table 5.7) ranges only between 7.0 and 12.5% of the average values. Precision, therefore, is considered high.

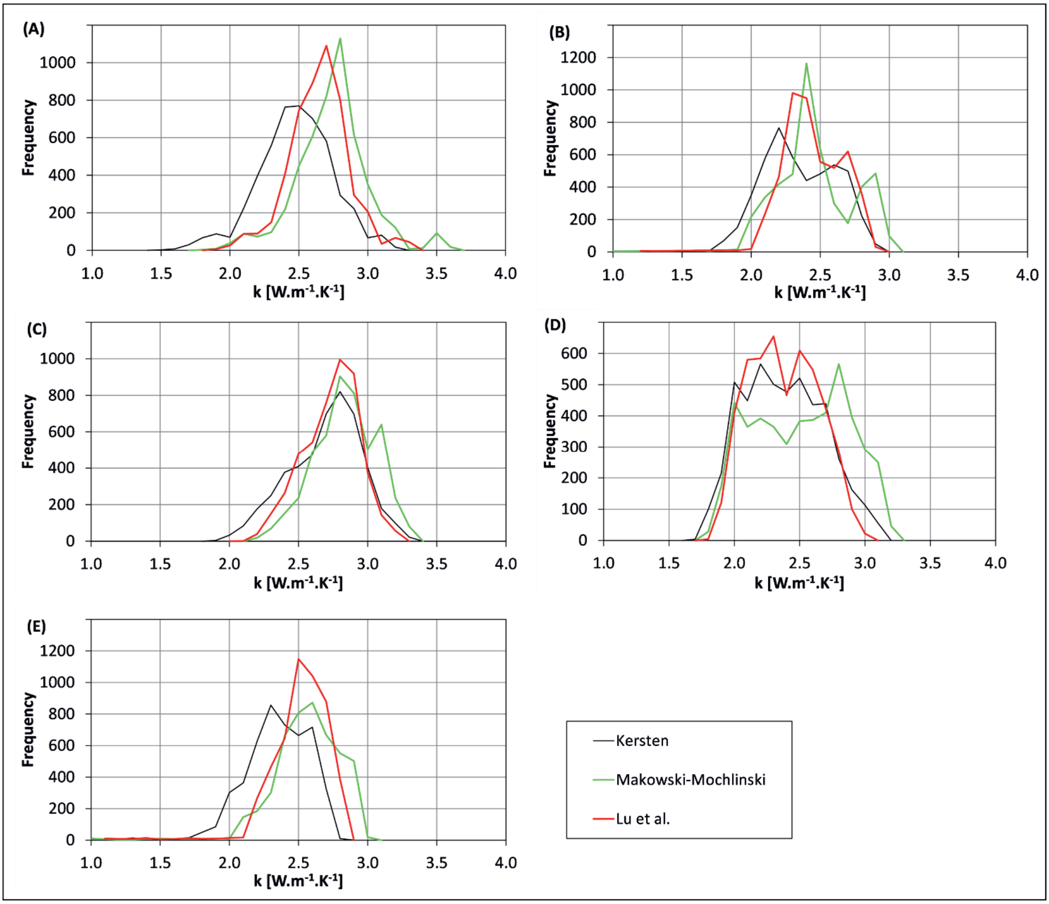

Figure 5.8: Frequency distribution of the calculated thermal conductivities in borehole B32C0433 (A), B32C0434 (B), B32C0435 (C), B32C0436 (D), and B32C0437 (E).

Box-and-whisker plots of calculated thermal conductivities in Figure 5.9 show that almost all outliers are low values. Low values cause negative skweness in the frequency plots and are caused by thin clay or gravel layers with low thermal conductivity. Negative outliers comprise 0.00 to 3.20% of the data. Positive outliers only occur in borehole B32C0433 and comprise 2.55% of the Makowski-Mochlinski method calculated data.

Table 5.8: Skewness of the thermal conductivity frequency distribution.

Borehole	Method	Skewness shape	Skewness
B32C0433	Kersten	Asymmetrical, left/negative	-0.2425
	Makowski-Mochlinski	Potentially symmetrical	0.0584
	Lu et al.	Potentially symmetrical	-0.0447
B32C0434	Kersten	Asymmetrical, left/negative	-0.5669
	Makowski-Mochlinski	Asymmetrical, left/negative	-0.5938
	Lu et al.	Asymmetrical, left/negative	-0.6698
B32C0435	Kersten	Asymmetrical, left/negative	-03694
	Makowski-Mochlinski	Asymmetrical, left/negative	-0.2315
	Lu et al.	Asymmetrical, left/negative	-03450
B32C0436	Kersten	Asymmetrical, right/positive	0.1901
	Makowski-Mochlinski	Potentially symmetrical	-0.0663
	Lu et al.	Asymmetrical, right/positive	0.1263
B32C0437	Kersten	Asymmetrical, left/negative	-2.5830
	Makowski-Mochlinski	Asymmetrical, left/negative	-3.0117
	Lu et al.	Asymmetrical, left/negative	-3.1716

Over 90% of thermal conductivity calculated with the three different methods (including outliers) are within the probability range that follows from Table 5.6 (Table 5.9). Only values calculated for B32C0435 with the Makowski-Mochlinski method are too high, resulting in less than 80% of the values falling within the range defined above. The first and third quartile of all values are all within the range. Results of the three methods can, therefore, be classified as accurate.

Table 5.9: Percentages of calculated thermal conductivities within the 1.1 to 3.1 W.m^{-1}.K^{-1} range.

Borehole	Kersten method	Makowski-Mochlinski method	Lu et al. method
B32C0433	98.02%	91.10%	97.74%
B32C0434	99.62%	99.71%	99.98%
B32C0435	97.44%	79.71%	98.79%
B32C0436	100.00%	93.84%	100.00%
B32C0437	98.31%	98.50%	98.95%

Vertical distribution of the thermal conductivity as calculated with the three different models (Figure 5.7), is inversely proportional to the porosity (Figure 5.6). Relatively high thermal conductivities are found to a depth of approx. 40 m bgl. Between 40 and 60 m bgl, high porosities occur, resulting in lower thermal conductivities. Between 60 and 90 m bgl, porosity is lower, with associated higher thermal conductivities. High porosities between 90 and 120 m bgl result in lower thermal conductivities again. B32C0433 has penetrated loam and clay layers between 120 and 135 m bgl. Loam layers, with clay percentages of around 10%, show relatively high thermal conductivities (2.6-2.9 W.m^{-1}.K^{-1}), whilst in clay layers with a higher clay percentage, thermal conductivity is significantly lower (2.0-2.3 W.m^{-1}.K^{-1}). This is in accordance with the theory that a limited amount of clay particles forms bridges between the sand grains and, therefore, increases the thermal conductance. Where the clay minerals become more dominant, this effect is lost due to the higher porosity associated with the clay sediment and the low thermal conductivity of the clay particles themselves.

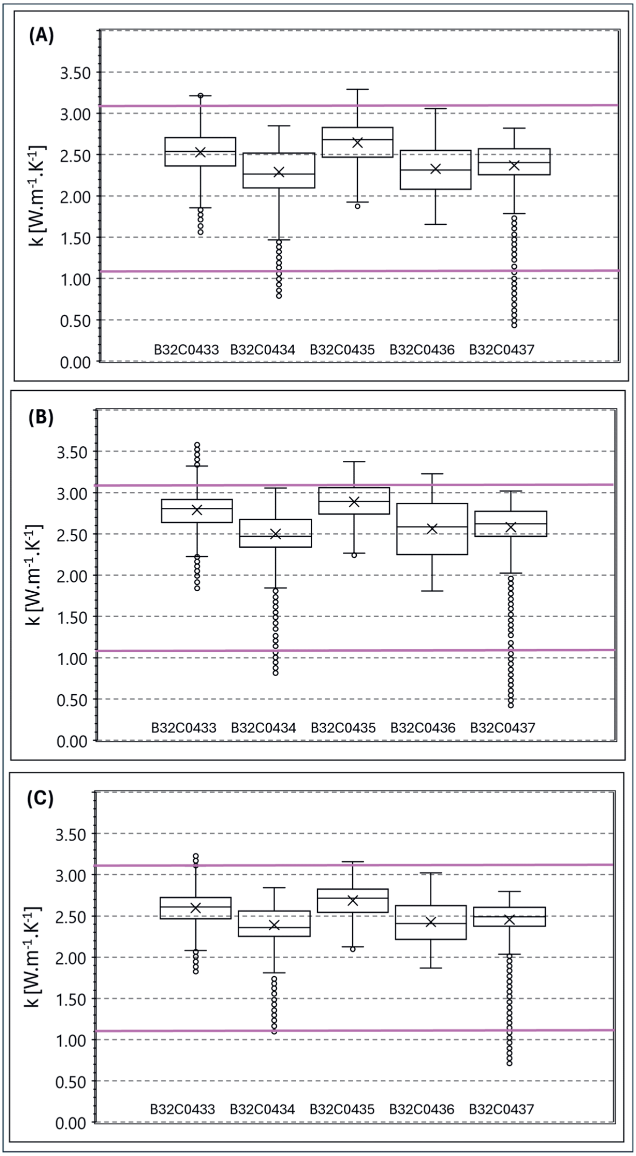

Figure 5.9: Box and whisker plots of calculated thermal conductivities: (A) Kersten method, (B) Makowski-Mochlinski method, (C) Lu et al. method. The middle line of the box represents the median and x represents the mean. The bottom line of the box represents the 1st quartile. The top line of the box represents the 3rd quartile. Whiskers extend from the ends of the box to the minimum and maximum value, excluding outliers. Open circles are outliers. A data point is considered an outlier if it exceeds a distance of 1.5 times the inter quartile range (IQR) below the 1st quartile or 1.5 times the IQR above the 3rd quartile. The purple lines indicate the upper and lower probability range of thermal conductivity of aquifers materials at the study site.

As c_b and $R_{app.}$ are related to the porosity as well, these parameters show the same vertical zoning as the thermal conductivity (Figure 5.7), although SD for these parameters is smaller (Table 5.10). Table 5.6 provides a range for c_b of 1.6-3.4 MJ.m^{-3}.K^{-1} expected to occur in the aquifer materials of the study area. Values outside this range are only found in the upper few meters of boreholes B32C0434 and B32C0437. High values up to 3.6 and 4.0 MJ.m^{-3}.K^{-1} occur in these boreholes where a high clay percentage and porosity are inferred from the gamma-ray logs.

Ranges of thermal diffusivity α (based on the Lu et al-k) are also shown in Table 5.10. Both $R_{app.}$ and α can be seen as measures of the speed of propagation of the thermal front due to conduction. The maximum values of these parameters are almost the twofold of the minimum values. The α shows even larger ranges in B32C0434 and B32C0436.

Table 5.10: Calculated aquifer volumetric heat capacities, apparent thermal retardation and thermal diffusivity to 100 m bgl.

B/H	c_b [MJ.m^{-3}.K^{-1}]					$R_{app.}$					α [10E^{-6} m^2.s^{-1}]				
B32C0-	Min	Max	Med	Avg	SD	Min	Max	Med	Avg	SD	Min	Max	Med	Avg	SD
433	2.6	3.1	2.8	2.8	0.1	1.6	3.0	2.2	2.2	0.2	0.6	1.4	1.0	1.0	0.1
434	2.7	3.6	2.9	2.9	0.1	1.2	2.5	2.0	2.0	0.2	0.3	1.0	0.8	0.8	0.1
435	2.6	3.0	2.8	2.8	0.1	1.7	3.1	2.3	2.3	0.2	0.7	1.2	1.0	1.0	0.1
436	2.7	3.1	2.9	2.9	0.1	1.6	2.7	2.0	2.0	0.2	0.6	1.1	0.8	0.8	0.1
437	2.7	4.0	2.8	2.9	0.1	1.1	2.5	2.1	2.1	0.2	0.1	1.0	0.9	0.9	0.1

5.3.5 Sensitivity analysis

Thermal conductivity, as calculated by three methods, depends on moisture content and dry density of the aquifer. The Makowski-Mochlinski and Lu et al. methods additionally require clay (plus silt) content and thermal conductivity of water and solids fractions. Interdependency of these input parameters and other parameters is illustrated in Figure 5.10.

As only the saturated sections of the profiles are being studied here, the moisture content is equal to porosity. Porosity is calculated from measured bulk electrical resistivity (LN200) and formation factor, and, therefore, depends on clay content. Clay content is derived using well established and widely applied techniques and relations. While in previous studies GR_{Shale} and $GR_{Clean\ Rock}$ are either not derived nor reported, or the choice for the parameter values is unclear, in this study these parameters are set to values derived from the geophysical bore logs and calculated clay percentages show a good correspondence with reported clay percentages in the boreholes. Therefore, the calculated clay percentage is considered to be reliable. However, for sensitivity analysis purposes, V_{sh}, derived from natural gamma ray logs, has been varied by -20% to + 20% in the logs of B32C0433. This results in median calculated porosity changes of only +1.69% to -1.52%. This is illustrated in the box-and-whisker plot in Figure 5.11. Calculated porosity declines with increasing V_{sh} and C in the predominantly sandy aquifer. This is contrary to the findings of e.g. Fahmi (1961), who found an increasing porosity when mixing sand with clay particles. Decreasing calculated porosity with increasing C is due to the higher fraction of the electrical conductivity being attributed to clay particles, and, therefore, less to water content (~porosity). In the present case study, porosity shows a limited sensitivity to V_{sh} and, therefore, C.

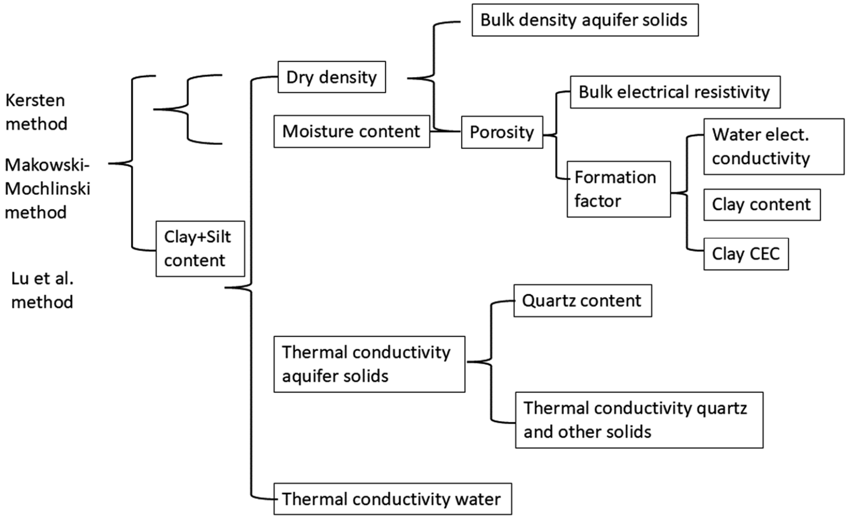

Figure 5.10: Input parameters for different methods of calculating thermal conductivity.

Varying V_{sh}, and therefore porosity, results in limited changes in calculated thermal conductivity as shown in Figure 5.11. Changing V_{sh} with -20% to +20% results in calculated thermal conductivity to change between -7.28% and + 6.18%. Median thermal conductivity in the V_{sh} range used varies between 2.36 to 2.57 W.m^{-1}.K^{-1} when the Kersten method is applied. For the Makowski-Mochlinski method the median thermal conductivity ranges between 2.90 and 2.98 W.m^{-1}.K^{-1}. Lu et al. 's method results in a median thermal conductivity range from 2.47 to 2.63 W.m^{-1}.K^{-1}. Sensitivity of calculated thermal conductivity to V_{sh} and associated porosity variations is limited.

However, larger changes occur when applying Kersten's method where a change in V_{sh} results in a $C + S$ % undershooting or exceeding 50%. In that case, Eq.(5.10) is applied instead of Eq.(5.9) and v.v. Applying a V_{sh} range then leads to thermal conductivity changes of over 30% and can be seen as a weakness of the Kersten method for profiles where $C + S$ is around 50%. In borehole B32C0433, this is only the case in 0.54 m of the upper 100 m of the borehole.

The first and third quartiles of the calculated thermal conductivities with variable V_{sh} are all within the probability range derived in the previous section (1.1-3.1 W.m^{-1}.K^{-1}). Lower porosity in all three methods results in a higher thermal conductivity. This is in accordance with the fact that aquifers solids are more thermally conductive than the water fraction. Secondly, a higher clay content, resulting in clay particles filling intergranular spaces between sand grains, results in increasing thermal conductivity by forming bridges between the grains. Thermal conductivity, therefore, shows an upward trend with increasing V_{sh}.

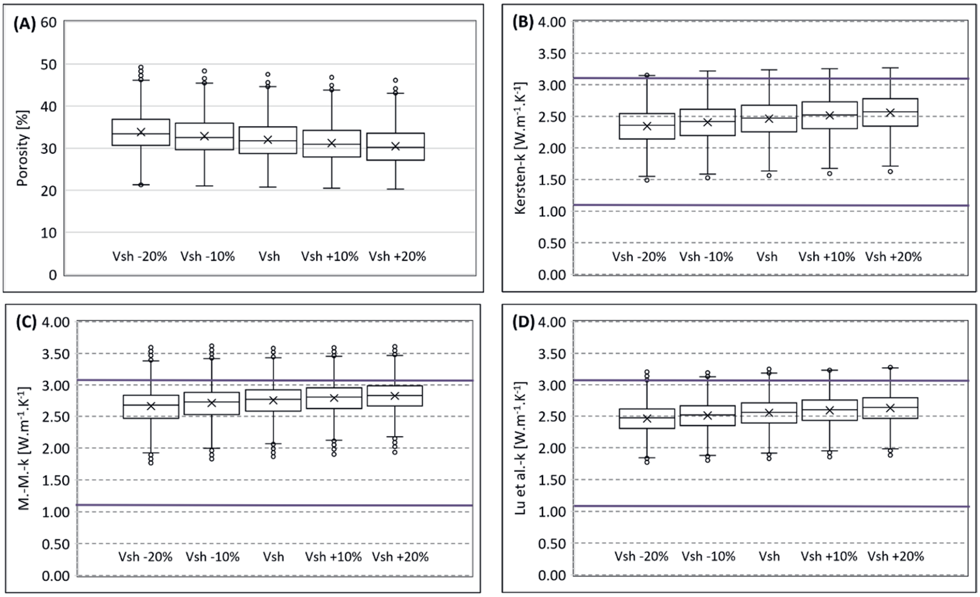

Figure 5.11: Sensitivity analysis of porosity (A) and thermal conductivity according to Kersten (B), Makowski-Mochlinski (C) and Lu et al. (D) with variable V_{sh}. For explanation of the box-and-whisker plots, see Figure 5.9. The horizontal purple lines represent the probability interval for thermal conductivity at the site.

The method by Lu et al. (2007) requires input for the thermal conductivity of the aquifer solids. Percentages quartz and other aquifer materials, therefore, need to be assessed In the present case study, Q of 70% of the sand fraction was derived from Griffioen et al. (2016). This results in thermal conductivities that match those derived by Kersten's method and the Makowski-Mochlinski method. However Q may vary between 60 and 80% in different petrological provinces, as shown by Van Baren (1934). Increase of Q from 60% to 80% results in an increase in calculated thermal conductivity with the Lu et al. method. Median thermal conductivity increases from 2.34 to 2.80 W.m^{-1}.K^{-1} (Figure 5.12).

Absolute calculated thermal conductivites show a maximum decrease of 10.05% at $Q = 60\%$ to a maximum increase of 11.18% at $Q = 80\%$. This high sensitivity of the Lu et al. method to Q is explained by the high thermal conductivity of quartz (7.7 W.m^{-1}.K^{-1}) compared to other aquifer solids (2.0 W.m^{-1}.K^{-1}). Despite the high sensitivity to Q, the first and third quartiles of the calculated thermal conductivities (Figure 5.12) remain within the probablility range defined in the previous section (1.1-3.1 W.m^{-1}.K^{-1}).

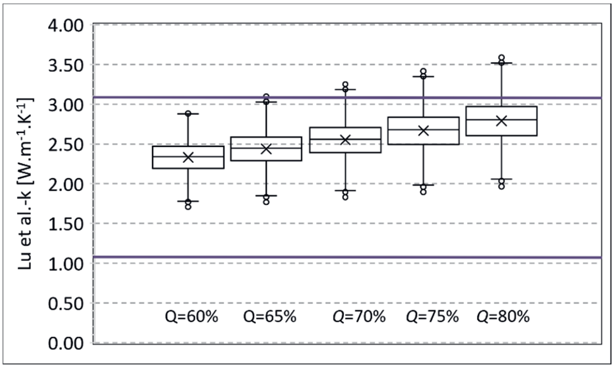

Figure 5.12: Sensitivity of the thermal conductivity calculated with the Lu et al. method to variable Q. The horizontal purple lines indicate the upper and lower limit of the probability range for the aquifer materials.

5.4 Conclusions

In this chapter, it is demonstrated that 'standard' geophysical borehole logging techniques, can be used to assess aquifer properties such as porosity and clay percentage. By applying empirical relations between the aquifer parameters and thermal properties, the magnitude and variability of thermal properties of the aquifer can be derived. This allows for detailed investigation of thermal properties of aquifers. However, interpretation of the geophysical logs and application of empirical relationships is not straightforward.

Assessment of aquifer physical properties by using gamma ray and resistivity logs in this case study required insight into the clay content of the subsurface in nearby reference boreholes. Use of the Waxman-Smits model to correct for electrical conduction of clay, shows that characteristic clay mineral CEC could not be used. As indicated by Qi & Wu (2022), at a low porewater conductivity, clay conductivity cannot be derived from CEC. The parameter representing CEC in the Waxman-Smits model had, therefore, to be derived iteratively, such that the calculated porosities match those known to be representative (Olsthoorn, 1977) for the aquifer studied.

Three empirical relationships used here for deriving the thermal conductivity yield similar results for the magnitude and variability of the thermal conductivity of the aquifer. The methods are not very sensitive to variations in clay content and porosity. However, the method of Lu et al. (2007) is sensitive to quartz content of the aquifer material. In the present study, quartz content was derived from literature data resulting in thermal conductivities within the probability range and comparable to results of the other methods. This illustrates the importance of not using a single empirical method for estimating the thermal conductivity.

Despite the required manipulation of some of the models and relationships, ranges of thermal properties are found that match those in literature, such as the extensive inventory by Dalla Santa et al. (2020). The application of the use of publicly available geophysical logs in this study reveals that hydrogeologically uniform formations and aquifers actually show a broad bandwidth of thermal parameters. In this study, thermal conductivity values of the aquifer do not show a normal but skewed distribution. Therefore, use of an average thermal conductivity for the aquifer should be considered with caution.

Dedicated geophysical borehole logging techniques, yielding direct measurement of water content (or porosity) or density of the aquifer, will improve the assessment of thermal aquifer parameters. These techniques are not yet being widely applied. Therefore, widely available gamma ray and resistivity logs provide a good alternative.

Chapter 6

Synthesis

6.1 Main conclusions

Groundwater is a major source for the production of drinking water, worldwide and in the Netherlands. Groundwater temperature (GWT) is crucial for the physical and chemical quality of groundwater. As is demonstrated in this thesis, GWT varies laterally, with depth, and in time, even on a small scale as in the Netherlands (Chapter 2). Aquifers in the Netherlands generally occur to depths of several hundreds of meters (up to >450 m according to Dufour (1998)), although locally (e.g. the Roer Valley Graben) deeper aquifers exist. GWT is determined by semi-equilibrium between the geothermal heat flow from the Earth' interior, the temperature at the Earth surface (ground surface temperature, GST) and the thermal properties of the strata through which the heat flow propagates.

The geothermal heat flow in mainland Netherlands varies between 51.4 and 128.2 mW.m^{-2}, with a median of 77.2 W.m^{-2} (Jennings et al., 2021). This implies that, assuming a uniform thermal conductivity and ground surface temperature (GST), in absence of a shallow heat source, the subsurface temperature at e.g. 100 m depth varies by several ^{o}C, due to variations in geothermal heat flux alone. Thermal properties of the aquifers and aquicludes differ laterally and vertically, even within apparently uniform hydrogeological units (Chapter 5). Therefore, the subsurface temperature field is non-uniform. Secondly, GST is variable in space and time, being a function of land cover and climatological conditions (Chapter 2). GST changes are disseminated to the subsurface by both conduction and advection through groundwater flow. Where groundwater infiltration (recharge) occurs, GST changes are transferred to groundwater temperatures more rapidly and with less attenuation.

These processes cause the GWT at 20-35 m depth (T20-35) to vary between 5.7 and 16.6^{o}C, with 1991-2011 averages between 8.8 and 15.1^{o}C (Chapter 2). In this study it is demonstrated that field temperature measurements of groundwater samples, which are being collected extensively and over longer periods of time, is a useful data source to map GWT and GWT trends, if measured in a standardized manner. Clearly discernable T20-35 patterns were identified.

Surface atmosphere radiation balance (SARB) modelling shows that lowest GWTs are found in the topographically higher areas of the country, where low simulated GSTs prevail in combination with groundwater recharge especially during winter. High GWTs occur in the southeast of the country, where the SARB modeling resulted in the highest simulated GSTs. The west of the country is strongly urbanized, resulting in an extensive area with relatively high GWT. Cities are associated with subsurface urban heat islands (SUHIs) where T20-35 occur exceeding rural background by 4^{o}C (Chapter 3). Building density, type of road surface, presence of green spaces and the age of the urbanization determine the urban GWT (Chapter 3).

GWT patterns and trends mapped by means of T20-35 observations are broadly confirmed by the abstracted water temperatures at public supply well fields (PSWF). PSWF water temperature observations also show that the GWT along the major rivers is, in part, influenced by infiltrating river water temperatures.

Trends in the 1991-2011 T20-35 show predominantly a climbing GWT, in particular in areas of groundwater recharge. In seepage dominated areas, more stable T20-35 occur. This, however, does not mean that the GWT in those areas does not increase. SAT shows an accelerated rise after the late 1970’s. In areas with less groundwater recharge or seepage, this rise propagates downward more slowly, by conduction only, or is in part attenuated by advection in the reverse direction. Accelerated ascent of SAT and GST will, therefore, exert its influence on GWT later than the 1991-2011 observation period. The topographically lower areas that are characterized by higher groundwater levels or seepage are highly urbanized regions (Central and West Netherlands). Urbanization is associated with high GST and SUHIs, resulting in a higher than average mapped T20-35.

SARB modeling, inverse modeling of (repeated) temperature-depth (TD) profiles and field observations of surface temperatures show that GST, for the land cover types considered, is mainly controlled by land cover, surface air temperature (SAT) and incoming (global) radiation. Forest is associated with the lowest GSTs, followed by GSTs of grassland. Built up terrain is associated with the highest GSTs. SAT and global radiation show a steady increase as a result of climate change, in particular since the late 1970’s, resulting in rising GSTs. This rise is irrespective of land cover or topographical position in the country. Precipitation (amounts and temporal patterns) and evapotranspiration also evolve under climate change. Theoretically, this could, in part, compensate for the GST increase. However, the 1991-2011 T20-35 trends indicate in majority a GWT increase that is similar to the expected rise of GST. Change to different types of land use, in particular afforestation, could compensate the GST evolution. Urbanization results in the reverse, strengthening GWT increase (Chapter 3).

Produced water temperature trends at PSWFs tapping from phreatic and semi-confined aquifers and river bank filtrate, despite extraction from greater depths than the T20-35 observations, confirm increasing GWT trends. This is most prominent for river bank filtrate and phreatic PSWFs. River bank filtrate is influenced by rising river water temperatures due to higher air and run-off temperatures and use of river water as cooling water. Climate change results in retracting glaciers and less snow in the source areas of the Rhine, resulting in lower amounts of meltwater in summer. The deeper semi-confined PSWFs have a higher percentage of stable temperatures, as changes at the surface take longer and are more attenuated to reach these depths. (Probably) decreasing trends in produced water for a minor fraction, except for the limestone PSWFs.

Synthesized GST values and the groundwater recharge regime correlate well with the observed GWTs and trends. Recharge largely depends on rainfall excess over evapotranspiration, land cover and topographical position. GST is mainly determined by land cover, SAT and incoming radiation. Land use, rainfall, SAT and radiation show regional patterns, explaining distinct GWT variations throughout the country, answering research questions 1 and 3.

Climate change results in GST increases, irrespective of the land cover. Conduction and groundwater recharge are mechanisms through which higher surface temperatures disseminates into the subsurface and groundwater. Groundwater recharge areas, therefore, show increasing GWT trends, while areas with less recharge or even seepage (urbanized west of the country), have more stable GWT temperatures. The identified GWT trends and drivers of changes answer research question 2.

Recent (last 150 years) climate change is attributed to human-induced causes, mainly the use of fossil fuels. Other anthropogenic impacts on GWT are more localized. These include changes of land use (sometimes as a result of climate change) such as deforestation, changing agricultural practices (grassland to arable land and v.v.) and urbanization. The use of the subsurface and aquifers for various purposes may cause local but strong GWT impacts. Pumping high amounts of groundwater for drinking water production potentially disturbs the temperature field. Energy transition requires accelerated construction of underground infrastructure, such as power transmission lines and district heating networks. These types of underground infrastructure emit heat to their environs, affecting GWT. Their effects are very local, due to the nature of the infrastructure spreading laterally along great distances. A strong growth of underground thermal energy storage (UTES) systems is also associated with the need of energy transition to sustainable or renewable sources. In particular aquifer thermal energy storage (ATES) systems form an efficient technique for storing and utilizing seasonal energy. The Netherlands, with distinct summer and winter seasons and having thick aquifers, provides a perfect setting for the utilization of ATES, leading to a substantial growth of ATES systems since introduction in the 1980's. To date (2024) it is estimated (based on data from www.warmteatlas.nl) that over 79,000 closed loop UTES have been installed and over 3,000 ATES systems. Each ATES system has an impact on the GWT in its vicinity. The lateral extent of the impact is usually limited as long as there is a thermal balance. This thermal balance, however, is not achieved in all systems. A cold surplus is implicitly allowed under the current Environment and Planning Act ("Omgevingswet") of the Netherlands. Thermal impact by high system temperatures is limited by the maximum allowed infiltration temperature of 25^{o}C. In particular, the possibility of operating ATES systems with a cold surplus necessitates good planning as more systems are constructed in close proximity, increasing the risk of interference between them. Municipal authorities have the possibility (and task) to regulate this in masterplans. Both the design of individual ATES systems and the drafting of master plans requires modeling of the impacts of the ATES systems. When modeling is being utilized to these avails, the aquifers are generally considered to be uniform. However, apparently uniform hydrogeological strata can in reality be hydraulically and thermally heterogeneous (Chapter 5). The thermal impact assessed by models incorporating fine-scale heterogeneity is different from that by models using uniform layers, regarding the lateral and vertical extent of thermal impacts (Chapter 4).

The thermal impact is strongly controlled by actual operational conditions of the ATES system. The effects of operational conditions differing from the design conditions should be assessed in pre-operation impact studies by sensitivity analysis. Fine-scale heterogeneity is shown to be important to accurately model the ATES-impacted vertical temperature distribution and the maximum and minimum temperatures in the storage aquifer, and the spatial extent of the thermal plumes. The same applies to the relatively large pre-ATES-system horizontal and vertical temperature variations of the storage aquifer (caused by spatially varying land-cover and its historical changes). For ATES locations near sensitive groundwater uses (PSWFs) or where interference between systems has to be expected, these aspects should be applied in the impact assessment. It was shown that the methods used to quantify both hydraulic and thermal parameters from various borehole data (logs, samples) provide effective means to construct realistic thermal impact models, which account for fine-scale heterogeneity. Monitoring data of ATES-induced temperatures were interpreted in a useful way by groundwater and heat transport modeling. Observed and modeled thermal impact is limited to temperatures between 5 and 25ºC in the cold and warm water bubbles. The lateral extent of the thermal impact depends on the hydraulic and thermal heterogeneity of the subsurface, an aspect that is often overlooked or poorly understood. Therefore, ATES-induced thermal impact is easily underestimated.

6.2 Practical implications and outlook

In this research (repeated) TD profiling was used for studying GWT. It was demonstrated that also field temperature measurements of groundwater samples, which are being collected extensively and over longer periods of time, is a useful GWT measure, if measured in a standardized manner. This allowed to discern GWT patterns and trends in time over almost the entire country. To this avail, it is recommended to sample monitoring wells strictly following the sampling protocols and preferably using above ground peristaltic pumps. Abstracted water temperatures of PSWFs, despite being abstracted from greater and more variable depths, proved to align to T20-35 measurements and river water temperatures. Data from PSWFs can be used to complement sample temperatures from monitoring networks, thereby contributing to the study of GWT patterns and trends.

GWT patterns are indicative of ongoing processes. GWT is widely used as a tracer for groundwater flow, both laterally and vertically. Insight in the GWT field, trends and drivers are required for these studies. This thesis provides such information.

Changes in temperature induce groundwater quality variations. The average ambient temperature range at a national scale (in the Netherlands) is not large enough to expect groundwater quality to vary due to temperature variations that could be of importance for drinking water production. However, groundwater dependent eco-systems could be influenced by chemical and micro-biological changes as a result of small temperature impacts. Temperature buffering by groundwater seepage to ecologically valuable streams is impacted by changing GWT and, of course, its seepage flux.

In urban areas, GWT temperature in the SUHI is significantly higher (up to >4ºC higher at 20 m bgl) than in nearby rural areas. Local temperature anomalies are created by ATES systems. As most ATES systems are concentrated in urban areas, both the effects of the SUHI and ATES systems are mutually reinforcing. A higher ambient GWT requires larger amounts of groundwater (due to the maximum allowed injection temperature) to achieve the same cooling by ATES. This implies higher pumping rates and injection of more and/or warmer water into the aquifer. This could result in a self-strengthening effect, in particular as climate change and the urban heat island effect result in a higher cooling demand.

6.3 Remaining challenges and recommendations

The present study provides insight in the patterns, trends and drivers of GWT at 20-35 m depth, and impacts by various manmade causes. TD profiling and field temperatures from samples have been used. Based on the requirements from the European Water Framework Directive (WFD), the sampling frequency is every 6 years for regional groundwater monitoring networks. In 2015/2016 and 2018/2019, two sampling campaigns of the regional monitoring networks were performed. The sampled depths were <10 m (‘shallow’) or <25 m (‘deep’) (van Loon et al., 2020). By far, most samples were from depths <20 m. It is recommended that the next sampling campaign also includes monitoring wells deeper than 25 m, including field measurements of the GWT. A comparative study of in-situ measurements of GWT (by TD profiling) and above ground sample temperatures could enhance setting up protocols for “temperature monitoring”.

Many boreholes are being drilled for ATES systems, to depths of tens to hundreds of meters. Descriptions of the strata are being made and, usually, capacity tests are being performed. In rare cases, a natural-gamma log is performed. It would contribute to the understanding of the subsurface, its characteristics and heterogeneity, if at every ATES borehole a geophysical log would be performed. Relative to the cost of drilling and installation of the wells, the cost of geophysical logging is marginal (a few percent).

Witte et al. (2002) describe a method for in-situ measurement of thermal conductivity of the subsurface, not dissimilar to other types of tests that use a closed loop set-up in a borehole. This test, however useful, provides a bulk conductivity of the depth at which the closed loop is placed. A direct push Thermal Conductivity Profiler (TCP) has been developed (Chirla et al., 2016). Exploration depths of direct push techniques are limited to ca, 40 m under favorable conditions. To distinguish fine-scale heterogeneity to greater depths, development of logging tools for in-situ measurement of thermal properties of the subsurface are required. As long as these tools are not available, indirect methods, such as described in Chapter 5 of this thesis, can be applied. These indirect methods can be improved e.g. by direct measurement of porosity in bore logs. Insight in the thermal properties of the subsurface strata will greatly enhance the more accurate design of ATES systems, and also improve inversion models of TD measurements.

The evolution of GST and GWT is driven by climate change. Their “present” effects and trends have been assessed in this thesis. The methods used, such as SARB modeling, can be extrapolated into the future, using the climate scenario predictions based on the foreseen changes of meteorological parameters. SARB models can be improved by collecting more GST data by direct measurements or derived from TD profiling.

References

Dalla Santa, G., Galgaro, A., Sassi, R., Cultrera, M., Scotton, P., Mueller, J., . . . Bernardi, A. (2020). An updated ground thermal properties database for GSHP applications. *Geothermics*(85).

AHN. (2023). *Actueel Hoogtebestand Nederland*. Retrieved December 22, 2023, from https://www.ahn.nl/

Allen, A., Milenic, D., & Sikora, P. (2003). Shallow gravel aquifers and the urban “heat island” effect: a source of low enthalpy geothermal energy. *Geothermics 32*, pp. 569–578.

Allen, D., Bayer, P., Ferguson, G., & Blum, P. (2014). Preface: Hydrogeology of shallow thermal systems. *Hydrogeology Journal*.

Amsterdam Institute for Advanced Metropolitan Solutions. (2019). *Energy transition: what does the future look like?* Opgeroepen op 10 3, 2021, van https://www.ams-institute.org/news/the-future-of-urban-energy/

Anderson, M. (2005). Heat as a Ground Water Tracer. *Ground water*, pp. 951–968.

Appelo, C., & Postma, D. (2005). *Geochemistry, Groundwater and Pollution. Second edition.* Leiden: A.A. Balkema Publishers.

Archie, G. (1942). The electrical resistivity log as an aid in determining some reservoir characteristics. *Transactions of the American Institute of Mining & Metallurgical Engineers, 146*, 54-62.

Aziz, J., Ling, M., Rifai, H., Newell, C., & Gonzales, J. (2003). MAROS: A Decision Support System for Optimizing Monitoring Plans. *Ground Water, 41(3)*, pp. 355-367.

Baeyens, B., & Bradbury, M. (2004). Cation exchange capacity measurements on illite using the sodium and cesium isotope dilution technique: effects of the index cation, electrolyte concentration and competition: modeling. *Clays and Clay Minerals* (Volume 52, Number 4), 421-431.

Bakema, G., Bloem, J., Heinen, M., Knotters, M., & Van Rooijen, N. (2022). *De invloed van klimaatverandering op de bodemtemperatuur [in Dutch: 'The influence of climate change on the soil temperature].* Wageningen: Wageningen University & Research.

Bakr, M., Van Oostrom, N., & Sommer, W. (2013). Efficiency of and interference among multiple Aquifer Thermal Energy Storage systems; A Dutch case study. *Renewable Energy*(60), 53-62.

Bates, B., Kundzewicz, Z., Wu, S., & Palutikof, J. (2008). *Climate Change and Water. IPCC Technical Paper VI.* Geneva: IPCC Secretariat.

Bayer, P., Attard, G., B. P., & Menberg, K. (2019). The geothermal potential of cities. *Renewable Sustainable Energy Review 106(C)*, pp. 17–30.

Bayer, P., Rivera, J., Schweizer, D., Schärli, U., Blum, P., & Rybach, L. (2016). Extracting past atmospheric warming and urban heating effects from borehole temperature profiles. *Geothermics 64*, pp. 289–299.

Becker, B., & Fricke, B. (1997). Effects of Saturation and Dry Density on Soil Thermal Conductivity, Heat Pumps in Cold Climates. In *Proceedings of the third international conference on heat pumps in cold climates* (pp. 121-135). Wolfville: Acadia University, Nova Scotia, Canada.

Beets, C., & Beets, D. (2002). A high resolution stable isotope record of the penultimate deglaciation in lake sediments below the city of Amsterdam, The Netherlands. *Quaternary Science Reviews 22*, pp. 195–207.

Beltrami, H. (2001). On the relationship between ground temperature histories and meteorological records: a report on the Pomquet station. *Global and Planetary Change 29*, pp. 327-348.

Beltrami, H. (2002). Climate from borehole data: Energy fluxes and temperatures since 1500. *Geophysical Research Letters 29(23)*.

Beltrami, H., & Kellman, L. (2003). An examination of short- and long-term air–ground temperature coupling. *Global and Planetary Change 38*, pp. 291-303.

Bennema, J. (1954). Holocene movements of land and sea-level in the coastal area of the Netherlands. *Geologie en Mijnbouw*, pp. 254-264.

Bennett, A. (2004). *Heat Fluxes from Street Canyons. MSc dissertation.* The University of Reading, UK.

Bense, V. (2004). *The hydraulic properties of faults in unconsolidated sediments and their impact on groundwater flow. A study in the Roer Valley Rift System and adjacent areas in the Lower Rhine Embayment (PhD thesis).* Amsterdam: Vrije Universiteit.

Bense, V., & Beltrami, H. (2007). Impact of horizontal groundwater flow and localized deforestation on the development of shallow temperature anomalies. *Journal of Geophysical Research Vol.112*.

Bense, V., & Kooi, H. (2004). Temporal and spatial variations of shallow subsurface temperature as a record of lateral variations in groundwater flow. *Journal of geophysical Research. Vol. 109*.

Bense, V., & Kurylyk, B. (2017). Tracking the subsurface signal of decadal climate warming to quantify vertical groundwater flow rates. *Geophysical Research Letters, 44*, pp. 12,244-12,253.

Bense, V., de Bruin, J., Kurylyk, B., & Visser, P. (2020). Transient subsurface thermal profiles reveal temporal variability in groundwater flow conditions. *Water Resources Research*.

Bense, V., Kurylyk, B., van Daal, J., van der Ploeg, M., & Carey, S. (2017). Interpreting Repeated Temperature-Depth Profiles for Groundwater Flow. *Water Resources Research 53*, pp. 8639-8647.

Bense, V., Read, T., Bour, O., Le Borgne, T., Coleman, T., Krause, S., . . . Selker, J. (2016). Distributed Temperature Sensing as a downhole tool in hydrogeology. *Water Resources Research*, pp. 9259–9273.

Benz, S., Bayer, P., & Blum, P. (2017a). Global patterns of shallow groundwater temperatures. *Environmental Research Letters, 12*.

Benz, S., Bayer, P., & Blum, P. (2017b). Identifying anthropogenic anomalies in air, surface and groundwater temperatures in Germany. *Science of the Total Environment*, pp. 145–153.

Benz, S., Bayer, P., Blum, P., Hamamoto, H., Arimoto, H., & Taniguchi, M. (2018). Comparing anthropogenic heat input and heat accumulation in the subsurface of Osaka, Japan. *Science of the Total Environment*, pp. 1127–1136.

Benz, S., Bayer, P., Menberg, K., J. S., & B. P. (2015). Spatial resolution of anthropogenic heat fluxes into urban aquifers. *Science of the Total Environment*, pp. 427-439.

Benz, S., Bayer, P., Olesen, F., Goettsche, F., & Blum, P. (2015b). Linking Surface Urban Heat Islands with Groundwater Temperature. *Environmental Science and Technology*, pp. 70-78.

Benz, S., Irvine, D., Rau, G., Bayer, P., Menberg, K., Blum, P., . . . Kurylyk, B. (2024). Global groundwater warming due to climate change. *Nature Geoscience. Volume 17*, pp. 545–551.

Berthold, S., & Resagk, C. (2012). Investigation of thermal convection in water columns using particle image velocimetry. *Experiments in Fluids*, pp. 1465–1474.

Bidarmaghz, A., Choudhary, R., Soga, K., Kessler, H., Terrington, R., & Thorpe, S. (2019). Influence of geology and hydrogeology on heat rejection from residential basements in urban areas. *Tunneling and Underground Space Technology, 92*.

Bloemendal, M. (2018). *The hidden side of cities: Methods for governance, planning and design for optimal use of subsurface space with ATES (dissertation).* Delft: TU Delft.

Bloemendal, M., & Olsthoorn, T. (2018). ATES systems in aquifers with high ambient groundwater flow velocity. *Geothermics*(75), 81-92.

Bloemendal, M., Olsthoorn, T., & Van de Ven, F. (2015). Combining climatic and geo-hydrological preconditions as a method todetermine world potential for aquifer thermal energy storage. *Science of the Total Environment*(538), 621-633.

Boers (ed.), P., & Noij (ed.), I. (1996). *Huidige en toekomstige belasting van het oppervlaktewater met stikstof en fosfaat vanuit de landbouw [in Dutch: 'Present and future agricultural emissions of nitrogen and phosfate into surface waters'] .* Lelystad: RIZA, SC-DLO, WL.

Bolt, G., & Bruggenwert, M. (1978). *Soil Chemistry - A. Basic Elements* (second revised edition ed.). Amsterdam-Oxford-New York: Elsevier Scientific Publishing Company.

Bonté, D., Van Wees, J.-D., & Verweij, J. (2012). Subsurface temperature of the onshore Netherlands: new temperature dataset and modelling. *Netherlands Journal of Geosciences/Geologie en Mijnbouw 91(4)*, pp. 491–515.

Bonte, M., Geris, J., Post, V., Bense, V., Van Dijk, H., & Kooi, H. (2013). Mapping surface water-groundwater interactions and associated geological faults using temperature profiling. In L. Ribeiro, T. Stigter, A. Chambel, T. Condesso de Melo, P. Monteiro, & A. Medeiros (Eds.), *Groundwater and Ecosystems* (pp. 81-94). London: CRC Press.

Bonte, M., Stuyfzand, P., & Van Breukelen, B. (2014). Reactive Transport Modeling of Thermal Column Experiments to Investigate the Impacts of Aquifer Thermal Energy Storage on Groundwater Quality. *Environmental Science & Technology*.

Bonte, M., Stuyfzand, P., Hulsman, A., & Van Beelen, P. (2011). Underground Thermal Energy Storage: Environmental Risks and Policy Developments in the Netherlands and European Union. *Ecology and Society, 16(l): 22*.

Bonte, M., Stuyfzand, P., van Beelen, P., & Visser, P. (2010). Onderzoek naar duurzame toepassing van warmte-/koudeopslag. *H2O #3*, pp. 30-32.

Bonte, M., Stuyfzand, P., Van den Berg, G., & Hijnen, W. (2011a). Effects of aquifer thermal energy storage on groundwater quality and the consequences for drinking water production: a case study from the Netherlands. *Water Science & Technology*, pp. 1922-1931.

Bonte, M., Van Breukelen, B., & Stuyfzand, P. (2013). Temperature-induced impacts on groundwater quality and arsenic mobility in anoxic aquifer sediments used for both drinking water and shallow geothermal energy production. *Water Research, 4(47)*, pp. 5088-5100.

Bonte, M., Visser, P., Stuyfzand, P., Kooi, H., & van Breukelen, B. (2011). Effects of aquifer thermal energy storage on groundwater quality elucidated by field and laboratory investigations. *Congress Bodemenergie 13-14 oktober 2011.*

Bonte, M., Wols, B., Maas, K., & Stuyfzand, P. (2017). Sources of dissolved oxygen in monitoring and pumping wells. *Hydrogeology Journal*, pp. 55-66.

Bosveld, F., Baas, P., Beljaars, A., Holtslag, A., Vilà-Guerau de Arellano, J., & van de Wiel, B. (2020). Fifty Years of Atmospheric Boundary-Layer Research at Cabauw Serving Weather, Air Quality and Climate. *Boundary-Layer Meteorology, 177(2-3)*, pp. 583-612.

Bredehoeft, J., & Papadopulos, I. (1965). Rates of Vertical Groundwater Movement Estimated from the Earth's Thermal Profile. *Water Resources Research, Vol.1, No.2*, pp. 325-328.

Breukel, R., Silva, W., van Vuuren, W., Botterweg, J., & Venema, R. (1992). *De Maas, verleden, heden en toekomst [in Dutch: The Meuse, past, present and future].* Lelystad: RIZA.

Bridger, D., & Allen, D. (2010). Heat transport simulations in a heterogeneous aquifer use for aquifer thermal energy storage (ATES). *Canadian Geotechnical Journal, 47*, pp. 96–115.

Bridger, D., & Allen, D. (2014). Influence of geologic layering on heat transport and storage in an aquifer thermal energy storage system. *Hydrogeology Journal, 22*, pp. 233–250.

Brons, H., Griffioen, J., Appelo, C., & Zehnder, A. (1991). (Bio)geochemical reactions in aquifer material from a thermal energy storage site. *Water Research, 25*, pp. 729-736.

Buitink, J., Tsiokanos, A., Geertsema, T., ten Velden, C., Bouaziz, L., & Sperna Weiland, F. (2023). *Implications of the KNMI'23 climate scenarios for the discharge of the Rhine and Meuse.* Deltares.

Bulté, M., Duren, T., Bouhon, O., Petitclerc, E., Agniel, M., & Dassargues, A. (2021). Numerical Modeling of the Interference of Thermally Unbalanced Aquifer Thermal Energy Storage Systems in Brussels (Belgium). *Energies, 19*(6241).

Buscheck, T., Doughty, C., & Tsang, C. (1983). Prediction and analysis of a field experiment on a multilayered aquifer thermal energy storage system with strong buoyancy flow. *Water Resources Research, 19*, pp. 1307–1315.

Carslaw, H., & Jaeger, J. (1959). *Conduction of heat in solids.* Oxford: Oxford University Press.

CBS. (2011). *Hernieuwbare energie in Nederland 2010 [in Dutch: 'Renewable energy in The Netherlands 2010'].* Den Haag, the Netherlands: Centraal Bureau voor de Statistiek.

Central Bureau of Statistics. (2022). *Bestand bodemgebruik (in Dutch: Land use data set)*. Retrieved November 11, 2023, from https://www.cbs.nl/nl-nl/dossier/nederland-regionaal/geografische-data/bestand-bodemgebruik

Central Bureau of Statistics. (2023). *The Netherlands in figures*. Retrieved November 11, 2023, from https://opendata.cbs.nl/statline/#/CBS/en/

Cermak, V. (1971). Underground temperature and inferred climatic temperature of the past millenium. *Palaeogeography, Palaeoclimatology, Palaeoecology, Vol.10*, pp. 1-19.

Cermak, V., & Bodri, L. (2018). Attribution of precipitation changes on ground–air temperature offset: Granger causality analysis. *International Journal of Earth Sciences*, pp. 145-152.

Chen, K., Yin, M., Guo, Z., Liang, X., Wei, X., Yang, S., . . . Zheng, C. (2023). Estimating lateral groundwater inflow to rivers using heat as a tracer . *Journal of Hydrology*.

Chen, S., Hu, D., Wong, M., Ren, H., Cao, S., Yu, C., & Ho, H. (2019). Characterizing spatiotemporal dynamics of anthropogenic heat fluxes: A 20-year case study in Beijing-Tianjin-Hebei region in China. *Environmental Pollution, 249*, pp. 923–931.

Chirla, M., Vienken, T., Dietrich, P., & Bumberger, J. (2016). Development of a direct push based in-situ thermal conductivity measurement system. *Geophysical Research Abstracts, Vol. 18, EGU2016-7347*.

Choo, H., Song, J., Lee, W., & Lee, C. (2016). Effects of clay fraction and pore water conductivity on electrical conductivity of sand-kaolinite mixed soils. *Journal of Petroleum Science and Engineering*(147), 735-745.

Clauser, C. (2011). Thermal Storage and Transport Properties of Rocks, I: Heat Capacity and Latent Heat. In H. Gupta (Ed.), *Encyclopedia of Solid Earth Geophysics. Encyclopedia of Earth Sciences Series* (pp. 1423-1431). Dordrecht: Springer.

Cohen, K., Gibbard, P., & Weerts, H. (2014). North Sea palaeogeographical reconstructions for the last 1 Ma. *Netherlands Journal of Geosciences*, pp. 7-29.

Colombani, N., Giambastiani, B., & Mastrocicco, M. (2016). Use of shallow groundwater temperature profiles to infer climate and land use change: interpretation and measurement challenges. *Hydrological Processes. Vol. 30, Issue14*, pp. 2512-2524.

Commissie Bescherming Waterwingebieden. (1980). *Richtlijnen en aanbevelingen voor de bescherming van waterwingebieden [in Dutch: 'Guidelines for the protection of drinking water sources and recommendations'].* Rijswijk, the Netherlands: Waterwingebieden, Commissie Bescherming, VEWIN-RID.

Corti, H., & Fernandez-Prini, R. (1982). Thermodynamics of solution of gypsum and anhydrite in water over a wide temperature range . *Canadian Journal of Chemistry, 62*, pp. 484-488.

Crundwell, F. (2017). On the Mechanism of the Dissolution of Quartz and Silica in Aqueous Solutions. *ACS Omega*, pp. 1116-1127.

Dao, P., Heuzard, A., Le, T., Zhao, J., Yin, R., Chang, C., & Fan, C. (2024). The impacts of climate change on groundwater quality: A review. *Science of the Total Environment, 912*.

De Mulder, E., Geluk, M., Ritsema, I., Westerhoff, W., & Wong, T. (2003). *De Ondergrond van Nederland.* Groningen/Houten: Wolters-Noordhof bv.

De Vries, H., Haarsma, R., & Hazeleger, W. (2013). On the future reduction of snowfall in western and central Europe. *Climate Dynamics*, pp. 2319-2330.

Dědeček, P., Šafanda, J., & Rajver, D. (2012). Detection and quantification of local anthropogenic and regional climatic transient signals in temperature logs from Czechia and Slovenia. *Climate Change 113*, pp. 787–801.

Deer, D., Howie, R., & Zussman, J. (1966). *An Introduction to the Rock Forming Minerals.* Essex: Longman Scientific & Technical.

Deltares. (2021). *Warmteoverdracht agrarische percelen. Warmteleiding Vlaardingen – Den Haag.* Delft: Deltares.

Des Tombe, B., Bakker, M., Schaars, F., & van der Made, K.-J. (2018). Estimating Travel Time in Bank Filtration Systems from a Numerical Model Based on DTS Measurements. *Groundwater, Vol. 56, No. 2*, pp. 288-299.

Des Tombe, B., Bakker, M., Smits, F., Schaars, F., & van der Made, K.-J. (2019). Estimation of the Variation in Specific Discharge Over Large Depth Using Distributed Temperature Sensing (DTS) Measurements of the Heat Pulse Response. *Water Resources Research, 55*.

Dolman, A., Moors, E., Elbers, J., & Snijders, W. (1996). De waterbalans van grove den op de Veluwe 1995 [in Dutch: 'The water balance of black pine in the Veluwe']. *H2O*, pp. 467-468.

Doornenbal, H., Stevenson, A., & (editors). (2010). *Petroleum Geological Atlas of the Southern Permian Basin Area.* Houten: EAGE Publications b.v.

Droogers, P. (2009). *Verbetering bepaling actuele verdamping voor het strategisch waterbeheer [in Dutch: 'Improving better calculation actual evaporation for strategic water management'].* Utrecht: STOWA.

Dufour, F. (1998). *Grondwater [in Dutch: Groundwater].* Delft: NITG-TNO.

Duynkerke, P. (1991). The roughness length for heat and other vegetation parameters for a surface of short grass. *Journal of Applied Meteorology, Vol. 31*, pp. 579-586.

Dwyer, T., & Eckstein, Y. (1987). Finite-element simulation of low-temperature, heat-pump-coupled, Aquifer thermal energy storage. *Journal of Hydrology, 85*, pp. 19-38.

Earman, S., & Dettinger, M. (2011). Potential impacts of climate change on groundwater resources – a global review. *Journal of Water and Climate Change*, pp. 213-229.

Elbers, J., Moors, E., & Jacobs, C. (2009). *Gemeten actuele verdamping voor twaalf locaties in Nederland [in Dutch: 'Measured actual evaporation at twelve locations in the Netherlands'].* Wageningen: Alterra.

Epting, J., & Huggenberger, P. (2013). Unraveling the heat island effect observed in urban groundwater bodies. *Journal of Hydrology, 501*, pp. 193–204.

Epting, J., Baralis, M., Künze, R., Mueller, M., Insana, A., Barla, M., & Huggenberger, P. (2020). Geothermal potential of tunnel infrastructures – development of tools at the city-scale of Basel, Switzerland. *Geothermics, 83*.

Epting, J., García-Gil, A., Huggenberger, P., Vázquez-Suñe, E., & Mueller, M. (2017). 2017Development of concepts for the management of thermal resources in urban areas – Assessment of transferability from the Basel (Switzerland) and Zaragoza (Spain) case studies. *Journal of Hydrology*, pp. 697–715.

Epting, J., Müller, M., Genske, D., & Huggenberger, P. (2018). Relating groundwater heat-potential to city-scale heat-demand: a theoretical consideration for urban groundwater resource management. *Applied Energy, 228*, pp. 1499–1505.

Erkan, K., & Balkan-Pazvantoğlu, E. (2023). Distribution of surface heat flow and effects on the subsurface temperatures in the northern part of Thrace Basin, NW Turkey. *Geothermal Energy 11, 13*.

European Environment Agency. (2022). *Europe's groundwater - a key resources under pressure.* EEA.

Fahmi, M. (1961). The influence of clay particles on the hydraulic conductivity of sandy soils (PhD Thesis). Wageningen.

Fan, J., Zhang, Y., Hu, J., & Rosenfeld, D. (2020). Urbanization-induced land and aerosol impacts on sea-breeze circulation and convective precipitation. *Atmospheric Chemistry and Physics*, pp. 14163–14182.

Farouki, O. (1981). *Thermal properties of soils - CRREL Monograph 81-1.* Hannover, New Hampshire, Unites States: U.S.Army Corps of Engineers, Cold Regions Research and Engineering Laboratory.

Feldhake, C., & Boyer, D. (1986). Effect of soil temperature on evapotranspiration by C3 and C4 grasses. *Agricultural and Forestry Meteorology 37*, pp. 309-318.

Ferguson, G., & Woodbury, A. (2004). Subsurface heat flow in an urban environment. *Journal of Geophysical research*.

Ferguson, G., & Woodbury, A. (2007). Urban heat island in the subsurface. *Geophysical Research Letters, Vol 34*.

Ferguson, G., Beltrami, H., & Woodbury, A. (2006). Perturbation of Ground Surface Temperature Reconstructions by Groundwater Flow? *Geophysical Research Letters 33(13)*.

Fleuchaus, P., Godschalk, B., Stober, I., & Blum, P. (2018). Worldwide application of aquifer thermal energy storage – A review. *Renewable and Sustainable Energy Reviews, V94*, 861-876.

Focaccia, S. (2012). Characterization of geothermal reservoirs' parameters by inverse problem resolution and geostatistical simulations. PhD thesis Geoengineering, Georesources and Geotechnical Engineering. Bologna, Italy: University of Bologna.

Fuchs, S., & Förster, A. (2013). Well log based prediction of the conductivity of sedimentary successions: a case study from the North German Basin. *Geophysical Journal International 196*, pp. 291-311.

Fuchs, S., Neumann, F., Norden, B., Beardsmore, G., Chiozzi, P., Colgan, W., . . . Fuentes, K. (2023). *The Global Heat Flow Database: Update 2023. V. 1.* Potsdam: GFZ Data Services.

Fujii, H., Okubo, H., & Chono, M. (2009b). Application of optical fiber thermometers in thermal response tests for detailed geological descriptions. In *Proceedings of Effstock 2009 Conference on Thermal Energy Storage for Efficiency and Sustainability.* Stockholm.

Fujii, H., Okubo, H., Nishi, K., Itoi, R., Ohyama, K., & Shibata, K. (2009a). An improved thermal response test for U-tube ground heat exchanger based on optical fiber thermometers. *Geothermics, 38*(4), 399-406.

Fukuoka, Y. (1969). Relation of precipitation to soil temperature (1st Report). Cooling effect of ground surface by rain water. *Geographical Review of Japan, 42*, pp. 735-746.

García-Gil, A., Vázquez-Suñe, E., Garrido Schneider, E., Sánchez-Navarro, J., & Mateo-Lázaro, J. (2014). The thermal consequences of river-level variations in an urban groundwater body highly affected by groundwater heat pumps. *Science of the Total Environment*, pp. 575–587.

García-Gil, A., Vázquez-Suñé, E., Sánchez-Navarro, J., & Lázaro, J. (2015). Recovery of energetically overexploited urban aquifers using surface water. *Journal of Hydrology, 531*, pp. 602–611.

Gasior, I., & Prezelaskowska, A. (2014). Estimating Thermal Conductivity from Core and Well Log Data. *Acta Geophysica vol. 62, no. 4*, pp. 785-801.

Geudens, P. (2010). *Dutch Drinking Water Statistics 2008.* Rijswijk, the Netherlands: Association of Dutch Drinking Water Companies (VEWIN).

Gies, C., Struijk, M., Békési, E., Veldkamp, H., & Van Wees, J. (2021). An effective method for paleo-temperature correction of 3D thermal models: A demonstration based on high resolution datasets in the Netherlands. *Global and Planetary Change, Vol. 199*.

Gillen, K., Douglass, D., & Hoch, M. (1972). Self-Diffusion in Liquid Water to -31°C. *The Journal of Chemical Physics*, pp. 5117–5119.

Glover, P. (2008). Petrophysique. Petrophysics MSc Course Notes. GLG-66565. Département de Géologie et de Génie Géologioque, Université Laval, Canada.

Glover, P. (2010). A generalized Archie's law for n phases. *Geophysics*(Vol.75, No.6), 247-265.

Gluyas, J., Adams, C., & Wilson, I. (2020). The theoretical potential for large-scale underground thermal energy storage (UTES) within the UK. *Energy Reports*(6), 229-237.

Gnatowski, T. (2016). Thermal properties of degraded lowland peat-moorsh soils. *Geophysical Research Abstracts Vol. 18, EGU2016-8105*.

Göbel, L., Coners, H., Hertel, D., Willinghöfer, S., & Leuschner, C. (2019). The Role of Low Soil Temperature for Photosynthesis and Stomatal Conductance of Three Graminoids From Different Elevations. *Frontiers in Plant Science 10:330*.

Gossler, M., Bayer, P., & Zosseder, K. (2019). Experimental investigation of thermal retardation and local thermal non-equilibrium effects on heat transport in highly permeable, porous aquifers. *Journal of Hydrology*(578).

Greinaert, W., & Sprong, D. (1983). Verzilting van de twee waterwingebieden te Noordbergum (Friesland). *H2O*, pp. 244-261.

Griffioen, J., Klaver, G., & Westerhoff, W. (2016). The mineralogy of suspended matter, fresh and Cenozoic sediments in the fluvio-deltaic Rhine–Meuse–Scheldt–Ems area, the Netherlands: An overview and review. *Netherlands Journal of Geosciences*, pp. 23–107.

Haesen, S., Lembrechts, J., De Frenne, P., Lenoir, J., Aalto, J., Ashcroft, M., . . . Van Meerbeek, K. (2021). ForestTemp – Sub-canopy microclimate temperatures of European forests. *Global Change Biology, 27*, pp. 6307–6319.

Hähnlein, S., Bayer, P., Ferguson, G., & Blum, P. (2013). Sustainability and policy for the thermal use of shallow geothermal energy. *Energ. Policy, 2013*(59), 914–925.

Harbaugh, A., Banta, E., Hill, M., & McDonald, M. (2000). *MODFLOW-2000, the U.S. Geological Survey modular ground-water model: user guide to modularization concepts and the ground-water flow process. US Geological Survey Open-File Rep 00-92.*

Harris, R., & Chapman, D. (1998). Geothermics and climate change. 1. Analysis of borehole temperatures with emphasis on resolving power. *Journal of Geophysical Research, Vol 103*, pp. 7363-7370.

Hartman, A., Rath, V., & Clauser, C. (2005). Thermal Conductivity from Core and Well log Data. *International Journal of Rock Mechanics and Mining Sciences*.

Hartog, N., Drijver, B., Dinkla, I., & Bonte, M. (2013). Field assessment of the impacts of Aquifer Thermal Energy Storage (ATES) systems on chemical and microbial groundwater composition. *EGC 2013.*

Hazeu, G. (2014). Operational land cover and land use mapping in the Netherlands. In I. Manakos, & M. Braun (Red.), *Land Use and Land Cover Mapping in Europe. Practices & Trends. Series: Remote Sensing and Digital Image Processing, Vol. 18, 300* (pp. 283-296). Dordrecht: Springer.

Hecht-Méndez, J., Molina-Giraldo, N., Blum, P., & Bayer, P. (2010). Evaluating MT3DMS for Heat Transport Simulation of Closed Geothermal Systems. *Ground Water 48(5)*, pp. 741–756.

Hemmerle, H., Ferguson, G., Blum, P., & Bayer, P. (2022). The evolution of the geothermal potential of a subsurface urban heat island. *Environmental Research Letters 17*.

Herb, W., Janke, B., Mohseni, O., & Stefan, H. (2006). *All-Weather Ground Surface Temperature Simulation. Project Report No. 478.* Minneapolis, MN: University of Minnesota, St. Antony Falls Laboratory.

Herb, W., Janke, B., Mohseni, O., & Stefan, H. (2018). Ground surface temperature simulation for different land covers. *Journal of Hydrology, 356*, pp. 327-343.

Hermans, T., Nguyen, F., Tanguy, R., & Revil, A. (2014). Geophysical Methods for Monitoring Temperature Changes in Shallow Low Enthalpy Geothermal Systems. *Energies 2014(7)*, pp. 5083–5118.

Hermans, T., Vandenbohede, A., Lebbe, L., & Nguyen, F. (2012). A shallow geothermal experiment in a sandy aquifer monitored using electric resistivity tomography. *Geophysics 77(1)*, pp. 11–21.

Hermans, T., Wildemeersch, S., Jamin, P., Orban, P., Brouyère, S., Dassargues, A., & Nguyen, F. (2015). Quantitative temperature monitoring of a heat tracing experiment using cross-borehole ERT. *Geothermics*, pp. 14-26.

Hijma, M. (2017). *Geology of the Dutch coast. The effect of lithological variation on coastal morphodynamics.* Deltares.

Hillel, D. (1982). *Introduction to soil physics.* San Diego, CA: Academic Press.

Hirsch, R., Slack, J., & Smith, R. (1982). Techniques of trend analysis for monthly water quality data. *Water Resources Research*, pp. 18(1): 107-121.

Hoekstra, N., Pellegrini, M., Bloemendal, M., Spaak, G., Andreu Gallego, A., Rodriguez Comins, J., . . . Saccani, C. (2020). Increasing market opportunities for renewable energy technologies with innovations in aquifer thermal energy storage. *Science of the Total Environment*(709).

Högström, U. (1985). Von Kármán's Constant in Atmospheric Boundary Layer Flow: Reevaluated. *Journal of Atmospheric Sciences 42(3)*.

Holtslag, A., & Van Ulden, A. (1980). *Estimates of incoming shortwave radiation and net radiation from standard meteorological data. Scientific Report W.R. 80-6.* De Bilt, the Netherlands: Koninklijk Nederlands Meteorologisch Instituut.

Hooghart, J., & Lablans, W. (1988). *Van Penman naar Makkink: een nieuwe berekeningswijze voor de klimatologische verdampingsgetallen. Technische Rapporten TR-111.* De Bilt: KNMI.

Hu, J. J. (2021). Thermal Conductivity Estimation Based on Well Logging. *Mathematics 9*.

Huang, S., Taniguchi, M., Yamanoc, M., & Wang, C. (2009). Detecting urbanization effects on surface and subsurface thermal environment - A case study of Osaka. *Science of the Total Environment, 407(9)*, pp. 3142–3152.

Huber, M., Perkins, R., Laesecke, A., Friend, D., Sengers, J., Assael, M., . . . Miyagawa, K. (2009). New International Formulation for the Viscosity of H2O. Special Collection: International Water Property Standards. *Journal of Physical and Chemical Reference Data 38*, pp. 101-125.

IF Technology BV. (2007). *Koude/warmteopslag in de praktijk, Meetgegevens van 67 projecten [in Dutch: 'Cold/heat storage in practice, Monitoring data from 67 projects'].* Arnhem, the Netherlands: IF Technology.

IHW. (2019). *Water quality data – chemistry*. Retrieved from https://www.waterkwaliteitsportaal.nl/Beheer/Data/Bulkdata

Ingersoll, L. (1932). Geothermal Gradient Determinations in the Lake Superior Copper Mines. *Physics, Vol. 2, Issue 3*, pp. 154-159.

Irvine, T., & Duignan, M. (1985). Isobaric thermal expansion coefficients for water over large temperature and pressure ranges. *International Communications in Heat and Mass Transfer. Vol. 12, Issue 4*, pp. 465-478.

Jakubczyk, D., Zientara, M., Kolwas, K., & Kolwas, M. (2007). Temperature Dependence of Evaporation Coefficient for Water Measured in Droplets in Nitrogen under Atmospheric Pressure. *Journal of the Atmospheric Sciences. Volume 64: Issue 3*, pp. 996–1004.

Jayalakshmy, M., & Philip, J. (2010). Thermophysical Properties of Plant Leaves and Their Influence on the Environment Temperature. *International Journal of Thermophysics*, pp. 2295-2304.

Jennings, S., Hasterok, D., & Lucazeau, F. (2021). ThermoGlobe: Extending the global heat flow database. *Journal TBD*.

Jesußek, A., Grandel, S., & Dahmke, A. (2013). Impacts of subsurface heat storage on aquifer hydrogeochemistry. *Environmental Earth Science*, pp. 1999–2012.

Johansen, O. (1975). *Varmeledningsevne Av Jordarter [Translated by Rosetta Stone, Nashua, N.H. for U.S. Army Cold Regions Research and Engineering Laboratory, 1977].* Trondheim: Group for Thermal Analysis of Frost in the Ground.

John, D., & Rose, J. (2005). Review of Factors Affecting Microbial Survival in Groundwater. *Environmental Science & Technology, Vol 39, No 19*, pp. 7345-7356.

Johnson, V. (2013). Revised standards for statistical evidence. *PNAS Vol. 110, No. 48*, pp. 19313-19317.

Jones, F., & Harris, G. (1992). ITS-90 Density of Water Formulation for Volumetric Standards Calibration. *Journal of Research of the National Institute of Standards and Technology. Volume 97, Number 3*, pp. 335-340.

Joseph, T., Whitehead, D., & Turnbull, M. (2014). Soil water availability influences the temperature response of photosynthesis and respiration in a grass and a woody shrub. *Functional Plant Biology, 41*, pp. 468–481.

Jyväsjärvi, J., Marttila, H., Rossi, P., Ala-Aho, P., Olofsson, B., Nisell, J., . . . Muotka, T. (2015). Climate-induced warming imposes a threat to north European spring ecosystems. *Global Change Biology, 21*, pp. 4561-4569.

Kaandorp, V., Doornenbal, P., Kooi, H., Broers, H., & de Louw, P. (2019). Temperature buffering by groundwater in ecologically valuable lowland streams under current and future climate conditions. *Journal of Hydrology X 3*.

Kannberg, L. (1982). *Underground Energy Storage Program: 1981 annual report. Volume II. Technical summaries.* Richmond, WA: Pacific Northwest Lab.

Kell, G. (1975). Density, thermal expansivity, and compressibility of liquid water from 0°C to 150°C: Correlations and tables for atmospheric pressure and saturation reviewed and expressed on 1968 temperature scale. *Journal of Chemical and Engineering Data. Vol. 20, No. 1*, pp. 97-105.

Kellerer-Pirklbauer, A., & Eulenstein, J. (2024). Long-term ground temperature monitoring, repeated ERT measurements, and historical sources reveal increasing permafrost degradation at a high-mountain pass in Austria (Hochtor, Hohe Tauern Range). *EGU General Assembly 2023, Vienna, Austria, 24–28 Apr 2023.* Vienna: EGU.

Kendall, M. (1975). *Rank correlation methods.* New York: Oxford University Press.

Kersten, M. (1949). *Thermal properties of soils. Bulletin No.28.* Minneapolis : University of Minnesota: Engineering Experiment Station.

Klein Goldewijk, C. (2016). *A historical land use data set for the Holocene; HYDE 3.2 (replaced)*. Retrieved November 11, 2023, from https://doi.org/10.17026/dans-znk-cfy3

Klok, E., Schaminée, S., Duyzer, J., & Steeneveld, G. (2012). *De stedelijke hitte-eilanden van Nederland in kaart gebracht met satellietbeelden. TNO-060-UT-2012-01117. (In Dutch: The urban heat islands of the Netherlands mapped with satellite images).* Utrecht: TNO.

KNMI. (2000). *Handbook for the Meteorological Observation.* De Bilt: Koninklijk Nederlands Meteorologisch Instituut (KNMI).

KNMI. (2012). *Klimaatdesk (Climate data desk)*. Retrieved from http://www.knmi.nl/klimatologie/uurgegevens/

KNMI. (2014). *Klimatologie, Antieke Reeksen [in Dutch: Climatology, Antique Time Series].* Retrieved June 28, 2014, from http://projects.knmi.nl/klimatologie/daggegevens/

KNMI. (2014b). *SCIAMACHY (Scanning Imaging Absorption Spectrometer for Atmospheric Chartography)*. Retrieved from http://www.sciamachy-validation.org/klimatologie/stadswaterkantoor/index.cgi

KNMI. (2023). *KNMI - Klimaatviewer*. Retrieved November 23, 2023, from https://www.knmi.nl/klimaat-viewer/kaarten

KNMI. (2023a). *KNMI Dataplatform*. Retrieved November 11, 2023, from https://www.knmi.nl/nederland-nu/klimatologie-metingen-en-waarnemingen

KNMI. (2023b). *KNMI national climate scenarios 2023 for the Netherlands - WR 23-02.* De Bilt: KNMI.

Kooi, H. (2008). Spatial variability in subsurface warming over the last three decades; insight from repeated borehole temperature measurements in The Netherlands. *Earth and Planetary Science Letters 270*, pp. 86-94.

Kooi, H. (2016). Groundwater flow as a cooling agent of the continental lithosphere. *Nature Geoscience*, pp. 227-231.

Koubikana Pambou, C., Raymond, J., & Lamarche, L. (2019). Improving thermal response tests with wireline temperature logs to evaluate ground thermal conductivity profiles and groundwater fluxes. *Heat Mass Transfer, 55*, pp. 1829–1843.

Kroener, E., Vallati, A., & Bittelli, M. (2014). Numerical simulation of coupled heat, liquid water and water vapor in soils for heat dissipation of underground electrical power cables. *Applied Thermal Engineering*, pp. 510-523.

Kuijer, L., & Watson, M. (2017). ‘That’s when we started using the living room’: Lessons from a local history of domestic heating in the United Kingdom. *Energy Research & Social Science*, pp. 77-85.

Kurylyk, B., Irvine, D., & Bense, V. (2019). Theory, tools, and multidisciplinary applications for tracing groundwater fluxes from temperature profiles. *WIREs Water*.

Kurylyk, B., Irvine, D., Carey, S., Briggs, M., Werkema, D., & Bonham, M. (2017). Heat as a groundwater tracer in shallow and deep heterogeneous media: Analytical solution, spreadsheet tool, and field applications. *Hydrological Processes, 31(14)*, pp. 2648–2661.

Kutasov, I., & Eppelbaum, L. (2005). Determination of formation temperature from bottom-hole temperature logs - a generalized Horner method. *Journal of Geophysics and Engineering*, pp. 90-96.

Laban, C., & Van der Meer, J. (2011). Chapter 20 - Pleistocene Glaciation in The Netherlands. *Developments in Quaternary Sciences. Vol. 15*, pp. 247-260.

Labrijn, A. (1945). *The climate of the Netherlands during the last two and a half centuries. Mededeelingen en Verhandelingen No. 49.* De Bilt: Koninklijk Nederlandsch Meteorologisch Instituut.

Labrijn, A. (1948). *The climate of the Netherlands - Temperature/Precipitation and Wind. Mededelingen en Verhandelingen Serie A 53.* 's Gravenhage: Staatsdrukkerij en Uitgeverijbedrijf.

Langevin, C., Thorne, D., Dausman, A., Sukop, M., & Guo, W. (2008). *SEAWAT Version 4: A Computer Program for Simulation of Multi-Species Solute and Heat Transport. UD Geological Survey Survey Techniques and Methods, book 6, chap A22.* Reston, VA: US Geological Survey.

Larionov, V. (1969). *Borehole radiometry.* Moscow: Nedra.

Lee, K. (2013). Aquifer Thermal Energy Storage. In *Underground thermal energy storage* (pp. 59–93). London, UK: Springer.

Lee, M. (2011). *Connection equation and shaly-sand correlation for electrical resistivity: U.S. Geological Survey Scientific Investigation Report 2011-5005.* U.S. Geological Survey.

Lembrechts, J., Van den Hoogen, J., Aalto, J., Ashcroft, M., De Frenne, P., Kemppinen, J., & plus 90 others. (2021). Global maps of soil temperature. *Global Change Biology, 28*, pp. 3110-3144.

Lesperance, M., Smerdon, J., & Beltrami, H. (2010). Propagation of linear surface air temperature trends into the terrestrial subsurface. *Journal of Geophysical Research, 115*.

Lo Russo, S., Gnavi, L., Roccia, E., Taddia, G., & Verda, V. (2014). Groundwater Heat Pump (GWHP) system modeling and Thermal Affected Zone (TAZ) prediction reliability: Influence of temporal variations in flow discharge and injection temperature. *Geothermics 51*, pp. 103–112.

Loague, K., & Green, R. (1991). Statistical and graphical methods for evaluating solute transport models: overview and application. *Journal of Contaminant Hydrology, 7*, pp. 51–73.

Londoño-Londoño, J., Condesso de Melo, M., & Nascimento, J. (2023). Thermal-Based Remote Sensing Solution for Identifying Coastal Zones with Potential Groundwater Discharge. *Journal of Marine Science and Engineering*.

Longsworth, L. (1954). Temperature Dependence of Diffusion in Aqueous Solutions. *The Journal of Physical Chemistry. Vol. 58, No. 9* , pp. 770–773.

Lu, S., Ren, T., Gong, Y., & Horton, R. (2007). An Improved Model for Predicting Soil Thermal Conductivity from Water Content at Room Temperature. *Soil Physics*(Volume 71: Number 1), 8-14.

Luijendijk, E., ter Voorde, M., van Balen, R., Verweij, H., & Simmelink, E. (2010). Thermal state of the Roer Valley Graben, part of the European Cenozoic Rift System. *Basin Research 23 (1)*, pp. 65-82.

Machel, H. (1999). Effects of groundwater flow on mineral diagenesis, with emphasis on carbonate aquifers. *Hydrogeology Journal, 7*, pp. 94–107.

Madigan, M., Martinko, J., Stahl, D., & Clark, D. (2012). *Brock Biology of Microorganisms, 13th edn.* San Fransico: Pearson.

Makowski, M., & Mochlinski, K. (1956). An evaluation of two rapid methods of assessing the thermal resistivity of soils. *Proc. of Inst. of Electrical Engineers, 103*(Part A), 53-70.

Mallamace, F., Corsaro, C., Mallamace, D., Fazio, E., Chen, S.-H., & Cupane, A. (2020). Specific Heat and Transport Functions of Water. *International Journal of Molecular Sciences*.

Manger, G. (1963). *Porosity and Bulk Density of Sedimentary Rocks - United States Geological Survey Bulletin 1144-E.* Washington: United States Government Printing Office.

Mann, H. (1945). Nonparametric Tests Against Trend. *Econometrica. Vol.13. No.3*, pp. 245-259.

Mann, M., & Schmidt, G. (2003). Ground vs. surface air temperature trends: implications for borehole surface temperature reconstructions. *Geophys Research Letters 30(12)*, p. 1607.

Marif, K. (2019). *Counteraction of buoyancy flow in high temperature aquifer thermal energy storage systems by applying multiple partially penetrating wells. MSc thesis.* Delft: TU Delft.

Massop, H., Van Bakel, P., Kroon, T., Kroes, J., Tiktak, A., & Wekman, W. (2005). *Op zoek naar de ‘ware’ neerslag en verdamping. Toetsing van de met het STONE 2.1-instrumentarium berekende verdamping aan literatuurgegevens en aan regionale waterbalansen, en de gevoeligheid van het neerslagoverschot op de uitspoeling van nutriënten.* Wageningen: Alterra.

Matiz-León, J. (2023). Spatial Prediction for Bottom Hole Temperature and Geothermal Gradient in Colombia. *Proceedings, 48th Workshop on Geothermal Reservoir Engineering.* Stanford: Stanford University.

Meals, D., Spooner, J., Dressing, S., & Harcum, J. (2011). *Statistical analysis for monotonic trends, Tech Notes 6.* U.S. Environmental Protection Agency.

Mehrer, H. (2007). Dependence of Diffusion on Temperature and Pressure. In H. Mehrer, *Diffusion in Solids. Springer Series in Solid-State Sciences, vol 155.* Berlin, Heidelberg: Springer.

Menberg, K., Bayer, P., & Blum, P. (2013b). Elevated temperatures beneath cities: An enhanced geothermal resource. *Proceedings of the European Geothermal Congress 2013.* Pisa, Italy 3–7 June 2013.

Menberg, K., Bayer, P., Zosseder, K., Rumohr, S., & Blum, P. (2013c). Subsurface urban heat islands in German cities. *Science of the Total Environment, 442*, pp. 123–133.

Menberg, K., Blum, P., Rivera, J., Benz, S., & Bayer, P. (2015). Exploring the Geothermal Potential of Waste Heat beneath Cities. *Proceedings World Geothermal Congress 2015.* Melbourne, Australia, 19–25 April 2015.

Menberg, K., Blum, P., Schaffitel, A., & Bayer, P. (2013a). Long-term evolution of anthropogenic heat fluxes into a subsurface urban heat island. *Environmental Science and Technology, 47*, pp. 9747–9755.

Mendizabal, I., & Stuyfzand, P. (2009). Guidelines for interpreting hydrochemical patterns in data from public supply well fields and their value for natural background groundwater quality determination. *Journal of Hydrology, 379(1-2)*, pp. 151-163.

Mendizabal, I., Stuyfzand, P., & Wiersma, A. (2011). Hydrochemical system analysis of public supply well fields, to reveal water-quality patterns and define groundwater bodies: The Netherlands. *Hydrogeology Journal*, pp. 83-100.

Miller, J., Peterson, E., & Budikova, D. (2019). Diurnal and seasonal variation in nitrate-nitrogen concentrations of groundwater in a saturated buffer zone. *Hydrogeology Journal*, pp. 1373–1387.

Molson, J., Frind, E., & Palmer, C. (1992). Thermal energy storage in an unconfined aquifer: 2. Model development, validation, and application. *Water Resources Research, 28(10)*, pp. 2857–2867.

Montijn, I. (2000). *Leven op stand 1890-1940. [in Dutch: 'Living well 1890-1940'] .* Amsterdam: Thomas Rap.

Morita, R., & Moyer, C. (2001). Psychrophiles. In S. Levin, *Encyclopedia of Biodiversity (Second Edition)* (pp. 298-303). Academic Press.

Mueller, M., Huggenberger, P., & Epting, J. (2018). Combining monitoring and modelling and modelling tools as a basis for city-scale concepts for a sustainable thermal management of urban groundwater resources. *Science of the Total Environment, 627*, pp. 1121–1136.

Nikiforova, T., Savytskyi, M., Limam, K., Bosschaerts, W., & Belarbi, R. (2013). Methods and results of experimental researches of thermal conductivity of soils. *Energy Procedia 42*, pp. 775-783.

NLOG, Nederlands Olie- en Gasportal. (2023). *SCAN Dinantien 2D Seismische Interpretatie en Diepte Conversie*. Retrieved December 22, 2023, from https://www.nlog.nl/scan-dinantien-2d-seismische-interpretatie-en-diepte-conversie

Normcommissie 390 09 "Bodemkwaliteit". (1991). *Soil - Sampling of groundwater for the determination of metals, inorganic compounds, moderate volatile organic compounds and physico-chemical properties.* Utrecht: Nederlands Normalisatie-instituut.

Ocłon, P., Pobedza, J., Walczak , P., Cisek, P., & Vallati, A. (2020). Experimental Validation of a Heat Transfer Model in Underground Power Cable Systems. *Energies*.

Oerter, E., & Amundson, R. (2016). Climate controls on spatial and temporal variations in the formation of pedogenic carbonate in the western Great Basin of North America. *Geological Society of America Bulletin 128(7-8)*, pp. 1095–1104.

Olive, M., Gan, C., Carratalà, A., & Kohn, T. (2020). Control of Waterborne Human Viruses by Indigenous Bacteria and Protists Is Influenced by Temperature, Virus Type, and Microbial Species. *Applied Environmental Microbiology, Vol 86, 3*.

Olsthoorn, T. (1977). In Nederlandse zandformaties zijn het doorstroomde en het totale porievolume aan elkaar gelijk (in Dutch). *H2O*(Nr.5), 118-122.

Olsthoorn, T. (1982). *The clogging of recharge wells, main subjects.* Rijswijk: KIWA.

Palmer, C., Blowes, D., Frind, E., & Molson, J. (1992). Thermal energy storage in an unconfined aquifer: 1. Field Injection Experiment. *Water Resources Research, 28(10)*, pp. 2845–2856.

Palmer, J., & Cooper, I. (2012). *United Kingdom housing energy fact file.* London: Department of Energy and Climate Change.

Papadopulos, S., & Larson, S. (1978). Aquifer storage of heated water (Part II): Numerical simulation of field results. *Gorund Water, 16(6)*, pp. 242–248.

Pinon, A., & Vialette, M. (2018). Survival of Viruses in Water. *Intervirology*, pp. 214–222.

Pollack, H., & Huang, S. (2000). Climate reconstruction from subsurface temperatures. *Annual Review of Earth and Planetary Sciences*, pp. 339-365.

Pollack, H., & Smerdon, J. (2004). Borehole climate reconstructions: Spatial structure and hemispheric averages. *Journal of Geophysical Research, Vol. 109*.

Prommer, H., & Stuyfzand, P. (2005). Identification of temperature-dependent water quality changes during a deep well injection experiment in a pyritic aquifer. *Enviromental Science & Technology, Vol.39, No. 7*, pp. 2200-2209.

Province of Utrecht. (2009). *Grondwaterwet; wijzigingsvergunning grondwateronttrekking KWO RIVM Bilthoven [in Dutch: 'Groundwater law: change of groundwater abstraction permit ATES system RIVM, Bilthoven'].* Utrecht, the Netherlands: Province of Utrecht.

Qi, Y., & Wu, Y. (2022). Electrical Conductivity of Clayey Rocks and Soils: A Non-Linear Model. *Geophysical Research* (49).

Quan, L., Fu, C., Si, W., Yang, J., & Wang, Q. (2019). Numerical study of heat transfer in underground power cable system. *Energy Procedia 158*, pp. 5317-5322.

Quist, W., & Tolboom, H. (2017). *Natuursteen in Limburg, Natuursteen uit Limburg [in Dutch: 'Natural stone in Limburg, Natural stone from Limburg'].* Delft: Delftdigitalpress .

Randhawa, D., Flanders, C., & Visser, P. (2016). Thermal In Situ Sustainable Remediation (TISR): Linking Renewable Energy to Sustainable Site Restoration. *H.V. Rectanus and P. Rodgers (Chairs). Remediation of Chlorinated and Recalcitrant Compounds—2016. Tenth International Conference on Remediation of Chlorinated and Recalcitrant Compounds.* Palm Springs, CA.

Rawat, P., Agarwal, S., Malhotra, A., Gulhati, S., & Rao, G. (1982). Determination of thermal conductivity of soils: a need for computing heat loss through buried submarine pipelines. *SPE Journal, Vol.22*(No.4), 558-562.

Revil, A., Cathles III, L., & Losh, S. (1998). Electrical conductivity in shaly sands with geophysical applications. *Journal of Geophysical Research*(Vol.103, No.B10), 23925-23936.

Riedel, T. (2019). Temperature-associated changes in groundwater quality. *Journal of Hydrology 572*, pp. 206-212.

Rijksgebouwendienst. (2012). *Buildings Catalogue Central Government Real Estate Agency*. Retrieved from http://192.113.208.81/Catalogus/objectview/tabularview.html?siteId=509

Rijkswaterstaat. (2023). *Waterinfo*. Retrieved November 11, 2023, from https://waterinfo.rws.nl/#/expert/Watertemperatuur?parameters=Temperatuur___20Oppervlaktewater___20oC

Rimstidt, J. (1997). Quartz solubility at low temperatures. *Geochimica et Cosmochimica Acta, Vol 61, No 13*, pp. 2553-2558.

Robertson, E. (1988). *Thermal properties of rocks. Open-File Report 88-441.* Reston, Viginia: United States Geological Survey.

Robie, R., & Bethke, P. (1962). *Molar volumes and densities of minerals.* Reston, Virginia: United States Department of the Interior, Geological Survey.

Romero, C., & Dukes, M. (2016). Review of turfgrass evaporation and crop coefficients. *Transactions of the ASABE. Vol. 59(1)*, pp. 207-223.

Royal Haskoning. (2006). *Effectenstudie warmte/koude-opslag Cohengebouw, RIVM te Bilthoven [in Dutch].* Groningen: Haskoning Nederland B.V.

Royal Netherlands Meteorological Institute (KNMI). (2023). *Klimaatviewer*. Retrieved from https://www.knmi.nl/klimaat-viewer/kaarten/temperatuur/gemiddelde-temperatuur/jaar/Periode_1991-2020

Sammel, E. (1968). Convective flow and its effect on temperature logging in small-diameter wells. *Geophysics, Vol. 33, No. 6*, pp. 1004-1012.

Sato, H., Watanabe, K., Levelt Sengers, J., Gallagher, J., Hill, P., Straub, J., & Wagner, W. (1991). Sixteen Thousand Evaluated Experimental Thermodynamic Property Data for Water and Steam (supplementary material). *Journal of Physical and Chemical Reference Data, Vol. 20, Issue 5*, pp. 1023–1044.

Schilperoort, B., Coenders-Gerrits, M., Jiménez Rodríguez, C., van der Tol, C., van de Wiel, B., & Savenije, H. (2020). Decoupling of a Douglas fir canopy: a look into the subcanopy with continuous vertical temperature profiles. *Biogeosciences, 17*, pp. 6423–6439.

Shafigh, P., Asadi, I., Akhiani, A., Mahyuddin, N., & Hashemi, M. (2020). Thermal properties of cement mortar with different mix proportions. *Materiales de Construcción. Vol. 70, Issue 339*.

Sheldon, H., Wilkins, A., & Green, C. (2021). Recovery efficiency in high-temperature aquifer thermal energy storage systems. *Geothermics 96*.

Shen, P., & Beck, A. (1992). Paleoclimate change and heat flow density inferred from temperature data in the Superior Province of the Canadian shield. *Palaeogeography, Palaeoclimatology, Palaeoecology (Global and Planetary Change Section), 98*, pp. 143-165.

Shepherd, R. (1989). Correlations between Permeability and Grain Size. *Ground Water, 27(5)*, pp. 633–638.

Sluiter, R. (2012). *Interpolation Methods for the Climate Atlas.* De Bilt: Royal Meteorological Institute (KNMI).

Smith, K., O'Sullivan, A., Kennedy, G., Benz, S., Somers, L., & Kurylyk, B. (2023). Shallow groundwater temperature patterns revealed through a regional monitoring well network. *Hydrological Processes*.

Sommer, W. (2015). *Modelling and monitoring of Aquifer Thermal Energy Storage. Impacts of soil heterogeneity, thermal interference and bioremediation. PhD thesis.* Wageningen University: Wageningen.

Sommer, W., Doornenbal, P., Drijver, B., Gaans, P., Leusbrock, I., Grotenhuis, J., & Rijnaarts, H. (2014). Thermal performance and heat transport in aquifer thermal energy storage. *Hydrogeology Journal, 22*, pp. 263–279.

Sommer, W., Valstar, J., van Gaans, P., Grotenhuis, J., & Rijnaarts, H. (2013). The impact of aquifer heterogeneity on the performance of Aquifer Thermal Energy Storage. *Water Resources Research, 49*(12), 8128-8138.

Song, Y., Huang, A., & Chen, H. (2020). The Storage of Antecedent Precipitation and Air Temperature Signals in Soil Temperature over China. *Journal of Hydrometeorology. Vol 23: Issue 3*, pp. 377-388.

Sprenger, M., Tetzlaff, D., & Soulsby, C. (2017). Soil water stable isotopes reveal evaporation dynamics at the soil–plant–atmosphere interface of the critical zone. *Hydrology and Earth System Sciences, 21*, pp. 3839–3858.

Środoń, J., Douglas, K., & McCarthy, K. (2008). Surface area and layer charge of smectite from CEC and EGME/H2O-retention Measurements. *Clays and Clay Minerals*(Vol. 56, No. 2), 155-174.

Stallman, R. (1963). Computation of ground-water velocity from temperature data, in: Methods of Collecting and Interpreting Ground-Water Data. In *Methods of collecting and interpreting groundwater data. US Geological Survey Water Supply Paper 1544-H* (pp. 35-46).

Sterl, A. (2018). *Brief review of wind and drag transformations in WBI2017.* De Bilt: Royal Netherlands Meteorological Institute.

Stewart, J., Humes, K., Nichols, W., Moran, M., & De Brun, H. (1994). Sensible Heat Flux-Radiometric Surface Temperature Relationship for Eight Semiarid Areas. *Journal of Applied Meteorology, 33*, pp. 1110–1116.

Stichting Bouwresearch. (1985). *Een kruipruimte thermisch doorgemeten. Rapport 118. [in Dutch: 'Thermal measurements of a crawl space. Report 118'].* Rotterdam, the Netherlands: Stichting Bouwresearch.

Stichting Climate Adaptation. (2023). *Klimaateffectatlas*. Retrieved November 23, 2023, from https://www.klimaateffectatlas.nl/nl/

Stonestrom, D., & Blasch, K. (2003). Determining temperature and thermal properties for heat-based studies of surface-water groundwater interactions. In D. Stonestrom, & J. Constantz, *Heat as a Tool for Studying the Movement of Ground Water Near Streams* (pp. 73-80). Reston, Virginia: U.S. Geological Survey.

Stowa / NHI. (2023). *Model output*. Retrieved from NHI Data Portal: https://data.nhi.nu/bekijk

Struijk, M., Veldkamp, H., Gies, C., & Van Wees, J.-D. (2019). Thermal structure of the subsurface of the Netherlands – a review and outlook on temperature data and predictive models. *European Geothermal Congress 2019.* The Hague, the Netherlands, 11-14 June 2019: EGEC.

Stumm, W., & Morgan, J. (1981). *Aquatic Chemistry: An Introduction Emphasizing Chemical Equilibria in Natural Waters. 2nd Edition.* New York: John Wiley & Sons Ltd.

Stuurman, R. (1984). *Regenwaterlensvorming op kunstmatig geinfiltreetd, zijdelingsafstromend Lekwater in de Duinwaterwinplaats van de Gemeentewaterleidingen. Stagerapport.* Amsterdam: VU University.

Stuyfzand, P. (1987). Effects of vegetation and air pollution on groundwater quality in calcareous coastal dunes near Castricum, the Netherlands: Lysimetric observations. In N. N. Hydrology (Red.), *Proc. Int. Symp. on "Acidification and Water Pathways". Vol. 2* (pp. 115-125). Bolkesjø, Norway.

Stuyfzand, P. (1988). *Hydrochemie en hydrologie van duinen en aangrenzende polders tussen Noordwijk en Zandvoort aan Zee (kaartbladen 24H en 25C). KIWA-rapport SWE 87.007.* Nieuwegein: KIWA.

Stuyfzand, P., & Rambags, F. (2011). *Hydrologie en hydrochemie van de vier lysimeters te Castricum [in Dutch: 'Hydrology and hydro-chemistry of the four lysimeters at Castricum'].* Nieuwegein: KWR Watercylcle Research Institute.

Stuyfzand, P., Juhàsz-Holterman, M., & de Lange, W. (2006). Riverbank filtration in the Netherlands: well fields, clogging and geochemical reactions. *In: Hubbs, S.A. (eds) Riverbank Filtration Hydrology. Nato Science Series: IV: Earth and Environmental Sciences, vol 60* (pp. 119-153). Dordrecht: Springer.

Stuyfzand, P., Ludwig, R., & Kristensen, P. (2007). *Impact of climate change on groundwater - a background note for EEA.* Copenhagen: European Environmental Agency.

Stuyfzand, P., Rolf, H., & Lebbink, J. (2006). *Water tracers getraceerd; onderzoek naar tracers ter herkenning van infiltratiewater en naar verspreiding van infiltratiewater bij Castricum en Wijk aan Zee. Kiwa-rapport KWR 06.002.* Nieuwegein: KIWA.

Taniguchi, M., Shimada, J., Fukuda, Y., Yamano, M., Ondora, S., Buapeng, S., . . . Yamamoto, K. (2009). *Degradation of subsurface environment due to human activities and climate variability in Asia. IAHS Publ. 329.* Wallingford, UK: IAHS.

Taniguchi, M., Shimada, J., Tanaka, T., Kayane, I., Sakura, Y., Shimano, Y., . . . Kawashima, S. (1999). Disturbances of temperature-depth profiles due to surface climate change and subsurface water flow: 1. An effect of linear increase in surface temperature caused by global warming and urbanization in the Tokyo metropolitan area, Japan. *Water Resources Research, 1999*(Vol. 35, No. 5), 1507–1517.

Taniguchi, M., Uemura, T., & Jago-on, K. (2007). Combined Effects of Urbanization and Global Warming on Subsurface Temperature in Four Asian Cities. *Vadose Zone Journal. Vol. 6, No. 3*, pp. 591–596.

Tarnawski, V., Leong, W., & Bristow, K. (2000). Developing a temperature-dependent Kersten function for soil thermal conductivity. *International Journal of Energy Research*, pp. 1335-1350.

Taylor, C., & Heinz, S. (2009). Shallow groundwater temperature response to climate change and urbanization. *Journal of Hydrology, 375*, pp. 601–612.

Thorne, D., Langevin, C., & Sukop, M. (2006). Addition of simultaneous heat and solute transport and variable fluid viscosity to SEAWAT. *Computer and Geosciences, Vol.32*, pp. 1758–1768.

TNO. (2011). *Lithostratigrafische nomenclator van de ondiepe ondergrond*. Retrieved December 28, 2012, van https://www.dinoloket.nl/stratigrafische-nomenclator

TNO. (2012, January 10). *Data and Information on the Dutch Subsurface from DINOloket:*. Retrieved from https://www.dinoloket.nl/ondergrondmodellen

TNO. (2012, December 28). *Lithostratigrafische nomenclator van de ondiepe ondergrond*. Retrieved from https://www.dinoloket.nl/stratigrafische-nomenclator

TNO Geological Survey of The Netherlands. (2020, December 22). *Subsurface data*. Retrieved from Data and Information of the Dutch Subsurface: https://www.dinoloket.nl/en/subsurface-data

TNO Geologische Dienst Nederland. (2012a, January 2). *Ondergrondgegevens*. Retrieved from DINOLoket: https://www.dinoloket.nl/ondergrondgegevens

TNO Geologische Dienst Nederland. (2012b, January 10). *DINOLoket*. Retrieved from http://www2.dinoloket.nl/nl/DINOLoket.html

TNO Geologische Dienst Nederland. (2013, March 13). *DINOLoket*. Retrieved from https://www.dinoloket.nl/ondergrondmodellen

TNO Geologische Dienst Nederland. (2022). *DINOloket: data and infromation of the Netherlands subsurface*. Retrieved October 17, 2022, from https://www.dinoloket.nl/ondergrondgegevens

TNO Geologische Dienst Nederland. (2022, October 17). *Ondergrondgegevens*. Retrieved from DINOloket: data and infromation of the Netherlands subsurface: https://www.dinoloket.nl/ondergrondgegevens

TNO-NITG. (2023). *DINOloket. Data en informatie van de Nederlandse Ondergrond. Stratigrafische Nomenclator.* Retrieved December 23, 2023, from https://www.dinoloket.nl/stratigrafische-nomenclator/naar-ouderdom/pleistoceen

Todorov, O., Alanne, K., Virtanen, M., & Kosonen, R. (2020). A method and analysis of aquifer thermal energy storage (ATES) system for district heating and cooling: A case study in Finland. *Sustainable Cities and Society*(53).

Totten, M., Hanan, M., Knight, D., & Borges, J. (2002). Characteristics of mixed-layer smectite/illite density separates during burial diagenesis. *American Mineralogist*(87), 1571–1579.

Tsang, C. (1978). Aquifer Thermal Energy Storage. *Institute of Gas Technology Symposium on Advanced Technologies for Storing Energy. July 10–13, 1978.* Chicago, IL.

Tsang, C., Buscheck, T., & Doughty, C. (1981). Aquifer thermal energy storage: A numerical simulation of Auburn University field experiments. *Water Resources Research, 17(3)*, pp. 647–658.

Túri, M., Saadi, R., Marah, H., Temovski, M., Molnár, M., & Palcsu, L. (2020). Paleotemperature reconstruction using environmental isotopes and noble gases in groundwater in Morocco. *Hydrogeology Journal, 28*, pp. 973–986.

Tyler, S., Selker, J., Hausner, M., Hatch, C., Torgersen, T., Thodal, C., & Schladow, S. (2009). Environmental temperature sensing using Raman spectra DTS fiber-optic methods. *Water Resources Research, 45*.

UNESCO. (2022). *Groundwater - Making the invisible visible. The United Nations World Water Development Report 2022.* Paris: Unesco.

USACE. (2024). *HEC-HMS Technical Reference Manual*. Retrieved January 24, 2024, from https://www.hec.usace.army.mil/confluence/hmsdocs/hmstrm

Van Balen, R., Houtgast, R., & Cloethingh, G. (2005). Neotectonics of The Netherlands:a review. *Quaternary Science Reviews 24*, pp. 439-454.

Van Baren, F. (1934). *Het voorkomen en de betekenis van kalihoudende mineralen in Nederlandsche gronden. Ph.D. thesis.* Wageningen: Landbouw Hogeschool.

van Dalfsen, W. (1981). *Geothermal investigation in shallow observation wells. The shallow subsurface temperature field in the Netherlands. TNO-rapport OS 81-05.* Utrecht: TNO, Nederlands Instituut voor Toegepaste Geowetenschappen.

Van Dalfsen, W. (1983). *Het Ondiepe Ondergrondse Temperatuurveld in Nederland (volgens temperatuurmetingen tot 1984) (in Dutch: the shallow temperature field in the Netherlands, according to measurements up to 1984).* Utrecht: TNO, Nederlands Instituut voor Toegepaste Geowetenschappen.

Van de Meulen, M., Van Gessel, S., & Veldkamp, J. (2005). Aggregate resources in the Netherlands. *Netherlands Journal of Geosciences*, pp. 379 - 387.

Van den Berg, M. (2023). *Do salt diapirs promote the geothermal potential of shallow depth aquifers? MSc thesis.* Utrecht: Universiteit Utrecht.

Van den Berg, M., & Beets, D. (1986). Saalian glacial deposits and morphology in the Netherlands. *In: Proceedings of the INQUA symposium on the Genesis and Lithology of Glacial Deposits*, pp. 235-251.

Van der Hoeve, P. (2011). *Lysimeters Castricum - Meetproject en Datafiles [in Dutch: Lysimeters Castricum - Measurement project and Data files].* Wageningen: Alterra.

Van der Made, K., Caljé, R., Bakker, M., Schaars, F., De Haas, S., & Rasenberg, E. (2014). Grondverdringend in de bodem brengen van glasvezelkabels voor temperatuurmetingen . *H2O*.

Van der Veer, G. (2006). *Geochemical soil survey of the Netherlands. Atlas of major and trace elements in topsoil and parent material; assessment of natural and anthropogenic enrichment factors. PhD thesis.* Utrecht: Koninlijk Nederlands Aardrijkskundig Genootschap. Faculteit Geowetenschappen Universiteit Utrecht .

Van Engelen, A., Buisman, J., & IJnsen, F. (2001). A Millennium of Weather, Winds and Water in The Low Countries. In *History and climate: memories of the future?* Dordrecht, the Netherlands: Kluwer.

Van Lier, H. (1991). Historical land use changes: The Netherlands. In F. Brouwer, A. Thomas, & M. Chadwick (Eds.), *Land use changes in Europe : processes of change, environmental transformations and future patterns* (pp. 379-401). Dordrecht: Springer Science+Business Media.

Van Loon, A., Pronk, T., Raterman, B., Ros, S., & van Gelderen, J. (2020). Grondwaterkwaliteit uniform in beeld met landelijke dataset. *H2O*.

Vandenbohede, A., Hermans, T., Nguyen, F., & Lebbe, L. (2011). Shallow heat injection and storage experiment: Heat transport simulation and sensitivity analysis. *Journal of Hydrology, 409*, pp. 262–272.

Vandenbohede, A., Louwyck, A., & Lebbe, L. (2009). Conservative solute versus heat transport in porous media during push–pull tests. *Transport in Porous Media 76*, pp. 265–287.

Verein Deutscher Ingenieure. (2000). *Thermal use of the underground - Fundamentals, approvals, environmental aspects.* Berlin: Beuth Verlag GmbH.

Verkaik, J. (2006). On Wind and Roughness over Land (PhD thesis). Wageningen: WUR.

Vernes, R. (2013). Over watervoerende pakketten en slecht doorlatende lagen (in Dutch). *Grondboor & Hamer*(Nr. 4/5), 168-177.

VEWIN. (2022). *Drinkwaterstatistieken 2022 (in Dutch: Drinking water statitics).* The Hague: Vereniging van waterbedrijven in Nederland (Vewin).

Visser, P., Kooi, H., & Stuyfzand, P. (2015). The thermal impact of aquifer thermal energy storage (ATES) systems: a case study in the Netherlands, combining monitoring and modeling. *Hydrogeology Journal*.

Visser, P., Kooi, H., Bense, V., & Boerma, E. (2020). Impacts of progressive urban expansion on subsurface temperatures in the city of Amsterdam (The Netherlands). *Hydrogeology Journal* , pp. 1755-1772.

Vitens. (2012). *Waterkwaliteit Utrecht [Water quality data Utrecht]*. Opgehaald van http://www.vitens.nl/overvitens/water/waterkwaliteit/Paginas/Overzicht-Utrecht.aspx

Voogt, J., & Grimmond, C. (2000). Modelling Surface Sensible Heat Flux Using Surface Radiative Temperatures in a Simple Urban Area. *Journal of Applied Meteorology*, pp. 1679–1699.

Voss, C. (1984). *A Finite-element Simulation Model for Saturated–Unsaturated, Fluid-Density-Dependent Ground-water Flow with Energy Transport or Chemically-Reactive Single-species Solute Transport. US Geological Survey Water Resour Invest Rep 84-4369.* US Geological Survey.

Wallenstein, M., & Hall, E. (2012). A trait-based framework for predicting when and where microbial adaptation to climate change will affect ecosystem functioning. *Biogeochemistry, 109*, pp. 35–47.

Wang, S. (2015). *Pavement albedo assessment: methods, aspects, and implications. MSc thesis.* Iowa City, IA, USA: Iowa State University.

Waxman, M., & Smits, L. (1968). Electrical Conductivities in Oil-Bearing Shaly Sands. *Society of Petroleum Engineers Journal*(8), 107-122.

Weerts, H., Westerhoff, W., Cleveringa, P., Bierkens, M., Veldkamp, J., & Rijsdijk, K. (2005). Quaternary geological mapping of the lowlands of The Netherlands, a 21st century perspective. *Quaternary International*, pp. 159-178.

Welch, S., & Ullman, W. (2000). The temperature dependence of bytownite feldspar dissolution in neutral aqueous solutions of inorganic and organic ligands at low temperature (5–35oC). *Chemical Geology 167*, pp. 337–354.

Westerhoff, W. (2009). Stratigraphy and sedimentary evolution: The lower Rhine-Meuse system during the Late Pliocene and Early Pleistocene (southern North Sea Basin) (PhD Thesis). Rotterdam: TNO Built Environment and Geosciences.

Willeit, M., & Ganopolski, A. (2018). The importance of snow albedo for ice sheet evolution over the last glacial cycle. *Climate of the Past, 14*, pp. 697–707.

Willems, C., Vondrak, A., Mijnlieff, H., Donselaar, M., & Van Kempen, B. (2020). Geology of the Upper Jurassic to Lower Cretaceous geothermal aquifers in the West Netherlands Basin – an overview. *Netherlands Journal of Geosciences Vol. 99*.

Williams, J., Bandstra, J., Pollard, D., & Brantley, S. (2010). The temperature dependence of feldspar dissolution determined using a coupled weathering–climate model for Holocene-aged loess soils. *Geoderma 156*, pp. 11-19.

Winsauer, W., Shearin, H., Masson, P., & Williams, M. (1952). Resistivity of brine saturated sands in relation to pore geometry. *American Association of Petroleum Geologists Bulletin, 36*(2), 253-277.

Witmans, N., Duin, E., Doornenbal, J., Van Bergen, F., Kloosterman, F., & De Gans, W. (2004). *Geological Atlas of the Subsurface of the Netherlands. Explanation to map sheet IX Harderwijk-Nijmegen.* Utrecht: TNO-NITG Natinal Geological Survey.

Witte, H., Van Gelder, G., & Spitler, J. (2002). In situ measurement of ground thermal conductivity: the Dutch perspective. *ASHRAE Transactions, 108*(1), 263-272.

Wong, T., Batjes, D., & De Jager, J. (2007). *Geology of the Netherlands.* Amsterdam: Royal Netherlands Academy of Arts and Sciences.

Wong, T., Doornenbal, J., Duin, E., Van Bergen, F., Bos, C., Van Dalfsen, W., & Lokhorst, A. (2004). *Geological Atlas of the Subsurface of the Netherlands - onshore.* Utrecht: NITG TNO - National Geological Survey.

Wuijts, S., Schijven, J., van der Aa, N., Dik, H., Versluijs, C., & van Wijnen, H. (2007). *Bouwstenen Leidraad Grondwaterbescherming. [in Dutch: 'Building blocks Guideline Groundwater Protetction']. RIVM rapport 734301029/2007.* Bilthoven, the Netherlands: RIVM.

Xue, Y., Xie, C., & Li, Q. (1990). Aquifer thermal energy storage: A numerical simulation of field experiments in China. *Water Resources Research, 26(10)*, pp. 2365 – 2375.

Yalcin, T., & Yetemen, Y. (2009). Local warming of groundwaters caused by the urban heat island effect in Istanbul, Turkey. *Hydrogeology Journal*, pp. 1247–1255.

Yukutake, T. (2000). The inner core and the surface heat flow as clues to estimating the initial temperature of the Earth's core. *Physics of the Earth and Planetary Interiors, 121*, pp. 103-137.

Zagwijn, W. (1986). The pleistocene of The Netherlands with special reference to glaciation and terrace formation. *Quaternary Science Reviews. Vol. 5*, pp. 341-345.

Zagwijn, W. (1989). The Netherlands during the Tertiary and the Quaternary: A case history of Coastal Lowland evolution. *Geologie en Mijnbouw 68*, pp. 107-120.

Zerihun, B., Kitterod, N., Krogstad, H., & Harald & Kværnø, A. (2015). Numerical modeling of aquifer thermal energy efficiency under regional groundwater flow: A case study at Oslo Airport. *Hydrology Research*(46).

Zhang, Q., & Alves, T. (2024). Contrasting influence of salt structures and faults on the geothermal potential of regional structural highs: The Cleaver Bank High, Southern North Sea. *Geothermics 116*.

Zhu, K., Bayer, P., Grathwohl, P., & Blum, P. (2014). Groundwater temperature evolution in the subsurface urban heat island of Cologne, Germany. *Hydrological Processes 29(6)*, pp. 965–978.

Zhu, K., Blum, P., Ferguson, G., Balke, K., & Bayer, P. (2010). The geothermal potential of urban heat islands. *Environmental Research Letters, 5*.

Ziegler, P. (1992). European Cenozoic rift system. *Tectonophysics, 208*, pp. 91-111.

Zog, G., Zak, D., Ringelberg, D., MacDonald, N., Pregitzer, K., & White, D. (1997). Compositional and Functional Shifts in Microbial Communities Due to Soil Warming. *Soil Science Society of America Journal, 61(2)*, pp. 475–481.

Zuurbier, K., Hartog, N., Valstar, J., Post, V., & Van Breukelen, B. (2013). The impact of low temperature seasonal aquifer thermal energy storage (SATES) systems on chlorinated solvent contaminated groundwater: Modelling of spreading and degradation. *Journal of Contaminant Hydrology*, pp. 1-13.

Dankwoord

Sinds 2007 ben ik als geohydroloog werkzaam bij Arcadis. In 2009 besloot Arcadis deel te nemen als company participant in Wetsus (European centre of excellence for sustainable water technology). Dit bood mij de gelegenheid om als parttime PhD onderzoeker aan de slag te gaan bij TTIW-Wetsus binnen het onderzoeksthema “Underground Water Functions and Well Management”. Ik ben Hans Aalderink, destijds mijn lijnmanager bij Arcadis, dankbaar dat hij mij daarvoor heeft gevraagd. Het zou een traject van 4 jaar parttime onderzoek worden, waarbij ik een deel van mijn tijd bij KWR in Nieuwegein doorbracht. Vier jaar in parttime is wel erg optimistisch. En het hele traject tot en met afronding van dit proefschrift is dan ook een stuk langer geworden. Ik zou het iemand niet snel aanraden dit voorbeeld te volgen. Desondanks is het een mooie periode geweest, waarin ik steun heb gehad van veel mensen zonder wie dit nooit zou zijn gelukt. En die ik daar graag hartelijk voor wil bedanken.

Om te beginnen Pieter Stuijfzand. Je hebt zo in je carrière een aantal namen waar je tegenop kijkt. Pieter Stuijfzand, bekend van onder andere de “Stuyfzand classificatie” is zo een. Ik heb me daarom altijd vereerd gevoeld dat Pieter mijn promotor wilde zijn. En heb in al die jaren een niet-aflatende steun en vooral vertrouwen van Pieter ondervonden. Zonder dat vertrouwen had ik dit traject niet afgerond. Heel veel dank daarvoor. En vooral ook voor de inspanningen van het afgelopen jaar, een jaar dat voor jou persoonlijk zwaar was.

Henk Kooi, destijds werkzaam aan de Vrije Universiteit in Amsterdam, is bereid gevonden om als copromotor mijn onderzoek te begeleiden. Henk, met een altijd scherpe en kritische blik, heeft veel aan de kwaliteit van mijn werk bijgedragen. Ook sinds Henk een drukbezette baan bij Deltares heeft, was hij bereid om copromotor te blijven en vrije tijd daarvoor op te offeren. Ik ben hem daar zeer dankbaar voor.

In de periode dat ik regelmatig bij KWR aan het werk was heb ik daar veel leuke en interessante mensen mogen ontmoeten en met een aantal kunnen samenwerken. Dat zijn er teveel om allemaal hier te noemen. Maar ik wil in ieder geval Jan-Willem Kooiman danken voor zijn gastvrijheid en ondersteuning. En natuurlijk Matthijs Bonte, die gelijktijdig met mij tussen 2009 en 2013 zijn promotieonderzoek uitvoerde. Het was plezierig met Matthijs samen te werken op de locaties waar we allebei veldonderzoek deden.

In de afgelopen jaren heb ik regelmatig met Victor Bense op de Wageningen University ideeën kunnen uitwisselen, brainstormen over mogelijke onderzoeken en we hebben samen in het veld metingen gedaan. Altijd wanneer ik na een middag met Victor uit Wageningen vertrok, was het met een glimlach op mijn gezicht. Ik ben Victor dan ook dankbaar voor al de leuke uren en inspiratie. Ik dank ook Jelte de Bruin van de Wageningen University voor de fijne samenwerking tijdens de metingen die we in 2018 hebben verricht.

Ondanks de vele mensen die aan mijn promotieonderzoek hebben bijgedragen, is het soms een eenzaam traject geweest. Het is natuurlijk inherent aan een dergelijk onderzoek dat je laat zien dat zelfstandig te kunnen uitvoeren. Dat had ik nooit volgehouden zonder de steun en het begrip van mijn levensgezel Fatiha Balghiti. Lieve Fatiha, dank je wel!

Acknowledgements

This work was performed within the cooperation framework of Wetsus, European centre of excellence for sustainable water technology (www.wetsus.eu). Wetsus is co-funded by the Dutch Ministry of Economic Affairs and Ministry of Infrastructure and Environment, the Province of Fryslân and the Northern Netherlands Provinces. The author would like to thank the participants of the research theme ‘Groundwater technology’ for the fruitful discussions and their financial support.

Fieldwork would not have been possible without the co-operation of the RIVM, in particular Dr. Patrick van Beelen, and Waternet, Brabant Water and Vitens, allowing access to their monitoring wells. These persons and organizations are gratefully thanked for their assistance.

The KWR Watercycle Research Institute (KWR) and VU University Amsterdam are thanked for facilitating the research. Arcadis Nederland B.V. is thanked for allowing me to spend office hours on finalizing this thesis.

About the author

Philip Visser was born in 1962 in Zoetermeer, the Netherlands. He grew up in Roden and obtained in 1987 his MSc at Wageningen University, the Netherlands. During his university study, he spent one and a half years in Kenya. After graduation and a temporary employment at Rijkswaterstaat in Arnhem, he swiftly moved back to Kenya to work for a local company in groundwater exploration and groundwater management. From 1991 to 1993, Philip worked in Yemen in a TNO project at the General Department of Hydrogeology of the Ministry of Oil in Sana'a. After that period, he was employed in the Natural Resources section of the United Nations Economic and Social Commission for Asia and the Pacific (ESCAP) in Bangkok, Thailand. Upon return to the Netherlands in 1995, he first worked for Fugro as a hydrogeologist, mainly in the field of groundwater contamination and remediation. In 2001 he made a career switch by accepting an employment as a policy maker for the province of Flevoland. Groundwater contamination and groundwater protection for drinking water supply were his main focus. Strong growth of aquifer thermal energy storage (ATES) systems during this period sparked his interest in this technology and concerns about the possible environmental impacts. From 2007 to date, he is working with Arcadis as a hydrogeologist. In 2009, Philip initiated the part-time PhD study, next to his full-time job for Arcadis. The study was carried out at Delft University of Technology, KWR (Watercycle Research Institute), VU University Amsterdam and Wetsus (European centre of excellence for sustainable water technology).

Publications

<u>Books</u>

Visser, P. (1995). *Guidebook to Water Resources, Use and Management in Asia and the Pacific. Volume one: Water resources and Water use. Water Resources Series No.74.* New York: United Nations.

<u>Peer reviewed papers</u>

Visser, P., Kooi, H., & Stuyfzand, P. (2015). The thermal impact of aquifer thermal energy storage (ATES) systems: a case study in the Netherlands, combining monitoring and modeling. *Hydrogeology Journal*.

Visser, P., Kooi, H., Bense, V., & Boerma, E. (2020). Impacts of progressive urban expansion on subsurface temperatures in the city of Amsterdam (The Netherlands). *Hydrogeology Journal* , pp. 1755-1772.

Bense, V., de Bruin, J., Kurylyk, B., & Visser, P. (2020). Transient subsurface thermal profiles reveal temporal variability in groundwater flow conditions. *Water Resources Research*.

Veldkamp, A., & Visser, P. (1992). Erosion surfaces in the Chuka-South area, Central Kenya. *Zeitschrift für Geomorphologie. Supplementbände 84*, pp. 147-158.

Professional journals

Rawee, N., Visser, P., & Vlaar, T. (2008). Funderingstechnieken in grondwaterbeschermingsgebieden. *H2O #22*.

Wesselingh, F., Visser, P., & Meijer, T. (2010). Het Eemien in zuidelijk Flevoland: een blik in de bodem van het bekken van Amersfoort. *Afzettingen WTKG 31 (4)*, pp. 87-91.

Bonte, M., Stuyfzand, P., van Beelen, P., & Visser, P. (2010). Onderzoek naar duurzame toepassing van warmte-/koudeopslag. *H2O #3*, pp. 30-32.

Conference contributions

Bonte, M., Visser, P., Stuyfzand, P., Kooi, H., & van Breukelen, B. (2011). Effects of aquifer thermal energy storage on groundwater quality elucidated by field and laboratory investigations. *Congress Bodemenergie 13-14 oktober 2011.*

De Bruin, J., Visser, P., & Bense, V. (2019). Subsurface temperature impacts of groundwater abstraction. *Geophysical Research Abstracts, Vol. 21, , EGU2019-7594, 2019. EGU General Assembly 2019.* Vienna: EGU.

Kooi, H., Visser, P., & Bonte, M. (2011). Geothermie van de Nederlandse ondergrond tot enkele honderden meters onder maaiveld. *Congres Bodemenergie 13-14 oktober 2011.*

Randhawa, D., Flanders, C., & Visser, P. (2016). Thermal In Situ Sustainable Remediation (TISR): Linking Renewable Energy to Sustainable Site Restoration. *H.V. Rectanus and P. Rodgers (Chairs). Remediation of Chlorinated and Recalcitrant Compounds—2016. Tenth International Conference on Remediation of Chlorinated and Recalcitrant Compounds.* Palm Springs, CA.

Veldkamp, A., & Visser, P. (1989). Erosion surfaces in the Chuka-South area, Central Kenya. *Abstracts 2nd International Conference Geomorphology and Geo-ecology. Geoöko-PLUS Vol. 1* (p. 304). Bensheim: Geook-Verlag W. Seuffert.

Visser, P., Bense, V., & De Bruin, J. (2019). Impact of climate change and land use change on groundwater quality through changes in subsurface temperatures. *Groundwater Quality 2019.* Liege.

Visser, P., Kooi, H., & Bonte, M. (2011). Invloed van WKO op de warmtehuishouding van de ondergrond in relatie tot natuurlijke en artificiele invloeden. *Congres Bodemenergie 13-14 oktober 2011.*